

1

²A SEARCH FOR LONG-LIVED, CHARGED, SUPERSYMMETRIC PARTICLES
³USING IONIZATION WITH THE ATLAS DETECTOR

4

BRADLEY AXEN

5

September 2016 – Version 0.67

6



⁸ Bradley Axen: *A Search for Long-Lived, Charged, Supersymmetric Particles using*
⁹ *Ionization with the ATLAS Detector*, Subtitle, © September 2016

¹⁰ The dissertation of Bradley Axen, titled *A Search for Long-Lived, Charged, Super-*
¹¹ *symmetric Particles using Ionization with the ATLAS Detector*, is approved:

¹² _____
¹³ Chair Date

¹⁴ _____
¹⁵ Date

¹⁶ _____
¹⁷ Date

¹⁸ University of California, Berkeley

19 ABSTRACT

20 Several extensions of the Standard Model predict the existence of charged, very
21 massive, and long-lived particles. Because of their high masses these particles
22 would propagate non-relativistically through the ATLAS pixel detector and would
23 therefore be identifiable through a measurement of large specific energy loss.
24 Measuring heavy, long-lived particles through their track parameters in the pixel
25 detector allows sensitivity to particles with lifetimes in the nanosecond range
26 and above. This dissertation presents an inner detector driven method for iden-
27 tifying such particles in proton-proton collisions at 13 TeV with the 2015 LHC
28 dataset corresponding to an integrated luminosity of 3.5 pb^{-1} .

To be filled.

³⁰ ACKNOWLEDGEMENTS

³¹ To be filled.

³²

33 CONTENTS

34	1	INTRODUCTION	1
35	I	THEORETICAL CONTEXT	3
36	2	STANDARD MODEL	5
37	2.1	Action and the Lagrangian	5
38	2.2	Gauge Invariance and Forces	6
39	2.2.1	$SU(2) \times U(1)$ and the Electroweak Force	8
40	2.2.2	$SU(3)$ and the Strong Force	8
41	2.3	Noether's Theorem, Charges, and Matter	9
42	2.3.1	Quarks	9
43	2.3.2	Leptons	10
44	2.3.3	Chirality	11
45	2.4	Higgs Mechanism and Mass	11
46	2.5	Phenomenology	13
47	2.5.1	Standard Model Calculations	13
48	2.5.2	Electroweak Physics	15
49	2.5.3	Strong Physics	15
50	2.5.4	Proton-Proton Collisions	16
51	2.5.5	Simulation	16
52	2.6	Limitations	17
53	2.6.1	Theoretical Concerns	18
54	2.6.2	Cosmological Observations	18
55	3	SUPERSYMMETRY	21
56	3.1	Structure	21
57	3.2	Motivation	23
58	3.3	Simplified Models	24
59	3.4	Long-Lived Particles	25
60	II	EXPERIMENTAL STRUCTURE AND RECONSTRUCTION	27
61	4	THE LARGE HADRON COLLIDER	29
62	4.1	Injection Chain	30
63	4.2	Design	31
64	4.2.1	Layout	31
65	4.2.2	Magnets	32
66	4.2.3	Radio Frequency Cavities	33
67	4.2.4	Beam	35
68	4.3	Luminosity Parameters	35
69	4.4	Delivered Luminosity	37
70	5	THE ATLAS DETECTOR	39
71	5.1	Coordinate System	41
72	5.2	Magnetic Field	42
73	5.3	Inner Detector	44

74	5.3.1	Pixel Detector	47
75	5.3.2	Semiconductor Tracker	49
76	5.3.3	Transition Radiation Tracker	51
77	5.4	Calorimetry	51
78	5.4.1	Electromagnetic Calorimeter	53
79	5.4.2	Hadronic Calorimeters	54
80	5.5	Muon Spectrometer	56
81	5.5.1	Monitored Drift Tube	58
82	5.5.2	Resistive Plate Chamber	59
83	5.5.3	Cathode Strip Chamber	59
84	5.5.4	Thin Gap Chamber	59
85	5.6	Trigger	61
86	6	EVENT RECONSTRUCTION	65
87	6.1	Charged Particles	65
88	6.1.1	Pixel Neural Network	68
89	6.1.2	Pixel dE/dx	69
90	6.1.3	Vertex Reconstruction	70
91	6.2	Electrons and Photons	71
92	6.2.1	Photon Identification	72
93	6.2.2	Electron Identification	72
94	6.3	Muons	73
95	6.3.1	Muon Identification	73
96	6.4	Jets	74
97	6.4.1	Topological Clustering	74
98	6.4.2	Jet Algorithms	75
99	6.4.3	Jet Energy Scale	76
100	6.5	Missing Transverse Energy	77
101	III	CALORIMETER RESPONSE	79
102	7	RESPONSE MEASUREMENT WITH SINGLE HADRONS	81
103	7.1	Dataset and Simulation	82
104	7.1.1	Data Samples	82
105	7.1.2	Simulated Samples	82
106	7.1.3	Event Selection	82
107	7.2	Inclusive Hadron Response	83
108	7.2.1	E/p Distribution	83
109	7.2.2	Zero Fraction	84
110	7.2.3	Neutral Background Subtraction	86
111	7.2.4	Corrected Response	87
112	7.2.5	Additional Studies	89
113	7.3	Identified Particle Response	92
114	7.3.1	Decay Reconstruction	93
115	7.3.2	Identified Response	94
116	7.3.3	Additional Species in Simulation	96
117	7.4	Summary	96
118	8	JET ENERGY RESPONSE AND UNCERTAINTY	99

119	8.1	Motivation	99
120	8.2	Uncertainty Estimate	99
121	8.3	Summary	102
122	IV	SEARCH FOR LONG-LIVED PARTICLES	105
123	9	LONG-LIVED PARTICLES IN ATLAS	107
124	9.1	Event Topology	107
125	9.1.1	Detector Interactions	108
126	9.1.2	Lifetime Dependence	110
127	9.2	Simulation	113
128	10	EVENT SELECTION	117
129	10.1	Trigger	118
130	10.2	Kinematics and Isolation	119
131	10.3	Particle Species Rejection	123
132	10.4	Ionization	127
133	10.4.1	Mass Estimation	127
134	10.5	Event Selection	129
135	11	BACKGROUND ESTIMATION	131
136	11.1	Background Sources	131
137	11.2	Prediction Method	132
138	11.3	Validation	133
139	11.3.1	Closure in Simulation	133
140	11.3.2	Validation Region in Data	134
141	11.4	Expected Background	135
142	12	SYSTEMATIC UNCERTAINTIES	137
143	12.1	Background Estimate	137
144	12.1.1	Analytic Description of dE/dx	138
145	12.1.2	Muon Fraction	138
146	12.1.3	IBL Corrections	138
147	12.1.4	Normalization	138
148	12.2	Signal Yield	139
149	12.2.1	initial state radiation (ISR) Modeling	139
150	12.2.2	Pileup Reweighting	139
151	12.2.3	Trigger Efficiency Reweighting	140
152	12.2.4	Missing Transverse Momentum Scale	141
153	12.2.5	Momentum Parametrization	141
154	12.2.6	Ionization Requirement	142
155	12.2.7	Electron and Jet Rejection	142
156	12.2.8	Muon Veto	142
157	12.2.9	Luminosity	143
158	12.2.10	Signal Cross Section	143
159	13	RESULTS	145
160	13.1	Cross Section Limits	145
161	13.2	Mass Limits	148
162	14	SUMMARY AND OUTLOOK	153

163	V APPENDIX	155
164	A EXPANDED R-HADRON YIELDS AND LIMITS	157
165	BIBLIOGRAPHY	163

166 LIST OF FIGURES

167	Figure 1	A Feynman diagram representing the interaction of the A field with a generic fermion, f	8
168	Figure 2	The particle content of the SM, including the names, masses, spins, and charges of each of the particles.	10
170	Figure 3	A feynman diagram for photon propagation including a loop of electrons.	14
172	Figure 4	An approximation of the running of the coupling constants in the SM up to the Planck scale [2].	14
174	Figure 5	The Feynman diagrams representing the decays of the W and Z bosons to fermions. Here f indicates a generic fermion, \bar{f} its antiparticle, and f' the partner of that fermion in the same generation.	15
176	Figure 6	The PDFs for proton-proton collisions at $Q^2 = 10 \text{ GeV}^2$ and $Q^2 = 10^4 \text{ GeV}^2$. Each shows the fraction x of the total proton energy at the specified scale [4]. The distribution for gluons is scaled by 0.1 to fit within the axis range.	17
178	Figure 7	The distribution of velocities of stars as a function of the radius from the center of the galaxy. The contributions to the velocity from the various components of matter in the galaxy are shown [8].	19
180	Figure 8	An approximation of the running of the coupling constants in the MSSM up to the Planck scale [2].	24
182	Figure 9	The decay of a gluino to quarks and an LSP, which precedes through a squark.	25
184	Figure 10	The four collision points and corresponding experiments of the LHC. The image includes the location of the nearby city of Geneva as well as the border of France and Switzerland [21].	30
186	Figure 11	The cumulative luminosity over time delivered to the ATLAS experiment from high energy proton-proton collisions since 2011. The energies of the collisions are listed for each of the data-taking periods. The figure shows the delivered luminosity as of the conclusion of data collection in 2016 [22].	31
188	Figure 12	The accelerator complex that builds up to the full design energies at the LHC. The protons are passed in order to Linac 2, the PSB, the PS, the SPS and then the LHC [23].	32

206	Figure 13	A schematic of the layout of the LHC, not to scale. The arched and straight sections are illustrated at the bottom of the schematic, and all four crossing sites are indicated with their respective experiments [14].	33
207			
208			
209			
210	Figure 14	A cross section of the the cryodipole magnets which bend the flight path of protons around the circumference of the LHC. The diagram includes both the superconducting coils which produce the magnetic field and the structural elements which keep the magnets precisely aligned [14].	34
211			
212			
213			
214			
215			
216	Figure 15	The arrangement of four RF cavities within a cryomodule [14].	34
217			
218	Figure 16	The cumulative luminosity versus time delivered to ATLAS (green), recorded by ATLAS (yellow), and certified to be good quality data (blue) during stable beams for pp collisions at 13 TeV in 2015 [22].	37
219			
220			
221			
222	Figure 17	The luminosity-weighted distribution of the mean number of interactions per crossing for the 2015 pp collision data at 13 TeV [22].	38
223			
224			
225	Figure 18	A cut-away schematic of the layout of the ATLAS detector. Each of the major subsystems is indicated [17]. .	40
226			
227	Figure 19	A cross-sectional slice of the ATLAS experiment which illustrates how the various SM particles interact with the detector systems.	40
228			
229			
230	Figure 20	The layout of the four superconducting magnets in the ATLAS detector [17].	43
231			
232	Figure 21	A quarter section of the ATLAS inner detector which shows the layout of each of the subdetectors in detail. The lower panel shows an enlarged view of the pixel detector. Example trajectories for a particle with $\eta = 1.0, 1.5, 2.0, 2.5$ are shown. The IBL, which was added after the original detector commissioning, is not shown [17].	45
233			
234			
235			
236			
237			
238	Figure 22	A computer generated three-dimensional view of the inner detector along the line of the beam axis. The subdetectors and their positions are labeled [17].	46
239			
240			
241	Figure 23	An alternative computer generated three-dimensional view of the inner detector transverse to the beam axis. The subdetectors and their positions are labeled [17]. .	46
242			
243			
244	Figure 24	The integrated radiation lengths traversed by a particle at the exit of the ID envelope (outside of the TRT after 108.2 cm), including the services and thermal enclosures. The distribution is shown as a function of $ \eta $ and averaged over ϕ . The breakdown indicates the contributions of individual sub-detectors, including services in their active volume [17].	47
245			
246			
247			
248			
249			
250			

251	Figure 25	A cut away image of the outer three layers of the pixel detector [17].	48
252			
253	Figure 26	An image of the insertion of the IBL into the current pixel detector [25].	49
254			
255	Figure 27	A three-dimensional computer-generated image of the geometry of the IBL with a view (a) mostly transverse to the beam pipe (b) mostly parallel to the beam pipe [24].	50
256			
257			
258	Figure 28	An expanded view of the geometry of the SCT double layers in the barrel region [17].	50
259			
260	Figure 29	An overview of the ATLAS calorimeter systems [17]. . .	52
261	Figure 30	The depth of (a) the electromagnetic barrel calorimeter in radiation lengths and of (b) all calorimeters in interaction lengths as a function of pseudorapidity [17].	53
262			
263			
264	Figure 31	A schematic of the LAr calorimeter in the barrel region, highlighting the accordion structure [17].	53
265			
266	Figure 32	A schematic of a hadronic tile module which shows the alternating layers of steel and plastic scintillator [17].	55
267			
268	Figure 33	The segmentation in depth and η of the tile-calorimeter modules in the central (left) and extended (right) barrels [17].	55
269			
270			
271	Figure 34	A cut-away diagram of the muon systems on ATLAS [17].	56
272	Figure 35	A quarter view of the muon spectrometer which highlights the layout of each of the detecting elements. The BOL, BML, BIL, EOL, EML, and EIL are all MDT elements, where the acronyms encode their positions [17].	57
273			
274			
275			
276	Figure 36	A schematic of the cross-section of the muon spectrometer in the barrel region [17].	57
277			
278	Figure 37	A schematic of a single MDT chamber, which shows the multilayers of drift tubes as well as the alignment system [17].	58
279			
280			
281	Figure 38	A schematic of the CSC endcap, showing the overlapping arrangement of the eight large and eight small chambers [17].	60
282			
283			
284	Figure 39	A schematic of the TGC doublet and triplet layers [17]. .	60
285	Figure 40	The L1 Trigger rate broken down into the types of triggers as a function of the luminosity block for the 2015 data collection period [26].	62
286			
287			
288	Figure 41	The HLT Trigger rate broken down into the types of triggers as a function of the luminosity block for the 2015 data collection period.	63
289			
290			
291	Figure 42	An illustration of the perigee representation of track parameters for an example track. The charge is not directly shown, but is indicated by the direction of curvature of the track [29].	66
292			
293			
294			

295	Figure 43	The x and y locations of the hits generated in a simulated $t\bar{t}$ event in the inner detector. The hits which belong to tracks formed using the inside-out algorithm are highlighted in red, while the hits which belong to tracks formed using the outside-in algorithm are circled in black. This figure does not include hits in the IBL.	67
296			
297			
298			
299			
300			
301			
302	Figure 44	The tracking reconstruction efficiency as a function of (a) η and (b) p_T [30].	68
303			
304	Figure 45	Examples of the clusters formed in a single layer of the pixel detector for (a) a single isolated particle, (b) two nearly-overlapping particles, and (c) a particle which emits a δ -ray [31].	69
305			
306			
307			
308	Figure 46	The vertex reconstruction efficiency as a function of the number of associated tracks [33].	71
309			
310	Figure 47	The total, fractional JES uncertainties estimated for 2015 data as a function of jet p_T	77
311			
312	Figure 48	The E/p distribution and ratio of simulation to data for isolated tracks with (a) $ \eta < 0.6$ and $1.2 < p/\text{GeV} < 1.8$ and (b) $ \eta < 0.6$ and $2.2 < p/\text{GeV} < 2.8$	84
313			
314			
315	Figure 49	The fraction of tracks as a function (a, b) of momentum, (c, d) of interaction lengths with $E \leq 0$ for tracks with positive (on the left) and negative (on the right) charge.	85
316			
317			
318			
319	Figure 50	An illustration (a) of the geometry of energy deposits in the calorimeter. The red energy deposits come from the charged particle targeted for measurement, while the blue energy deposits are from nearby neutral particles and must be subtracted. The same diagram (b) for the neutral-background selection, described in Section 7.2.3.	86
320			
321			
322			
323			
324			
325			
326	Figure 51	$\langle E/p \rangle_{\text{BG}}$ as a function of the track momentum for tracks with (a) $ \eta < 0.6$, (b) $0.6 < \eta < 1.1$, and as a function of the track pseudorapidity for tracks with (c) $1.2 < p/\text{GeV} < 1.8$, (d) $1.8 < p/\text{GeV} < 2.2$	87
327			
328			
329			
330	Figure 52	$\langle E/p \rangle_{\text{COR}}$ as a function of track momentum, for tracks with (a) $ \eta < 0.6$, (b) $0.6 < \eta < 1.1$, (c) $1.8 < \eta < 1.9$, and (d) $1.9 < \eta < 2.3$	88
331			
332			
333	Figure 53	$\langle E/p \rangle_{\text{COR}}$ calculated using LCW-calibrated topological clusters as a function of track momentum for tracks with (a) zero or more associated topological clusters or (b) one or more associated topological clusters.	89
334			
335			
336			
337	Figure 54	Comparison of the $\langle E/p \rangle_{\text{COR}}$ for tracks with (a) less than and (b) greater than 20 hits in the TRT.	90
338			

339	Figure 55	Comparison of the $\langle E/p \rangle_{\text{COR}}$ for (a) positive and (b) negative tracks as a function of track momentum for tracks with $ \eta < 0.6$	91
340			
341			
342	Figure 56	Comparison of the E/p distributions for (a) positive and (b) negative tracks with $0.8 < p/\text{GeV} < 1.2$ and $ \eta < 0.6$, in simulation with the FTFP_BERT and QGSP_BERT physics lists.	91
343			
344			
345			
346	Figure 57	Comparison of the response of the hadronic calorimeter as a function of track momentum (a) at the EM-scale and (b) after the LCW calibration.	92
347			
348			
349	Figure 58	Comparison of the response of the EM calorimeter as a function of track momentum (a) at the EM-scale and (b) with the LCW calibration.	92
350			
351			
352	Figure 59	The reconstructed mass peaks of (a) K_S^0 , (b) Λ , and (c) $\bar{\Lambda}$ candidates.	93
353			
354	Figure 60	The E/p distribution for isolated (a) π^+ , (b) π^- , (c) proton, and (d) anti-proton tracks.	94
355			
356	Figure 61	The fraction of tracks with $E \leq 0$ for identified (a) π^+ and π^- , and (b) proton and anti-proton tracks	95
357			
358	Figure 62	The difference in $\langle E/p \rangle$ between (a) π^+ and π^- (b) p and π^+ , and (c) \bar{p} and π^-	96
359			
360	Figure 63	$\langle E/p \rangle_{\text{COR}}$ as a function of track momentum for (a) π^+ tracks and (b) π^- tracks.	97
361			
362	Figure 64	The ratio of the calorimeter response to single particles of various species to the calorimeter response to π^+ with the physics list FTFP_BERT.	97
363			
364			
365	Figure 65	The spectra of true particles inside anti- k_t , $R = 0.4$ jets with (a) $90 < p_T/\text{GeV} < 100$, (b) $400 < p_T/\text{GeV} < 500$, and (c) $1800 < p_T/\text{GeV} < 2300$	100
366			
367			
368	Figure 66	The JES response uncertainty contributions, as well as the total JES uncertainty, as a function of jet p_T for (a) $ \eta < 0.6$ and (b) $0.6 < \eta < 1.1$	103
369			
370			
371	Figure 67	The correlations between bins of average reconstructed jet momentum as a function of jet p_T and $ \eta $ for jets in the central region of the detector.	104
372			
373			
374	Figure 68	The processes which contribute to gluino pair production in the proton proton collisions, where the quarks and gluons are proton constituents.	108
375			
376			
377	Figure 69	The generated p_T and β distributions for R-Hadrons with $M = 1600 \text{ GeV}$	108
378			
379	Figure 70	A schematic diagram of an R-Hadron event with a lifetime around 0.01 ns. The diagram includes one charged R-Hadron (solid blue), one neutral R-Hadron (dashed blue), LSPs (dashed green) and charged hadrons (solid orange). The pixel detector, calorimeters, and muon system are illustrated but not to scale.	111
380			
381			
382			
383			
384			

385	Figure 71	Schematic diagram of an R-Hadron event with a life-time around 5 ns, where the masses of the R-Hadron and LSP are nearly degenerate. The diagram includes charged R-Hadrons (solid blue), neutral R-Hadrons (dashed blue), LSPs (dashed green) and charged hadrons (solid orange). The pixel detector, calorimeters, and muon system are illustrated but not to scale.	112
386			
387			
388			
389			
390			
391			
392	Figure 72	Schematic diagram of an R-Hadron event with a life-time around 5 ns, where the masses of the R-Hadron and LSP are not degenerate. The diagram includes charged R-Hadrons (solid blue), neutral R-Hadrons (dashed blue), LSPs (dashed green) and charged hadrons (solid orange). The pixel detector, calorimeters, and muon system are illustrated but not to scale.	113
393			
394			
395			
396			
397			
398			
399	Figure 73	A schematic diagram of an R-Hadron event with a life-time around 20 ns. The diagram includes one charged R-Hadron (solid blue), one neutral R-Hadron (dashed blue), LSPs (dashed green) and charged hadrons (solid orange). The pixel detector, calorimeters, and muon system are illustrated but not to scale.	114
400			
401			
402			
403			
404			
405	Figure 74	A schematic diagram of a VLL R-Hadron event. The diagram includes one charged R-Hadron (solid blue) and one neutral R-Hadron (dashed blue). The pixel detector, calorimeters, and muon system are illustrated but not to scale.	115
406			
407			
408			
409			
410	Figure 75	The distribution of (a) E_T^{miss} and (b) Calorimeter E_T^{miss} for simulated signal events before the trigger requirement. The final bin includes all events above the axis range.	119
411			
412			
413			
414	Figure 76	The distribution of E_T^{miss} for data and simulated signal events, after the trigger requirement. The final bin includes all events above the axis range.	120
415			
416			
417	Figure 77	The trigger efficiency for the HLT_xe70 trigger requirement as a function of (a) E_T^{miss} and (b) Calorimeter E_T^{miss} for simulated signal events.	121
418			
419			
420	Figure 78	The dependence of dE/dx on N_{split} in data after basic track hit requirements have been applied.	122
421			
422	Figure 79	The distribution of dE/dx with various selections applied in data and simulated signal events. The final bin includes all tracks above the axis range.	122
423			
424			
425	Figure 80	The distribution of track momentum for data and simulated signal events, after previous selection requirements have been applied. The final bin includes all tracks above the axis range.	123
426			
427			
428			

429	Figure 81	The distribution of M_T for data and simulated signal events, after previous selection requirements have been applied. The final bin includes all tracks above the axis range.	124
430			
431			
432			
433	Figure 82	The distribution of summed tracked momentum within a cone of $\Delta R < 0.25$ around the candidate track for data and simulated signal events, after previous selection requirements have been applied. The final bin includes all tracks above the axis range.	125
434			
435			
436			
437			
438	Figure 83	The normalized, two-dimensional distribution of E/p and f_{EM} for simulated (a) 1200 GeV very long-lived (VLL) R-Hadron, and (b) 1200 GeV, 10 ns R-Hadron, (c) $Z \rightarrow ee$, and (d) $Z \rightarrow \tau\tau$ events.	126
439			
440			
441			
442	Figure 84	Two-dimensional distribution of dE/dx versus charge signed momentum (qp) for minimum-bias tracks. The fitted distributions of the most probable values for pions, kaons and protons are superimposed.	128
443			
444			
445			
446	Figure 85	The distribution of mass estimated using dE/dx for simulated VLL R-Hadrons with masses between 1000 and 1600 GeV.	128
447			
448			
449	Figure 86	The acceptance \times efficiency as a function of R-Hadron (a) mass and (b) lifetime. (a) shows all of the combinations of mass and lifetime considered in this search, and (b) highlights the lifetime dependence for 1000 GeV and 1600 GeV R-Hadrons.	130
450			
451			
452			
453			
454	Figure 87	The distribution of (a) dE/dx and (b) momentum for tracks in data and simulated signal after requiring the event level selection and the track selection on p_T , hits, and N_{split} . Each sub-figure shows the normalized distributions for tracks classified as hadrons, electrons, and muons in data and R-Hadrons in the simulated signal.	132
455			
456			
457			
458			
459			
460			
461	Figure 88	The distribution of $M_{dE/dx}$ (a) before and (b) after the ionization requirement for tracks in simulated W boson decays and for the randomly generated background estimate.	134
462			
463			
464			
465	Figure 89	The distribution of $M_{dE/dx}$ (a) before and (b) after the ionization requirement for tracks in the validation region and for the randomly generated background estimate.	135
466			
467			
468			
469	Figure 90	The trigger efficiency for the HLT_xe70 trigger requirement as a function of Calorimeter E_T^{miss} for simulated data events with a W boson selection. Simulated signal events and simulated W boson events are also included.	140
470			
471			
472			
473			

474	Figure 91	The efficiency of the muon veto for R -hadrons of two different masses, as a function of $\frac{1}{\beta}$ for simulated R-Hadron tracks.	143
475			
476			
477	Figure 92	The average reconstructed MDT β distribution for $Z \rightarrow \mu\mu$ events in which one of the muons has a late arrival time in the MDT, for both data and simulation. A gaussian fit is superimposed.	144
478			
479			
480			
481	Figure 93	The observed mass distribution of events in data and the generated background distribution in (a) the VLL and (b) the LL signal region. A few example simulated signal distributions are superimposed.	146
482			
483			
484			
485	Figure 94	The observed and expected cross section limits as a function of mass for the VLL simulated signal. The predicted cross section values for the corresponding signals are also shown.	148
486			
487			
488			
489	Figure 95	The observed and expected cross section limits as a function of mass for each generated lifetime. The predicted cross section values for the corresponding signals are also shown. An example of Run 1 cross section limits and predicted cross sections are shown in (d) for comparison.	149
490			
491			
492			
493			
494			
495	Figure 96	The excluded range of masses as a function of gluino lifetime. The expected lower limit (LL), with its experimental $\pm 1\sigma$ band, is given with respect to the nominal theoretical cross section. The observed 95% LL obtained at $\sqrt{s} = 8$ TeV [92] is also shown for comparison.	151
496			
497			
498			
499			
500	Figure 97	The constraints on the gluino mass as a function of lifetime for a split-supersymmetry model with the gluino R-Hadrons decaying into a gluon or light quarks and a neutralino with mass of 100 GeV. The solid lines indicate the observed limits, while the dashed lines indicate the expected limits. The area below the curves is excluded. The dots represent results for which the particle is assumed to be prompt or VLL. This curve representing this analysis is shown in orange.	154
501			
502			
503			
504			
505			
506			
507			
508			

509 LIST OF TABLES

510 Table 1	The particles in the SM and their corresponding superpartners in the MSSM	22
511		
512 Table 2	The design parameters of the LHC beam that determines the energy of collisions and the luminosity, for both the injection of protons, at the nominal circulation, and during the 2015 data-taking period.	36
513		
514		
515		
516 Table 3	The performance goals for each of the subsystems of the ATLAS detector. The $ \eta $ coverage specifies the range where the subsystem needs to be able to provide measurements with the specified resolution. The resolutions include a p_T or E dependence that is added in quadrature with a p_T/E independent piece.	41
517		
518		
519		
520		
521		
522 Table 4	A summary of the parameters of each of the three magnet systems on ATLAS.	43
523		
524 Table 5	A summary of the parameters of the inner detector and each of the subdetectors [17].	48
525		
526 Table 6	A subset of the trigger menu for the 2015 data collection with $L = 5 \times 10^{33} \text{ cm}^{-2} \text{ s}^{-1}$. Both the L1 and HLT selection requirements and their trigger rates are shown measured at the specified luminosity are shown. The typical offline selections represent a typical set of offline requirements imposed after the trigger in an analysis [26].	62
527		
528		
529		
530		
531		
532		
533 Table 7	The dominant sources of corrections and systematic uncertainties in the JES estimation technique, including typical values for the correcting shift (Δ) and the associated uncertainty (σ).	101
534		
535		
536		
537 Table 8	The radial distances of each of the subdetectors and example arrival times for an R-Hadron with $\eta = 0$ and the specified β	109
538		
539		
540 Table 9	The expected number of events at each level of the selection for long-lived (LL) 1600 GeV, 10 ns R-Hadrons, along with the number of events observed in data, for 3.2 fb^{-1} . The simulated yields are shown with statistical uncertainties only. The total efficiency \times acceptance is also shown for the signal and the rejection factor relative to initial track requirement is shown for data. 129	129
541		
542		
543		
544		
545		
546		
547 Table 10	The expected number of background events within each of the mass windows for the stable and metastable signal regions.	136
548		
549		

550	Table 11	A summary of the sources of systematic uncertainty for the data-driven background in the signal region. If the uncertainty depends on the mass, the maximum values are reported.	137
551			
552			
553			
554	Table 12	A summary of the sources of systematic uncertainty for the simulated signal yield. The uncertainty depends on the mass and lifetime, and the maximum negative and positive values are reported in the table.	139
555			
556			
557			
558	Table 13	Example of the contributing systematic variations to the total systematic for the E_T^{miss} Scale, as measured in a 1200 GeV, VLL R-Hadron signal sample.	141
559			
560			
561	Table 14	The estimated number of background events and the number of observed events in data for the specified selection regions prior to the requirement on mass. The background estimates show statistical and systematic uncertainties.	145
562			
563			
564			
565			
566	Table 15	The left and right extremum of the mass window for each generated mass point with a 10 ns lifetime.	146
567			
568	Table 16	The left and right extremum of the mass window used for each generated VLL mass point.	146
569			
570	Table 17	The expected number of signal events, the expected number of background events, and the observed number of events in data with their respective statistical errors within the respective mass window for each generated VLL mass point	147
571			
572			
573			
574			
575	Table 18	The expected number of signal events, the expected number of background events, and the observed number of events in data with their respective statistical errors within the respective mass window for each generated mass point with a lifetime of 10 ns.	147
576			
577			
578			
579			
580	Table 19	The observed and expected 95% CL lower limit on mass for gluino R-Hadrons for each considered lifetime.	150
581			
582	Table 20	The left and right extremum of the mass window for each generated mass point with a 50 ns lifetime.	157
583			
584	Table 21	The left and right extremum of the mass window for each generated mass point with a 30 ns lifetime.	157
585			
586	Table 22	The left and right extremum of the mass window for each generated mass point with a 10 ns lifetime.	158
587			
588	Table 23	The left and right extremum of the mass window used for each generated mass point with a lifetime of 3 ns.	158
589			
590	Table 24	The left and right extremum of the mass window used for each mass point with a lifetime of 1 ns.	158
591			
592	Table 25	The left and right extremum of the mass window for each generated mass point with a lifetime of 0.4 ns.	159
593			
594	Table 26	The left and right extremum of the mass window used for each generated stable mass point.	159
595			

596	Table 27	The expected number of signal events, the expected number of background events, and the observed number of events in data with their respective statistical errors within the respective mass window for each generated mass point with a lifetime of 50 ns.	159
597			
598			
599			
600			
601	Table 28	The expected number of signal events, the expected number of background events, and the observed number of events in data with their respective statistical errors within the respective mass window for each generated mass point with a lifetime of 30 ns.	160
602			
603			
604			
605			
606	Table 29	The expected number of signal events, the expected number of background events, and the observed number of events in data with their respective statistical errors within the respective mass window for each generated mass point with a lifetime of 10 ns.	160
607			
608			
609			
610			
611	Table 30	The expected number of signal events, the expected number of background events, and the observed number of events in data with their respective statistical errors within the respective mass window for each generated mass point with a lifetime of 3 ns.	161
612			
613			
614			
615			
616	Table 31	The expected number of signal events, the expected number of background events, and the observed number of events in data with their respective statistical errors within the respective mass window for each generated mass point with a lifetime of 1 ns.	161
617			
618			
619			
620			
621	Table 32	The expected number of signal events, the expected number of background events, and the observed number of events in data with their respective statistical errors within the respective mass window for each generated mass point with a lifetime of p4 ns.	162
622			
623			
624			
625			
626	Table 33	The expected number of signal events, the expected number of background events, and the observed number of events in data with their respective statistical errors within the respective mass window for each generated stable mass point	162
627			
628			
629			
630			

631 ACRONYMS

- 632 SM Standard Model
633 CERN European Organization for Nuclear Research
634 SUSY Supersymmetry
635 MSSM Minimal Supersymmetric Model
636 cMSSM Constrained MSSM
637 pMSSM Phenomenological MSSM
638 LSP Lightest Supersymmetric Particle
639 LHC Large Hadron Collider
640 ATLAS A Toroidal LHC ApparatuS
641 CMS Compact Muon Solenoid
642 ALICE A Large Ion Collider Experiment
643 LHCb Large Hadron Collider beauty experiment
644 LEP the Large Electron Positron collider
645 PS Proton Synchrotron
646 PSB Proton Synchrotron Booster
647 SPS Super Proton Synchrotron
648 SCT silicon microstrip
649 TRT Transition Radiation Tracker
650 LAr liquid argon
651 EM electromagnetic
652 RPC Resistive Plate Chamber
653 TGC Thin Gap Chamber
654 MDT Monitored Drift Tube
655 CSC Cathode Strip Chamber
656 ToT time over threshold
657 RoI Region of Interest

- 658 LCW local cluster weighted
659 MIP minimally ionizing particle
660 IP impact parameter
661 EPJC European Physical Journal C
662 JES jet energy scale
663 LLP Long-Lived Particle
664 LL long-lived
665 VLL very long-lived
666 CR Control Region
667 LO leading order
668 NLO next-to-leading order
669 NLL next-to-leading logarithmic
670 PDF parton distribution function
671 ISR initial state radiation
672 RMS root mean square
673 IBL Insertible B-Layer
674 CP Combined Performance
675 MDT Monitored Drift Tube
676 RF radiofrequency
677 L1 Level 1
678 HLT high level trigger
679 QCD quantum chromodynamics
680 BSM Beyond the Standard Model

681

682 INTRODUCTION

683 As of 2012, with the discovery of the Higgs boson, the Standard Model ([SM](#)) pro-
684 vides a complete and validated description of the interactions of fundamental
685 particles. It describes a remarkable range of phenomena given its simple foun-
686 dation, and has been successful in explaining high energy physics in all experi-
687 ments yet performed. However, it is clear that the picture is incomplete: without
688 a description of gravity or an explanation for dark matter, an extension is nec-
689 essary to describe new physics at higher energies. These deficiencies motivate
690 a wide range of experiments that search for new physics. The Large Hadron
691 Collider ([LHC](#)) provides the highest energy approach, seeking to discover unob-
692 served particles or interactions in high energy proton collisions.

693 The experiments at the [LHC](#) have searched for a variety of new phenomena
694 in the years since collisions began in 2010. A major focus of these searches has
695 been on Supersymmetry ([SUSY](#)), an extension to the [SM](#) which has the potential
696 to ameliorate many of its shortfalls. None of the searches have found evidence of
697 new physics, and between them they have begun to rule out a number of models
698 that would predict new particles at the TeV scale. This motivates searches for
699 more exotic signals that may have been missed, using analysis techniques tuned
700 specifically for those signals.

701 This dissertation presents a search for Long-Lived Particles ([LLPs](#)) using the
702 13 TeV collisions collected during 2015 at the [LHC](#). Charged [LLPs](#) are predicted
703 to exist in a subset of [SUSY](#) models, and have dramatically different detector sig-
704 natures than both [SM](#) processes and other [SUSY](#) models. This search focuses on
705 isolating that unique signature using ionization measurements in the ATLAS de-
706 tector.

707 Part I provides the theoretical context and motivation for a search for new
708 physics in high energy collisions. Chapter 2 outlines the basic framework of the
709 [SM](#) and describes its particles and interactions. It also discusses the limitations of
710 the [SM](#) that motivate the existence of new physics. Chapter 3 discusses a possible
711 solution to the shortcomings of the [SM](#), the theory of Supersymmetry, and the
712 ways that it can generate [LLP](#).

713 Part II discusses the structure of the accelerator complex that provides col-
714 lisions as well as the experiment that measures them. Chapter 4 summarizes
715 the design and performance of the [LHC](#) and the features of the proton-proton
716 collisions it produces. Chapter 5 then discusses the components of the ATLAS
717 detector and how they can be used to measure the particles produced in [LHC](#) col-
718 lisions. Chapter 6 describes the algorithms used to reconstruct physics particles
719 and processes from the electronic signals in the detector.

720 Part III presents a measurement of calorimeter response, an important compo-
721 nent of event reconstruction used in many physics analyses. Chapter 7 describes
722 a direct, in situ measurement of calorimeter response using isolated hadrons, and

723 investigates the modeling of that response in simulation. Chapter 8 uses those
724 measurements to construct a correction for the energy of jets in simulation, the
725 jet energy scale ([JES](#)), and to estimate an uncertainty for that correction.

726 Part [IV](#) details the search for [LLPs](#). It begins with a discussion of the simulation
727 of [LLPs](#) in ATLAS, focusing on the detector signatures and how they vary with
728 the properties of those particles in Chapter 9. Then Chapter 10 discusses the
729 strategy of the search and the requirements used to select [LLPs](#) and to reject [SM](#)
730 backgrounds. Chapter 11 explains a method for predicting the background from
731 [SM](#) processes, and shows a validation of the technique. Chapter 12 describes the
732 systematic uncertainties on both the selection efficiency for signal events and
733 the background method. The results of the search are presented in Chapter 13.
734 Chapter 14 concludes with a summary of the search and its context in the com-
735 bined search for [LLP](#), as well as an outlook for future searches.

736

PART I

737

THEORETICAL CONTEXT

738

2

739

740 STANDARD MODEL

741 The SM of particle physics seeks to explain the symmetries and interactions of
742 fundamental particles. The SM provides predictions in particle physics for inter-
743 actions up to the Planck scale (10^{19} GeV). It has been tested by several genera-
744 tions of experiments and has been remarkably successful; no significant devia-
745 tions from its predictions have been found.

746 The theory itself is a quantum field theory grown from an underlying sym-
747 metry, $SU(3) \times SU(2) \times U(1)$, that generates all of the interactions consist-
748 ent with experimental observations¹. These interactions are referred to as the
749 Strong, Weak, and Electromagnetic forces. Each postulated symmetry necessi-
750 tates the existence of an associated conserved charge, which appear as properties
751 of the observed particles in nature.

752 Although this model has been very predictive, the theory is incomplete; for
753 example, it is not able to describe gravity or astronomically observed dark mat-
754 ter. These limitations suggest a need for an extension or new theory to describe
755 physics at higher energies.

756 2.1 ACTION AND THE LAGRANGIAN

Originally, both action and the Lagrangian were constructed for an integral reformulation of the laws of classical mechanics, which is a purely mathematical step: any differential equation can be re-expressed in terms of an integral equation. The Lagrangian, \mathcal{L} , is classically given by the difference of kinetic energy and potential energy. The Lagrangian is defined this way so that the action, \mathcal{S} , given by

$$\mathcal{S}[\mathbf{q}(t)] = \int_{t_1}^{t_2} \mathcal{L}(\mathbf{q}, \dot{\mathbf{q}}, t) dt \quad (1)$$

757 returns the classical equations of motion when one requires it to be stationary
758 in the path, $\mathbf{q}(t)$. This formulation of classical mechanics is extremely useful in
759 calculations, and generalizes beautifully to cover all types of physics.

760 In particular, with the development of quantum mechanics in the twentieth
761 century, the concepts of action and the Lagrangian were found to generalize to
762 more complicated physics for which the classical laws do not hold. Quantum
763 mechanics and quantum field theory can be constructed from the action, using
764 the path integral formulation, by assuming that a particle undergoes all possible
765 paths $\mathbf{q}(t)$ with an imaginary phase given by $e^{i\mathcal{S}[\mathbf{q}(t)]/\hbar}$. This reduces to classical
766 mechanics in the limit as \hbar goes to zero, as all paths for which the action is not
767 stationary interfere with each other so as to cancel their contributions. Because

¹ excluding gravity

768 the wavefunction of a particle can be completely determined through the action
 769 and the action depends only on the Lagrangian, the Lagrangian itself is sufficient
 770 to describe the physics governing the particle.

771 So, in both classical and quantum mechanics, the Lagrangian of a system con-
 772 tains everything there is to know about the system, apart from initial conditions.
 773 Thus, the most natural way to express that a system has a certain symmetry is to
 774 require that the Lagrangian is invariant under a corresponding symmetry trans-
 775 formation. This makes the Lagrangian the central piece of the discussion of
 776 gauge invariance; the mathematical representation of gauge invariance is that a
 777 gauge transformation on the appropriate components of the Lagrangian returns
 778 an identical Lagrangian. That is,

$$\mathcal{L}(\psi, D^\mu) = \mathcal{L}(U\psi, D'^\mu) \quad (2)$$

779 where ψ is the wavefunction and D^μ is the derivative operator, both of which
 780 may transform under a symmetry operation. There are a number of immedi-
 781 ate and surprisingly powerful consequences of requiring that the Lagrangian is
 782 invariant under a symmetry operation.

783 2.2 GAUGE INVARIANCE AND FORCES

784 The simplest possible relativistic, quantum Lagrangian for matter particles is the
 785 free Dirac Lagrangian, which describes a relativistic fermion in a vacuum.

$$\mathcal{L} = i\bar{\psi}\not{d}\psi - m\bar{\psi}\psi \quad (3)$$

786 A fermion denotes a particle with spin-1/2, and the kinematic term ($i\bar{\psi}\not{d}\psi$) is
 787 chosen to correctly describe the free propagation of a fermionic particle with
 788 mass m . This equation is invariant under a global $U(1)$ transformation, that is
 789 changing ψ by a complex phase has no effect. The derivative operator commutes
 790 with a constant phase factor, and wherever ψ appears its complex conjugate also
 791 appears so as to cancel out the change of phase. However, the Lagrangian as writ-
 792 ten is not invariant under the local $U(1)$ symmetry postulated for the **SM**, which
 793 can be written as $U = e^{i\alpha(x)}$. The piece of the Lagrangian involving a derivative
 794 will return an extra term that will break the invariance of the Lagrangian under
 795 this transformation:

$$\begin{aligned} \mathcal{L}' &= i(\bar{\psi}U^\dagger)\not{d}(U\psi) - m(\bar{\psi}U^\dagger)(U\psi) \\ &= i(\bar{\psi}U^\dagger)U(\not{d} - \gamma^\mu\partial_\mu\alpha(x))\psi - m(\bar{\psi}U^\dagger)(U\psi) \\ &= i\bar{\psi}\not{d}\psi - m\bar{\psi}\psi - i\gamma^\mu\partial_\mu\alpha(x)\bar{\psi}\psi \\ &= \mathcal{L} - i\gamma^\mu\partial_\mu\alpha(x)\bar{\psi}\psi \\ &\neq \mathcal{L} \end{aligned}$$

796 So, in order to enforce the required symmetry, the typical approach is to con-
 797 struct a covariant derivative, that is to add a term to the derivative operator

so that the unwanted term in \mathcal{L}' is exactly canceled. A generic form for such a derivative is given by

$$D^\mu = \partial^\mu - iqA^\mu$$

where at this point A^μ is an arbitrary field that transforms under the $U(1)$ operator and q is a scaling factor. Adding this component to the above Lagrangian gives

$$\mathcal{L}' = i(\bar{\psi}U^\dagger)U(\not{D} - \gamma^\mu\partial_\mu\alpha(x) - iq\gamma^\mu A'_\mu)\psi - m(\psi U^\dagger)(U\psi) \quad (4)$$

$$\mathcal{L}' = \mathcal{L} + \gamma^\mu(-i\partial_\mu\alpha(x) - iqA'_\mu + iqA_\mu)\bar{\psi}\psi \quad (5)$$

and because the transformation of A^μ is unspecified, $\mathcal{L} = \mathcal{L}'$ whenever

$$A'_\mu = A_\mu - \frac{1}{q}\partial_\mu\alpha(x)$$

The above procedure demonstrated that beginning with the Lagrangian for a free fermion and imposing a local $U(1)$ symmetry required the existence of a vector field A^μ , and specified its transformation under the $U(1)$ gauge group. The additional term in the derivative can be expanded to form a completely separate term in the Lagrangian,

$$\mathcal{L} = i\bar{\psi}\not{D}\psi - m\bar{\psi}\psi - (q\bar{\psi}\gamma^\mu\psi)A^\mu \quad (6)$$

and in this form it is clear that the A^μ term has the exact form of the electromagnetic interaction. That is, this is the Lagrangian which reproduces the relativistic form of Maxwell's equations for a particle interacting with an electromagnetic field. It is natural to also introduce a term to the Lagrangian at this point to describe the free propagation of the vector A field, where the propagation of a vector field has the form of

$$-\frac{1}{16\pi}F^{\mu\nu}F_{\mu\nu} \quad \text{with} \quad F_{\mu\nu} = \partial_\mu A_\nu - \partial_\nu A_\mu \quad (7)$$

This then also describes the electromagnetic interactions in a vacuum and the propagation of a photon. This component of the Lagrangian could also potentially include a mass term, but such a term would not be gauge invariant and so must be excluded. The photon is an example of a gauge boson, a spin-1 particle required to exist by a gauge symmetry of the Lagrangian and one that corresponds to a force. In summary, requiring the $U(1)$ symmetry was enough to recover all of electromagnetism and to predict the existence of a photon in the [SM](#).

The interaction term that was placed into the Lagrangian by this procedure can be conveniently summarized with Feynman diagrams, which diagrammatically represent a transition from an initial state to a final state. The contribution

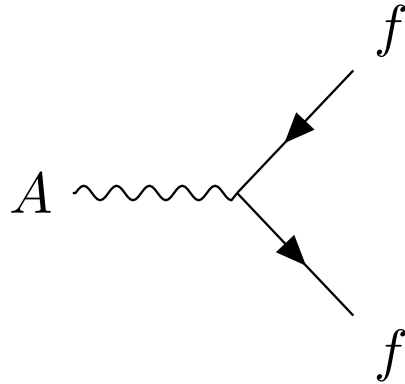


Figure 1: A Feynman diagram representing the interaction of the A field with a generic fermion, f .

826 of all diagrams that start with the same initial state and end with the same final
 827 state must be summed, but more complicated diagrams can be built by linking
 828 together the simplest versions. A diagram that corresponds to the above term,
 829 $(q\bar{\psi}\gamma^\mu\psi)A^\mu$, is shown in Figure 1, for an interaction with a generic fermion.

830 2.2.1 $SU(2) \times U(1)$ AND THE ELECTROWEAK FORCE

831 The full picture of the electroweak section of the SM is more complicated than
 832 the simplified explanation of the electromagnetic piece described above. In prac-
 833 tice, it is necessary to consider the entire $SU(2) \times U(1)$ symmetry together, but
 834 the procedure is the same. Enforcing the symmetry on the Lagrangian requires
 835 the introduction of a covariant derivative, this time with four total distinct terms,
 836 one for each of the generators of $SU(2) \times U(1)$. The result is a series of terms
 837 in the Lagrangian which describe the interaction of a fermion with four vector
 838 (spin-1) fields, the W_1 , W_2 , W_3 , and B fields. These fields can mix in the quan-
 839 tum sense, and linear combinations form the W^+ , W^- , Z , and A fields that are
 840 considered actual particles in the SM².

841 2.2.2 $SU(3)$ AND THE STRONG FORCE

842 The same procedure can be applied starting with the $SU(3)$ symmetry require-
 843 ment, where eight additional fields must be introduced, one for each of the gen-
 844 erators of $SU(3)$. The resulting Lagrangian describes quantum chromodynam-
 845 ics (QCD) and predicts the existence of eight massless gauge bosons known col-
 846 lectively as gluons. The complexity of the interactions of those eight gluons leads
 847 to surprising phenomena, discussed in Section 2.5.3.

² These states are the actual particles because they are mass eigenstates, but the full explanation of this will have to wait for the discussion of the Higgs mechanism in Section 2.4.

848 2.3 NOETHER'S THEOREM, CHARGES, AND MATTER

849 Another direct consequence of the symmetries stipulated in the SM are a series
 850 of conserved quantities, Noether charges, named after the mathematician and
 851 physicist Emmy Noether. The charges arise as a direct consequence of Noether's
 852 theorem, which can be informally stated as

853 *For every symmetry of the Lagrangian, there exists a corresponding phys-
 854 ical quantity whose value is conserved in time.*

855 Or, stated another way, symmetries of the Lagrangian mathematically require
 856 the conservation of specific quantities taken from the Lagrangian. This rela-
 857 tionship can also be thought of as operating in the other direction, the exis-
 858 tence of a conserved charge can be shown to generate the symmetry in the La-
 859 grangian. This theorem is actually quite striking in a somewhat unexpected re-
 860 lation between simple geometric symmetries and physically observable conser-
 861 vation laws. For example, the theorem connects the translation invariance of
 862 the Lagrangian in space to the conservation of momentum and the translation
 863 invariance in time to the conservation of energy.

864 In the context of the SM, the required symmetries of $U(1) \times SU(2) \times SU(3)$
 865 correspond to the charges that are considered properties of all elementary par-
 866 ticles. The most familiar of these properties is the electric charge, Q, which is
 867 one of the conserved quantities of $SU(2) \times U(1)$. The remaining pieces of
 868 $SU(2) \times U(1)$ correspond to weak isospin, T and T_3 , where T has only non-
 869 negative values and T_3 can be positive and negative. T is the magnitude of the
 870 full three vector of weak isospin, T, and T_3 is the projection along the third com-
 871 ponent that is the other conserved quantity derived from $SU(2) \times U(1)$. The
 872 $SU(3)$ symmetry is generated by the three colors of QCD, red, green, and blue,
 873 each with a corresponding opposite color, anti-red, anti-green, and anti-blue.
 874 The color charges are also conserved in the SM.

875 The matter in the observable universe consists of a collection of particles which
 876 carry these charges, in addition to spin and mass. The matter particles are all
 877 fermions: particles with spin-1/2. All of the fermions belong to one of two
 878 groups, quarks and leptons, and one of three generations. Each of the genera-
 879 tions have the same quantum numbers and charges but significantly different
 880 masses; the particles in higher generations have increasing mass. Quarks are dis-
 881 tinguished from leptons in that they carry color charge, in addition to electric
 882 charge and weak isospin. The particles in the SM are summarized in Figure 2,
 883 and the matter particles are the twelve types of fermions displayed on the left
 884 side of the graphic.

885 2.3.1 QUARKS

886 The three generations of quarks each consist of a quark with electric charge +2/3
 887 and one with charge -1/3. They are called up and down, charm and strange,
 888 and top and bottom respectively, and these are referred to as the quark flavors.
 889 Although Figure 2 only shows these six flavors, there is a unique particle for each

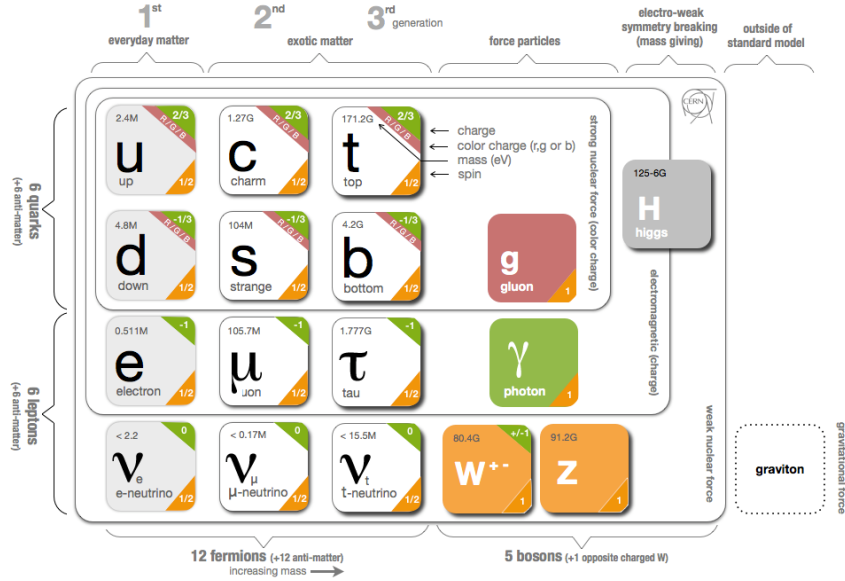


Figure 2: The particle content of the SM, including the names, masses, spins, and charges of each of the particles.

combination of the three colors and flavor. And each quark has an anti-particle with the opposite electric charge values.

However, individual quarks are never observed in nature, but instead form color-neutral bound states. This is a consequence of interaction of gluons with color charge called confinement, discussed in Section 2.5.3. One way to form a color neutral combination is a bound state of three quarks with three different color charges, called a baryon. Baryons are the most common type of quark configuration in conventional matter, and include protons and neutrons. The other common configuration is a bound state of a quark and an anti-quark, called a meson, where the two quarks have opposite colors. Although there is no direct conservation law resulting from the symmetries of the SM Lagrangian, an accidental symmetry results in the approximate conservation of baryon number, B , where baryons have $B = 1$ and mesons have $B = 0$. That is, no interactions have been observed which directly alter baryon number.

2.3.2 LEPTONS

The remaining fermions, the leptons, do not carry color charge. Each generation contains an electrically charged lepton, the electron, muon, and tau, and an electrically neutral lepton called a neutrino. For the charged leptons, the flavors are mass eigenstates, with the masses listed in Figure 2. The flavors of the neutrinos, on the other hand, are not mass eigenstates: their propagation in quantum superpositions of flavor states leads to oscillations between different flavors. The absolute masses of the neutrinos are not currently known, but the phenomenon

of oscillations shows that they have three different mass values. Another accidental symmetry leads to an approximate conservation of lepton number L , the difference in the number of leptons and anti-leptons; again there are no interactions present in the SM which directly alter lepton number.

2.3.3 CHIRALITY

All of the fermions described above have two possible values of the magnitude of weak isospin, T , either 0 or 1/2. The fermions with $T = 0$ are called right-handed, while those with $T = 1/2$ are called left-handed. Because T is the charge corresponding to the weak force, right-handed particles do not interact with the weak gauge bosons in the same way that neutral particles do not interact with photons. For left-handed fermions, each of the quark and lepton generations have one particle with $T_3 = -1/2$ and one with $T_3 = +1/2$. The neutrinos have $T_3 = +1/2$, while the charged leptons have $T_3 = -1/2$. Similarly, the positively charged quarks have $T_3 = +1/2$ and the negatively charged quarks have $T_3 = -1/2$. Because the right-handed neutrinos would have no charge of any type, it is not clear if they exist at all.

2.4 HIGGS MECHANISM AND MASS

The description of the electroweak forces above left out an important part of the observed nature of the electroweak force. Many physical experiments observed phenomena corresponding to the interaction of the weak bosons that were best explained if they had significant masses. But as mentioned before, massive bosons would break the gauge invariance of the Lagrangian. A large mass for the W and Z bosons is necessary to explain the relative weakness of their interactions compared to the electromagnetic field. The Lagrangian's discussed above did not include a mass term for the gauge bosons, and in fact such a term would not be allowed by the requirement of gauge invariance. This was a significant problem for the SM, and the symmetry of the electroweak sector would have to be broken in order to allow for non zero masses for some of the gauge bosons.

One mechanism to allow for this symmetry breaking is the Higgs mechanism, which posits the existence of an additional scalar field. It begins with a $SU(2) \times U(1)$ invariant Lagrangian of the form

$$\mathcal{L} = |D_\mu \phi|^2 - \frac{1}{2}\mu^2\phi^+\phi - \frac{1}{4}\lambda(\phi^+\phi)^2 \quad (8)$$

where ϕ is the new scalar field with two components and, importantly, μ^2 is negative. This leads to a minimum value of the field at a non-zero value of ϕ , specifically where

$$\langle \phi \rangle = \frac{1}{\sqrt{2}} \begin{pmatrix} 0 \\ v \end{pmatrix} \quad \text{with} \quad v = \frac{2\mu^2}{\lambda} \quad (9)$$

947 Expanding the original Lagrangian about its expectation value in terms of the
948 perturbation H ,

$$\langle \phi \rangle = \frac{1}{\sqrt{2}} \begin{pmatrix} 0 \\ v + H \end{pmatrix} \quad (10)$$

949 gives potential terms in the Lagrangian like

$$\mathcal{L}_H = -\frac{1}{2} m_H^2 H^2 - \sqrt{\frac{\lambda}{2}} m_H H^3 - \frac{1}{4} \lambda H^4 \quad (11)$$

950 where $m_H = \sqrt{2}\mu$. The form of this Lagrangian shows that the non-zero ex-
951 pectation value of the ϕ field has introduced a massive scalar field H with self
952 interaction terms. It has an additional important consequence on the description
953 of the gauge bosons, through the expansion of the term involving the covariant
954 derivative:

$$|D_\mu \phi|^2 \supset \frac{1}{8} (g^2 (W_{1\mu} W_1^\mu + W_{2\mu} W_2^\mu) + (g' B_\mu - g W_3 \mu)^2) \quad (12)$$

955 where the W_i and B fields are the original $SU(2) \times U(1)$ gauge fields men-
956 tioned previously. The above equation can be rearranged using linear combina-
957 tions of the fields to form mass terms for the gauge bosons, and the mass eigen-
958 states are exactly the W^\pm , Z , and A fields. Only the A field, corresponding to the
959 photon, results in a zero mass, and the remaining three particles have non-zero
960 mass values. Because the previously introduced Lagrangian, written in terms of
961 ϕ , was clearly gauge invariant, this resulting configuration must also be gauge
962 invariant.

963 This is the Higgs mechanism, where the introduction of a gauge invariant
964 scalar field with a non-zero expectation value can generate masses for the gauge
965 bosons without violating the underlying symmetries. The particle that is associ-
966 ated with the perturbations of this field, H , is called the Higgs boson, and is said
967 to generate the masses of the remaining bosons because the vacuum expectation
968 value introduces mass-like terms for each of the bosons. The resulting masses
969 are listed in Figure 2. Because this mechanism was so successful in describing
970 the observed properties of the W and Z bosons, it has been considered part of
971 the SM for decades, although the actual Higgs boson was only recently observed
972 in 2012, fully confirming the theory.

973 The Higgs mechanism is also responsible for generating the masses of the
974 fermions. The original mass terms that were listed in the Lagrangian for fermions
975 are replaced with Yukawa coupling terms, which introduce interactions between
976 the ϕ field and the fermions. Like with the gauge bosons, the non-zero expec-
977 tation value of the field yields mass terms, and the expansion about that value
978 introduces interaction terms between the fermions and the Higgs boson. The
979 masses are different between each fermion because each has a different Yukawa
980 coupling, which results in the masses listed in Figure 2.

981 2.5 PHENOMENOLOGY

982 The **SM** Lagrangian described above contains all of the information necessary
 983 to describe particle physics through the path integral formulation. However, a
 984 tremendous amount of complexity emerges from that description because of the
 985 diverse allowed interactions between the ensemble of particles in the **SM**. A qual-
 986 itative understanding of the phenomenology produced by those interactions is
 987 immensely helpful in understanding the analysis of particle physics.

988 2.5.1 STANDARD MODEL CALCULATIONS

989 The terms in the Lagrangian describing interactions of particles can be used to
 990 evaluate cross sections or decay widths through perturbation theory. Pertur-
 991 bation theory uses a diagrammatic expansion to approximate **SM** interactions
 992 as a series of feynman diagrams, each representing an amplitude for the transi-
 993 tion between initial and final state. The feynman diagrams uniquely specify that
 994 transition amplitude through the feynman rules [1]. The transition amplitude
 995 includes a phase space component to account for the initial and final momenta,
 996 and an addition matrix element which describes the interaction. The complex
 997 amplitude for each process with the same initial and final state must be summed,
 998 and then the cross section or decay width is calculated as the square of the am-
 999 plitude integrated over all valid final state momenta. For example, the decay rate
 1000 for a particle of mass m_A to two final state particles with momenta \mathbf{p}_i and \mathbf{p}_j is
 1001 given by

$$\Gamma = \int \frac{d^3 p_i d^3 p_j}{(2\pi)^6 4E_i E_j} (2\pi)^4 \delta^{(4)}(\mathbf{p}_A - \mathbf{p}_i - \mathbf{p}_j) |\mathcal{M}|^2$$

1002 where the prefactor is the phase space term, the delta function enforces conser-
 1003 vation of four-momentum, and \mathcal{M} is the matrix element. The matrix element
 1004 includes dimensionless constant terms that describe the strength of the interac-
 1005 tion, called coupling constants: α for the photon, α_W for the weak bosons, and
 1006 α_s for the gluons.

1007 The sum over all diagrams with the same initial and final state leads to im-
 1008 portant consequences in the **SM**. Most process have a small number of leading
 1009 order diagrams, where leading order indicates the diagram with the fewest fac-
 1010 tors of the coupling constants. When the coupling constants are less than unity,
 1011 the diagrams of higher order have diminishing contributions. This is called the
 1012 perturbative regime, and allows for approximate calculations by using a set or-
 1013 der, referred to as leading order (**LO**), next-to-leading order (**NLO**), and so on. A
 1014 coupling constant greater than unity results in a non-perturbative regime, and
 1015 requires other calculation techniques.

1016 However, even in a perturbative theory, the sum over all diagrams in the ampli-
 1017 tude includes loop diagrams; for example any photon line in a feynman diagram
 1018 can be replaced with the line in Figure 3 and still form a valid interaction. These
 1019 and other types of loop diagrams introduce divergent contributions to **SM** pro-

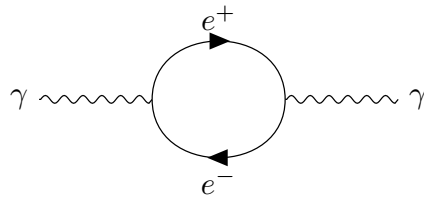


Figure 3: A feynman diagram for photon propagation including a loop of electrons.

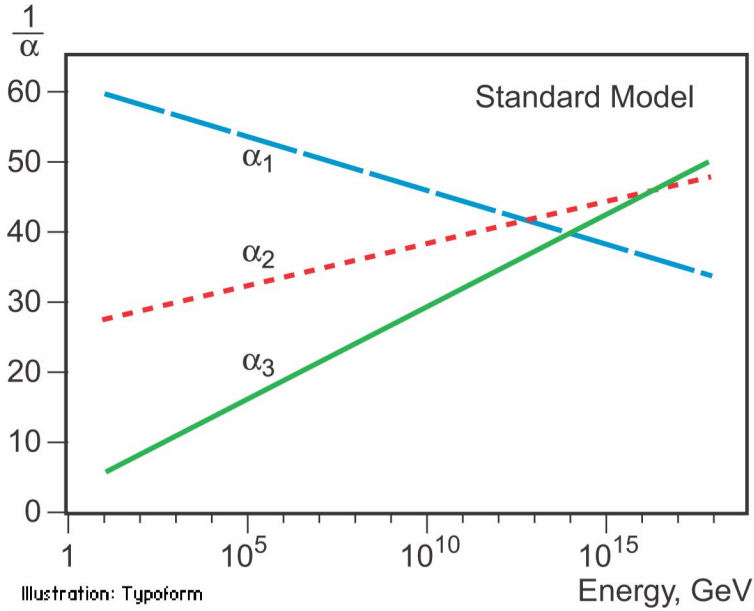


Figure 4: An approximation of the running of the coupling constants in the SM up to the Planck scale [2].

cesses, which would seem to make the theory inconsistent. The solution to this problem is to absorb those contributions into the coupling constants and charges in the Lagrangian, so that the combination of the bare value and the loop contributions gives the correct physical observables. This process is called renormalization, and a theory where the divergences can consistently be absorbed into the definition of the constants in the Lagrangian is called renormalizable.

Setting the renormalized coupling constants requires a measurement at a specific energy scale, and only at that scale are the contributions of the loop diagrams precisely cancelled. At a different energy the loop diagram contribution changes, and can be thought of as a modification to the coupling constant. The renormalization procedure thus predicts a variation of the coupling constants with the scale of the interaction, and specifies how they change with energy. The energy dependence is called the running of the coupling constants, and the effect on the three couplings in the SM is shown in Figure 4.

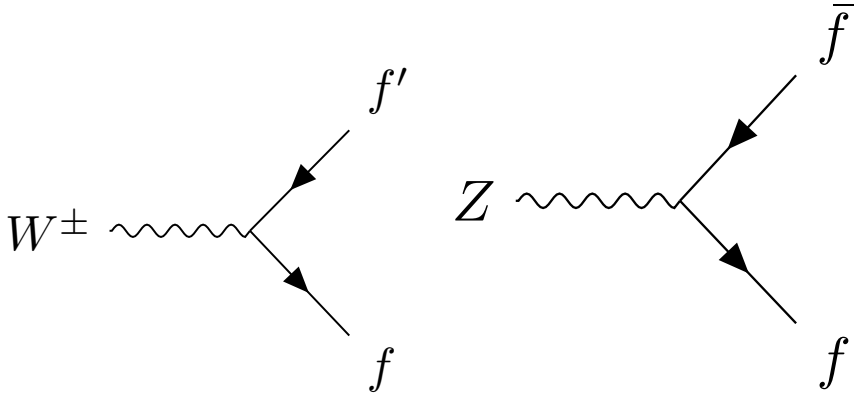


Figure 5: The Feynman diagrams representing the decays of the W and Z bosons to fermions. Here f indicates a generic fermion, \bar{f} its antiparticle, and f' the partner of that fermion in the same generation.

1034 2.5.2 ELECTROWEAK PHYSICS

1035 The masses of the W and Z bosons result in significantly different processes
 1036 for the weak fields than the electromagnetic field, despite their interactions be-
 1037 ing similar before symmetry breaking. The massless photon is stable, and can
 1038 propagate in a vacuum, resulting in the familiar long range interactions of elec-
 1039 tromagnetism. The W and Z bosons, however, are unstable, as they have large
 1040 enough masses to decay to fermions, such as the decays shown in Figure 5. For
 1041 this reason, photons can be observed directly, while the other bosons are suffi-
 1042 ciently short-lived (with lifetimes around 10^{-25} s) that they can only be measured
 1043 from their decay products.

1044 Because the electroweak bosons interact with both quarks and leptons, they
 1045 are responsible for the production of leptons in proton-proton collisions. Z bosons
 1046 and photons produce pairs of opposite sign, same flavor leptons. W bosons, on
 1047 the other hand, produce a single lepton and the corresponding neutrino. The
 1048 electroweak bosons also decay to hadrons by producing pairs of quarks, as shown
 1049 in Figure 5. The Z boson decays to hadrons with a branching ratio of 69.9%, to
 1050 neutrinos with 20.0%, and to charged leptons 10.1% of the time [3]. The W boson
 1051 decays to hadrons with a branching ratio of 67.6% and to leptons 32.4% [3].

1052 2.5.3 STRONG PHYSICS

1053 The phenomenology of the strong sector differs significantly from the weak sec-
 1054 tor because the gluons are massless but color charged. Because of this, gluons
 1055 can interact with each other, and contributions from multiple gluon interactions
 1056 lead to a significant growth in the strength of the field at low energies. The depen-
 1057 dence of the field strength on the energy scale is described by renormalization,
 1058 and in QCD the coupling is only small at high energies. Below approximately 1
 1059 GeV, the strength of those interactions results in confinement: the interactions

1060 are so strong that when quark-antiquark pairs separate, the fields between them
 1061 generate additional quarks to form color neutral bound states. Above around
 1062 the GeV scale, the interactions of quarks become perturbative, similar to the
 1063 electroweak fields; this phenomenon is known as asymptotic freedom.

1064 At lower energies, however, the strength of the strong interaction is so signif-
 1065 icant that the interactions of color-charged particles create additional particles
 1066 until they form neutral bound-states. This process is known as hadronization,
 1067 and explains why no quarks are observed isolated in nature: they all form bound
 1068 states of hadrons like protons, neutrons, and pions. The hadronization process
 1069 can produce a significant number of particles, so that a single energetic quark
 1070 recoiling against another quark can generate a cascade of dozens of hadrons.
 1071 Because of the initial boost of such an energetic configuration, the resulting
 1072 hadrons are collimated, and conical spray of particles often referred to as a jet.

1073 2.5.4 PROTON-PROTON COLLISIONS

1074 Proton-proton collisions are a convenient way to generate high energy interac-
 1075 tions to probe the SM and to search for new physics. At the energies that will be
 1076 discussed in this analysis, the substructure of the protons is very important to the
 1077 description of the resulting interactions. At lowest order, protons are composed
 1078 of two up quarks and one down quark, but this description is incomplete. The ac-
 1079 tual bound state includes a chaotic sea of additional gluons and $q\bar{q}$ pairs, each of
 1080 which carries a variable fraction of the proton's energy. When a proton-proton
 1081 collision takes place, it is these constituents that interact with each other, result-
 1082 ing in a highly variable collision energy even when the proton-proton energy is
 1083 consistent.

1084 The fraction of the energy carried by each constituent varies moment to mo-
 1085 ment, but can be modelled probabilistically by parton distribution functions (PDFs).
 1086 These are difficult to predict theoretically, as the QCD calculations are non-perturbative,
 1087 and instead are measured in hard-scattering experiments. They are usually rep-
 1088 resented by how often a given type of particle carries a fraction x of the total
 1089 proton energy. Those fractions change significantly with the scale of the in-
 1090 teraction, Q ; the PDFs of proton-proton collisions at both $Q^2 = 10 \text{ GeV}^2$ and
 1091 $Q^2 = 10^4 \text{ GeV}^2$ are shown in Figure 6.

1092 2.5.5 SIMULATION

1093 Although the SM provides the necessary components to model the proton-proton
 1094 collisions at the LHC, the complexity of the processes make direct predictions dif-
 1095 ficult. The LHC experiments rely on simulations that break down the collisions
 1096 and resulting detector interactions into several steps in order to predict expected
 1097 SM and even Beyond the Standard Model (BSM) events. The simulation begins
 1098 with a selection of two proton constituents to collide from the PDFs described
 1099 in Section 2.5.4, which fully specify the particle types and their momenta. The
 1100 initial momenta are then fed into an event generator, which calculates the cross
 1101 section and predicts the final momentum using the matrix element formulation

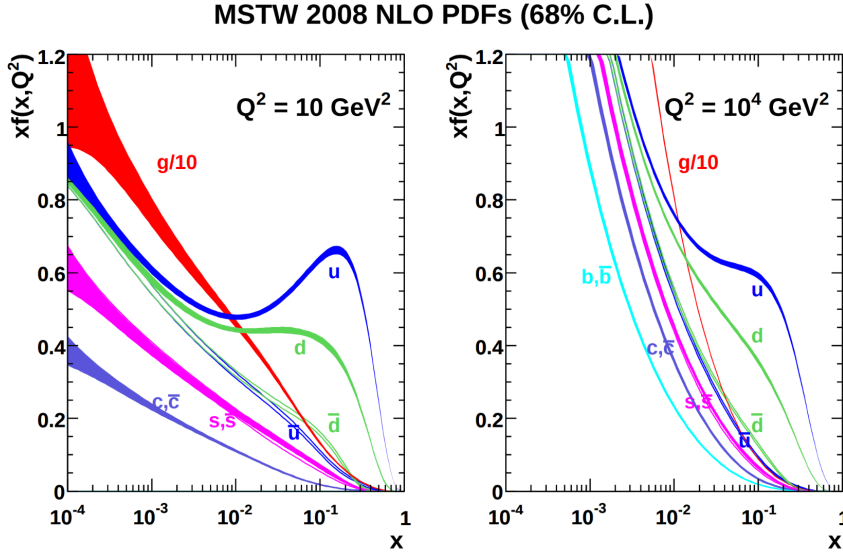


Figure 6: The PDFs for proton-proton collisions at $Q^2 = 10 \text{ GeV}^2$ and $Q^2 = 10^4 \text{ GeV}^2$. Each shows the fraction of particles which carry a fraction x of the total proton energy at the specified scale [4]. The distribution for gluons is scaled by 0.1 to fit within the axis range.

described in Section 2.5.1. This analysis uses both the Pythia 6.4.27 [5] and MG5_aMC@NLO [6] generators in simulated events. The next step calculates additional processes that occur during the primary interaction, including hadronization, fragmentation, and initial state radiation. The result of this intial event generation is a series of particles and momentum that were produced in the collision. These initial particle states are recorded for simulation studies, and are often referred to as truth.

These particles must then be propagated through a simulated detector geometry, where the signal they produce in the detector models can be modeled. Geant4 [7] provides a toolbox that describes the propagation of particles in the magnetic field as well as their interactions with the detector material. It also simulates secondary interactions where additional particles may be produced, such as a photon interacting with the detector material and converting to two electrons. Each particle is tracked until its energy is lost or it exits the volume of the detector, and the signals it generates in the active regions of the detector simulation are recorded. Those signal are then converted into the expected electronic outputs of the detector in a process called digitization. The result of this step has precisely the same format as collected data, so that both can be fed into the same reconstruction algorithms for analysis.

2.6 LIMITATIONS

Despite the great success of the relatively simple SM in describing such a broad range of emergent phenomena, it is clear that the picture it presents of the interactions of fundamental particles is incomplete. The SM contains concerning

1125 coincidences that suggest a more ordered underlying substructure that is not ex-
 1126 pressed in the current form. It also fails to explain a number of cosmological
 1127 measurements of the nature of matter in the universe. These limitations suggest
 1128 the need for new, BSM physics that would provide a more complete description
 1129 at higher energies.

1130 2.6.1 THEORETICAL CONCERNS

1131 There have been no successful integrations of the SM's description of the elec-
 1132 troweak and strong forces with the description of gravity, and it is still unclear
 1133 how to account for the effects of gravity at the Planck scale of approximately 10^{19}
 1134 GeV, where its interactions are as strong as the remaining forces. The Planck
 1135 scale is an important cutoff for the SM, as it is clear that the SM must break down
 1136 somewhere between the current highest energy tests of the SM, around 1 TeV,
 1137 and the Planck scale.

1138 One example of this is the Higgs mass, which is determined by a sum of its
 1139 bare mass and the interactions in the vacuum with all massive particles. As there
 1140 must be new physics at the Planck scale to describe gravity, some of those cor-
 1141 rections would include contributions at a scale seventeen orders of magnitude
 1142 above the mass of the Higgs. Either the bare mass of the Higgs boson precisely
 1143 cancels those contributions to leave a remainder seventeen orders of magnitudes
 1144 smaller, or a new theory exists at a lower scale that shields the Higgs mass from
 1145 those terms. A theory where such a unlikely cancellation of free parameters oc-
 1146 curs is called fine-tuned, and one that is free from such cancellations is called
 1147 natural. Theories where the mass of the Higgs is natural are usually preferred,
 1148 as they suggest an underlying, coherent structure. The enormous difference in
 1149 scales between the weak scale (including the Higgs mass), and the Planck scale,
 1150 is often referred to as the hierarchy problem.

1151 There is also a compelling argument that the $SU(3) \times SU(2) \times U(1)$ gauge
 1152 structure of the SM might originate from a single, unified gauge theory. For ex-
 1153 ample, it is possible to represent that gauge structure as a $SU(5)$ gauge group
 1154 with only a few inconsistencies with the current implementation. This unifica-
 1155 tion is suggested by the scaling of the coupling constants for each of the forces
 1156 under renormalization; they come close to converging to a single value at higher
 1157 energies, as seen in Figure 4. An additional correction to the scaling of the cou-
 1158 pling constants from new physics above the TeV scale could cause them to merge
 1159 into a single value at high energies.

1160 2.6.2 COSMOLOGICAL OBSERVATIONS

1161 The SM contains a symmetry in the description of matter and antimatter that is
 1162 not reflected in cosmological observations. The processes of the standard model
 1163 create or remove matter and antimatter in equal amounts, so a universe that be-
 1164 gins with an equal quantity of each should result in a universe with an approxi-

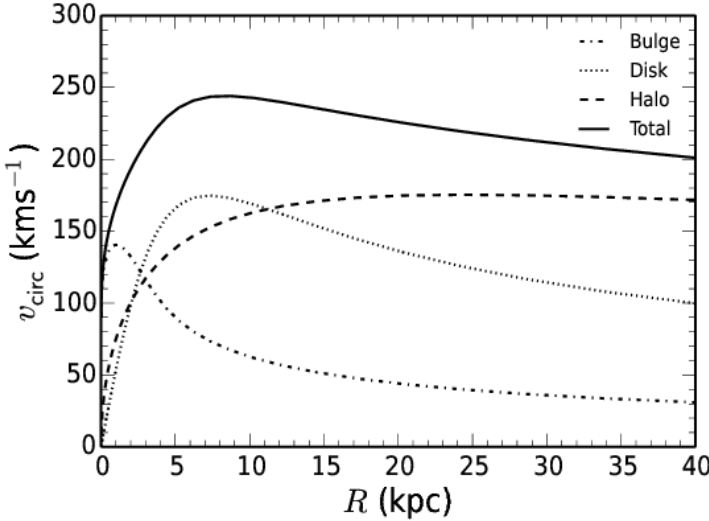


Figure 7: The distribution of velocities of stars as a function of the radius from the center of the galaxy. The contributions to the velocity from the various components of matter in the galaxy are shown [8].

mate³ balance of matter and antimatter. However, cosmological observations of the relative amount of each type clearly show that the directly observable mass of the universe is overwhelmingly made of matter. As this difference is largely a difference in the generation of baryons and anti-baryons, this discrepancy is often referred to as the baryogenesis problem.

A number of astrophysical observations of large scale gravitational interactions suggest the presence of a significant amount of non-luminous matter that interacts with the normal matter only gravitationally. The first evidence of this came from the observation of galactic rotation curves, the velocities of stars as a function of the radius from the center of a galaxy. These can be directly predicted from the amount of matter contained within the sphere up to the radius of the star. An estimate of velocity based only on the luminous matter in the galaxies would predict a dependence that falls off with the radius, but the observed curves show a mostly constant distribution of velocities [8], as seen in Figure 7. The higher velocities than predicted by the luminous matter can be explained by a halo of dark matter that extends significantly outside the galactic disk.

This dark matter accounts for a majority of the matter in the universe, and is incompatible with the matter particles predicted by the SM. Many observations support its existence, but there have been no direct detections of a particle which could account for the large quantity of gravitationally interacting dark matter. The SM would have to require a significant extension to include the particles needed to explain dark matter and the processes needed to explain the observed matter-antimatter asymmetry.

³ There are some processes in the standard model which can result in a small imbalance of matter and antimatter, but not at the scale observed cosmologically.

3

1188

1189 SUPERSYMMETRY

1190 The theory of **SUSY** presents an extension to the **SM** that solves a number of the
1191 outstanding issues. It is based on another proposed symmetry, one which intro-
1192 duces an equality between the fermionic particles and proposed bosonic partners
1193 and also between bosonic particles and their proposed fermionic partners. The
1194 symmetry is defined by extending spacetime into a superspace, which includes
1195 one dimension that describes a particle's spin: a transformation in this space
1196 moves a fermion with spin-1/2 to a boson with spin-0 or vice-versa. Requiring
1197 the **SM** to be symmetrical under these transformations requires the existence of a
1198 bosonic partner for every current matter fermion in the **SM** and a fermionic part-
1199 ner for every boson. The partners are called superparticles (sparticles), where
1200 quarks partner with squarks and leptons partner with sleptons, and each boson
1201 has a fermionic partner called a gaugino. The superpartners, in the original form
1202 of the theory, should be identical to the original particle in every way except for
1203 spin; that is they would have the same quantum charges and the same mass.

1204 However, the simplest version of the theory, where the symmetry is unbro-
1205 ken, is incompatible with current observations of physics in a number of sys-
1206 tems. The most striking example comes from the electron, as the superpartner
1207 of an electron would introduce a stable, negatively charged, and bosonic parti-
1208 cle. Such a particle would drastically alter atomic properties by providing a way
1209 to create atoms without the valence structure of electrons that results from the
1210 Pauli exclusion principle for fermions. Various high energy physics measure-
1211 ments have also confirmed the spin of the W and Z bosons, for example, and
1212 a fermionic gaugino has never been produced at those masses. The solution to
1213 this incompatibility with observation is to conjecture that the symmetry exists
1214 but is spontaneously broken, where the masses of the supersymmetric particles
1215 are significantly larger than those of the current **SM** particles. Like the sponta-
1216 neous symmetry breaking of the electroweak system, this symmetry breaking
1217 can be accomplished by introducing an additional Higgs mechanism.

1218 3.1 STRUCTURE

1219 There are a number of ways to model the particulars of **SUSY**, but many of the
1220 resulting phenomena are similar, and a discussion of an example is sufficient
1221 to describe the structure and results of the theory. The Minimal Supersymmetric
1222 Model (**MSSM**) is one example of a complete description that includes the neces-
1223 sary symmetry breaking to result in the different masses between particles and
1224 sparticles [9]. It is called minimal because it is designed to use the simplest pos-
1225 sible extension to the **SM** that incorporates **SUSY**. However even a minimal ver-
1226 sion includes a remarkable number of free parameters, over 100, and the **MSSM**

Sector	Particles	Sparticles
Baryonic Matter	(u, d)	(\tilde{u}, \tilde{d})
	(c, s)	(\tilde{c}, \tilde{s})
	(t, b)	(\tilde{t}, \tilde{b})
Leptonic Matter	(ν_e, e)	$(\tilde{\nu}_e, \tilde{e})$
	(ν_μ, μ)	$(\tilde{\nu}_\mu, \tilde{\mu})$
	(ν_τ, τ)	$(\tilde{\nu}_\tau, \tilde{\tau})$
Higgs	(H_u^+, H_u^0)	$(\tilde{H}_u^+, \tilde{H}_u^0)$
	(H_d^0, H_d^-)	$(\tilde{H}_d^0, \tilde{H}_d^-)$
Strong	g	\tilde{g}
Electroweak	(W^\pm, W^0)	$(\tilde{W}^\pm, \tilde{W}^0)$
	B^0	\tilde{B}^0

Table 1: The particles in the **SM** and their corresponding superpartners in the **MSSM**.

1227 is often further constrained to include fewer parameters in models such as the
 1228 Phenomenological MSSM (**pMSSM**) and the Constrained MSSM (**cMSSM**) [10].

1229 The theory includes a sparticle partner for every **SM** particle, which are listed
 1230 in Table 1. To then provide the different masses for those sparticles, the **MSSM**
 1231 introduces a second Higgs interaction. The resulting scalar field, along with the
 1232 original Higgs field, generates five total particles, h^0 , the original Higgs boson,
 1233 A^0 , H^0 , and H^\pm , where the last two are electrically charged. These Higgs bosons
 1234 can mix with the supersymmetric gauginos to form a series of mass eigenstates.
 1235 These are usually referred to by the order of their masses, where the neutral
 1236 gauginos (neutralinos) are labeled $\tilde{\chi}_1^0$, $\tilde{\chi}_2^0$, $\tilde{\chi}_3^0$, and $\tilde{\chi}_4^0$. The charged gauginos
 1237 (charginos) are similarly labeled $\tilde{\chi}_1^\pm$ and $\tilde{\chi}_2^\pm$. Table 1, lists the gauginos which are
 1238 direct partners of the original gauge bosons in the **SM** rather than these resulting
 1239 mass eigenstates.

In addition to the new particle content, the **MSSM** introduces new interactions for the gauge bosons and gauginos. All interaction terms are added to the Lagrangian which describe the interaction of a gauge boson or gaugino with a particle or sparticle with the appropriate charge. Such terms include a few interactions which would violate the observed $B - L$ symmetry that prevents proton decay. Either the couplings on these terms must be extremely small to match the experimental limits on those decays, or an additional symmetry must be imposed to exclude the terms. The **MSSM** and several other **SUSY** models choose to introduce a new symmetry known as R-parity, where the conserved quantity, P_R is defined as

$$P_R = (-1)^{2s+3(B-L)}$$

1240 with s as the spin of the particle. Sparticles are R-parity odd while **SM** particles
 1241 are R-parity even. And by requiring that each term in the supersymmetric La-
 1242 grangian conserves R-parity, it is enforced that sparticles are produced in pairs.

1243 The conservation of R-parity removes the $B - L$ violating terms from the La-
 1244 grangian. The remaining terms include all of the interactions of the **SM** where
 1245 two of the particles are replaced with their **SUSY** partners, so that R-parity is con-
 1246 served in the interactions. This also has an important significance in making the
 1247 Lightest Supersymmetric Particle (**LSP**), the $\tilde{\chi}_1^0$, stable, as it cannot decay to only
 1248 **SM** particles without violating the conservation of R-parity. The heavier sparti-
 1249 cles then decay in chains, emitting an **SM** particle in each step, and leave behind
 1250 the **LSP** at the end of the chain.

1251 3.2 MOTIVATION

1252 **SUSY** models, including the **MSSM**, ameliorate many of the issues in the **SM** dis-
 1253 cussed in Section 2.6. **SUSY** is particularly well motivated as a natural extension
 1254 to the **SM** because the simple underlying assumption solves three major, seem-
 1255 ingly unrelated concerns. And these benefits all require that at least some of the
 1256 sparticles exist at the TeV scale, within the reach of modern collider experiments.

1257 The first, a solution to the hierarchy problem, comes as a direct consequence
 1258 of the introduction of massive superpartners for each **SM** particle. The contribu-
 1259 tions to the Higgs mass from the much higher energy Planck scale come from a
 1260 series of loop diagrams in the **SM**, where each massive **SM** particle has a loop con-
 1261 tribution. The introduction of superpartners generates a series of corresponding
 1262 diagrams for correction to the Higgs mass, with opposite sign contributions be-
 1263 cause the superpartners have different spins. Those opposite sign contributions
 1264 cancel the divergences from the original loop diagrams at high energies, leaving
 1265 behind a correction to the Higgs mass that is at the same scale as the masses of the
 1266 superpartners. If the superpartners exist at the TeV scale, then the Higgs mass
 1267 of 125 GeV can be explained without significant fine-tuning, and the theory be-
 1268 comes natural.

1269 **SUSY** also has the potential to precisely enable the unification of the coupling
 1270 constants at high energy. Without supersymmetric contributions, the coupling
 1271 constants come close to a single value near the Planck scale suggesting an un-
 1272 derlying trend, as shown in Figure 4, but they do not exactly merge. With the
 1273 addition of the **MSSM**, they can join almost exactly at a single point, enabling a
 1274 unification into a single gauge theory at high energy, as shown in Figure 8. This
 1275 precise unification, like the naturalness argument, also requires that the masses
 1276 of the superpartners be near the TeV scale.

1277 The presence of R-parity in a **SUSY** model also provides an explanation for
 1278 dark matter. The **LSP**, as discussed in Section 3.1, is a massive, neutral, and stable
 1279 particle as long as R-parity is conserved. In the early universe, when the energy
 1280 density was extremely high, **LSPs** could be spontaneously produced just as often
 1281 as other particles like photons, and would result in a thermal equilibrium. Then,
 1282 as the universe cooled, the average energy would be too low to create additional
 1283 **LSPs**, and they would be left behind and only interact with the remaining matter
 1284 gravitationally, a process called freeze out. Since those particles are stable, they
 1285 would remain indefinitely. With the existence of an **LSP** at around the TeV scale,
 1286 this process can explain the observed amount of dark matter in the universe. A

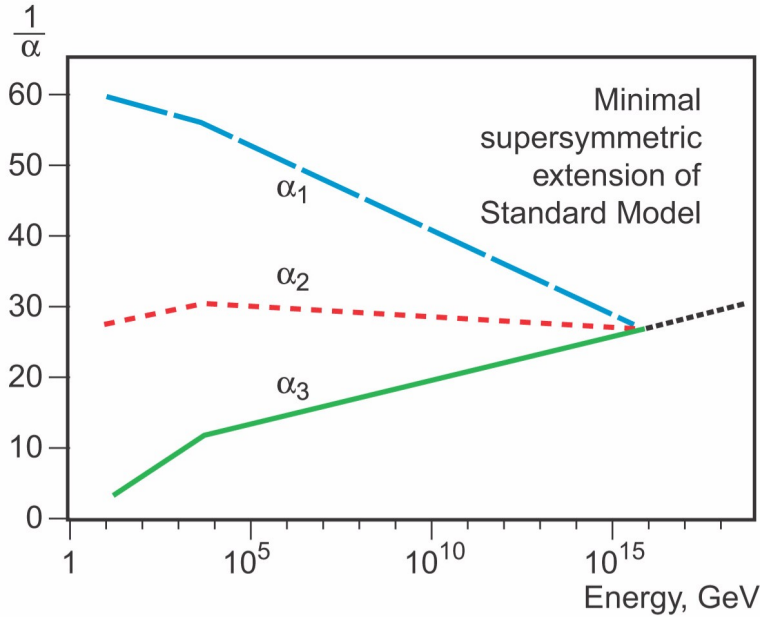


Figure 8: An approximation of the running of the coupling constants in the [MSSM](#) up to the Planck scale [2].

1287 **WIMP!** ([WIMP!](#)), exactly what is proposed in the [LSP](#), provides the correct interaction
 1288 rate to predict the currently observed ratio of dark matter to baryonic
 1289 matter.

1290 Together, this variety of solutions to existing problems provides strong theoretical
 1291 support for the existence of [SUSY](#) near the TeV scale. The [LHC](#) is the first
 1292 collider experiment to be able to probe into TeV scale interactions, providing a
 1293 new opportunity to search for this extension to the [SM](#). A range of models have
 1294 begun to be excluded with masses above 1 TeV [3], leading to a motivation to
 1295 explore a wider variety of models with phenomena that may have been missed
 1296 by the most direct search strategies.

1297 3.3 SIMPLIFIED MODELS

1298 The [MSSM](#) is just one example of a large suite of [SUSY](#) models with similar results.
 1299 Each of those models can have hundreds of individual parameters that ultimately
 1300 determine the masses and interactions of the supersymmetric particles. To avoid
 1301 this complexity in making experimental measurements, the analyses of high en-
 1302 ergy collisions often rely on simplified models. These models focus on a single
 1303 process predicted by a theory, and the observable parameters such as the mass
 1304 of the particles and their lifetimes are controlled directly, rather than tuning the
 1305 hundreds of underlying parameters. This allows straightforward simulation of
 1306 a specific event topology with control over the parameters that most directly
 1307 influence the experimental signatures.

1308 Experimental analyses use these models to search for new physics and to set
 1309 limits on the production rates for a given type of process with working points
 1310 of a few observable parameters. As one example, a simplified model may specify

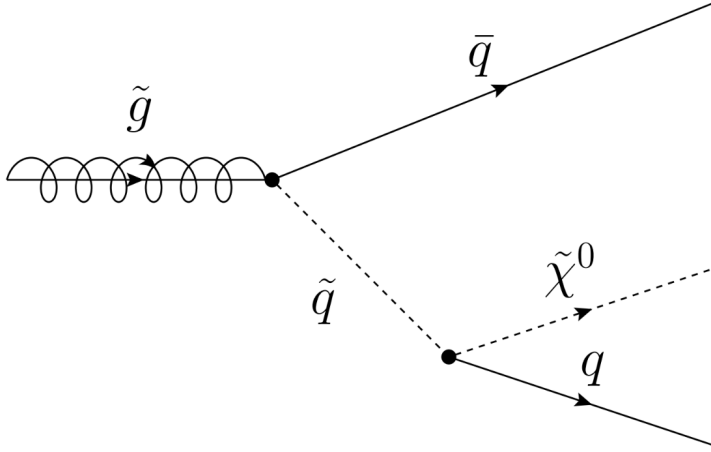


Figure 9: The decay of a gluino to quarks and an LSP, which precedes through a squark.

pair production of gluinos where the free parameters are the mass of the gluino and the types and masses of the particles it can decay into. The small number of parameters allows the phase space to be searched in a grid by simulating events with a few examples for the parameters and interpolating between them. The resulting analysis can set cross sectional limits as a function of the simplified parameters, and this allows for an easy interpretation of the result in a number of SUSY models.

3.4 LONG-LIVED PARTICLES

Some proposed SUSY models can produce LLPs other than just the LSP. The most direct search strategies for SUSY often assume that the various non-stable sparticles decay promptly, rather than propagating through some fraction of the detector. Although the processes involved are very similar, the long-lifetime of the produced particles can lead to very different experimental signatures, and often require separate dedicated searches. It is important to design and execute search strategies for LLPs in order to completely cover possible production of new physics.

There are several ways to generate long lifetimes for the massive SUSY particles, depending on the specific model. In examples like Spread Supersymmetry [11] and Split Supersymmetry [12, 13], the introduction of a split between two mass scales suppresses the decay of gluinos. In these and similar models, the squarks are much heavier than the gluino, where the mass scale of the squarks is roughly 10^6 GeV while the mass scale of the gluinos is roughly 10^3 GeV. The gluino must decay through the production of a virtual squark, as shown in the diagram of Figure 9. The large mass of the squarks in the split models suppresses the decay rate, and can result in lifetimes of the order of 1 ns [11].

Nearly degenerate particles can also result in long lifetimes, again by suppressing decay rates. When a particle must decay to another particle with nearly the same mass, the phase space factor in the decay results in a low decay rate. For

1339 example, a neutron has a lifetime of roughly fifteen minutes because its mass is
1340 so close to the proton. Models which result in a nearly degenerate chargino and
1341 LSP provide a long-lived chargino as well.

1342 Again, because of the wide variety of models which can produce LLPs and the
1343 large number of parameters which determine their masses and lifetimes, the anal-
1344 ysis presented here focuses on simplified models rather than assuming any par-
1345 ticular underlying theory. The models directly specify the decay mode of the
1346 LLPs as well as their masses and lifetimes, using a grid of values. The results of
1347 searches using these simplified models can be interpreted over a very wide range
1348 of models that predict LLPs, even including non-supersymmetric extensions to
1349 the SM.

1350

PART II

1351

EXPERIMENTAL STRUCTURE AND RECONSTRUCTION

1352

4

1353

1354 THE LARGE HADRON COLLIDER

1355 The LHC, a two-ring superconducting hadron accelerator, provides high energy
1356 proton-proton collisions for several large experiments at European Organization
1357 for Nuclear Research (CERN) in Geneva, Switzerland [14, 15]. It is the largest,
1358 highest-luminosity, and highest-energy proton collider ever built, and was con-
1359 structed by a collaboration of more than 10,000 scientists and engineers from
1360 the more than 100 countries that contribute to CERN. The original design of
1361 the LHC focused on providing collision energies of up to 14 TeV and generating
1362 enough collisions to reveal physics beyond the SM which is predicted to exist at
1363 higher energy scales.

1364 The LHC was installed in an existing 27 km tunnel at CERN which was orig-
1365 inally designed to house the Large Electron Positron collider (LEP) [16]. This
1366 allows the collider to use existing accelerators at the same complex to provide
1367 the initial acceleration of protons up to 450 GeV before injecting into LHC. The
1368 injected hadrons are accelerated up to as much as 14 TeV while being focused
1369 into two beams traveling in opposite directions. During this process the protons
1370 circulate around the tunnel millions of times, while the beams are intermittently
1371 crossed at the four locations of the experiments to provide collisions. These col-
1372 lision points correspond to the four major LHC experiments: ATLAS, Compact
1373 Muon Solenoid (CMS), Large Hadron Collider beauty experiment (LHCb), and A
1374 Large Ion Collider Experiment (ALICE), and Figure 10 shows the layout of the
1375 experiments both on the surface and below. ATLAS and CMS are both general
1376 purpose, high-luminosity detectors which search for a wide range of new types
1377 of physics [17, 18]. LHCb studies the interactions of b-hadrons to explore the
1378 asymmetry between matter and antimatter [19]. ALICE focuses on the collisions
1379 of lead ions, which the LHC also provides for about one month per year, in order
1380 to study the properties of quark-gluon plasma [20].

1381 During the first five years of continued operation, after the LHC turned on in
1382 2010, the LHC has provided four major data collecting periods. In 2010 the LHC
1383 generated collisions at several energies, starting at 900 GeV. It increased the
1384 energy from 900 GeV to 2.76 TeV and then subsequently to 7 TeV, with a peak
1385 luminosity of $2 \times 10^{32} \text{ cm}^{-2}\text{s}^{-1}$, and a total delivered luminosity of 50 pb^{-1} .
1386 The next run, during 2011, continued the operation at 7 TeV and provided an
1387 additional 5 fb^{-1} with a peak luminosity of $4 \times 10^{33} \text{ cm}^{-2}\text{s}^{-1}$. The energy was
1388 then increased to 8 TeV for the data collection during 2012, which provided 23 fb^{-1}
1389 with a peak luminosity of $7.7 \times 10^{33} \text{ cm}^{-2}\text{s}^{-1}$. After the first long shutdown
1390 for 2013 and 2014, the LHC resumed operation and increased the energy to 13
1391 TeV in 2015, where it delivered 4.2 fb^{-1} with a peak luminosity of $5.5 \times 10^{33} \text{ cm}^{-2}\text{s}^{-1}$.
1392 The LHC is currently providing additional 13 TeV collisions in 2016
1393 with higher luminosities than during any previous data collection periods. These
1394 running periods are summarized in Figure 11, which shows the total delivered

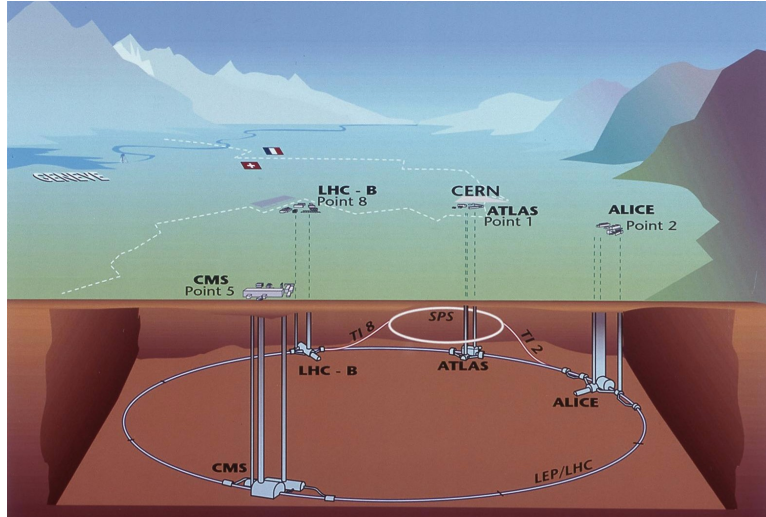


Figure 10: The four collision points and corresponding experiments of the LHC. The image includes the location of the nearby city of Geneva as well as the border of France and Switzerland [21].

luminosity over time for the ATLAS experiment during each of the four years of data collection since 2011. The full design energy of 14 TeV can only be reached after further magnet training that is scheduled for the long shutdown over 2019–2020.

4.1 INJECTION CHAIN

The LHC takes advantage of the presence of previously built accelerators at CERN to work up to the target energy in consecutive stages. The series of accelerators that feed into the LHC are known collectively as the injection chain, and together with the LHC form the accelerator complex. The full complex is illustrated in Figure 12, which details the complex series required to reach high energy collisions in the LHC experiments.

Protons at the LHC begin as hydrogen atoms in the Linac 2, a linear accelerator which replaced Linac 1 as the primary proton accelerator at CERN in 1978. In Linac 2, the hydrogen atoms are stripped of their electrons by a strong magnetic field, and the resulting protons are accelerated up to 50 MeV by cylindrical conductors charged by radio frequency cavities. The protons are then transferred to the Proton Synchrotron Booster (PSB), which uses a stack of four synchrotron rings to accelerate the protons up to 1.4 GeV. Then the protons are injected into the Proton Synchrotron (PS) which again uses synchrotron rings to bring the energy up to 25 GeV. The intermediate step between Linac 2 and the PS is not directly necessary, as the PS can accelerate protons starting from as low as 50 MeV. The inclusion of the PSB allows the PS to accept a higher intensity of injection and so increases the deliverable luminosity in the LHC. The penultimate stage of acceleration is provided by the Super Proton Synchrotron (SPS), a large synchrotron with a 7 km circumference that was commissioned at CERN

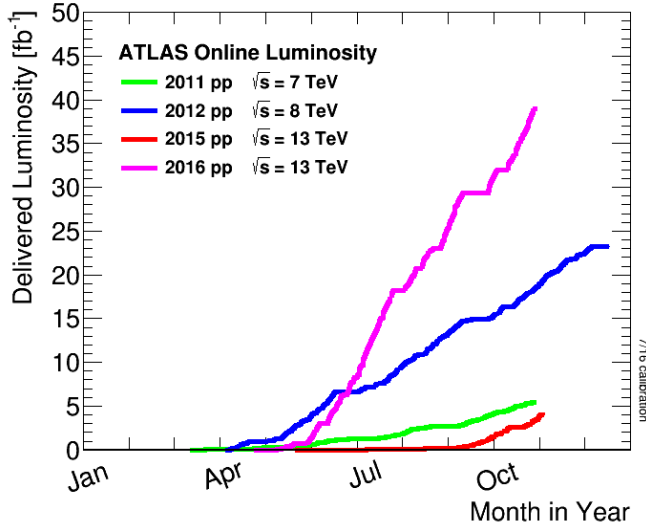


Figure 11: The cumulative luminosity over time delivered to the ATLAS experiment from high energy proton-proton collisions since 2011. The energies of the collisions are listed for each of the data-taking periods. The figure shows the delivered luminosity as of the conclusion of data collection in 2016 [22].

in 1976. During this step the protons increase in energy to 450 GeV, after which they can be directly injected into the [LHC](#).

The final step is the [LHC](#) itself, which receives protons from the [SPS](#) into two separate beam pipes which circulate in opposite directions. The filling process at this steps takes approximately 4 minutes, and the subsequent acceleration to the final energy (6.5 TeV during 2015 and up to 7 TeV by design) takes approximately half an hour. At this point the protons circulate around the circumference tens of thousands of times a second and continue for up to two hours.

4.2 DESIGN

4.2.1 LAYOUT

Many of the aspects of the [LHC](#) design are driven by the use of the existing [LEP](#) tunnel. This tunnel slopes gradually, with a 1.4% decline, with 90% of its length built into molasse rock which is particularly well suited to the application. The circumference is composed of eight 2987 meter arcs and eight 528 meter straight sections which connect them; this configuration is illustrated in Figure 13. The tunnel diameter is 3.7 m throughout its length.

The design energy is directly limited by the size of this tunnel, with its radius of curvature of 2804 m. A significant magnetic field is required to curve the protons around that radius of curvature; the relationship is given by

$$p \simeq 0.3BR \quad (13)$$

where p is the momentum of the particle in GeV, B is the magnetic field in Tesla, and R is the radius of curvature in meters. From the target design energy of

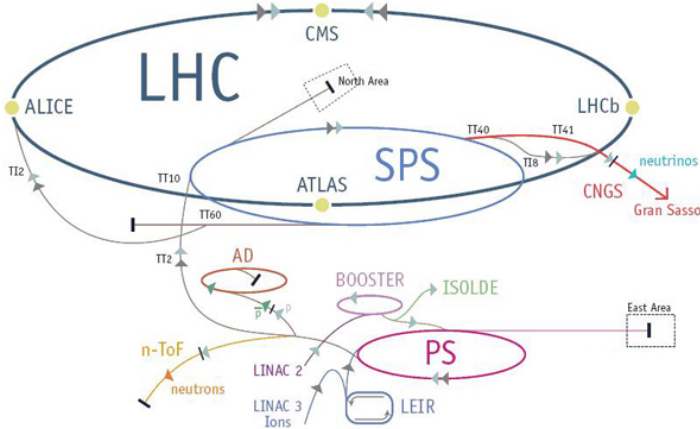


Figure 12: The accelerator complex that builds up to the full design energies at the LHC. The protons are passed in order to Linac 2, the PSB, the PS, the SPS and then the LHC [23].

1438 14 TeV, or 7 TeV of momentum for protons in each beam, the required magnetic field is 8.33 Tesla. This is too large a field strength to be practical with
 1439 iron electromagnets, because of the enormous power required and the resulting
 1440 requirements for cooling. Because of these constraints, the LHC uses supercon-
 1441 ducting magnets which can maintain that field strength with significantly less
 1442 power consumption.
 1443

1444 4.2.2 MAGNETS

1445 The magnets chosen were made of Niobium and Titanium (NbTi) which allow
 1446 for field strengths as high as 10 Tesla when cooled down to 1.9 K. Reaching the
 1447 target temperature of 1.9 K for all of the magnets requires superfluid helium
 1448 and a large cryogenic system along the entire length of the tunnel. During nor-
 1449 mal operation, the LHC uses 120 tonnes of helium within the magnets, and the
 1450 entire system is cooled by eight cryogenic helium refrigerators. The tempera-
 1451 ture increase that occurs during transit from the refrigerator along the beam
 1452 necessitates that the refrigerators cool the helium down to 1.8 K. Any significant
 1453 increase above this temperature range can remove the superconductive proper-
 1454 ties of the magnets, which in turn generates drastically larger heat losses from
 1455 the current within the magnets and causes a rapid rise in temperature called a
 1456 quench.

1457 There are approximately 8000 superconducting magnets distributed around
 1458 the LHC. The 1232 bending magnets, which keep the protons curving along the
 1459 length of the beam, are twin bore cryodipoles, which allow both proton beams
 1460 to be accommodated by one magnet and all of the associated cooling structure.
 1461 Figure 14 shows the cross section of the design for these dipoles. The magnets
 1462 are very large, 16.5 m long with a diameter of 0.57 meters and a total weight of 28
 1463 tonnes. They are slightly curved, with an angle of 5.1 mrad, in order to carefully
 1464 match the beam path. The twin bore accommodates both magnets inside the

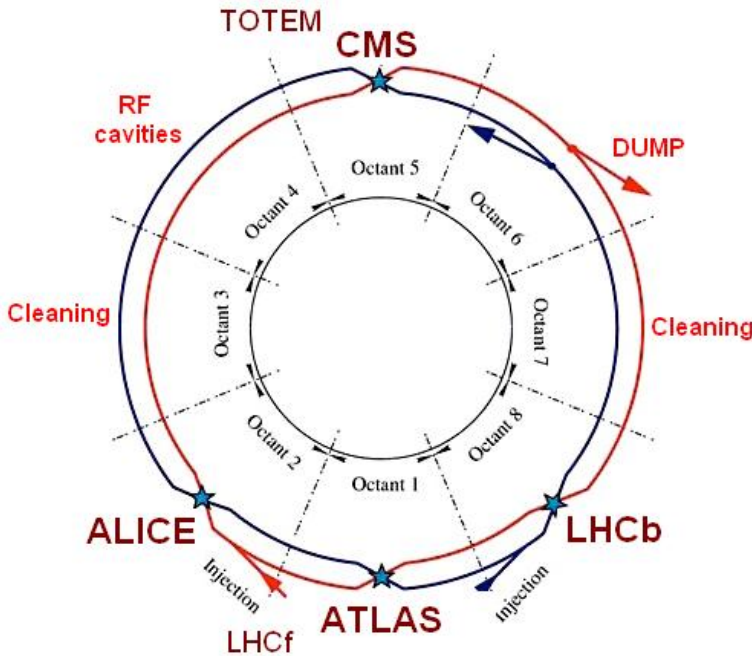


Figure 13: A schematic of the layout of the LHC, not to scale. The arched and straight sections are illustrated at the bottom of the schematic, and all four crossing sites are indicated with their respective experiments [14].

1465 two 5 cm diameter holes which are surrounded by the superconducting coils.
 1466 The coils require 12 kA of current in order to produce the required magnetic
 1467 field. These coils are comprised of NbTi cable wound in two layers; the wire in
 1468 the inner layer has a diameter of 1.065 mm while the wire in the outer layer has
 1469 a diameter of 0.825 mm.

1470 The large currents in the wires, along with the magnetic field produced, result
 1471 in forces on the magnets which would tend to push them apart with over 10,000
 1472 Newtons per meter. Constraining the magnets requires a significant amount of
 1473 structure including non-magnetic stainless steel collars. Both the presence of
 1474 these electromagnetic forces and the varying thermal contraction coefficient of
 1475 the pieces of the magnet produce significant forces on the cold mass structure.
 1476 The cold mass is carefully engineered to so that these stresses do not significantly
 1477 alter the magnetic field shape, which must be maintained between magnets to a
 1478 precision of approximately 10^{-4} for successful operation.

1479 The remaining 6800 magnets are a variety of quadrupole, sextapole, octopole,
 1480 and single bore dipole magnets. These are used to damp oscillations, correct
 1481 beam trajectories, focus the beams during circulation, and to focus the beams
 1482 before collisions.

1483 4.2.3 RADIO FREQUENCY CAVITIES

1484 Sixteen radiofrequency (RF) cavities produce the actual acceleration of the pro-
 1485 ton beam up to the design energy. These RF cavities are tuned to operate at 400
 1486 MHz, and are powered by high-powered electron beams modulated at the same

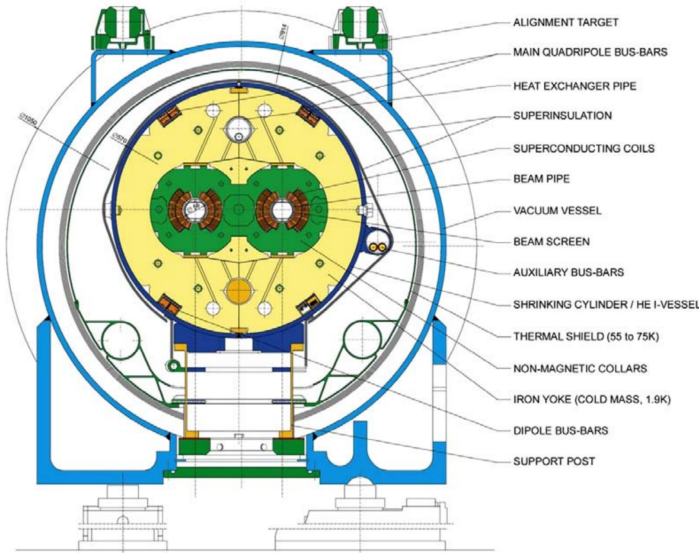


Figure 14: A cross section of the cryodipole magnets which bend the flight path of protons around the circumference of the LHC. The diagram includes both the superconducting coils which produce the magnetic field and the structural elements which keep the magnets precisely aligned [14].

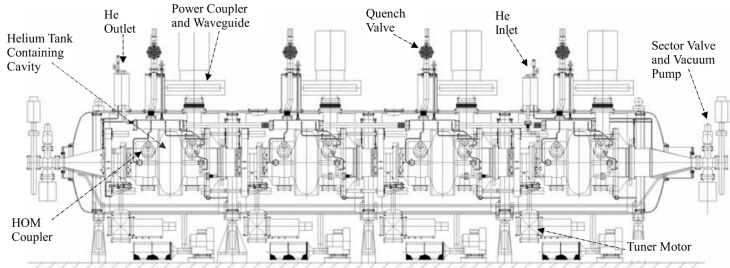


Figure 15: The arrangement of four RF cavities within a cryomodule [14].

frequency, called klystrons. The resonance within the cavity with the oscillating electric field establishes a voltage differential of 2 MV per cavity. The sixteen cavities are split between the two beams, so combined the cavities provide 16 MV per beam, which accelerate the protons on each consecutive pass through the cavity. This acceleration is also necessary during circulation even after the target energy has been reached in order to compensate for losses from synchrotron radiation.

The cavities are arranged in cryomodules which contain four cavities, with two cryomodules per beam; this arrangement is illustrated in Figure 15. These cryomodules are necessary to maintain the superconducting state of the cavities, which are also constructed from niobium. The RF cavities use niobium along with copper to allow for low power losses in the superconductors. The copper provides a reduced susceptibility to quenching, as it rapidly conducts away heat generated by imperfections in the niobium, as well as natural shielding from the earth's magnetic field which can interfere with the RF system.

1502 The nature of the radio frequency oscillations tends to group protons together
 1503 into buckets. A proton traveling exactly in phase with the RF oscillations will not
 1504 be displaced at all during a single circulation, and those slightly ahead or behind
 1505 of that phase will slightly decelerate or accelerate, respectively. This produces
 1506 separate clusters of protons which arrive in phase to the cavities every 2.5 ns,
 1507 corresponding to the 400 MHz frequency.

1508 4.2.4 BEAM

1509 The beams of protons circulate within 27 km of 5 cm diameter beam pipe. This
 1510 entire structure is kept under vacuum at 1.9 K to prevent interactions between
 1511 the beam pipe and the magnets as well as to prevent any interactions between the
 1512 circulating protons and gas in the pipe. The vacuum within the pipe establishes
 1513 a pressure as low as 10^{-9} mbar before the protons are introduced.

1514 Because of the very high energies of the circulating protons, synchrotron ra-
 1515 diation is not negligible in the bending regions. The protons are expected to
 1516 radiate 3.9 kW per beam at 14 TeV, with 0.22 W/m, which is enough power to
 1517 heat the liquid helium and cause a quench were it absorbed by the magnets. To
 1518 prevent this, a copper screen is placed within the vacuum tube that absorb the
 1519 emitted photons. This screen is kept between 5 and 20 K by the liquid helium
 1520 cooling system.

1521 4.3 LUMINOSITY PARAMETERS

In addition to the high energy of the collisions, the rate of collisions is extremely important to enabling the discovery of new physics. Many measurements and searches require a large number of events in order to be able to make statistically significant conclusions. The rate of collisions is measured using luminosity, the number of collisions per unit time and unit cross section for the proton-proton collisions. From the beam parameters, luminosity is given by

$$\mathcal{L} = \frac{N_b^2 n_b f_{rev} \gamma}{4\pi\epsilon_n \beta^*} F \quad (14)$$

1522 where N_b is the number of protons per bunch, n_b is the number of bunches col-
 1523 liding, f_{rev} is the frequency of revolution, γ is the Lorentz factor for the protons
 1524 at the circulating energy, ϵ_n is the emittance, β^* is the amplitude function at the
 1525 collision point, and F is a geometric factor that accounts for the crossing angle of
 1526 the beams at the collision point. The emittance measures the average spread of
 1527 particles in both position and momentum space, while the amplitude function is
 1528 a beam parameter which measures how much the beam has been squeezed. To-
 1529 gether ϵ_n and β^* give the size of the beam in the transverse direction, $\sigma = \sqrt{\epsilon\beta^*}$.
 1530 β changes over the length of the beam as the accessory magnets shape the distri-
 1531 bution of protons, but only the value at the point of collisions, β^* , affects the
 1532 luminosity.

1533 The luminosity is maximized to the extent possible by tuning the parameters
 1534 in Equation 14. A number of these are constrained by the design decisions. The

Parameter	Unit	Injection	Nominal	2015
Beam Energy	TeV	0.450	7	6.5
Peak Instantaneous Luminosity	$\text{cm}^{-2}\text{s}^{-1}$	-	10^{34}	5×10^{33}
Bunch Spacing	ns	25	25	25
Number of Filled Bunches	-	2808	2808	2240
Normalized Transverse Emittance	μm	3.75	3.75	-
Frequency	MHz	400.789	400.790	-
RF Voltage/Beam	MV	8	16	-
Stored Energy	MJ	-	362	-
Magnetic Field	T	0.54	8.33	-
Operating Temperature	K	1.9	1.9	1.9

Table 2: The design parameters of the [LHC](#) beam that determines the energy of collisions and the luminosity, for both the injection of protons, at the nominal circulation, and during the 2015 data-taking period.

revolution frequency is determined entirely by the length of the tunnel, as the protons travel at very close to the speed of light. The geometric factor F is determined by the crossing angle of the beams at the collision points, a tunable component of the tunnel design; this angle is already very small at $285 \mu\text{rad}$, which helps to maximize the geometric factor.

The major pieces that can be adjusted are the number of protons per bunch, N_b , the number of bunches in the beam, n_b , and the amplitude function β . Increasing either N_b or n_b increases the amount of energy stored in the beam, which presents a danger if control of the beam is lost. At design specifications, the beam stores 362 MJ, which is enough energy to damage the detectors or accelerator if the beam were to wander out of the beam pipe. So, the luminosity is primarily controlled at the [LHC](#) by adjusting β^* , where lowering β^* increases the luminosity. β^* is tuned to provide the various values of luminosity used at the [LHC](#) which can be raised to as much as $1.4 \times 10^{34} \text{ cm}^{-2}\text{s}^{-1}$.

The nominal bunch structure consists of 3654 bunches, each holding 10^{11} protons, which cross a collision point in 25 ns. These are further subdivided into the buckets mentioned in Section 4.2.3 by the clustering properties of the RF cavities. In 2015, the bunches are further grouped into trains of 72 bunches which are separated by a gap which would otherwise hold 12 bunches. At nominal operation 2808 of the bunches will actually be filled with protons, while the remainder are left empty to form an abort gap that can be used in case the beam needs to be dumped.

The various beam parameters are summarized in Table 2 for the designed operation. In practice, the beam has operated at lower energies and lower luminosities than the design values for the majority of its lifetime, but the [LHC](#) has begun to operate at full design values during Run 2.

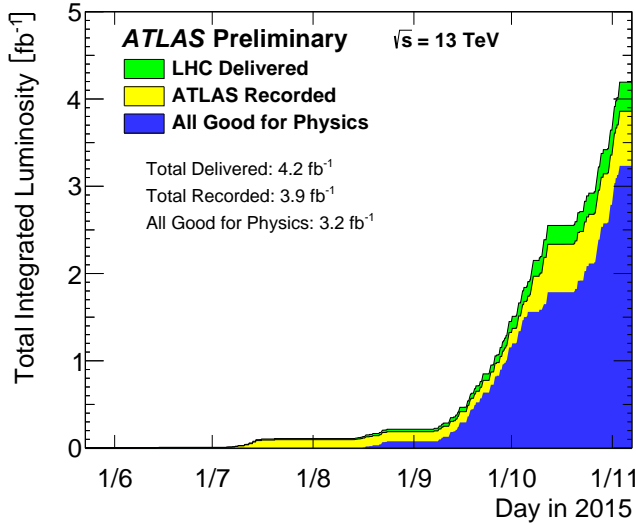


Figure 16: The cumulative luminosity versus time delivered to ATLAS (green), recorded by ATLAS (yellow), and certified to be good quality data (blue) during stable beams for pp collisions at 13 TeV in 2015 [22].

1561 4.4 DELIVERED LUMINOSITY

During the data collection of 2015, the LHC operated at luminosities as large as $5 \times 10^{33} \text{ cm}^{-2}\text{s}^{-1}$. It is convenient to refer to the integrated luminosity, the integral of the instantaneous luminosity, which corresponds directly to the number of delivered events for a given process.

$$N = \sigma \times \int \mathcal{L}(t) dt$$

1562 where σ is the cross section for the process of interest. The integrated luminosity
 1563 over time is shown in Figure 16. This includes the luminosity delivered by the
 1564 LHC as well as the luminosity that was recorded by ATLAS. ATLAS only records
 1565 collisions when the LHC reports that the beam conditions are stable, so some of
 1566 the delivered luminosity is not recorded. The figure also includes the amount of
 1567 luminosity marked as good for physics, which includes additional requirements
 1568 on the operation of the detector during data collection that are necessary for
 1569 precise measurements.

1570 Because the beam circulates and collides bunches of protons, it is possible
 1571 for a single crossing to produce multiple proton-proton collisions. As the instantane-
 1572 ous luminosity is increased, the average number of collisions generated per bunch
 1573 crossing increases. An event refers to the entire collection of interactions
 1574 during a single bunch crossing, while interactions refer to the individual
 1575 proton-proton collisions. The additional interactions produced during each
 1576 bunch crossing are referred to as pileup, which can be more precisely defined
 1577 quantified using the average number of additional proton-proton interactions
 1578 per crossing, often denoted μ . Figure 17 shows the luminosity-weighted distri-
 1579 bution of the mean number of interactions for events collected in 2015. The
 1580 presence of as many as twenty interactions in a single collision provides a sig-

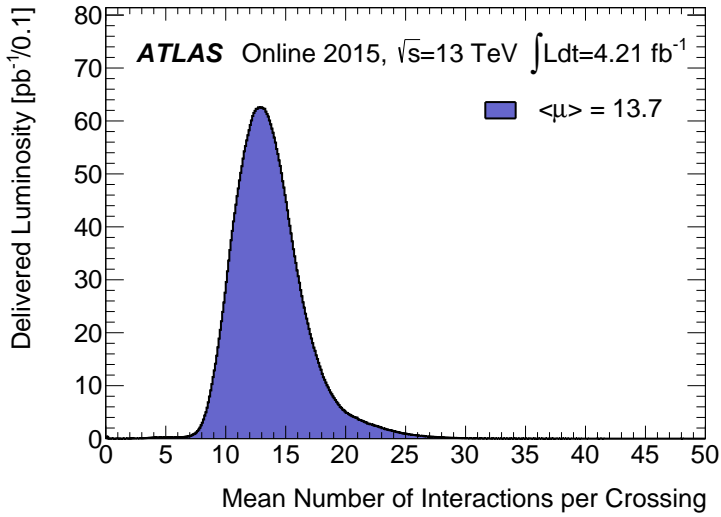


Figure 17: The luminosity-weighted distribution of the mean number of interactions per crossing for the 2015 pp collision data at 13 TeV [22].

1581 nificant challenge in reconstructing events and isolating the targeted physical
1582 processes.

1583

1584 THE ATLAS DETECTOR

1585 The four major LHC experiments at CERN seek to use the never before matched
1586 energies and luminosities of the new collider to explore the boundaries of par-
1587 ticle physics and to gain insight into the fundamental forces of nature. Two of
1588 these experiments, ATLAS and CMS, are general purpose detectors that seek to
1589 measure a variety of processes in the up to 13 TeV proton-proton collisions that
1590 occur as much as 800 million times per second at the LHC at the design lumi-
1591 nosity of $10^{34} \text{ cm}^{-2}\text{s}^{-1}$. ATLAS employs a hermetic detector design, one which
1592 encloses the particle collisions as completely as possible with detecting elements,
1593 that allows it to study a wide range of physics from SM precision measurements
1594 to searches for new physics in models like SUSY [17].

1595 Accommodating this wide variety of goals is a challenge for the design of the
1596 detector. The wide range of energies involved requires high measurement pre-
1597 cision over several orders of magnitude, and the numerous physics processes
1598 require an ability to measure a variety of particle types. At the time of the con-
1599 struction of ATLAS, the Higgs boson had yet to be discovered, but the diphoton
1600 decay mode was (correctly) expected to be important and necessitated a high
1601 resolution photon measurement. The potential for decays of new heavy gauge
1602 bosons, W' and Z', required a similarly high momentum resolution for leptons
1603 with momentum up to several TeV. Hadronic decay modes of several possible
1604 new high energy particles could result in very energetic jets, again up to several
1605 TeV, and reconstructing the decay resonances would again require good energy
1606 resolution. Several models, such as SUSY or Extra Dimensions, predict the exis-
1607 tence of particles which would not interact with traditional detecting elements.
1608 However these particles can still be observed in a hermetic detector by accurately
1609 measuring the remaining event constituents to observe an imbalance in energy
1610 called missing energy or E_T^{miss} . Measuring E_T^{miss} implicitly requires a good res-
1611 olution on all SM particles that can be produced. And at the lower end of the
1612 energy spectrum, precision SM measurements would require good resolution of
1613 a variety of particle types at energies as low as a few GeV, so the design needs to
1614 accommodate roughly three orders of magnitude.

1615 This broad spectrum of measurements requires a variety of detector systems
1616 working together to form a cohesive picture of each collision. Two large mag-
1617 net systems produce magnetic fields that provide a curvature to the propagation
1618 of charged particles and allows for precision momentum measurements in the
1619 subdetectors. The inner detector uses a combination of detector technologies
1620 to reconstruct particle trajectories and vertices for charged particles. A variety
1621 of calorimeters measure the energies of hadrons, electrons, and photons over a
1622 large solid angle. A large muon spectrometer identifies muons and uses the sec-
1623 ond magnet system to provide an independent measurement of their momentum

1624 from the inner detector and improve the resolution. The layout of all of these
 1625 systems is shown in Figure 18.

1626 The performance goals needed to achieve the various targeted measurements
 1627 and searches discussed above can be summarized as resolution and coverage re-
 1628 quirements on each of these systems. Those requirements are listed in Table 3.

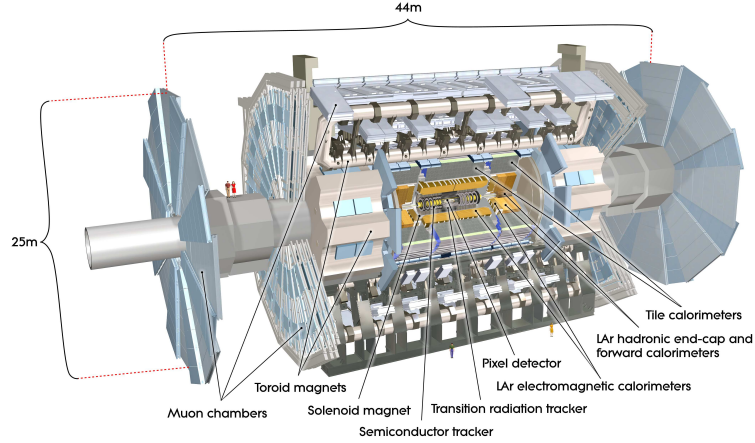


Figure 18: A cut-away schematic of the layout of the ATLAS detector. Each of the major subsystems is indicated [17].

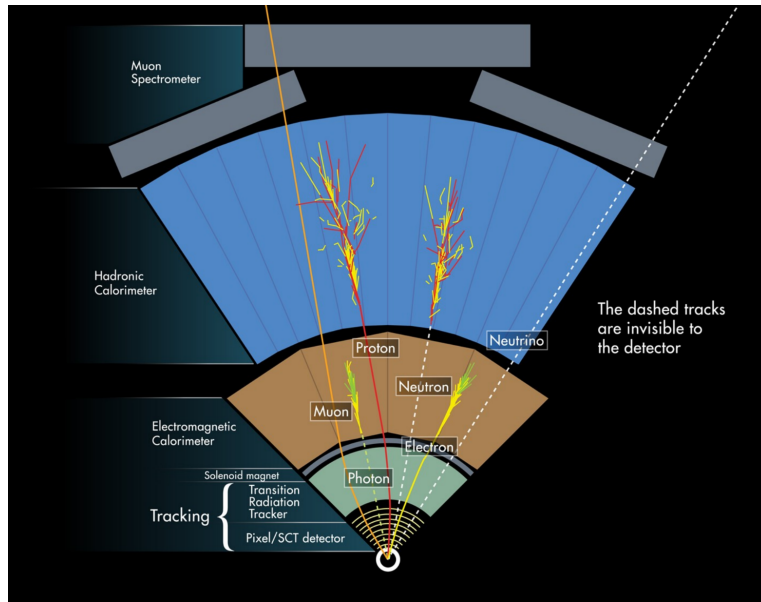


Figure 19: A cross-sectional slice of the ATLAS experiment which illustrates how the various SM particles interact with the detector systems.

1629 Incorporating these various pieces into a single detector is a significant tech-
 1630 nical challenge. The resulting detector has a diameter of 22 m, is 46 m long,
 1631 and weighs 7,000 tons; it is the largest volume particle detector ever constructed.
 1632 The various detector elements need to be constructed and assembled with pre-
 1633 cision as low as micrometers. These systems all need to function well even after
 1634 exposure to the significant radiation dose from the collisions. Designing, con-

Detector Component	Required Resolution	$ \eta $ Coverage	
		Measurement	Trigger
Tracking	$\sigma_{p_T}/p_T = 0.05\% p_T \oplus 1\%$	2.5	-
EM Calorimetry	$\sigma_E/E = 10\%/\sqrt{E} \oplus 0.7\%$	3.2	2.5
Hadronic Calorimetry			
Barrel and Endcap	$\sigma_E/E = 50\%/\sqrt{E} \oplus 3\%$	3.2	3.2
Forward	$\sigma_E/E = 100\%/\sqrt{E} \oplus 10\%$	3.1 – 4.9	3.1 – 4.9
Muon Spectrometer	$\sigma_{p_T}/p_T \leq 10\% \text{ for } p_T \leq 1 \text{ TeV}$	2.7	2.4

Table 3: The performance goals for each of the subsystems of the ATLAS detector. The $|\eta|$ coverage specifies the range where the subsystem needs to be able to provide measurements with the specified resolution. The resolutions include a p_T or E dependence that is added in quadrature with a p_T/E independent piece.

1635 structing, and installing the detector took the combined effort of more than 3000
 1636 scientists from 38 countries over almost two decades.

1637 5.1 COORDINATE SYSTEM

1638 The coordinate system defined for the ATLAS detector is used throughout all of
 1639 the sections of this thesis. The system begins with the choice of a z axis along
 1640 the beamline. The positive z side of the detector is commonly referred to as the
 1641 *A*-side, and the negative z side is referred to as the *C*-side. The $x - y$ plane is
 1642 then the plane transverse to the beam direction, with the x direction defined as
 1643 pointing from the interaction point to the center of the LHC ring and the y direc-
 1644 tion defined as pointing upwards. The nominal interaction point is the origin of
 1645 this system.

1646 It is more convenient in practice to use a cylindrical coordinate system; this
 1647 choice of coordinate system reflects the cylindrical symmetry of the ATLAS de-
 1648 tector. The distance from the beamline is the radius, r' , and the angle from the
 1649 z -axis is θ . The azimuthal angle, ϕ , runs around the z -axis with $\phi = 0$ corre-
 1650 sponding to the x -axis. Many aspects of the detector are independent of this
 1651 coordinate to first order; the detector is symmetric in ϕ . The θ direction is typi-
 1652 cally specified using rapidity or pseudorapidity, where rapidity is defined as

$$y = \frac{1}{2} \ln \frac{E + p_z}{E - p_z} \quad (15)$$

1653 Rapidity is particularly useful to indicate the component along the z direction
 1654 because differences in rapidity are invariant to boosts along the z -direction. A
 1655 similar quantity which depends only the θ is the pseudorapidity,

$$\eta = -\ln \tan \frac{\theta}{2} \quad (16)$$

1656 which approaches rapidity in the limit where the energy is much larger than the
 1657 particle's mass and is identical for massless particles. It is often useful to refer to
 1658 differences in solid angle using the pseudorapidity and the azimuthal angle:

$$\Delta R = \sqrt{\Delta\phi^2 + \Delta\eta^2} \quad (17)$$

1659 The pseudorapidity is also invariant to boosts along the z -axis for high mo-
 1660 mentum particles, and is preferable to rapidity because it does not depend on
 1661 the specific choice of particle. Pseudorapidity is also preferable to θ because par-
 1662 ticle production is roughly uniform in equal-width intervals of η up to about
 1663 $\eta = 5.0$. A particle traveling along the beampipe has $\eta = \infty$ and a particle
 1664 traveling perpendicular to the beampipe has $\eta = 0$. The extent of the tracker,
 1665 $|\eta| < 2.5$, corresponds to approximately $0.05\pi < \theta[\text{rad}] < 0.95\pi$ and the
 1666 extent of the calorimeters, $|\eta| < 4.9$ corresponds to approximately $0.005\pi <$
 1667 $\theta[\text{rad}] < 0.995\pi$. Many detector components are broken into multiple subsys-
 1668 tems to provide coverage at greater $|\eta|$. The lower $|\eta|$ region is referred to as the
 1669 barrel, typically with $|\eta| \lesssim 1.4$, and the greater $|\eta|$ region is often referred to as
 1670 the endcap.

1671 The initial momentum along the z direction of the constituents in a proton-
 1672 proton collision is unknown in hadron colliders because the constituent mo-
 1673 mента vary between collisions (Section 2.5.4). Along the transverse plane, how-
 1674 ever, the vector sum of momentum will be zero. For this reason, many physical
 1675 quantities are quantified in terms of their projection onto the transverse plan,
 1676 such as p_T or E_T . In addition, p_T alone determines the amount of curvature in
 1677 the magnetic field, and can be measured independently by measuring the curva-
 1678 ture of a particle's propagation.

1679 5.2 MAGNETIC FIELD

1680 The magnet system used in ATLAS is designed to provide a substantial magnetic
 1681 field in the two regions where the trajectory of particles is measured, the inner
 1682 detector and the muon spectrometer. The magnetic field generates a Lorentz
 1683 force that curves the trajectory of charged particles, following Equation 13. This
 1684 allows the precision tracking elements to make high resolutions measurements
 1685 of p_T . To provide a magnetic field in these regions, ATLAS uses a hybrid sys-
 1686 tem with four separate, superconducting magnets. A single solenoid provides
 1687 a 2 T axial, uniform magnetic field for the inner detector, while a barrel toroid
 1688 and two endcap toroids produce a non-uniform magnetic field of 0.5 and 1 T,
 1689 respectively, for the muon detectors. This geometry is illustrated in Figure 20,
 1690 and the parameters of the three magnet systems are summarized in Table 4.

1691 The central solenoid uses a single-layer coil with a current of 7.730 kA to gen-
 1692 erate the 2 T axial field at the center of the magnet. The single-layer coil design
 1693 enables a minimal amount of material to be used in the solenoid's construction,
 1694 which is important because the solenoid is placed between the inner detector
 1695 and the calorimeters. At normal incidence the magnet has only 0.66 radiation
 1696 lengths worth of material, where one radiation length is the mean distance over

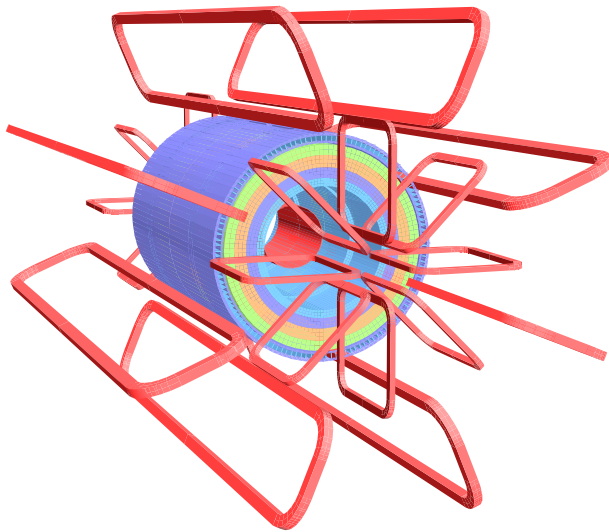


Figure 20: The layout of the four superconducting magnets in the ATLAS detector [17].

Parameter	Unit	Solenoid	Barrel Toroid	Endcap Toroids
Inner Diameter	m	2.4	9.4	1.7
Outer Diameter	m	2.6	20.1	10.7
Axial Length	m	5.3	25.3	5.0
Weight	tons	5.7	830	239
Conductor Size	mm ²	30×4.25	57×12	41×4.25
Peak Field	T	2.6	3.9	4.1
Heat Load	W	130	990	330
Current	kA	7.7	20.5	20.0
Stored Energy	MJ	38	1080	206

Table 4: A summary of the parameters of each of the three magnet systems on ATLAS.

1697 which a high-energy electron loses all but $1/e$ of its energy through material in-
 1698 teractions [3]. The coil is made of a high-strength aluminum stabilized NbTi
 1699 superconductor which was optimized to achieve a high field with minimal thick-
 1700 ness. The axial magnetic field produced by the solenoid bends charged particles
 1701 in the ϕ direction, following a circular path with a radius specified by Maxwell's
 1702 equations (see Equation 13).

1703 The barrel toroid consists of eight coils which generate a 0.5 T magnetic field,
 1704 on average, in the cylindrical region around the calorimeters with an approxi-
 1705 mately 20 kA current. The coils are separated only by air to reduce the scatter-
 1706 ing of muons as they propagate through the region. The coils are made of an
 1707 aluminum stabilized NbTiCu superconductor and each is separately housed in a
 1708 vacuum and cold chamber. This magnetic configuration produces a field in the
 1709 ϕ and so curves muons traversing the volume primarily in the η direction.

1710 The endcap toroids follow a similar design to the barrel toroid and produce a
 1711 1.0 T magnetic field, on average. Each has eight separate NbTiCu coils, and in
 1712 this case all eight are housed within a single cold mass. This extra structure is
 1713 necessary to withstand the Lorentz forces exerted by the magnets. These mag-
 1714 nets are rotated 22.5% relative to the barrel toroid to provide a uniform field in
 1715 the transition between the two systems. The endcap toroids also produce a field
 1716 in the ϕ direction and curve muons primarily in the η direction.

1717 5.3 INNER DETECTOR

1718 The ATLAS inner detector provides excellent momentum resolution as well as
 1719 accurate primary and secondary vertex measurements through robust pattern
 1720 recognition that identifies tracks left by charged particles. These tracks fulfill
 1721 a number of important roles in the ATLAS measurement system: they measure
 1722 the momentum of charged particles including electrons and muons, they can
 1723 identify electrons, they assign particles to different vertices, and they provide a
 1724 correction to E_T^{miss} measurements from low energy particles. The system has
 1725 to be accurate enough to separate tracks from dozens of vertices, to resolve each
 1726 vertex individually, and to measure the p_T of very high momentum tracks which
 1727 curve very little even in the large magnetic field. This is accomplished by sev-
 1728 eral independent layers of tracking systems. Closest to the interaction point is
 1729 the very high granularity Pixel detector, including the newly added Insertible B-
 1730 Layer (**IBL**), which is followed by the silicon microstrip (**SCT**) layers. These silicon
 1731 subdetectors both use discrete space-points to reconstruct track patterns. The fi-
 1732 nal layer, the Transition Radiation Tracker (**TRT**), uses many layers of straw tube
 1733 elements interleaved with transition radiation material to provide continuous
 1734 hits in the transverse plane. To provide the desired hermetic coverage, the sub-
 1735 detectors are divided into barrel and endcap geometries. Figure 21 shows the
 1736 layout of the subdetectors in more detail, and illustrates how tracks at various
 1737 pseudorapidities can traverse the subdetectors; tracks with $\eta > 1.1$ begin to tra-
 1738 vers the endcap subdetectors rather than those in the barrel, and tracks with
 1739 $\eta > 1.7$ use primarily endcap elements. The **IBL** was not present during the orig-
 1740 inal commissioning of the inner detector and is not shown in this figure.

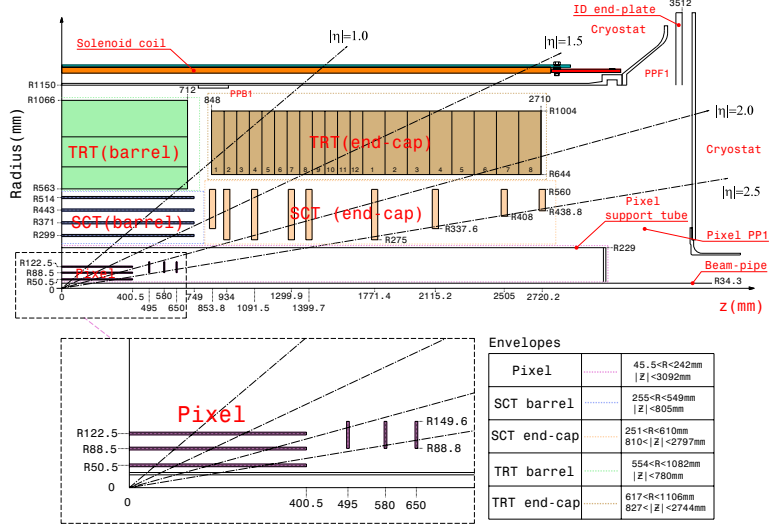


Figure 21: A quarter section of the ATLAS inner detector which shows the layout of each of the subdetectors in detail. The lower panel shows an enlarged view of the pixel detector. Example trajectories for a particle with $\eta = 1.0, 1.5, 2.0, 2.5$ are shown. The IBL, which was added after the original detector commissioning, is not shown [17].

1741 Figure 22 shows a computer generated three-dimensional view of the inner
 1742 detector along the beam axis, which emphasizes the straw tube structure of the
 1743 TRT as well as the overlapping geometry of the SCT. This figure also includes
 1744 the IBL, which was added during the long shutdown and provides an additional
 1745 measurement layer in the Pixel detector as of the beginning of Run 2. Figure 23
 1746 shows an alternative computer generated three-dimensional view transverse to
 1747 the beam axis which emphasizes the endcap structures of the SCT and TRT.

1748 As the closest system to the interaction point, it is crucial for the inner detector
 1749 to use as little material as possible to avoid scattering of charged particles before
 1750 they reach the remaining subdetectors. The various components, including the
 1751 readout electronics, cooling infrastructure, gas volumes, and support structures,
 1752 were designed to accommodate this need for minimal components. Even with
 1753 these optimizations, the combination of stringent performance requirements
 1754 and the harsh radiation environment in the inner detector requires a significant
 1755 amount of material. This material causes many electrons to lose most of their
 1756 energy before reaching the electromagnetic calorimeter and approximately 40%
 1757 of photons convert into an electron-positron pair while traversing the inner de-
 1758 tector. Figure 24 shows the integrated radiation lengths traversed by a straight
 1759 track in the inner detector as a function of η , grouped by subdetector. There is a
 1760 large increase in the amount of material for support structures around $|\eta| = 1.7$,
 1761 where the inner detector transitions from barrel to endcap.

1762 The inner detector is designed to work as a cohesive unit to provide complete
 1763 tracking information for charged particles. Table 5 summarizes the parameters
 1764 of each of the subdetectors as well as the parameters of the combined inner de-
 1765 tector.

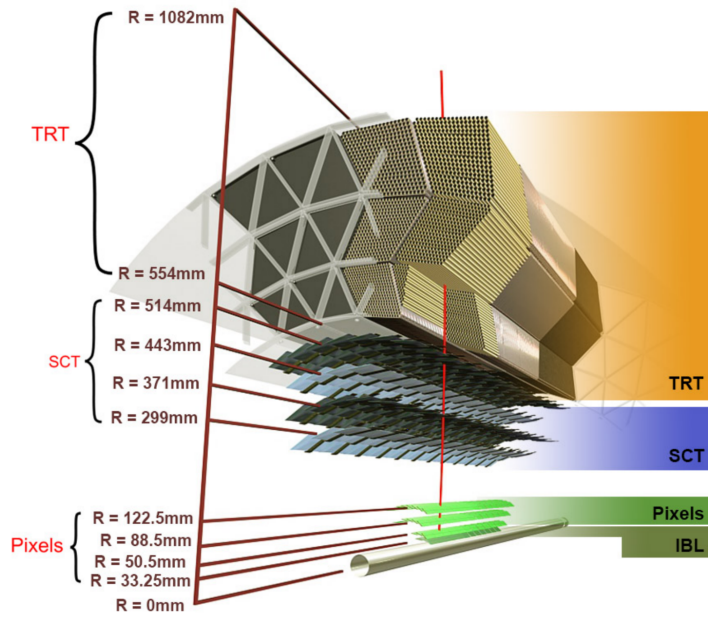


Figure 22: A computer generated three-dimensional view of the inner detector along the line of the beam axis. The subdetectors and their positions are labeled [17].

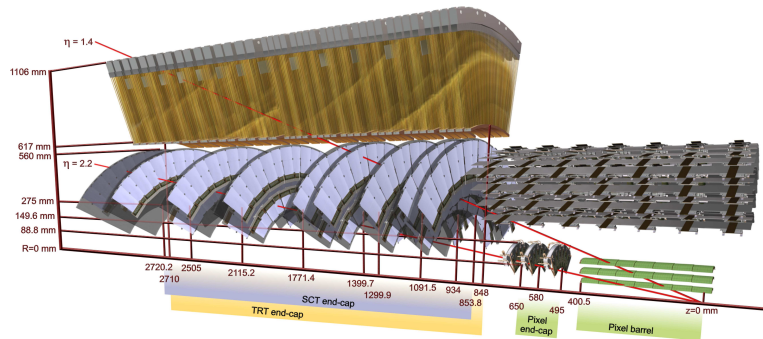


Figure 23: An alternative computer generated three-dimensional view of the inner detector transverse to the beam axis. The subdetectors and their positions are labeled [17].

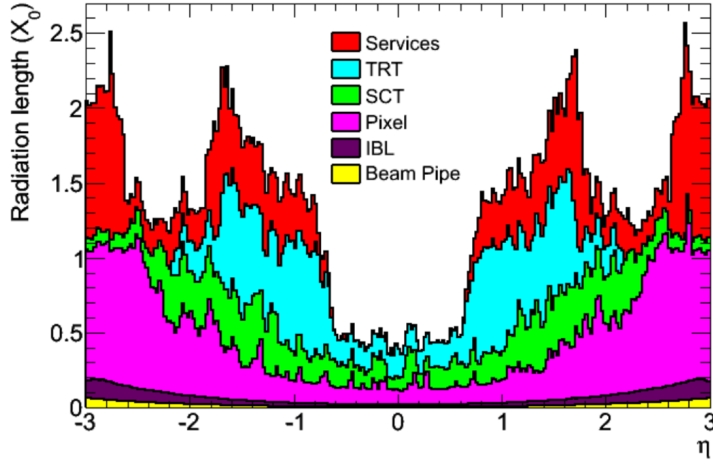


Figure 24: The integrated radiation lengths traversed by a particle at the exit of the ID envelope (outside of the TRT after 108.2 cm), including the services and thermal enclosures. The distribution is shown as a function of $|\eta|$ and averaged over ϕ . The breakdown indicates the contributions of individual sub-detectors, including services in their active volume [17].

1766 5.3.1 PIXEL DETECTOR

1767 The Pixel detector is the closest detector to the interaction point and therefore is
 1768 designed to provide high granularity while simultaneously handling a large dose
 1769 of radiation from collisions. It consists of four layers of silicon pixel modules,
 1770 each of which provides a precision measurement on the trajectory of any charged
 1771 particle. In the barrel region, the four layers are located at radial distances of
 1772 33 mm, 50.5 mm, 88.5 mm, and 122.5 mm. The three outer layers also include
 1773 endcap elements, illustrated in Figure 21, which are located at $z = 495$ mm,
 1774 $z = 580$ mm, and $z = 650$ mm away from the interaction point.

1775 The pixel sensor technology uses a p-n junction of n-type bulk that contains
 1776 both p^+ and n^+ impurities. This combination is crucial in maintaining perfor-
 1777 mance after a significant radiation dose, as the n^+ implants allow the sensor to
 1778 continue function after the n-type bulk has been converted to a p-type bulk by
 1779 the accumulation of radiation. In either configuration, when a charged particle
 1780 passes through the bulk, it ionizes thousands of electron-hole pairs. The elec-
 1781 trons and holes are pulled in opposite directions by the electric field established
 1782 between the anode and cathode of the junction, which then produces a current
 1783 that can be measured and recorded by readout electronics.

1784 The size of the pixels in the original three layers are $50 \mu\text{m} \times 400 \mu\text{m}$ in the
 1785 $r - \phi$ and z directions, respectively. Those pixels are bump-bonded to front-end
 1786 readout chips, the FE-I3, which contains a total of 2880 pixels per chip. In the
 1787 three original pixel layers, the chips are grouped into modules composed of 16
 1788 chips each with 46,080 pixels per module and a total size of $20 \text{ mm} \times 60 \text{ mm}$
 1789 $\times 250 \mu\text{m}$. The modules are further arranged into long rectangular structures
 1790 that run parallel to the beamline called staves. By tiling several staves with an
 1791 offset of 20° , the stave geometry provides full azimuthal coverage in the barrel

Parameter	Inner Detector	Pixel	SCT	TRT
Inner Radius	3.3 cm	3.3 cm	30 cm	56 cm
$ \eta $ Coverage	-	2.5	2.5	2.0
Cell Width	-	50 μm	80 μm	4 mm
Cell Length	-	400 μm	12 cm	70 cm
Material at $ \eta = 0.0$	$0.3 X/X_0$			
Material at $ \eta = 1.7$	$1.2 X/X_0$			
Material at $ \eta = 2.5$	$0.5 X/X_0$			
Number of Hits	48	4	8	36
Channels	99 M	92 M	6.3 M	350 k

Table 5: A summary of the parameters of the inner detector and each of the subdetectors [17].

1792 region while accommodating the readout and cable systems. The endcap regions
 1793 are instead arranged into petals and then into wheels. This arrangement can be
 1794 seen in Figure 25 which shows a computer-generated, cut-away image of the
 1795 outer three layers of the pixel detector. Together these three layers contain 1744
 1796 modules between the barrel and two endcap sections.

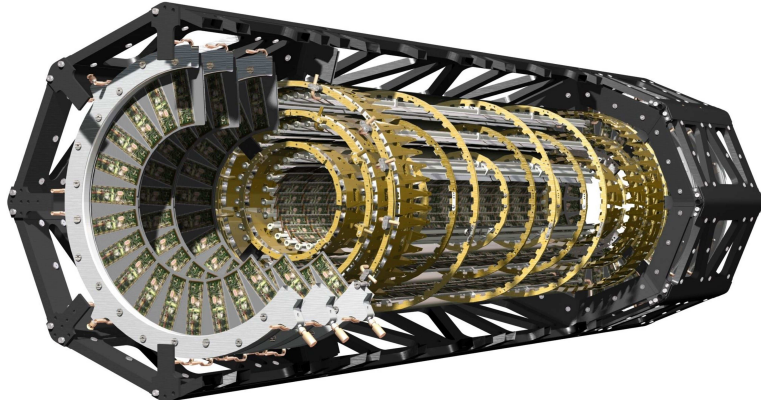


Figure 25: A cut away image of the outer three layers of the pixel detector [17].

1797 The innermost layer, the **IBL**, was added during the long shutdown before Run
 1798 2, and provides the fourth track measurement. It was inserted directly into the
 1799 existing pixel detector by removing the existing beam pipe and replacing it with
 1800 a significantly smaller version. This insertion can be seen in action in Figure 26,
 1801 which emphasizes the extreme precision required to place the the 70 cm long
 1802 layer with only 2 mm of clearance. The **IBL** was commissioned to provide con-
 1803 tinued tracking robustness and high precision in the higher luminosity environ-
 1804 ment of Run 2 [24]. The proximity of this layer to the collisions necessitated an
 1805 even higher granularity and better radiation hardness than the other pixel lay-
 1806 ers. And the strict space requirements to add an active sensing layer so close to
 1807 the interaction point required a sensor chip with a much higher active area and
 1808 a larger overall area per chip. These requirements led to the development of a

new chip type, the FE-I4 (compared to the FE-I3 chips used in the original pixel detector) with improved radiation hardness and a larger active area. The **IBL** is comprised of 448 of these individual chips arranged in 14 staves, with 26,880 pixels per chip and a chip size of 18.5 mm x 41.3 mm x 200 μm . The staves, like in the other layers of the pixel detector, are offset by 14° to provide full azimuthal coverage. This arrangement can be seen in Figure 27, which shows two computer-generated images of the **IBL** geometry and includes the some of the remaining pixel layers.

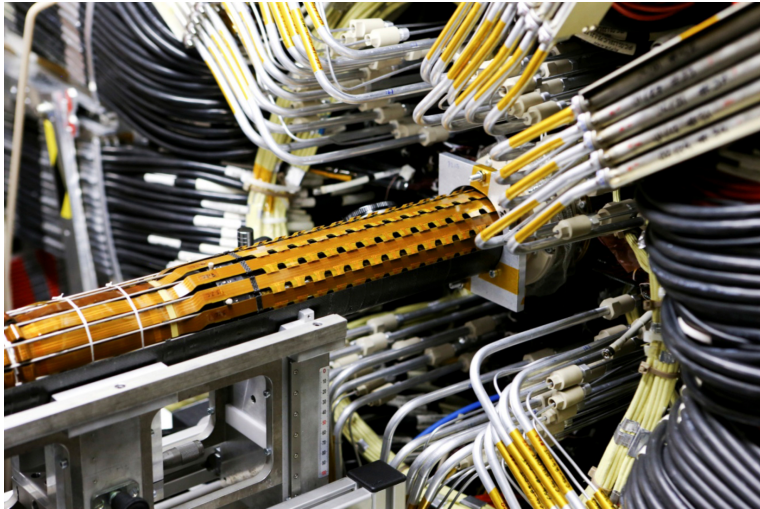


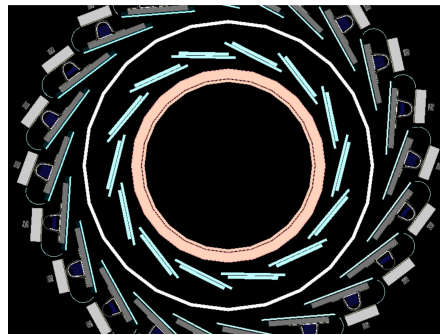
Figure 26: An image of the insertion of the **IBL** into the current pixel detector [25].

5.3.2 SEMICONDUCTOR TRACKER

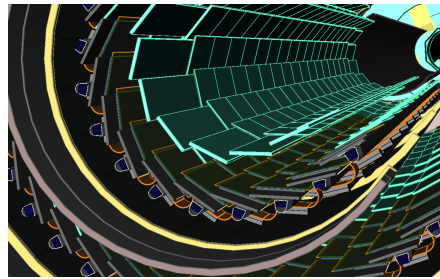
The **SCT**, the subdetector which immediately surrounds the Pixel detector, provides additional discrete measurements of the trajectory of a charged particle. Because the **SCT** is further away from the interaction point, the spatial resolution does not need to be as high as in the pixel detector, and so the **SCT** uses micro-strips instead of pixels. Although pixels provide a more accurate measurement, the number of pixels and readout channels required to cover the cylindrical area at the radius of the **SCT** layers would be prohibitively complicated and expensive.

Each individual silicon strip sensor contains 768 individual readout strips with a total area of 6.36 cm x 6.40 cm and a pitch of 80 μm . Pairs of these sensors are then bonded together to form a combined strip with a length of 12.8 cm. Two of these combined strips are then placed back to back with a relative tilt of 40 mrad. This geometry is illustrated in an expanded view in Figure 28. The purpose of angular offset of the consecutive layers is to allow the strip sensor areas to more accurately measure the position of a particle in the z direction by comparing the overlap of the two strips which were traversed by a track.

Four of these double layers are placed in the barrel region, with radii of 299 mm, 371 mm, 443 mm, and 514 mm. Together these layers provide eight additional measurements for each track that traverses the central $|\eta|$ region. In the endcap region, the layers are arranged in wheels, with the double layers simi-



(a)



(b)

Figure 27: A three-dimensional computer-generated image of the geometry of the **IBL** with a view (a) mostly transverse to the beam pipe (b) mostly parallel to the beam pipe [24].

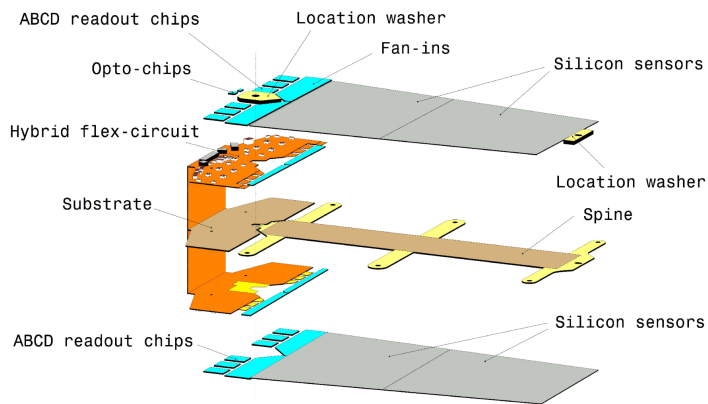


Figure 28: An expanded view of the geometry of the **SCT** double layers in the barrel region [17].

larly offset to provide improved resolution. With these configurations, the [SCT](#) achieves a spatial resolution of $17\ \mu\text{m}$ in the $r - \phi$ direction and $580\ \mu\text{m}$ in the z direction.

5.3.3 TRANSITION RADIATION TRACKER

The final component of the inner detector, the [TRT](#), provides continuous tracking using straw drift tubes. The tubes are made of Kapton and aluminum with a diameter of 4 mm and are filled with a gas mixture of 70% Xe, 27% CO₂, and 3% O₂. At the center of each tube is a gold-plated anode tungsten wire which is $30\ \mu\text{m}$ in diameter. When a charged particle passes through these tubes, it ionizes the gas within. The ions produced drift in the electric field established between the wire and the tube wall, and the large electric field near the wire produces avalanche multiplication and results in an electric current on the wire that is read out by the electronics and provides a track measurement. The time it takes the ionization to drift to the wire can be used to estimate the distance from the wire that the particle passed through the tube; this gives a resolution on the distance of approximately $130\ \mu\text{m}$. Combining several such measurements between consecutive hits in the [TRT](#) tubes allows the trajectory of the particle to be reconstructed with much better resolution than is available in each individual tube.

In addition to the continuous tracking, the detector can use transition radiation produced when a particle passes between the layers to distinguish between electrons and heavier charged particles. The space between the tubes is filled with CO₂, and so has a different dielectric constant than the gas within the tubes which contains Xe. At the transition between those media, a relativistic particle emits radiation proportional to γ , so inversely proportional to mass at a fixed momentum. The photons produced in this transition then produce an ionization cascade which is significantly larger than the signal for the minimally-ionizing charged particles. To distinguish between these two cases, the [TRT](#) defines two signal thresholds, a low threshold for the typical signal produced by a minimally ionizing particle ([MIP](#)) and a high threshold for the the signal produced by transition radiation. A high momentum electron is expected to produce approximately 7 to 10 high threshold hits as it traverses the [TRT](#), and thus these hits provide a way to distinguish electrons from other charged particles.

The [TRT](#) contains 351,000 tubes in total, divided between the barrel and endcap regions. In the barrel region, the tubes are 144 cm long and arranged in 73 layers parallel to the beampipe. In the endcap region, the tubes are 37 cm long and arranged in 160 layers transverse to the beampipe. These configurations can be seen in Figure 22 and Figure 23. With this geometry the [TRT](#) achieves a resolution of $130\ \mu\text{m}$ in the $r - \phi$ direction.

5.4 CALORIMETRY

The combination of calorimeter systems used in ATLAS can measure the energy of electrons, photons, hadrons, and hadronic jets with complete coverage up to

1879 $|\eta| < 4.9$ and across ϕ . Unlike the inner detector, the calorimeters are capable
 1880 of measuring neutral particles. To accomplish precision measurements of these
 1881 particle types, the ATLAS calorimeter system uses four individual calorimeters, a
 1882 liquid argon ([LAr](#)) electromagnetic calorimeter in the barrel region, a tile hadronic
 1883 calorimeter in the barrel region, a [LAr](#) hadronic endcap calorimeter, and a [LAr](#)
 1884 forward calorimeter. Together these provide hermetic coverage for the ATLAS
 1885 detector. The configuration of these calorimeters is illustrated in Figure 29.

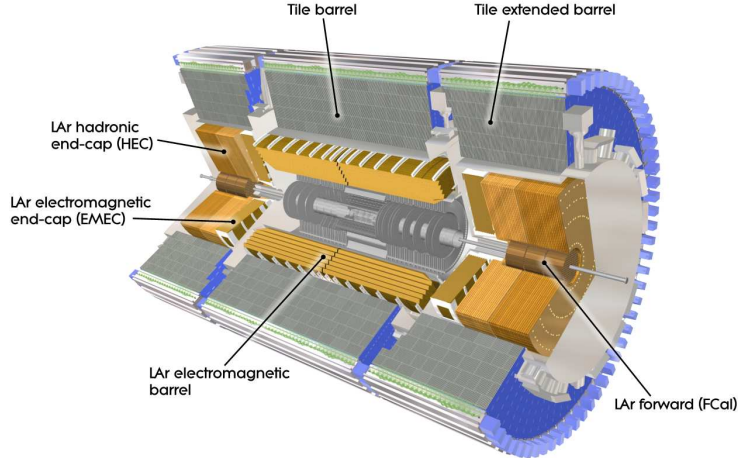


Figure 29: An overview of the ATLAS calorimeter systems [17].

1886 The calorimeters are designed to absorb and measure the energy carried by
 1887 a particle, and completely stop the particle's propagation in the process. This
 1888 requires a significant amount of material to provide interactions. These inter-
 1889 actions then produce secondary particles, which can produce tertiary particles
 1890 in turn, and thus form a cascade of particles called an electromagnetic ([EM](#)) or
 1891 hadronic shower, depending on the governing mechanism. Electromagnetic and
 1892 hadronic showers have very different properties and require different technolo-
 1893 gies to measure them accurately. All of the calorimeters in the ATLAS calorime-
 1894 ter system are sampling calorimeters: they use alternating layers of absorbing
 1895 and active material. The dense absorbing layers initiate the showers while the
 1896 active layers measure the energy of the produced particles. A fraction of the en-
 1897 ergy is lost in the inactive layers, so the energy measurement from the active
 1898 layers has to be corrected to estimate the actual energy of the particle.

1899 The [EM](#) calorimeter provides around 20 radiation lengths (X_0) while the hadronic
 1900 calorimeter provides around 10 interaction lengths (λ). As mentioned previ-
 1901 ously, radiation lengths measure the distance over which an electromagnetically
 1902 interacting particle loses a characteristic fraction of its energy. Interaction lengths,
 1903 on the other hand, measure the mean distance traveled by a hadronic particle be-
 1904 fore undergoing a nuclear interaction [3]. Figure 30 show the radiation lengths
 1905 in the layers of the [EM](#) calorimeter in the barrel region as well as the interaction
 1906 lengths for all calorimeters.

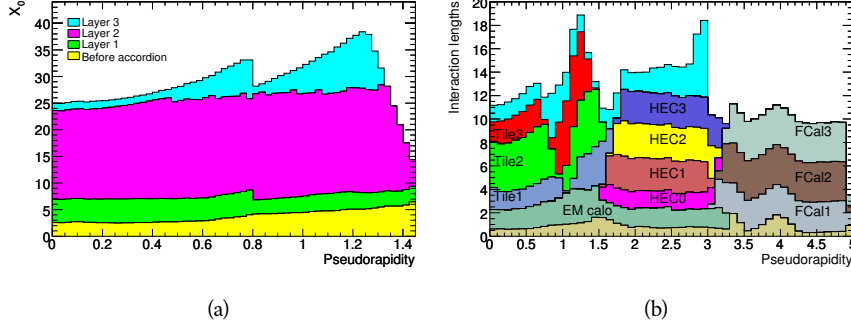


Figure 30: The depth of (a) the electromagnetic barrel calorimeter in radiation lengths and of (b) all calorimeters in interaction lengths as a function of pseudorapidity [17].

1907 5.41 ELECTROMAGNETIC CALORIMETER

1908 The electromagnetic calorimeters use alternating layers of liquid argon and lead
1909 in an accordion shape. The accordion shape provides complete coverage in the
1910 ϕ direction while also providing many alternating layers for the a particle to
1911 pass through. The configuration is detailed in Figure 31. When an electron or
1912 a photon passes through the lead, it produces an electromagnetic shower. The
1913 particles produced in those showers then pass into and ionize the liquid argon;
1914 the ions produced can then be collected by an electrode in the liquid argon layer
1915 to provide the actual energy measurement.

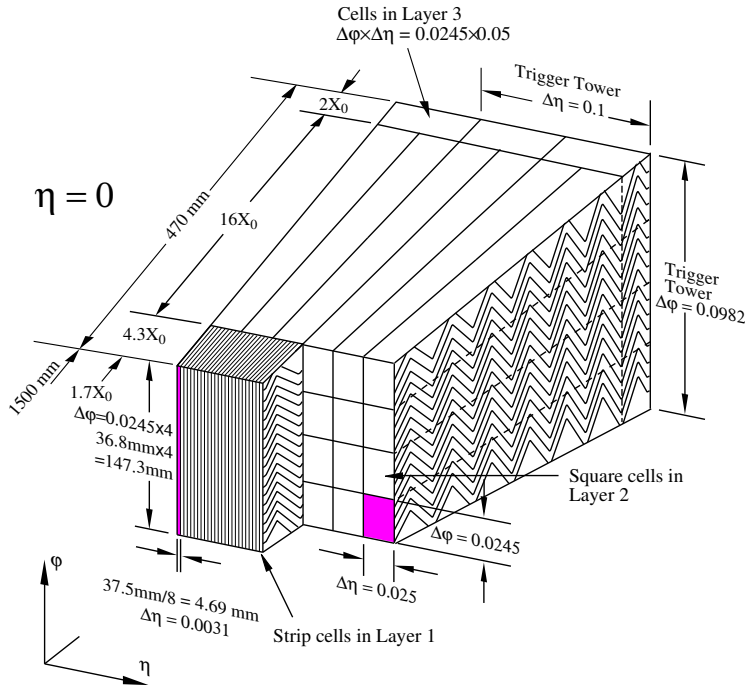


Figure 31: A schematic of the LAr calorimeter in the barrel region, highlighting the accordion structure [17].

1916 The barrel region is covered by a presampler and three separate sampling lay-
 1917 ers with decreasing segmentation. The presampler is a thin layer of liquid argon
 1918 which measures the energy of any electromagnetic showers which are initiated
 1919 before the particle reaches the calorimeter due to interactions with the detec-
 1920 tor material. The first layer is the strip layer, which has fine segmentation in η
 1921 to enhance the identification of shower shapes and to provide a precise η mea-
 1922 surement for reconstructing photons and electrons. The strip layer has only 4
 1923 radiation lengths worth of material, and has a segmentation of $\Delta\eta = 0.003$ and
 1924 $\Delta\phi = 0.1$. The second layer is also finely segmented, with a segmentation of
 1925 $\Delta\eta = 0.025$ and $\Delta\phi = 0.025$, and a thickness of $16 X_0$. This layer is designed
 1926 to contain an electromagnetic shower and to measure the majority of the energy
 1927 for photons and electrons. The third layer is only $2 X_0$ thick and measures the
 1928 energy of electromagnetic showers which leak out of the second layer, and helps
 1929 to separate electromagnetic showers from hadronic showers. The structure of
 1930 the LAr endcap calorimeter is similar except that the layers are arranged parallel
 1931 to the beampipe to measure energy deposits from high η particles.
 1932

5.4.2 HADRONIC CALORIMETERS

1933 The hadronic calorimeters use a few different technologies to satisfy the resolu-
 1934 tion demands in the different areas of the detector, and together they cover the
 1935 region $|\eta| < 2.7$. In the barrel region, for $|\eta| < 1.7$, the hadronic calorimeters
 1936 are constructed of alternating tiles of steel and plastic scintillator. Like in the
 1937 electromagnetic calorimeter, the dense layer initiates a shower (in this case the
 1938 dense layer is the steel and the shower is hadronic) of particles which pass into
 1939 and ionize the following layer. The ionization in the plastic scintillator instead
 1940 produces a light signal proportional to the amount of ionization produced by the
 1941 shower, and this signal is measured using photomultipliers and provides the ac-
 1942 tual energy measurement. The construction of a tile in the calorimeter is shown
 1943 Figure 32, which highlights the alternating layers of steel and scintillator.
 1944

1945 This tile calorimeter, as well as the remaining hadronic calorimeters, have a
 1946 much coarser granularity than the electromagnetic calorimeters. The high gran-
 1947 ularity is not needed for an accurate energy measurement, and the hadronic
 1948 calorimeters are not designed to distinguish particle types like the electromag-
 1949 netic calorimeters. The tile granularity is approximately $\Delta\eta = 0.1$ and $\Delta\phi = 0.1$,
 1950 and the segmentation in depth and η is shown in Figure 33.

1951 The remaining hadronic calorimeters all use the same alternating, sampling
 1952 structure but with different active and inactive materials. The hadronic endcap
 1953 calorimeter covers the range of $1.5 < |\eta| < 3.2$ and uses an inactive layer of
 1954 copper and an active layer of liquid argon. The forward calorimeter covers the
 1955 range of $3.1 < |\eta| < 4.9$ and uses a dense matrix of copper and tungsten filled
 1956 with liquid argon. Particles propagating through the sampling layers ionize the
 1957 liquid argon, and the ionization is collected at an electrode to provide a signal.

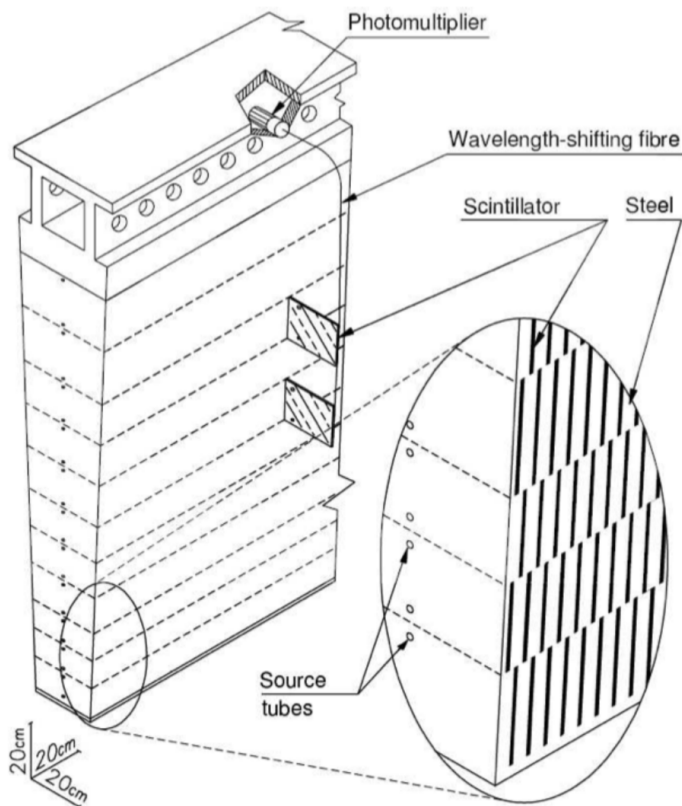


Figure 32: A schematic of a hadronic tile module which shows the alternating layers of steel and plastic scintillator [17].

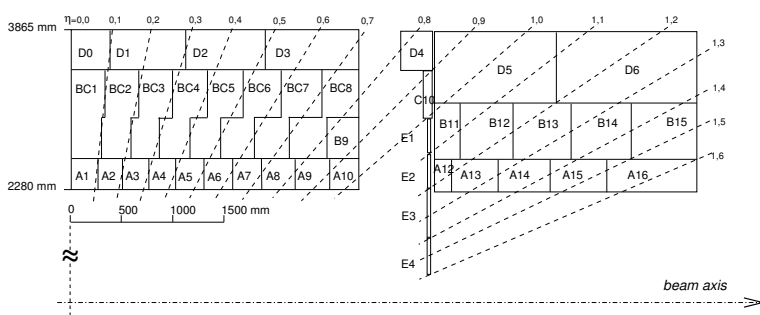


Figure 33: The segmentation in depth and η of the tile-calorimeter modules in the central (left) and extended (right) barrels [17].

1957 5.5 MUON SPECTROMETER

1958 Among SM particles, only muons and neutrinos consistently pass through the
 1959 calorimeters. Because the neutrinos are also electrically neutral, there is no fea-
 1960 sible option to measure them directly in ATLAS. The muons, on the other hand,
 1961 are charged and are thus already measured as a track in the inner detector. The
 1962 muon spectrometer provides a way to consistently identify muon tracks and also
 1963 a way to provide an additional measurement of their momentum.

1964 The muon spectrometer contains four subdetectors that cover the barrel and
 1965 endcap regions. In the barrel region, the muon spectrometer uses a combina-
 1966 tion of Resistive Plate Chambers (RPCs) and Monitored Drift Tubes (MDTs) to
 1967 provide both a coarse, fast measurement for triggering and a precise momentum
 1968 measurement for offline event reconstruction. Similarly, in the endcap region,
 1969 the Thin Gap Chambers (TGCs), MDTs, and Cathode Strip Chambers (CSCs) allow
 1970 for both triggering and precise measurements. The CSCs are used only in the in-
 1971 nermost layer of the endcap region between $2.0 < |\eta| < 2.7$ where the particle
 1972 flux is too large for the MDTs to provide accurate measurements. The overall
 1973 layout of the muon systems are shown in the cut-away diagram in Figure 34,
 1974 and Figure 35 shows a precise schematic of the layout of each of the detecting
 1975 elements. The geometric arrangement shown provides consistent coverage for
 1976 muons produced up to $|\eta| < 2.7$, and takes full advantage of the bending of the
 1977 muons in the toroidal magnetic field, described in Section 5.2, to measure their
 1978 momentum. Figure 36 shows a cross-section of the arrangement of the muon
 1979 spectrometer in the barrel; the layers are divided into eight small and eight large
 1980 chambers that are overlapped to provide complete coverage in ϕ .

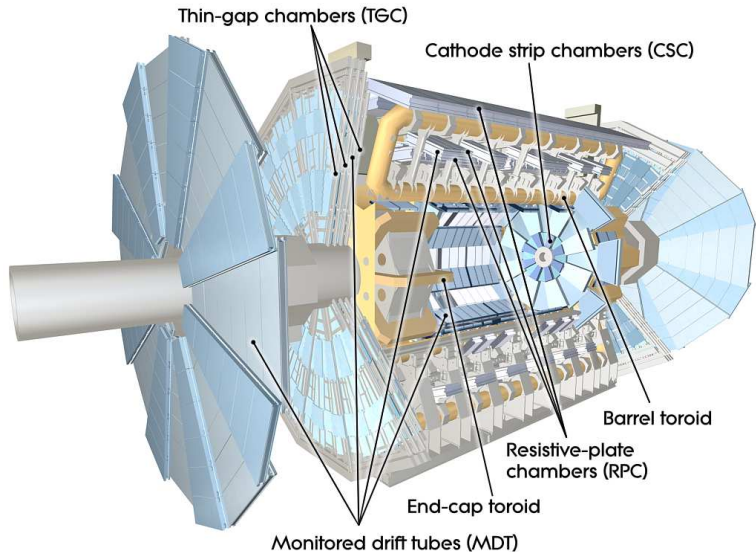


Figure 34: A cut-away diagram of the muon systems on ATLAS [17].

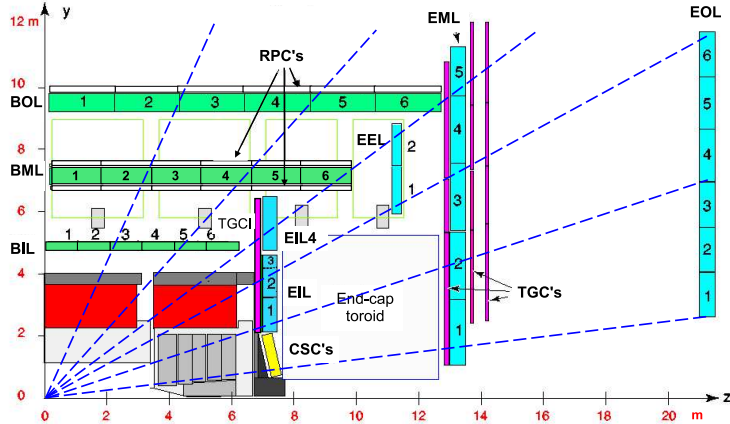


Figure 35: A quarter view of the muon spectrometer which highlights the layout of each of the detecting elements. The BOL, BML, BIL, EOL, EML, and EIL are all MDT elements, where the acronyms encode their positions [17].

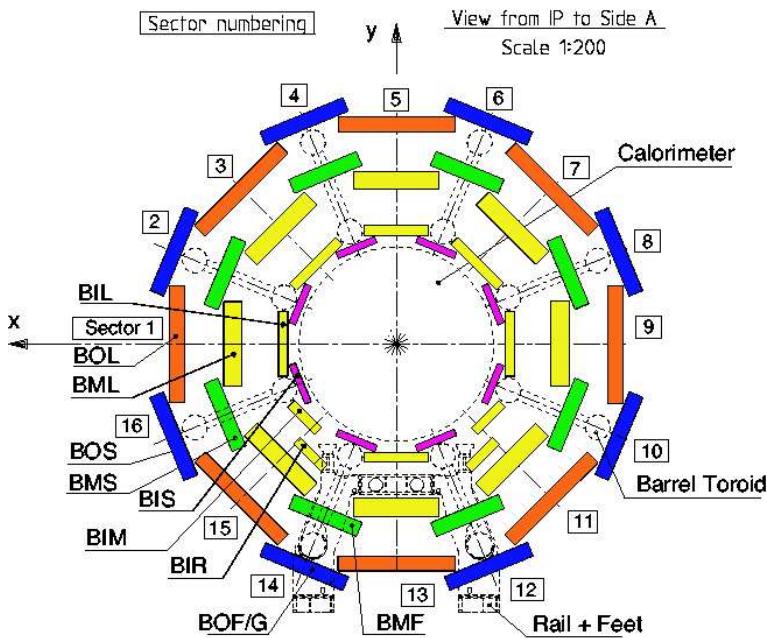


Figure 36: A schematic of the cross-section of the muon spectrometer in the barrel region [17].

1981 5.51 MONITORED DRIFT TUBE

1982 The momentum measurements in the barrel region are provided by three consecutive layers of MDT elements, located at approximately 5 m, 7 m, and 9 m from
 1983 the interaction point. Each of these layers is a composite of two multilayers of
 1984 drift tubes: two layers of three to four layers of tubes, as shown in Figure 37.
 1985 These aluminum tubes are 3 cm in diameter, with lengths between 0.9 and 6.2 m,
 1986 and are filled with a mixture of ArCO₂ kept at 3 bar absolute pressure. A central
 1987 tungsten-rhenium wire with a diameter of 50 μm runs along the length of the
 1988 tube, and is kept at a potential of 3080 V.

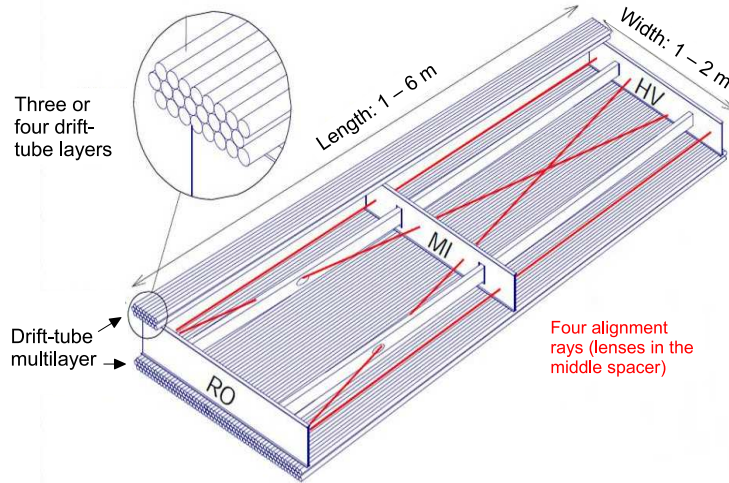


Figure 37: A schematic of a single MDT chamber, which shows the multilayers of drift tubes as well as the alignment system [17].

1990 A muon traversing these tubes ionizes the gas, and the ionization electrons
 1991 then drift in the electric field toward the central wire. Close to the wire, the
 1992 electric field is strong enough to cause the original ionization electrons to ionize
 1993 additional electrons, producing an avalanche that can be measured as a current
 1994 along the wire. The time of arrival of that current depends on how far the muon
 1995 entered from the wire, and can be used to achieve a position resolution of 80 μm
 1996 in an individual tube. The combination of the measurements in the consecutive
 1997 layers of tubes improves this position resolution to 35 μm transverse to the tubes,
 1998 with a resolution of 1 m along the tube direction.

1999 To achieve a good resolution over the entire length of a muon track, the rel-
 2000 ative positions of the tubes of the muon spectrometer must be known to an ac-
 2001 curacy of 30 μm . This is achieved by an optical laser alignment system placed in
 2002 each of the individual chambers and throughout the cavern. These monitor any
 2003 changes in position or alignment due to effects like gravitational sag, tempera-
 2004 ture shifts, and the magnetic field. The configuration of the alignment system
 2005 within an individual chamber is also shown in Figure 36.

2006 5.5.2 RESISTIVE PLATE CHAMBER

2007 The **RPC** is the provides a fast measurement of the ϕ position of muons for trig-
 2008 gering in the barrel region. The system has a lower spatial resolution than the
 2009 **MDTs** but has a faster measurement with a time resolution of just a few tens of
 2010 nanoseconds. There are three **RPCs** layers in the muon spectrometer, two located
 2011 on either side of the central **MDT** layer and one located outside the final **MDT**
 2012 layer, as shown in Figure 35. The **RPCs** consist of two layers of parallel plates
 2013 filled with a gas mixture of $C_2H_2F_4$. A muon passing through these systems ion-
 2014 izes the gas, like in the **MDT**, which causes an avalanche of ionization electrons
 2015 in the electric field maintained between the plates. Metal strips on the outside
 2016 of the chamber capacitively couple to the accumulated charge, and are read out
 2017 to measure the η and ϕ positions of the muon track.

2018 5.5.3 CATHODE STRIP CHAMBER

2019 The majority of the momentum measurements in the endcap region are provided
 2020 by the **MDTs**. In the most forward region of the muon spectrometer, between
 2021 $2.0 < \eta < 2.7$, the particle flux is very high due to contributions from low energy
 2022 photons and neutrons. The **MDT** can only sustain a hit rate of approximately 150
 2023 Hz/cm² because of limitations in the drift times of the gas and the capacity of
 2024 the readout electronics. The **CSCs** were designed to handle higher hit rates, up to
 2025 1000 Hz/cm², and provide the necessary coverage in that high flux region.

2026 The **CSC** consists of several multiwire proportional chambers, where the wires
 2027 are oriented in the radial direction out from the beampipe. There are eight large
 2028 and eight small chambers, arranged to partially overlap in the ϕ direction, as
 2029 shown in Figure 38. Like in the **MDT**, a muon traversing the system produces
 2030 ionization in the gas; here, however, the ionization is collected on a number of
 2031 wires. These wires couple to cathodes on the chambers which are segmented
 2032 into strips in two directions. The relative amount of charge on each of the neigh-
 2033 boring strips can be used to interpolate to the position of the muon in both η
 2034 and ϕ .

2035 5.5.4 THIN GAP CHAMBER

2036 Like in the barrel region, a separate, fast detector is required to provide position
 2037 measurements of muons for trigger in the endcap region. This is provided by
 2038 the **TGC** which consists of seven layers in the middle station of the endcap, two
 2039 doublet layers and one triplet layer, and a single doublet layer in the inner endcap
 2040 station. Figure 39 shows the arrangement of the triple and doublet layers of the
 2041 **TGCs**.

2042 Like the **CSCs**, the **TGCs** are multiwire proportional chambers with a wire-to-
 2043 cathode distance of 1.4 mm and a wire-to-wire distance of 1.8 mm. Readout
 2044 strips on the outside of the chambers run perpendicular to the wires, and couple
 2045 to the charge collected on the wires to provide a position measurement in the η
 2046 direction. The current induced on the wires is also readout to provide a position

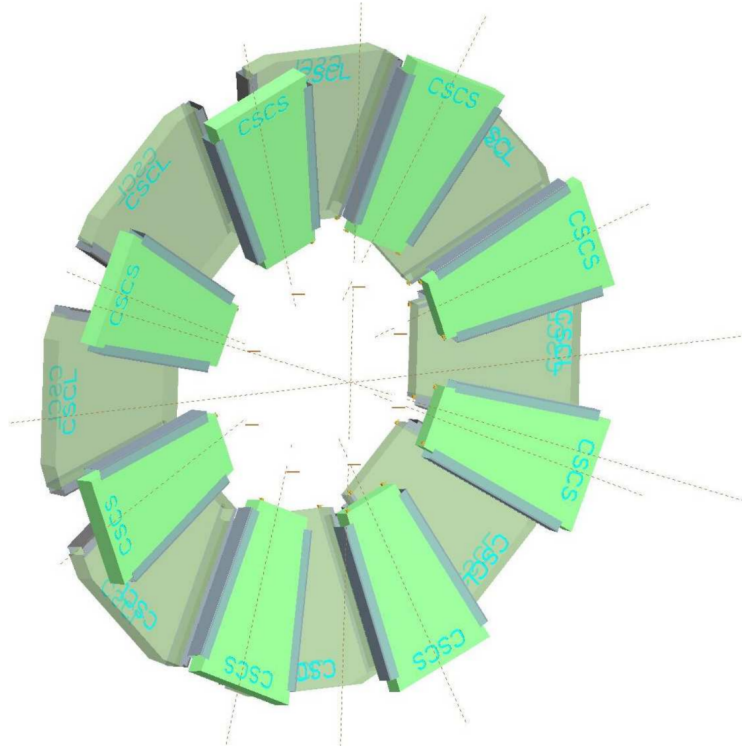


Figure 38: A schematic of the [CSC](#) endcap, showing the overlapping arrangement of the eight large and eight small chambers [17].

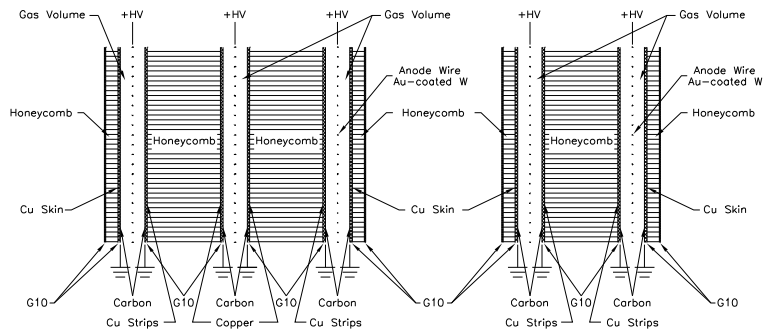


Figure 39: A schematic of the [TGC](#) doublet and triplet layers [17].

2047 measurement in the ϕ direction. The high electric field and small wire-to-wire
 2048 distance give it the required good time resolution to be used for triggering events.

2049 5.6 TRIGGER

2050 It is not possible for the detector and the associated computing systems to record
 2051 the 80 TB of data that the 40 MHz event rate produces every second. Instead, a
 2052 small fraction of these events are selected by the trigger system to be recorded
 2053 and later analyzed. Selecting interesting events at such a high rate poses a sig-
 2054 nificant challenge for both the detector design and the implementation of a
 2055 trigger decision and data acquisition system. The trigger must balance the time
 2056 needed to decide to keep an event, to avoid losing information, with the filtering
 2057 accuracy to consistently select a full menu of physics events that can be used for
 2058 the wide array of searches and measurements targeted by ATLAS.

2059 The ATLAS trigger system, as of Run 2, consists of two levels of decision mak-
 2060 ing. The first level, referred to as Level 1 ([L1](#)), is hardware based and uses inputs
 2061 from a subset of the detector elements to reduce the considered event rate from
 2062 the original 40 MHz down to 100 kHz. The 100 kHz rate is the maximal rate that
 2063 the event information can be transferred from the detector. The [L1](#) trigger deci-
 2064 sions must be made with $2.5 \mu\text{s}$, or else the information stored from the event is
 2065 still available to be read out to the next step. The second, software-based level, re-
 2066 ferred to as the high level trigger ([HLT](#)), makes the final decisions on which events
 2067 to keep for analysis and selects a rate of around 1 kHz. The collection of selection
 2068 criteria used to make the [L1](#) decisions feed into subsequent selection criteria in
 2069 the [HLT](#), and the set of these combinations of [L1](#) and [HLT](#) criteria from the trigger
 2070 menu which defines exactly what events are recorded on ATLAS. A subset of the
 2071 trigger menu used for 2015 data collection is shown in Table 6, which summa-
 2072 rizes the selection requirements at both levels and additionally shows the peak
 2073 measured rates contributed by each.

2074 At [L1](#), the trigger system uses information primarily from the calorimeters and
 2075 muon spectrometer to select high p_{T} jets, electrons, photons, and muons. The
 2076 electromagnetic calorimeter uses reduced granularity energy measurements as
 2077 well as isolation requirements to select electrons and photons. The hadronic
 2078 calorimeter also uses a combination of reduced granularity energy measurements
 2079 and isolation to select high momentum jets and hadronically decaying tau lep-
 2080 tons. The calorimeters are also used to provide triggers based on missing energy:
 2081 the coarse granularity energy measurements are used to calculate a directional
 2082 sum of energies and to trigger on a significant imbalance. The analysis discussed
 2083 here uses the E_T^{miss} trigger shown in Table 6, with a [L1](#) rate of 0.7 kHz and an [HLT](#)
 2084 rate of 55 Hz.

2085 Only the [RPCs](#) and [TGCs](#) muon subdetectors contribute to the decision at [L1](#),
 2086 and are used to identify high momentum muons. The contributions to the trig-
 2087 gering rate of the various types of [L1](#) triggers are shown in Figure 40. The total
 2088 rate is indicated in black and is lower than the sum of individual rates because
 2089 their is significant overlap between different trigger channels. The majority of
 2090 the rate comes from lepton and photon triggers.

Trigger	Typical offline selection	Trigger Selection		Level-1 Peak Rate (kHz)	HLT Peak Rate (Hz)
		Level-1 (GeV)	HLT (GeV)		
Single leptons	Single iso μ , $p_T > 21$ GeV	15	20	7	130
	Single e , $p_T > 25$ GeV	20	24	18	139
	Single μ , $p_T > 42$ GeV	20	40	5	33
	Single τ , $p_T > 90$ GeV	60	80	2	41
Two leptons	Two μ 's, each $p_T > 11$ GeV	2×10	2×10	0.8	19
	Two μ 's, $p_T > 19, 10$ GeV	15	18, 8	7	18
	Two loose e 's, each $p_T > 15$ GeV	2×10	2×12	10	5
	One e & one μ , $p_T > 10, 26$ GeV	20 (μ)	7, 24	5	1
	One loose e & one μ , $p_T > 19, 15$ GeV	15, 10	17, 14	0.4	2
	Two τ 's, $p_T > 40, 30$ GeV	20, 12	35, 25	2	22
	One τ , one μ , $p_T > 30, 15$ GeV	12, 10 (+jets)	25, 14	0.5	10
Three leptons	One τ , one e , $p_T > 30, 19$ GeV	12, 15 (+jets)	25, 17	1	3.9
	Three loose e 's, $p_T > 19, 11, 11$ GeV	15, 2×7	$17, 2 \times 9$	3	< 0.1
	Three μ 's, each $p_T > 8$ GeV	3×6	3×6	< 0.1	4
	Three μ 's, $p_T > 19, 2 \times 6$ GeV	15	$18, 2 \times 4$	7	2
	Two μ 's & one e , $p_T > 2 \times 11, 14$ GeV	2×10 (μ 's)	$2 \times 10, 12$	0.8	0.2
One photon	Two loose e 's & one μ , $p_T > 2 \times 11, 11$ GeV	$2 \times 8, 10$	$2 \times 12, 10$	0.3	< 0.1
	one γ , $p_T > 125$ GeV	22	120	8	20
Two photons	Two loose γ 's, $p_T > 40, 30$ GeV	2×15	35, 25	1.5	12
	Two tight γ 's, $p_T > 25, 25$ GeV	2×15	2×20	1.5	7
Single jet	Jet ($R = 0.4$), $p_T > 400$ GeV	100	360	0.9	18
	Jet ($R = 1.0$), $p_T > 400$ GeV	100	360	0.9	23
E_T^{miss}	$E_T^{\text{miss}} > 180$ GeV	50	70	0.7	55
Multi-jets	Four jets, each $p_T > 95$ GeV	3×40	4×85	0.3	20
	Five jets, each $p_T > 70$ GeV	4×20	5×60	0.4	15
	Six jets, each $p_T > 55$ GeV	4×15	6×45	1.0	12
b -jets	One loose b , $p_T > 235$ GeV	100	225	0.9	35
	Two medium b 's, $p_T > 160, 60$ GeV	100	150, 50	0.9	9
	One b & three jets, each $p_T > 75$ GeV	3×25	4×65	0.9	11
	Two b & two jets, each $p_T > 45$ GeV	3×25	4×35	0.9	9
b -physics	Two μ 's, $p_T > 6, 4$ GeV plus dedicated b -physics selections	6, 4	6, 4	8	52
Total				70	1400

Table 6: A subset of the trigger menu for the 2015 data collection with $L = 5 \times 10^{33} \text{ cm}^{-2} \text{s}^{-1}$. Both the L1 and HLT selection requirements and their trigger rates are shown measured at the specified luminosity are shown. The typical offline selections represent a typical set of offline requirements imposed after the trigger in an analysis [26].

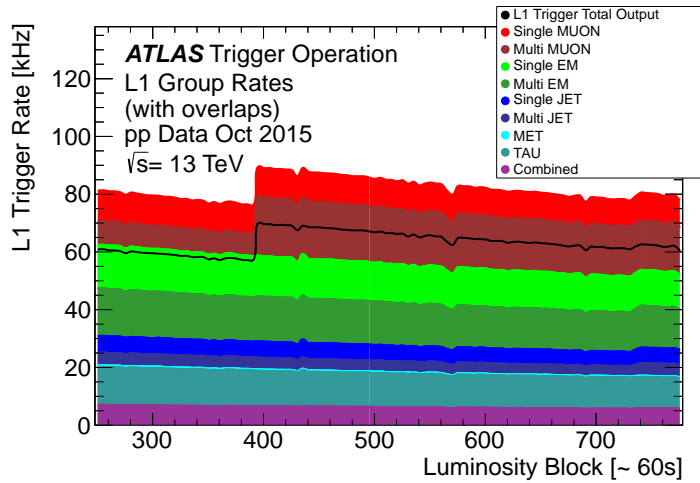


Figure 40: The L1 Trigger rate broken down into the types of triggers as a function of the luminosity block for the 2015 data collection period [26].

After an event is chosen by the L1 trigger, the detector measurements from the bunch crossing which fired the trigger is read out from the front-end electronics and stored on read-out boards. This inclusive information is necessary to make more the more precise event selections than is possible with the reduced information at L1. The HLT then uses this information with software algorithms to decide whether or not to permanently record the event. The L1 trigger also forwards which decision was made and Region of Interests (RoIs) to the HLT, which allows the HLT to focus on particular algorithms and particular sections of the detector to greatly improve the algorithmic selection speed. The additional information available to the HLT allows it to use full offline reconstruction algorithms (Chapter 6) to implement additional trigger targets, such as identified jets from the decays of b-hadrons. The contributions to the triggering rate of the various types of HLT triggers are shown in Figure 41.

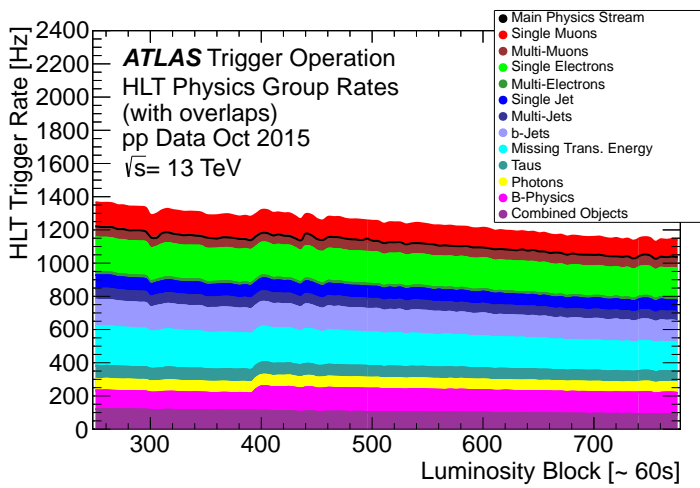


Figure 41: The HLT Trigger rate broken down into the types of triggers as a function of the luminosity block for the 2015 data collection period.

2104

2105 EVENT RECONSTRUCTION

2106 The ATLAS experiment combines measurements in the subdetectors to form a
2107 cohesive picture of each physics event. The majority of particles that traverse
2108 the detector leave behind some combination of ionization hits in the tracking
2109 detectors or energy deposits in the calorimeters, and these measurements can
2110 be used to reconstruct physical quantities like the particle's energy, momentum,
2111 or trajectory. Even the type of the particle can be distinguished by comparing
2112 the various ways that different species of stable particles interact with the sub-
2113 detectors. Reconstruction is the series of algorithms which take the electronic
2114 outputs of the detector and assigns them into individual physics objects. The
2115 physics objects summarize the properties of particles produced by the collision
2116 or subsequent decays, either for individual isolated particles like leptons, or for
2117 a collection of the cascade of products produced in the decay of an energetic
2118 hadron, called a jet. These are the objects and quantities most often used in anal-
2119 ysis to make measurements of SM processes or to search for new physics.

2120 6.1 CHARGED PARTICLES

2121 As described in Section 5.3, charged particles that traverse the inner detector
2122 leave behind hits in the subdetectors. Each of these hits translates into a position
2123 measurement along the trajectory of that particle, with position resolutions de-
2124 pending on the subdetector that provided the measurement. Track reconstruc-
2125 tion uses these position measurements to collect hits in consecutive layers of
2126 the detector into a trajectory consistent with a particle curving in a magnetic
2127 field [27, 28]. This reconstructed trajectory is called a track. The number of hits
2128 in the inner detector for each event makes a combinatorial method completely
2129 infeasible: the algorithms that form tracks must be significantly more intelligent
2130 so that event reconstruction does not exhaust computing resources.

2131 The first and primary algorithm employed in track reconstruction is called
2132 the inside-out method, which begins with the assumption that the track orig-
2133 inated from the interaction point. Its purpose is to identify primary particles,
2134 those which originate in the proton-proton collisions and with a lifetime long
2135 enough to reach the inner detector. Combinations of three hits are considered
2136 from measurements in the Pixel detector and the SCT, and form the seed for a
2137 track. Specifically, the seeding algorithm looks for a seed using three pixel hits,
2138 two pixel hits and one SCT hit, or three SCT hits. The seed is then extrapolated
2139 forwards and backwards into the Pixel and SCT detectors depending on the seed
2140 location, and hits in each layer are considered to be added to the track using a
2141 combinatorial Kalman filter [28]. After all of the silicon layers have been con-
2142 sidered, tracks are filtered to reduce ambiguities from other nearby tracks or
2143 from combinatorial coincidences. Then the tracks are extended outwards into

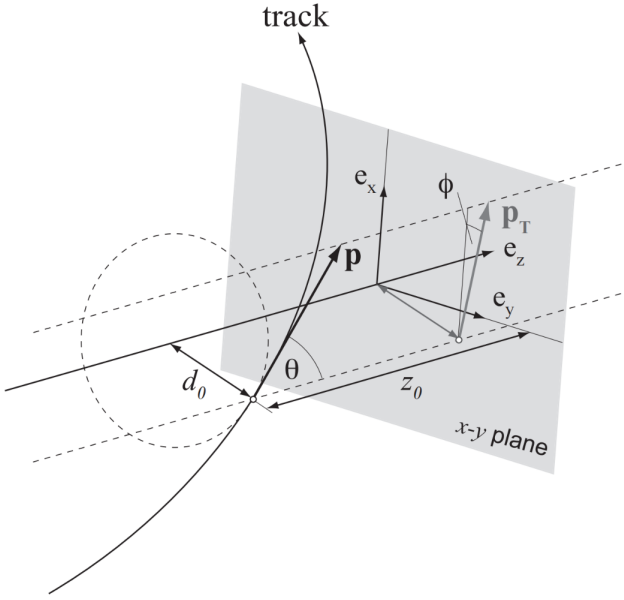


Figure 42: An illustration of the perigee representation of track parameters for an example track. The charge is not directly shown, but is indicated by the direction of curvature of the track [29].

2144 the [TRT](#) in the same way. The result of this clustering algorithm is a collection
 2145 of hits identified to belong to a single track. Once the hits are collected, a fitting
 2146 algorithm calculates the track parameters which best model the locations of the
 2147 hits and their resolutions. The fitting uses five parameters, $(d_0, z_0, \phi, \theta, q/p)$, to
 2148 specify a track in a perigee representation: d_0 and z_0 are the transverse and lon-
 2149 gitudinal impact parameters at the closest approach to the nominal beam axis,
 2150 ϕ and θ are the usual angular coordinates, and q/p is the charge divided by the
 2151 curvature. These parameters are illustrated in Figure 42. Those parameters di-
 2152 rectly determine the direction and momentum of the particle which produced
 2153 the track.

2154 This inside-out algorithm is complemented by an outside-in algorithm, which
 2155 is used to find tracks from secondary particles, those produced in the decays or
 2156 interactions of the primary particles inside the detector. As the name indicates,
 2157 the outside-in algorithm begins by seeding tracks in the outermost layers of the
 2158 inner detector, in the [TRT](#). The seed in this case is formed by a segment in the
 2159 [TRT](#), and the track is propagated backwards into the [SCT](#) before being refitted
 2160 to use all the included points. Some tracks are found with [TRT](#) segments only,
 2161 which can result from interactions with the detector following the [SCT](#). Figure 43
 2162 shows an example of the geometry of tracks formed by both algorithms, where
 2163 the hits belonging to tracks found using the inside-out algorithm are highlighted
 2164 in red, and the hits belonging to the tracks found using the outside-in algorithm
 2165 are circled in black. The figure highlights the presence of a large number of
 2166 both primary and secondary tracks in a single event, as well as the overall large
 2167 number of hits present in the inner detector.

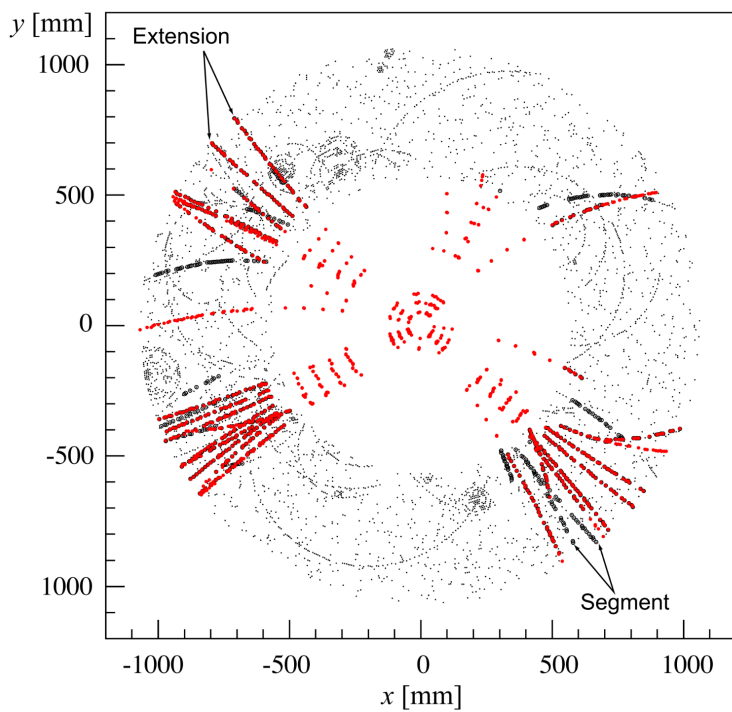


Figure 43: The x and y locations of the hits generated in a simulated $t\bar{t}$ event in the inner detector. The hits which belong to tracks formed using the inside-out algorithm are highlighted in red, while the hits which belong to tracks formed using the outside-in algorithm are circled in black. This figure does not include hits in the IBL.

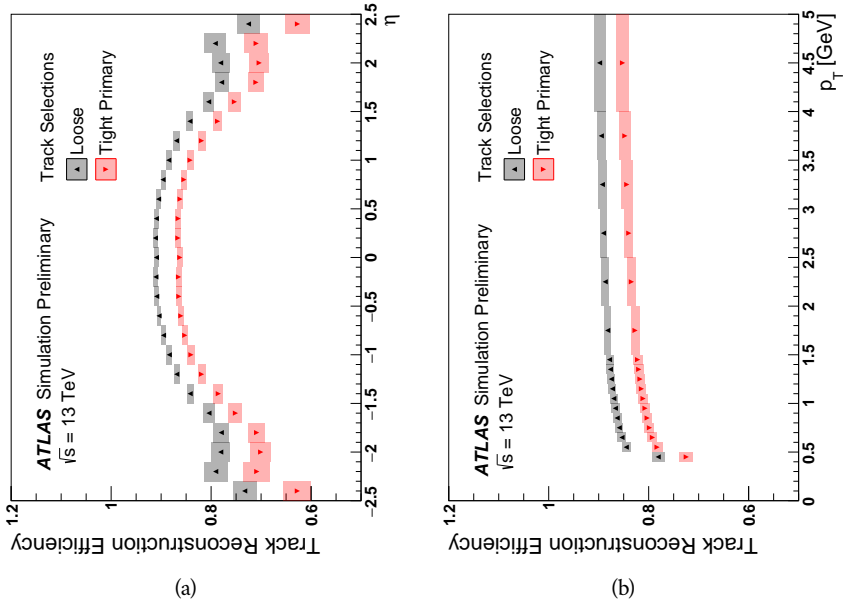


Figure 44: The tracking reconstruction efficiency as a function of (a) η and (b) p_T [30].

The tracks resulting from these algorithms can be contaminated by nearby particles confusing the tracking algorithm in a high luminosity environment. For example, enough hits present in the inner detector can lead to fake tracks from combinations of hits from multiple individual tracks. Therefore, after the tracks are formed and fitted, additional quality requirements are imposed in order to reduce such backgrounds. Most tracking applications require at least seven silicon hits, that is, seven hits between the Pixel detector and **SCT**. Then the tracks are required to have at most two holes in the Pixel detector, where holes are non-existing but expected measurements in a layer of the subdetector. If the missing hit corresponds to an inactive module, however, it is not counted as a hole but instead as a hit for tracking as the lack of a measurement is expected in that case. With these requirements, the inner detector achieves the reconstruction efficiencies shown in Figure 44 as a function of p_T and η . The efficiency ranges between 80% and 90% for the tight primary selection described above, and is maximized at high p_T and low $|\eta|$.

6.1.1 PIXEL NEURAL NETWORK

The hits in the Pixel detector are not typically confined to a single pixel, but rather the charge is spread over several pixels per layer which are grouped together into clusters. The clustering of these pixels for isolated tracks is relatively straightforward; a connected component analysis identifies groups of neighboring pixels above the readout threshold [31]. Complications can arise in the high occupancy environment where hits from multiple particles can overlap in a single cluster. Figure 45 shows examples of clusters generated by a single isolated

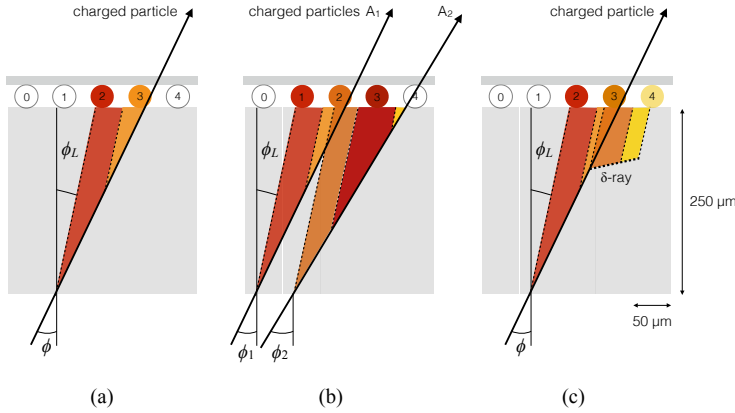


Figure 45: Examples of the clusters formed in a single layer of the pixel detector for (a) a single isolated particle, (b) two nearly-overlapping particles, and (c) a particle which emits a δ -ray [31].

2191 particle, two nearly overlapping particles, and a particle which emits a δ -ray. A
 2192 δ -ray is a secondary electron which is generated with enough energy to escape
 2193 a significant distance away from the original particle and to generate additional
 2194 ionization.

2195 A series of neural-networks analyzes the shape of the clusters to determine
 2196 how many particles produced the cluster and to estimate the positions of each
 2197 of the particles within the cluster. These allow for an identification of clusters
 2198 caused by more than one particle or by a particle that emits a δ -ray. In a high-
 2199 density tracking environment, the multiple position outputs can be used as the
 2200 locations of individual hits to allow reconstruction of tracks which almost over-
 2201 lap and with a much better separation than is possible without the splitting of
 2202 individual clusters.

2203 6.1.2 PIXEL DE/DX

2204 A hit in the Pixel detector corresponds to the voltage generated from ionization
 2205 current rising above a threshold value that is tuned to consistently record the
 2206 passing of MIPs. A larger amount of charge deposited results in a larger voltage,
 2207 and a larger signal remains above the threshold for a longer period of time. The
 2208 time over threshold (ToT) is read out of the Pixel detector, and can be used to
 2209 provide a measurement of the charge deposited in each pixel. The charge mea-
 2210 surements from each of the pixels included in a pixel cluster are summed to form
 2211 one charge measurement per layer of the pixel detector. That charge measure-
 2212 ment, combined with the angle of incidence of the track and the known sizes of
 2213 each detector element, can be converted into a measurement of dE/dx , the ion-
 2214 ization energy deposited per unit distance, measured in $\text{MeVg}^{-1}\text{cm}^2$. The IBL
 2215 only has sixteen available values (4 bits) of ToT to readout, compared to the 256
 2216 available values (8 bits) in the remaining pixel layers. To help alleviate this lack
 2217 of range, the IBL also records if it is in overflow: when the ionization is sufficient

2218 to generate a [ToT](#) above the largest value that can be recorded in the 4 bits. In the
 2219 remaining layers, the charge value is lost if the hit is in overflow; however the
 2220 significantly larger range of values makes this very rare in those layers.

2221 The measurements across multiple layers are combined to form an average
 2222 value of dE/dx for the track as a whole. Depending on where a charged particle
 2223 is produced, it will traverse four Pixel layers and create four clusters on average.
 2224 It can produce as few as two clusters in the Pixel detector if it passes through in-
 2225 active modules, and as many as five if it is in a region of the detector where multiple
 2226 modules overlap. To reduce the influence of the typical long Landau tails of the
 2227 distribution of dE/dx deposits [3], the average is calculated as a truncated mean
 2228 of these clusters. The value measured in the [IBL](#) is removed if it is in overflow, as
 2229 the measured value is not reliable in that case. If a track has five measurements
 2230 in the pixel detector, the two highest cluster values are removed. If a track has
 2231 two, three, or four measurements in the pixel detector, only the single highest
 2232 cluster value is removed. The remaining values are averaged to form the pixel
 2233 dE/dx .

2234 6.1.3 VERTEX RECONSTRUCTION

2235 A vertex represents the intersection of multiple tracks and corresponds to the
 2236 location of an interaction. If at least two charged particles result from the
 2237 interaction, the intersection of their resulting tracks reveals its position with high
 2238 precision. Vertices are divided into two groups, primary vertices which corre-
 2239 spond to the actual proton-proton collisions, and secondary vertices which cor-
 2240 respond to decays of short-lived particles or interactions with the detector. Pri-
 2241 mary vertices are particularly important, as they can provide a precise location
 2242 for the interaction which generated the observed particles. Understanding that
 2243 location is crucial in understanding the geometry of the event.

2244 Primary vertices are reconstructed by iteratively identifying seeds from recon-
 2245 structed tracks [32]. Each track's extrapolated z position at the beamline forms a
 2246 seed, and nearby tracks are fitted using that position as a point along their trajec-
 2247 tory. The goodness of fit with that vertex is considered for each track, measured
 2248 in χ^2 . The final position of the vertex is determined by a fit to all of the con-
 2249 sidered tracks, where the contribution from each track is weighted according to
 2250 the χ^2 compatibility with that vertex and by the error on its position. Any tracks
 2251 that are displaced by more than 7σ from that vertex are removed from the fit and
 2252 used to seed a new vertex. This procedure is iterated until no additional vertices
 2253 can be found.

2254 This procedure is typically performed twice. The first set of vertices is used
 2255 to fit a profile for the beamspot, which indicates the position of the intersec-
 2256 tion of beams in that particular bunch crossing. The fitted beamspot then pro-
 2257 vides a constraint for the second attempt to locate primary vertices, where both
 2258 the track fitting and seeding of vertices are required to be consistent with in-
 2259 teractions occurring within the beamspot. The vertex reconstruction algorithm
 2260 achieves the efficiency shown in Figure 46, increasing from 83% for vertices with

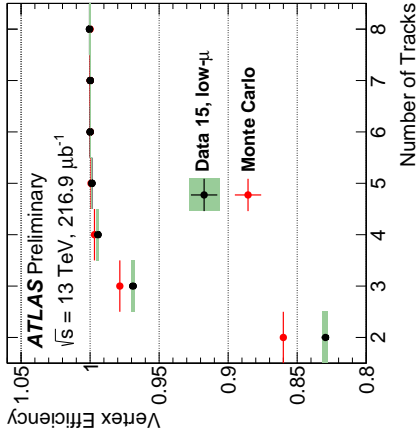


Figure 46: The vertex reconstruction efficiency as a function of the number of associated tracks [33].

2261 two associated tracks and up to nearly 100% for vertices with four or more asso-
 2262 ciated tracks.

2263 6.2 ELECTRONS AND PHOTONS

2264 Electrons are measured as both a charged particle track and energy deposits in
 2265 the electromagnetic calorimeter. Photons, on the other hand, leave energy de-
 2266 posits in the electromagnetic calorimeter but do not produce a corresponding
 2267 track. Because the electromagnetic interactions with the calorimeter of both
 2268 photons and electrons produces more photons and electrons, the behavior in the
 2269 calorimeter is very similar and there is significant overlap in the reconstruction
 2270 techniques for each.

2271 The reconstruction of a photon or an electron in the calorimeter is based on
 2272 clustering algorithms which identify groups of energy deposits [34–36]. For this
 2273 purpose, the entire electromagnetic calorimeter is subdivided into a grid of 200
 2274 by 256 towers in the η and ϕ directions, respectively, where the individual grid
 2275 units have a size of $\Delta\eta = 0.025$ and $\Delta\phi = 0.025$. These towers correspond to
 2276 individual cells in the middle, coarsest layer of the EM calorimeter, and in the re-
 2277 maining layers the cells are grouped together cover the same area in $\eta - \phi$ space.
 2278 The clustering begins by finding seeds with a sliding-window algorithm based
 2279 on the towers: a window of 3 by 5 towers is formed and translated until the sum
 2280 of the energy within the window is maximized. If that energy is above 2.5 GeV,
 2281 then that region becomes a seed. The choice of 2.5 GeV was chosen to com-
 2282 promise between maximizing reconstruction efficiency while minimizing fake
 2283 electron seeds from electronic noise or soft hadrons from additional interactions.
 2284 The seeds are rejected if the energy measured in the hadronic calorimeter behind
 2285 the seed is large, as this typically indicates a hadron rather than an electron or
 2286 photon.

2287 Next, the inner detector tracks within a cone of $\Delta R = 0.3$ are compared to
 2288 the location and energy of the seed. Tracks are matched to the cluster if the ex-

2289 trapolation of the track to the energy-weighted center in the middle layer of the
 2290 **EM** calorimeter falls within $\Delta\phi < 0.2$ in the direction of the curvature of the track or $\Delta\phi < 0.05$ in the direction opposite of the curvature of the track. If the
 2291 seed matches with a track that originated from a primary vertex, the combination
 2292 of track and electromagnetic cluster is reconstructed as an electron. If the
 2293 seed matches with a track that did not originate from a primary vertex, then the
 2294 electromagnetic cluster is reconstructed as a converted photon. And if there is
 2295 no corresponding track in the inner detector, than the cluster is reconstructed
 2296 as a photon.

2297 After classification, the final clustering of the energy in the **EM** calorimeter
 2298 calorimeter is performed. The classification must be done first, as the expected
 2299 size of the energy deposits in the calorimeter are different for electrons and pho-
 2300 tons. In the barrel region, the final clusters for electrons are formed in rectangles
 2301 of 3 towers in the η -direction and 7 towers in the ϕ -direction. This asymmetric
 2302 window accounts for the curving of the charged particles only in the ϕ direction.
 2303 For photons, the size of the rectangle is 3 towers by 5 towers. In the endcap re-
 2304 gion, all object types are clustered in rectangles of 5 towers by 5 towers, as the
 2305 effect of the magnetic field curvature is less pronounced in this region. The sum
 2306 of the energies in these clusters provide the final energy measurement for the
 2307 electron or photon.

2309 6.2.1 PHOTON IDENTIFICATION

2310 The original requirement for constructing a photon cluster, a significant energy
 2311 deposit in the electromagnetic calorimeter without a corresponding track or en-
 2312 ergy deposits in the hadronic calorimeter, is already effective in identifying pho-
 2313 tons. However, there is a significant background for prompt photon production
 2314 from the decays of pions, $\pi^0 \rightarrow \gamma\gamma$. These can be identified using the shape of
 2315 the cluster in the narrow η granularity in the first layer of the **EM** calorimeter.

2316 6.2.2 ELECTRON IDENTIFICATION

2317 Prompt electrons have a number of backgrounds, such as secondary electrons
 2318 from hadron decays or misidentified hadronic jets, that can be rejected using ad-
 2319 ditional information from the **EM** calorimeter and the inner detector. The most
 2320 basic level of electron identification, referred to as Loose, makes requirements
 2321 on the shower shapes in the high granularity first layer of the **EM** calorimeter
 2322 as well as the quality of the inner detector track. It also requires a good match
 2323 between the track and the calorimeter energy deposits and a small fraction of
 2324 energy in the hadronic calorimeter behind the electromagnetic cluster. ATLAS
 2325 defines several additional working points, including MediumLL and TightLL,
 2326 which provide progressively lower background rates for electrons by imposing
 2327 additionally strict requirements on the above variables as well as new require-
 2328 ments like the impact parameter of the inner detector track or the comparison
 2329 of the cluster energy to the momentum in the inner detector. The LL designates

2330 that the requirement is based on a threshold on the output of a likelihood func-
 2331 tion using the above quantities as an input [35].

2332 6.3 MUONS

2333 Muons produced in ATLAS first traverse the inner detector and leave behind a
 2334 track as described in Section 6.1. The muon then passes through the calorimeter,
 2335 leaving behind a small, characteristic amount of energy, and then passes through
 2336 the muon spectrometer where it produces hits in the MDTs or CSCs. Muon tracks
 2337 are formed from local segments of hits in each layer of the MDTs or CSCs, and
 2338 then the final muon spectrometer track is formed by combining the two local
 2339 segments [37]. When a track is reconstructed in both the inner detector and
 2340 the muon spectrometer, the track is refitted to include the hits in both the inner
 2341 detector and the muon spectrometer, and forms a combined muon.

2342 In a few regions of the detector, a muon may fail to leave behind both a com-
 2343 plete inner detector and muon system track. For a very small fraction of the
 2344 acceptance of the muon system, there is only one layer of muon chambers and a
 2345 global muon system track is not formed. In this case, as long as the track in the
 2346 inner detector exists and geometrically matches to a segment, a segment-tagged
 2347 muon is formed using momentum measurements from the inner detector. In
 2348 the region where the muon system has coverage but the inner detector does not,
 2349 $2.5 < |\eta| < 2.7$, a stand-alone muon is formed which uses only information
 2350 from the muon system. And for muons produced within one of the few holes in
 2351 the muon system, including $|\eta| < 0.1$, the characteristic energy deposits in the
 2352 calorimeter can be used to tag an inner detector track as a calo-tag muon. These
 2353 additional categories are used to achieve high efficiency over a larger range of
 2354 acceptance, but the combined muons are the most reliable.

2355 6.3.1 MUON IDENTIFICATION

2356 The various types of muons are incorporated into three working points: Loose,
 2357 Medium, and Tight, which reflect the increasing muon purity for each of the
 2358 selections definitions. Tight muons include only combined muons with a good
 2359 track fit quality and momentum resolution and at least two hits in a precision
 2360 muon system layer. Medium muons include those in tight as well as combined
 2361 muons with one precision hit and one precision hole, where hole is defined in
 2362 the same way as in Section 6.1. The medium working point also includes stand-
 2363 alone muons with $|\eta| > 2.5$ and at least two hits in precision layers. And finally
 2364 the loose working point includes both medium and tight muons, but additional
 2365 includes segment-tagged and calo-tagged muons in the region $|\eta| < 0.1$. The
 2366 reconstruction efficiencies for muons with $p_T > 20$ GeV range from 91.8% for
 2367 tight muons and up to 98.1% for loose muons [37].

2368 6.4 JETS

2369 A jet does not directly correspond to a physical particle, unlike all of the recon-
 2370 structed objects described above, but instead tries to capture the conical cascade
 2371 of particles produced in the hadronization of a quark or gluon from the proton-
 2372 proton collision. The hadronization process creates a very large number of col-
 2373 limated particles, with a high enough density that individually reconstructing all
 2374 of the produced particles in the calorimeter is not possible within ATLAS. How-
 2375 ever most analyses are interested only in the kinematics of the particle which
 2376 produced the cascade, rather than the individual products. Therefore, jets are
 2377 a useful tool to measure the combined energy and direction of the ensemble of
 2378 products and thus represents the kinematics of the original. Jet algorithms are
 2379 very generic and can be used to group together a number of types of objects to
 2380 form aggregate representations. For example, truth particles in simulation can
 2381 be grouped in truth jets, or tracks from the inner detector can be grouped to-
 2382 gether to form track jets. This section, however, will focus on calorimeter jets
 2383 which take topoclusters of energy deposits in the calorimeter as inputs and pro-
 2384 duce a combined object which represents the energy measured by the calorime-
 2385 ter and the location where it was deposited.

2386 6.4.1 TOPOLOGICAL CLUSTERING

2387 Hadrons often deposit their energy into multiple individual cells in both the elec-
 2388 tromagnetic and hadronic calorimeters. The purpose of topological clustering is
 2389 to group cells in all three dimensions into clusters that represent a single energy
 2390 deposit. The procedure must be robust enough to reject noise fluctuations in
 2391 the cell energy measurements that can come from both electronic noise and ad-
 2392 ditional low energy particles produced in pileup activity. The background level
 2393 of calorimeter noise is called σ_{noise} , and is an important component of the topo-
 2394 logical clustering.

2395 The topological clusters are formed in a three step process called the 4-2-0
 2396 threshold scheme, which uses three energy thresholds to build up a cluster from
 2397 cells [38]. First, any cells with a measured energy above $4\sigma_{\text{noise}}$ are identified
 2398 as seed cells. The cells adjacent to the seed cells with a measured energy above
 2399 $2\sigma_{\text{noise}}$ are called secondary cells. All of the cells which are adjacent to a sec-
 2400 ondary cell with $E_{\text{cell}} > 2\sigma_{\text{noise}}$ are also labeled secondary cells. Tertiary cells
 2401 are those immediately adjacent to a seed or secondary cell with a measured en-
 2402 ergy above zero. Adjacency in this sense is defined in three dimensions, cells are
 2403 adjacent if they are neighbors within a layer but also if they have the same $\eta - \phi$
 2404 coordinates but are in adjacent layers or even in an adjacent layer in another
 2405 calorimeter.

2406 From these definitions, clusters are built by resolving the seeds in order of
 2407 significance, the ratio $E_{\text{cell}}/\sigma_{\text{noise}}$. All adjacent secondary cells to the highest
 2408 significance seed are added to that seed's topocluster, and any of those cells which
 2409 would also have qualified as seeds are removed from the list of seeds. Once all
 2410 of the secondary cells have been added, the tertiary cells are then added to that

2411 cluster as well. This procedure is then iterated until no seeds remain, forming
 2412 the first round of topoclusters.

2413 It is also useful to split topoclusters into multiples if local maxima are present
 2414 within the topocluster, as clusters produced by multiple nearby particles can
 2415 merge. The splitting process begins by finding local maxima cells in the middle
 2416 layer of the calorimeters with a minimum energy of 500 MeV and at least four
 2417 neighboring secondary cells. These requirements reduce the likelihood to split
 2418 a cluster due to random fluctuations, as the middle layers provide the most reli-
 2419 able energy measurements. Cells between two local maxima can then be shared
 2420 between two clusters to account for overlapping contributions from two parti-
 2421 cles. The energy sharing is weighted by the energy of each cluster as well as the
 2422 distance of the cell to the centroid of that cluster.

2423 The energies of all the cells in the cluster are then summed together to form
 2424 the energy of that cluster. The energy needs to be corrected for the various losses
 2425 expected in the calorimeter, as described in Section 5.4. The simplest correction,
 2426 scaling the measured energy by the sampling fraction, brings the cluster energies
 2427 to the [EM](#) scale. It is called the [EM](#) scale because it accurately describes the energy
 2428 of electromagnetic showers.

2429 Another scale is defined to improve accuracy for hadronic processes, the local
 2430 cluster weighted ([LCW](#)) scale, that helps to correct for the expected variations in
 2431 hadronic energy deposits. The [LCW](#) correction first determines if the shower is
 2432 hadronic or electromagnetic, based on the depth of the shower and the cluster
 2433 energy density. For hadronic showers, the energy is corrected for calorimeter
 2434 non-compensation, an effect which reduces the measured energy of hadronic
 2435 showers because some of the energy goes into invisible processes like the break
 2436 up of nuclei. All clusters are then corrected for energy that may be deposited in
 2437 uninstrumented regions in that cluster’s location in the calorimeter, and they are
 2438 also corrected with an estimate of how much energy falls outside the extent of
 2439 the cluster based on its shape and the deposit type.

2440 6.4.2 JET ALGORITHMS

2441 Using the topological clusters as inputs, a jet algorithm groups them together
 2442 into a collection of adjacent energy deposits that is intended to correspond to
 2443 a single process [39]. Jet algorithms need a few key characteristics to be usable
 2444 for physics analysis. First, the jets produced by the algorithm should have little
 2445 dependence on the addition of soft particles to the event (infrared safety), as a
 2446 negligible addition of energy should not significantly modify the event topology.
 2447 The jets produced by the algorithm should also be collinear safe: a single quark
 2448 replaced by two, parallel quarks with half the original’s momentum should not
 2449 change the resulting jets. This requirement is important as the jets are intended
 2450 to capture only the properties of the aggregate and not those of individual parti-
 2451 cles. And finally the algorithm needs to be sufficiently simple and fast to be used
 2452 for the large rate of collected proton-proton collisions on ATLAS.

2453 The most commonly used algorithm on ATLAS that satisfies these require-
 2454 ments is called the anti- k_t algorithm [40]. The anti- k_t , in brief, relies on itera-

tively combining the input objects that are closest together, where closest is defined by a particular distance metric, $d_{i,j}$, where the index i represents the combination constructed so far and j is an additional object being considered. The combinations stop when the closest remaining object is the beam itself, where the distance to the beam is called $d_{i,B}$. An entire class of algorithms follows this procedure with the following distance metrics

$$d_{i,j} = \min(k_{ti}^{2p}, k_{tj}^{2p}) \frac{\Delta_{ij}^2}{R^2} \quad (18)$$

$$d_{i,B} = k_{ti}^{2p} \quad (19)$$

where $\Delta_{ij} = (y_i - y_j)^2 + (\phi_i - \phi_j)^2$, k_{ti} is the transverse momentum of the object, y is the rapidity, and p is a parameter of the algorithm. Anti- k_t is the particular case where $p = -1$, and is a choice that results in an algorithm that is both infrared and collinear safe.

The algorithm is repeated until there are no input objects remaining, which results in a series of jets. Each jet has a complete four momentum from the combination of its input clusters, where the combinations assume a mass of zero. The jet energies then need to be calibrated to attempt to match the energy of the object which produced the jet.

6.4.3 JET ENERGY SCALE

Though the [LCW](#) scheme attempts to correct the topoclusters to reflect the true deposited energy, the correction does not fully account for energy lost within the calorimeters. Because of these effects, the original reconstructed jet energy does not reflect the true energy of the particle which initiated the jet. Therefore it is necessary to additionally correct the reconstructed jet itself, in addition to the corrections on the inputs. This correction is referred to as the [JES](#), which combines several individual steps of calibration [41].

The first calibration step corrects the direction of the jet to ensure that it points back to the primary vertex. Next, the energy of the jet is corrected for pileup by subtracting the expected contribution from pileup based on the momentum, η , and area of the jet as well as the number of reconstructed vertices and the expected number of interactions per crossing, μ . The largest single correction adjusts the jet energy and pseudorapidity to attempt to match the energy and pseudorapidity of the parton which produced it. This correction is measured in simulation by comparing the reconstructed jet energies to the energy of the truth particle which produced it. However the simulation is not relied on alone to estimate this correction, and an additional step applies an additional energy correction based on in-situ measurements in data. These corrections come from various techniques which measure jet energies indirectly by balancing them with other, well-measured objects. In the central region ($|\eta| < 1.2$), jets are balanced against photons and the leptonic decays of Z bosons and high momentum jets ($p_T > 210$ GeV) are also balanced against multiple smaller jets in multijet events.

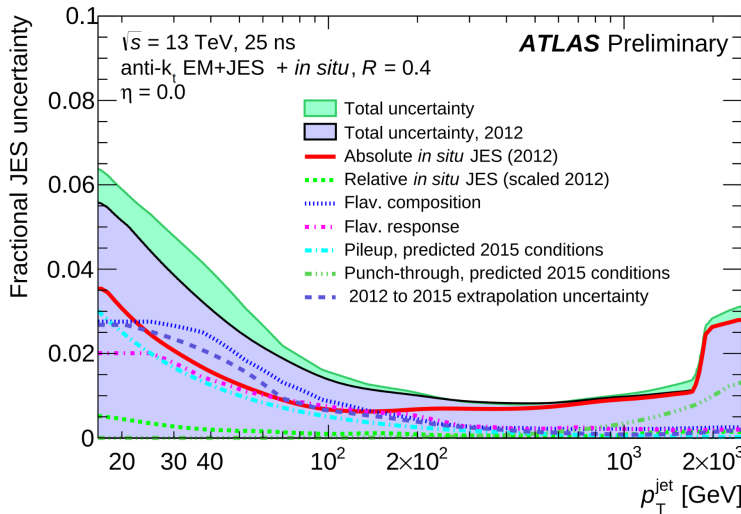


Figure 47: The total, fractional JES uncertainties estimated for 2015 data as a function of jet p_T .

2493 Jets at larger pseudorapidities, above $|\eta| = 1.2$, are calibrated by balancing with
 2494 lower pseudorapidity jets.

2495 These steps introduce a number of systematic uncertainties, referred to as
 2496 the JES uncertainty. The largest of these comes from the in-situ measurements,
 2497 which are statistically limited in measuring high momentum and high pseudora-
 2498 pidity jets. The total, fractional JES uncertainty is shown as a function of p_T in
 2499 Figure 47. The uncertainty falls to a minimum value of just over 1.0% around a
 2500 few hundred GeV, and rises again at high momentum because of the difficulty of
 2501 measuring jet balance in data above 2–3 TeV. The uncertainty is also minimized
 2502 at low $|\eta|$, and grows at large $|\eta|$ again where making in-situ measurements is
 2503 difficult. This technique does not actually provide a measurement of the uncer-
 2504 tainty for the highest energy jets, above 3 TeV, because there are not enough
 2505 measured data events to provide them. An alternative method for deriving the
 2506 JES and JES uncertainty that can be used even for very high p_T jets will be dis-
 2507 cussed in Chapter 8.

2508 6.5 MISSING TRANSVERSE ENERGY

2509 Among stable SM particles, only the neutrino cannot be directly measured in the
 2510 ATLAS detector. Because the neutrino carries neither electric nor color charge,
 2511 it is very unlikely to interact with the tracking detectors or the calorimeters,
 2512 and instead passes through the detector completely unobserved. Some particles
 2513 which have been conjectured to exist, like the LSP in many SUSY models, would
 2514 also have the same behavior. Therefore, it is important for ATLAS to provide
 2515 some way to assess the momentum carried away by a neutral, colorless parti-
 2516 cle. This can be accomplished through a measurement of missing energy in the
 2517 transverse direction, or E_T^{miss} , which quantifies the momentum imbalance of the
 2518 observed particles. From the conservation of momentum and the lack of the

2519 initial momentum in the transverse plane in the proton-proton collisions, any
 2520 imbalance of momentum can be inferred to be carried away by an unmeasured
 2521 particle.

2522 E_T^{miss} is more precisely defined as the magnitude of the vector sum of the
 2523 (p_x, p_y) components of each observed object's momentum. The definition is
 2524 simple, but there can be significant complexity in defining the inputs. As of Run
 2525 2, ATLAS uses a common algorithmic approach to carefully calculate missing en-
 2526 ergy, but each analysis is free to define it's own inputs. For the analysis discussed
 2527 throughout this thesis, the missing energy inputs consist of the electrons, pho-
 2528 tons, muons, and jets discussed in the previous sections, in addition to a track-
 2529 based term that accounts for the contribution of low p_T particles (soft term).

2530 To produce the most precise measurement of E_T^{miss} , it is important to use the
 2531 best representation of the momentum of each of the input objects, which can
 2532 often be reconstructed as multiple different types in a single event. For example,
 2533 an electron can be reconstructed separately as an electron (Section 6.2) and a
 2534 jet (Section 6.4), but the electron representation has the highest precision for
 2535 reconstructing the true electron momentum. To ensure no duplications in the
 2536 E_T^{miss} definition, the inputs are collectively considered for overlap removal. Only
 2537 the most precise object type is kept for objects that fall within a cone of $\Delta R < 0.2$
 2538 for pairs of electrons and jets and a cone of $\Delta R < 0.4$ for other pair types.

2539 The fully reconstructed objects do not include all of the energy within the
 2540 events, as some clusters do not enter into a jet and some tracks are not classified
 2541 as electrons or muons. These momentum carried by these objects is accounted
 2542 for in a soft-term, which tallies all of the energy carried by the particles too soft
 2543 to form separate objects. The track soft term uses only tracking information to
 2544 estimate the contribution of soft objects, and does so by vectorially summing the
 2545 momentum of all well-reconstructed tracks with momentum above 400 MeV
 2546 that are not associated to other objects.

2547 All of these contributions together give a single E_T^{miss} value for a given event.
 2548 The direction of that missing energy is taken as opposite the vector sum of all the
 2549 constituents, to correspond to the momentum an invisible particle would have to
 2550 have to make the event balanced. Depending on the context, this missing energy
 2551 can be considered the energy of a neutrino or an LSP, with a large missing energy
 2552 being a common signal criteria for searches for new physics.

2553

PART III

2554

CALORIMETER RESPONSE

2555

2556

2557 RESPONSE MEASUREMENT WITH SINGLE HADRONS

2558 As discussed in Section 6.4, colored particles produced in collisions hadronize
2559 into jets of multiple hadrons. One approach to understanding jet energy mea-
2560 surements in the ATLAS calorimeters is to evaluate the calorimeter response to
2561 those individual hadrons; measurements of individual hadrons can be used to
2562 build up an understanding of the jets that they form. The redundancy of the
2563 momentum provided by the tracking system and the energy provided by the
2564 calorimeter provides an opportunity to study calorimeter response using real
2565 collisions, as described further in Section 7.2.

2566 Calorimeter response includes a number of physical effects that can be ex-
2567 tracted to provide insight into many aspects of jet modeling. First, many charged
2568 hadrons interact with the material of the detector prior to reaching the calorime-
2569 ters and thus do not deposit any energy. Comparing this effect in data and simu-
2570 lation is a powerful tool in validating the interactions of particles with the mate-
2571 rial of the detector and the model of the detector geometry in simulation, see Sec-
2572 tion 7.2.2. The particles which do reach the calorimeter deposit their energy into
2573 several adjacent cells, which are then clustered together. The energy of the clus-
2574 ter is then the total energy deposited by that particle. Comparing the response of
2575 hadrons in data to that of simulated hadrons provides a direct evaluation of the
2576 showering of hadronic particles and the energy deposited by particles in matter
2577 (Section 7.2.4).

2578 The above studies all use an inclusive selection of charged particles, which are
2579 comprised predominantly of pions, kaons, and (anti)protons. It is also possible to
2580 measure the response to various identified particle types separately to evaluate
2581 the simulated interactions of each particle, particularly at low energies where
2582 differences between species are very relevant. Pions and (anti)protons can be
2583 identified through decays of long-lived particles, in particular Λ , $\bar{\Lambda}$, and K_S^0 , and
2584 then used to measure response as described above. This is discussed in detail in
2585 Section 7.3.

2586 The results in this chapter use data collected at 7 and 8 TeV collected in 2010
2587 and 2012, respectively. Both are included as the calorimeter was repaired and
2588 recalibrated between those two data-taking periods. Both sets of data are com-
2589 pared to an updated simulation that includes new physics models provided by
2590 Geant4 [7] and improvements in the detector description [42, 43]. The present
2591 results are published in European Physical Journal C (EPJC) [44] and can be com-
2592 pared to a similar measurement performed in 2009 and 2010 [45], which used
2593 the previous version of the simulation framework [46].

2594 7.1 DATASET AND SIMULATION

2595 7.1.1 DATA SAMPLES

2596 The two datasets used in this chapter are taken from dedicated low-pileup runs
 2597 where the fraction of events with multiple interactions was negligible. These
 2598 datasets are used rather than those containing full-pileup events to facilitate mea-
 2599 surement of isolated hadrons. The 2012 dataset at $\sqrt{s} = 8$ TeV contains 8 mil-
 2600 lion events and corresponds to an integrated luminosity of 0.1 nb^{-1} . The 2010
 2601 dataset at $\sqrt{s} = 7$ TeV contains 3 million events and corresponds to an inte-
 2602 grated luminosity of 3.2 nb^{-1} . The latter dataset was also used for the 2010 re-
 2603 sults [45], but it has since been reanalyzed with an updated reconstruction in-
 2604 cluding the final, best understanding of the detector description for the material
 2605 and alignment from Run 1.

2606 7.1.2 SIMULATED SAMPLES

2607 The two datasets above are compared to simulated single-, double-, and non-
 2608 diffractive events generated with Pythia8 [47] using the A2 configuration of
 2609 hadronization [48] and the MSTW 2008 parton-distribution function set [49,
 2610 50]. The admixture of the single-, double-, and non-diffractive events uses the
 2611 default relative contributions from Pythia8. The conditions and energies for
 2612 the two simulations are chosen so that they match those of the corresponding
 2613 dataset.

2614 To evaluate the interaction of hadrons with detector material, the simulation
 2615 uses two different collections of hadronic physics models, called physics lists, in
 2616 Geant4 9.4 [51]. The first, QGSP_BERT, combines the Bertini intra-nuclear
 2617 cascade [52–54] below 9.9 GeV, a parametrized proton inelastic model from 9.5
 2618 to 25 GeV [55], and a quark-gluon string model above 12 GeV [56–60]. The
 2619 second, FTFP_BERT, combines the Bertini intra-nuclear cascade [52–54] below
 2620 5 GeV and the Fritiof model [61–64] above 4 GeV. In either list, Geant4 en-
 2621 forces a smooth transition between models where multiple models overlap.

2622 7.1.3 EVENT SELECTION

2623 The event selection for this study is minimal, as the only requirement is selecting
 2624 good-quality events with an isolated track. Such events are triggered by requir-
 2625 ing at least two hits in the minimum-bias trigger scintillators. After trigger, each
 2626 event is required to have exactly one reconstructed vertex, and that vertex is re-
 2627 quired to have four or more associated tracks.

2628 The particles which are selected for the response measurements are first iden-
 2629 tified as tracks in the inner detector. The tracks are required to have at least 500
 2630 MeV of transverse momentum. To ensure a reliable momentum measurement,
 2631 these tracks are required to have at least one hit in the pixel detector, six hits in
 2632 the SCT, and small longitudinal and transverse impact parameters with respect
 2633 to the primary vertex [45]. For the majority of the measurements in this chapter,

the track is additionally required to have 20 hits in the TRT, which significantly reduces the contribution from tracks which undergo nuclear interactions. This requirement and its effect is discussed in more detail in Section 7.2.5. In addition, tracks are rejected if there is any other reconstructed track which extrapolates to the calorimeter within a cone of $\Delta R = \sqrt{(\Delta\phi)^2 + (\Delta\eta)^2} < 0.4$. This requirement guarantees that the contamination of energy from nearby charged particles is negligible [45].

7.2 INCLUSIVE HADRON RESPONSE

The calorimeter response is more precisely defined as the ratio of the measured calorimeter energy to the true energy carried by the particle, although this true energy is unknown. For charged particles, however, the inner detector provides a very precise measurement of momentum (with uncertainty less than 1%) that can be used as a proxy for true energy. The ratio of the energy deposited by the charged particle in the calorimeter, E , to its momentum measured in the inner detector p , forms the calorimeter response measure called E/p . Though the distribution of E/p contains a number of physical features, this study focuses on the trends in two aggregated quantities: $\langle E/p \rangle$, the average of E/p for the selected tracks, and the zero fraction, the fraction of tracks with no associated energy in the calorimeter for those tracks.

The calorimeter energy assigned to a track is defined using clusters. The clusters are formed using a 4–2–0 algorithm [65] that begins with seeds requiring at least 4 times the average calorimeter cell noise. The neighboring cells with at least twice that noise threshold are then added to the cluster, and all bounding cells are then added with no requirement. This algorithm minimizes noise contributions through its seeding process, and including the bounding cells improves the energy resolution [66]. The clusters are associated to a given track if they fall within a cone of $\Delta R = 0.2$ of the extrapolated position of the track, which includes about 90% of the energy on average [45].

7.2.1 E/P DISTRIBUTION

The E/p distributions measured in both data and simulation are shown in Figure 48 for two example bins of track momentum and for tracks in the central region of the detector. These distributions show several important features of the E/p observable. The large content in the bin at $E = 0$ comes from tracks that have no associated cluster, which occurs due to interactions with detector material prior to reaching the calorimeter or the energy deposit being insufficiently large to generate a seed, and are discussed in Section 7.2.2. The small negative tail also comes from tracks that do not deposit any energy in the calorimeter but are randomly associated to a cluster with an energy below the noise threshold. The long positive tail above 1.0 comes from the contribution of neutral particles. Nearby neutral particles deposit (sometimes large) additional energy in the calorimeter but do not produce tracks in the inner detector, so they cannot be rejected by the track isolation requirement. Additionally the peak and mean of

2676 the distribution falls below 1.0 because of the loss of energy not found within
 2677 the cone as well as the non-compensation of the calorimeter.

2678 The data and simulation share the same features, but the high and low tails
 2679 are significantly different. The simulated events tend to overestimate the con-
 2680 tribution of neutral particles to the long tail, an effect which can be isolated and
 2681 removed as discussed in Section 7.2.3. Additionally, the simulated clusters have
 2682 less noise on average, although this is a small effect on the overall response.

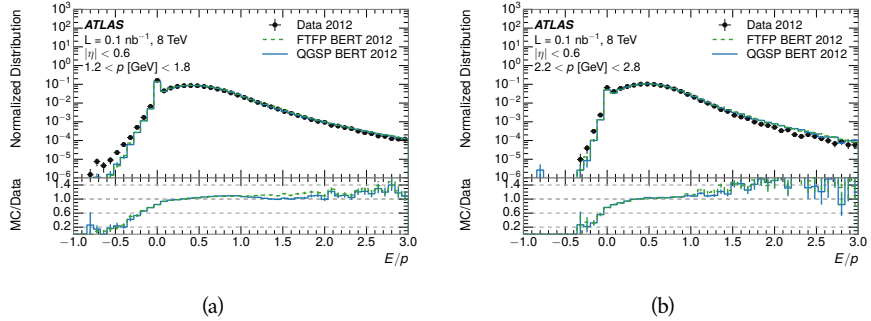


Figure 48: The E/p distribution and ratio of simulation to data for isolated tracks with
 (a) $|\eta| < 0.6$ and $1.2 < p/\text{GeV} < 1.8$ and (b) $|\eta| < 0.6$ and $2.2 < p/\text{GeV} < 2.8$.

2683 72.2 ZERO FRACTION

2684 The fraction of particles with no associated clusters, or similarly those with $E \leq$
 2685 0, reflects the modeling of both the detector geometry and hadronic interactions.
 2686 The zero fraction is expected to rise as the amount of material a particle traverses
 2687 increases, while it is expected to decrease as the particle energy increases. This
 2688 dependence can be seen in Figure 49, where the zero fraction in data and simula-
 2689 tion is shown as a function of momentum and the amount of material measured
 2690 in interaction lengths. The trends are similar between 2010 and 2012 and for
 2691 positively and negatively charged particles. The zero fraction decreases with
 2692 energy as expected. The absolute discrepancy in zero fraction between data and
 2693 simulation decreases with momentum from 5% to less than 1%, but this becomes
 2694 more pronounced in the ratio as the zero fraction shrinks quickly with increas-
 2695 ing momentum. The amount of material in the detector increases with η , which
 2696 is used to obtain results for interaction lengths ranging between 0.1 and 0.65 λ .
 2697 As the data and simulation have significant disagreement in the zero fraction
 2698 over a number of interaction lengths, the difference must be primarily from the
 2699 modeling of hadronic interactions with detector material and not just the detec-
 2700 tor geometry. Although two different hadronic interaction models are shown
 2701 in the figure, they have very similar discrepancies to data because both use the
 2702 same description (the BERT model) at low momentum.

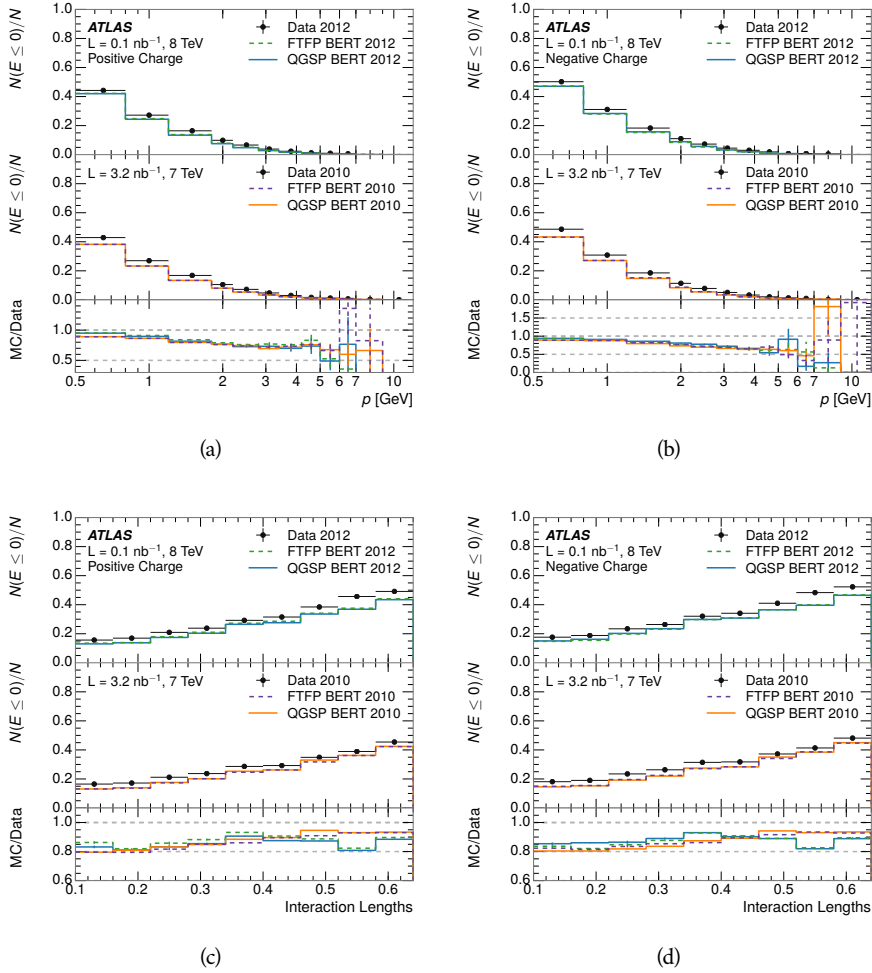


Figure 49: The fraction of tracks as a function (a, b) of momentum, (c, d) of interaction lengths with $E \leq 0$ for tracks with positive (on the left) and negative (on the right) charge.

2703 7.2.3 NEUTRAL BACKGROUND SUBTRACTION

2704 The isolation requirement on hadrons is only effective in removing an energy
 2705 contribution from nearby charged particles. Nearby neutral particles, predomi-
 2706 nantly photons from π^0 decays, also add their energy to the calorimeter clusters,
 2707 but mostly in the electromagnetic calorimeter. The arrangement of energy de-
 2708 posits is shown in Figure 50, which illustrates both energy deposits from the
 2709 hadronic particle and additional deposits from neutral particles. It is possible to
 2710 measure this contribution, on average, using late-showering hadrons that min-
 2711 imally ionize in the electromagnetic calorimeter. Such particles are selected by
 2712 requiring that they deposit less than 1.1 GeV in the EM calorimeter within a
 2713 cone of $\Delta R < 0.1$ around the track. To ensure that these particles are well mea-
 2714 sured, they are additionally required to deposit between 40% and 90% of their
 2715 energy in the hadronic calorimeter within the same cone.

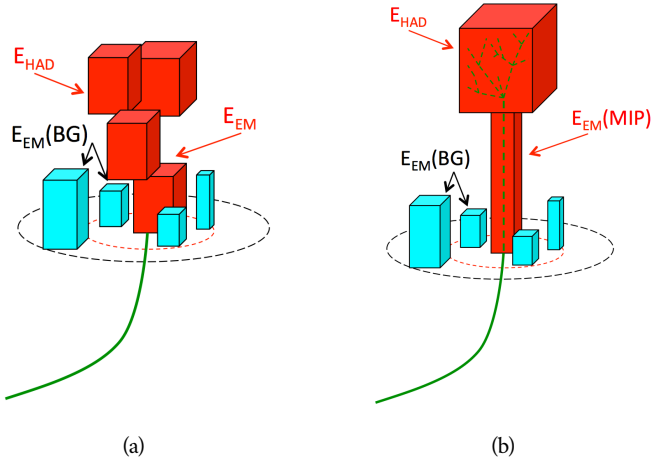


Figure 50: An illustration (a) of the geometry of energy deposits in the calorimeter. The red energy deposits come from the charged particle targeted for measurement, while the blue energy deposits are from nearby neutral particles and must be subtracted. The same diagram (b) for the neutral-background selection, described in Section 7.2.3.

2716 These particles provide a clean sample to measure the nearby neutral back-
 2717 ground because they do not deposit energy in the area immediately surround-
 2718 ing them in the EM calorimeter, as shown in Figure 50. So, the energy deposits in the
 2719 region $0.1 < \Delta R < 0.2$ can be attributed to neutral particles alone. To estimate
 2720 the contribution to the whole cone considered for the response measurement,
 2721 that energy is scaled by a geometric factor of $4/3$. This quantity, $\langle E/p \rangle_{BG}$, mea-
 2722 sured in aggregate over a number of particles, gives the contribution to $\langle E/p \rangle$
 2723 from neutral particles in the EM calorimeter. Similar techniques were used in
 2724 the individual layers of the hadronic calorimeters to show that the background
 2725 from neutrals is negligible in those layers [45].

2726 The distribution of this background estimate is shown in Figure 51 for data
 2727 and simulation with the two different physics lists. The contribution from neu-

2728 tral particles falls from 0.1 at low momentum to around 0.03 for particles above
 2729 7 GeV. Although the simulation captures the overall trend, it significantly over-
 2730 estimates the neutral contribution for tracks with momentum between 2 and 8
 2731 GeV. This effect was also seen in the tails of the E/p distributions in Figure 48.
 2732 This difference is likely due to modeling of coherent neutral particle radiation
 2733 in Pythia8 that overestimates the production of π^0 near the production of the
 2734 charged particles. The discrepancy does not depend on η and thus is unlikely to
 2735 be a mismodeling of the detector. This difference can be subtracted to form a
 2736 corrected average of E/p .

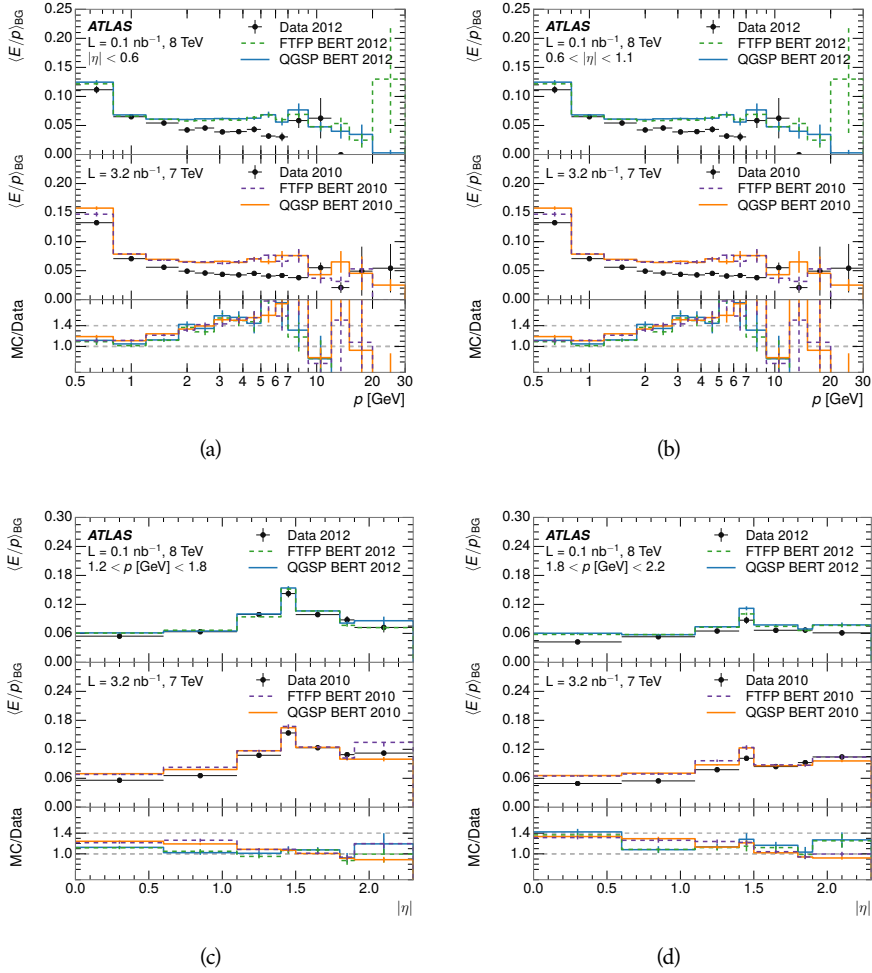


Figure 51: $\langle E/p \rangle_{BG}$ as a function of the track momentum for tracks with (a) $|\eta| < 0.6$,
 (b) $0.6 < |\eta| < 1.1$, and as a function of the track pseudorapidity for tracks
 with (c) $1.2 < p/\text{GeV} < 1.8$, (d) $1.8 < p/\text{GeV} < 2.2$.

2737 7.2.4 CORRECTED RESPONSE

2738 Figure 52 shows $\langle E/p \rangle_{COR}$ as a function of momentum for several bins of pseu-
 2739 dorapidity. This corrected $\langle E/p \rangle_{COR} \equiv \langle E/p \rangle - \langle E/p \rangle_{BG}$ measures the average
 2740 calorimeter response without the contamination of neutral particles. It is the

most direct measurement of calorimeter response in that it is the energy measured for fully isolated hadrons. The correction is performed separately in data and simulation, so that the mismodeling of the neutral background in simulation is removed from the comparison of response. The simulation overestimates the response at low momentum by about 5%, an effect that can be mostly attributed to the underestimation of the zero fraction mentioned previously. For $|\eta| < 0.6$, the data-simulation agreement has a larger discrepancy by about 5% for 2010 than 2012, although this is not reproduced in at higher pseudorapidity.

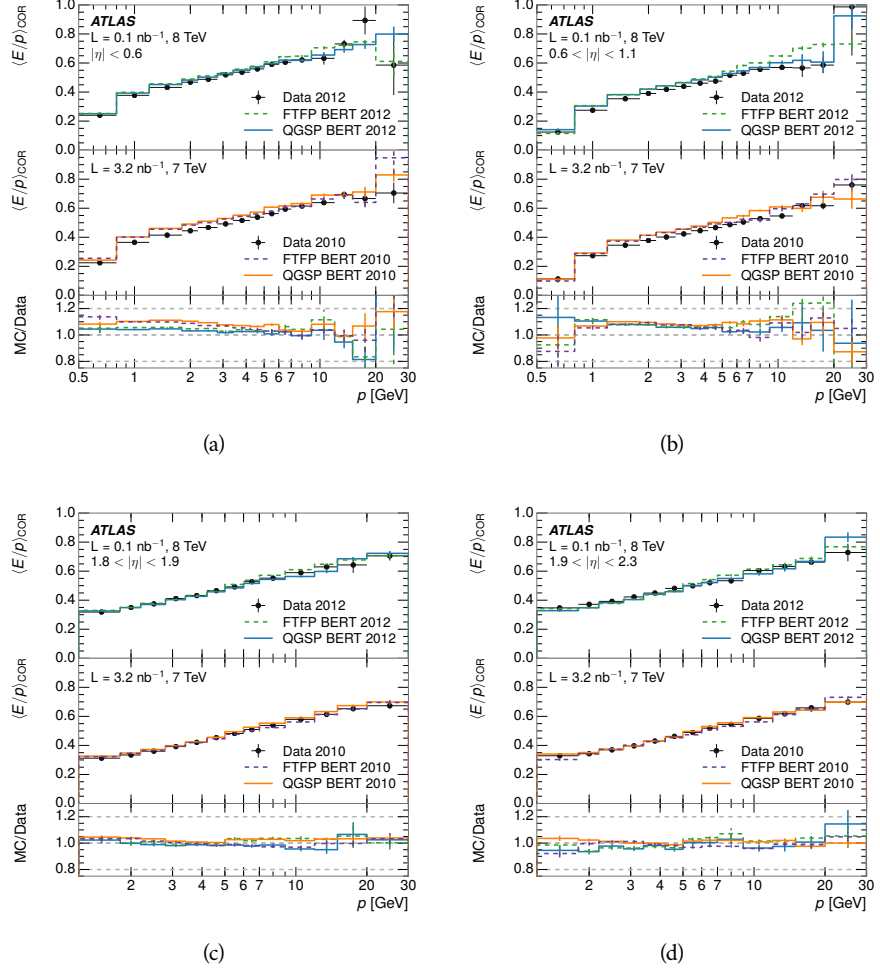


Figure 52: $\langle E/p \rangle_{\text{COR}}$ as a function of track momentum, for tracks with (a) $|\eta| < 0.6$, (b) $0.6 < |\eta| < 1.1$, (c) $1.8 < |\eta| < 1.9$, and (d) $1.9 < |\eta| < 2.3$.

The response measurement above used topological clustering at the EM scale, that is clusters were formed to measure energy but no corrections were applied to correct for expected effects like energy lost outside of the cluster or in uninstrumented material. It is also interesting to measure $\langle E/p \rangle_{\text{COR}}$ using LCW energies, which accounts for those effects by calibrating the energy based on the properties of the cluster such as energy density and depth in the calorimeter. Figure 53 shows these distributions for tracks with zero or more clusters and separately for tracks with one or more clusters. The calibration moves the mean

value of $\langle E/p \rangle_{\text{COR}}$ significantly closer to 1.0 as desired, but the discrepancy between data and simulation remains in the comparison that includes tracks with zero associated clusters. The agreement between data and simulation improves noticeably when at least one cluster is required, as this removes the contribution from the mismodeling of the zero fraction.

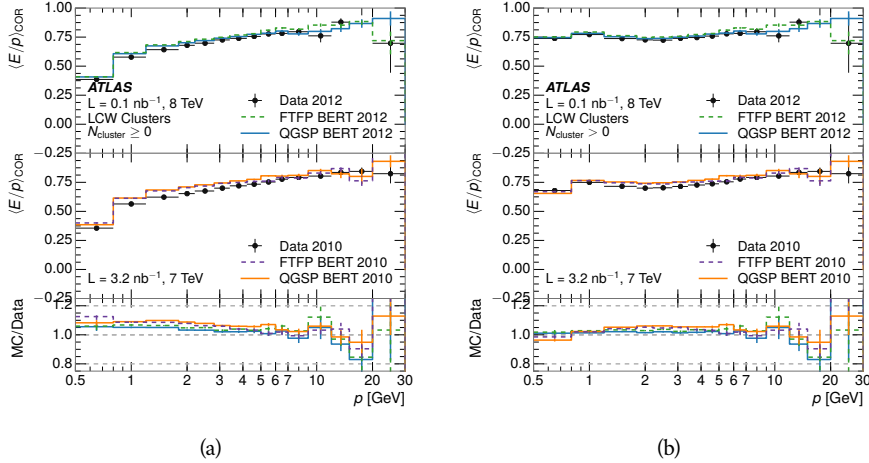


Figure 53: $\langle E/p \rangle_{\text{COR}}$ calculated using LCW-calibrated topological clusters as a function of track momentum for tracks with (a) zero or more associated topological clusters or (b) one or more associated topological clusters.

7.2.5 ADDITIONAL STUDIES

As has been seen in several measurements in previous sections, the simulation does not correctly model the chance of a low momentum hadron to reach the calorimeter. Because of the consistent discrepancy across pseudorapidity and interaction lengths, this can be best explained by incomplete understanding of hadronic interactions with the detector [44]. For example, a hadron that scatters off of a nucleus in the inner detector can be deflected through a significant angle and not reach the expected location in the calorimeter. In addition, these interactions can produce secondary particles that are difficult to model.

The requirement used throughout the previous sections on the number of hits in the TRT reduces these effects by preferentially selecting tracks that do not undergo nuclear interactions. It is interesting to check how well the simulation models tracks with low numbers of TRT hits, which selects tracks that are more likely to have undergone a hadronic interaction. Figure 54 compares the distributions with $N_{\text{TRT}} < 20$ to $N_{\text{TRT}} > 20$ for real and simulated particles¹. As expected, the tracks with fewer hits are poorly modeled in the simulation as $\langle E/p \rangle_{\text{COR}}$ differs by as much as 25% at low momentum. They also have significantly lower $\langle E/p \rangle_{\text{COR}}$ on average, because they are much less likely to have an associated cluster.

¹ The distribution with $N_{\text{TRT}} > 20$ is the same as shown in Figure 52 (a) and is included again here for the comparison.

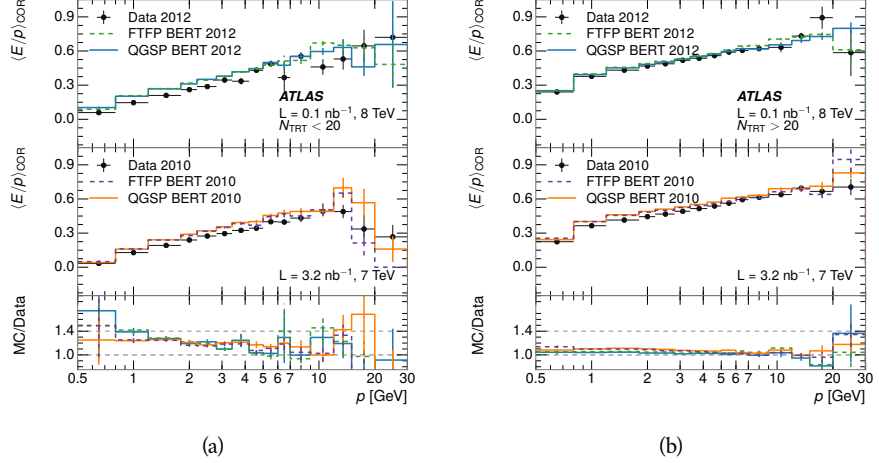


Figure 54: Comparison of the $\langle E/p \rangle_{\text{COR}}$ for tracks with (a) less than and (b) greater than 20 hits in the TRT.

Another interesting aspect of the simulation is the description of antiprotons at low momentum, where QGSP_BERT and FTFP_BERT have significant differences. This can be seen to have an effect in the inclusive response measurement when separated into positive and negative charge. The $\langle E/p \rangle_{\text{COR}}$ distributions for positive and negative particles are shown in Figure 55, where a small difference between QGSP_BERT and FTFP_BERT can be seen in the distribution for negative tracks. The figure also includes data, and the simulation overestimates $\langle E/p \rangle_{\text{COR}}$ mostly due to an underestimation in zero fraction. There is an approximately 5% difference between the 2010 and 2012 simulated events. The difference between positive and negative particles is demonstrated more clearly in Figure 56, which shows the E/p distribution in the two simulations separated by charge. There is a small difference around $E/p > 1.0$, which can be explained by the additional energy deposited by the annihilation of the antiproton in the calorimeter that is modeled well only in FTFP_BERT. This is also explored with data using identified antiprotons in Section 7.3.

The $\langle E/p \rangle$ results in previous sections have considered the electromagnetic and hadronic calorimeters together as a single energy measurement, to emphasize the total energy deposited for a given particle. However, the deposits in each calorimeter are measured separately and $\langle E/p \rangle$ can be constructed for each layer separately. As the layers are composed of different materials and are modeled separately in the detector geometry, confirmation that the simulation matches the data well in each layer adds confidence in both the description of hadronic interactions with the two different materials and also the geometric description of each.

The technique discussed in Section 7.2.3 for selecting MIPs in the electromagnetic calorimeter is also useful in studying deposits in the hadronic calorimeter. The tracks selected with the MIP requirements deposit almost all of their energy exclusively in the hadronic calorimeter. Figure 57 shows $\langle E/p \rangle_{\text{RAW}}^{\text{Had}}$, where RAW indicates that no correction has been applied for neutral backgrounds and

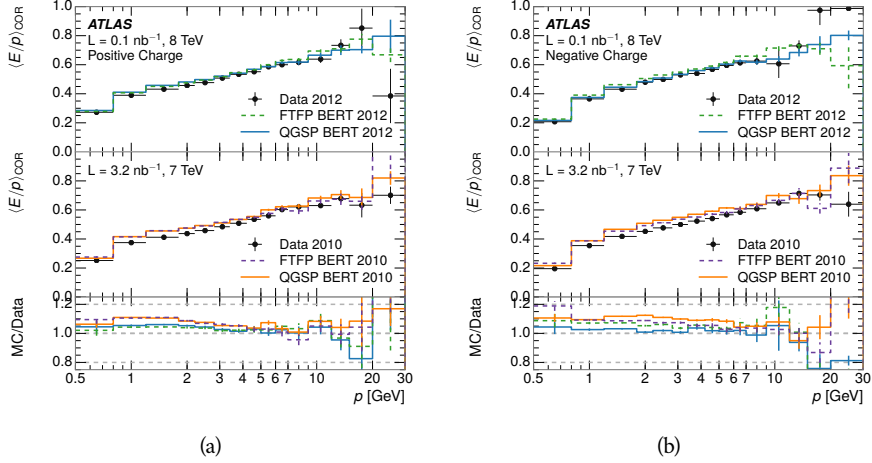


Figure 55: Comparison of the $\langle E/p \rangle_{\text{COR}}$ for (a) positive and (b) negative tracks as a function of track momentum for tracks with $|\eta| < 0.6$.

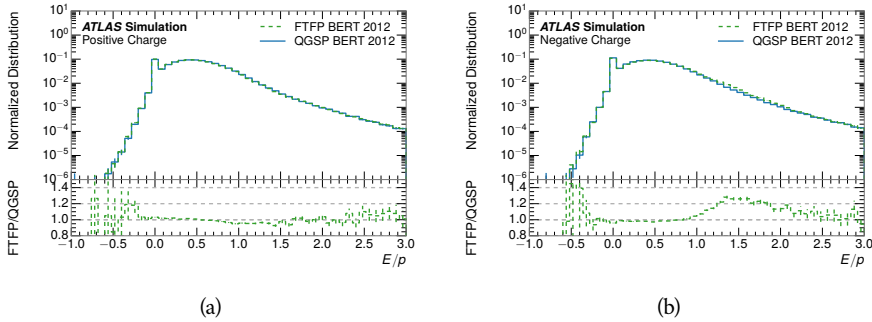


Figure 56: Comparison of the E/p distributions for (a) positive and (b) negative tracks with $0.8 < p/\text{GeV} < 1.2$ and $|\eta| < 0.6$, in simulation with the FTFP_BERT and QGSP_BERT physics lists.

Had indicates that only clusters for the hadronic calorimeter are included². The distributions are shown both for the original EM scale calibration and after LCW calibration. The data and simulation agree very well in this comparison, except in the lowest momentum bin where there is a 5% discrepancy that has already been seen in the measurements in Section 7.2.4.

A similar comparison can be made in the electromagnetic calorimeter by selecting particles which have no associated energy in the hadronic calorimeter. These results are measured in terms of $\langle E/p \rangle^{\text{EM}}_{\text{COR}}$, where EM designates that only clusters in the electromagnetic calorimeter are included and COR designates that the neutral background is subtracted as the neutral background is present in this case. Figure 58 shows the analogous comparisons to Figure 57 in the electromagnetic calorimeter. The $\langle E/p \rangle_{\text{COR}}$ values are lower on average in the EM calorimeter than in the hadronic calorimeter, which is an expected conse-

² The RAW and COR versions of $\langle E/p \rangle$ in this case are the same, as the neutral background is negligible in that calorimeter layer.

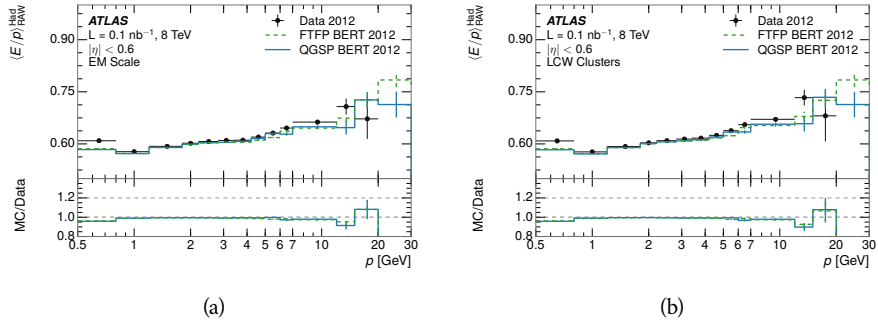


Figure 57: Comparison of the response of the hadronic calorimeter as a function of track momentum (a) at the EM-scale and (b) after the LCW calibration.

2823 sequence of their different material types (discussed in Section 5.4). In this case the
 2824 disagreement between data and simulation is more pronounced, with discrepancies
 2825 as high as 5% over a larger range of momenta. This level of discrepancy
 2826 indicates that the description of the electromagnetic calorimeter is actually the
 2827 dominant source of discrepancy in the combined distributions in Section 7.2.4.

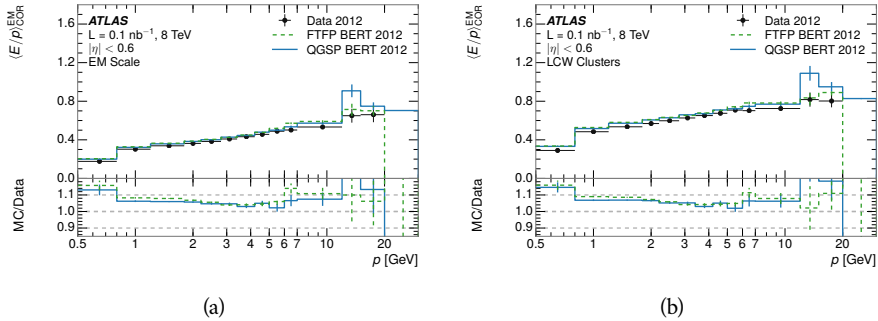


Figure 58: Comparison of the response of the EM calorimeter as a function of track momentum (a) at the EM-scale and (b) with the LCW calibration.

2828 7.3 IDENTIFIED PARTICLE RESPONSE

2829 The inclusive response measurement for hadrons can be augmented by measur-
 2830 ing the response for specific particle species. The simulation models each parti-
 2831 cle type separately, and understanding the properties of each is important in con-
 2832 straining the uncertainty on jets. In order to select and measure specific hadrons,
 2833 this section relies on the displaced decays of long-lived particles. Such decays
 2834 can be identified by reconstructing secondary vertices with a requirement on
 2835 mass. In particular, Λ , $\bar{\Lambda}$, and K_S^0 can be used to select a pure sample of protons,
 2836 antiprotons, and pions, respectively.

2837 7.3.1 DECAY RECONSTRUCTION

2838 The measurement of the response for identified particles uses the same selection
 2839 as for inclusive particles (Section 7.1.3) with a few additions. Each event used is
 2840 required to have at least one secondary vertex, as described in Section 6.1.3, and
 2841 the tracks are required to match to that vertex rather than the primary vertex.
 2842 Pions are selected from decays of $K_S^0 \rightarrow \pi^+ \pi^-$, which is the dominant decay for
 2843 K_S^0 to charged particles. Protons are selected from decays of $\Lambda \rightarrow \pi^- p$ and an-
 2844 tiprotons from $\bar{\Lambda} \rightarrow \pi^+ \bar{p}$, which are similarly the dominant decays of Λ and $\bar{\Lambda}$
 2845 to charged particles. The species of parent hadron in these decays is determined
 2846 by reconstructing the mass of the tracks associated to the secondary vertex. The
 2847 sign of the higher momentum decay particle can distinguish between Λ and $\bar{\Lambda}$,
 2848 which of course have the same mass, as the proton or antiproton is kinemati-
 2849 cally favored to have higher momentum. The proton or antiproton will carry
 2850 the higher momentum above 95% of the time. Examples of the reconstructed
 2851 masses used to select these decays are shown in Figure 59. The mass peaks in
 2852 data and both simulation models are very similar.

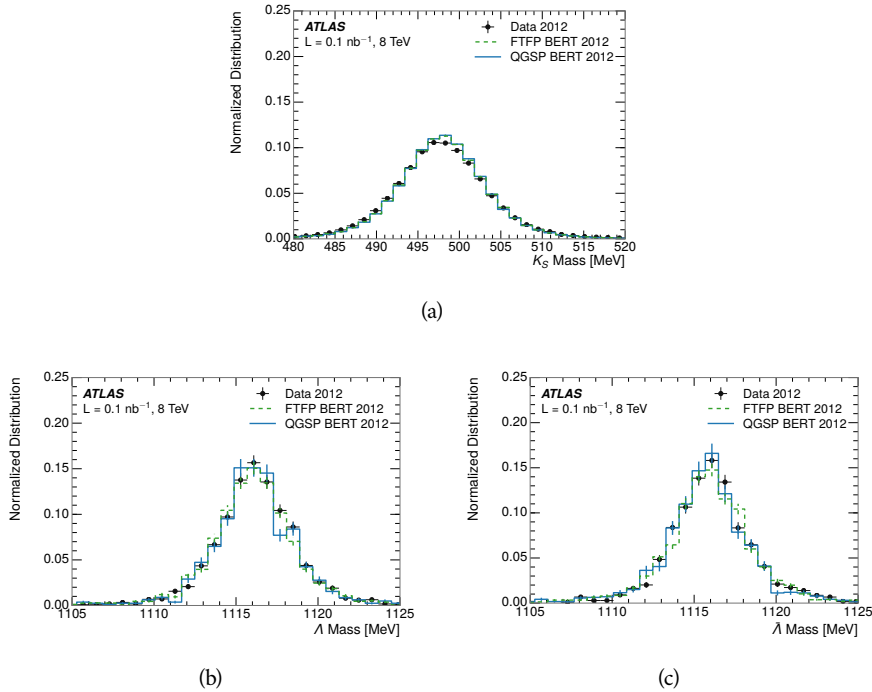


Figure 59: The reconstructed mass peaks of (a) K_S^0 , (b) Λ , and (c) $\bar{\Lambda}$ candidates.

2853 The dominant backgrounds for the identified particle decays are nuclear in-
 2854 teractions and combinatoric sources. These are suppressed by the kinematic re-
 2855 quirements on the tracks as well as an additional veto which removes candidates
 2856 that are consistent with both a Λ or $\bar{\Lambda}$ and a K_S^0 hypothesis, which is possible
 2857 because of the different assumptions on particle mass in each case [45]. After
 2858 these requirements, the backgrounds are found to be negligible compared to the
 2859 statistical errors on these measurements.

2860 73.2 IDENTIFIED RESPONSE

2861 With these techniques the E/p distributions are extracted in data and simulation
 2862 for each particle species and shown in Figure 60. These distributions are shown
 2863 for a particular bin of E_a ($2.2 < E_a/\text{GeV} < 2.8$), rather than p . E_a is the energy
 2864 available to be deposited in the calorimeter: for pions $E_a = \sqrt{p^2 + m_\pi^2}$, for pro-
 2865 tons $E_a = \sqrt{p^2 + m_p^2} - m_p$, and for antiprotons $E_a = \sqrt{p^2 + m_p^2} + m_p$. In the
 2866 pion case, the entire energy of the pion is deposited in the calorimeter, so E_a is
 2867 just the usual energy. For protons, the proton remains after depositing its energy
 2868 in the calorimeter, so its mass is not available and must be subtracted from E_a .
 2869 And for antiprotons, the antiproton constituents annihilate with the quarks in
 2870 the protons and neutrons of the calorimeter material, so it deposits its entire en-
 2871 ergy as well as an the additional energy from the annihilation; this extra energy
 2872 is equal to the mass of the antiproton and is added to the available energy. The
 2873 features of the E/p distributions are similar to the inclusive case, with a peak
 2874 around 0.5 at low momentum. The zero fraction is not as pronounced as in the
 2875 inclusive case. There is a small negative tail from noise and a large fraction of
 2876 tracks with zero energy from particles which do not reach the calorimeter. The
 2877 long positive tail is noticeably more pronounced for antiprotons because of the
 2878 additional energy generated by the annihilation of the antiproton with the mate-
 2879 rial of the detector, and the peak of the distribution is also increased for the same
 2880 reason. The simulation correctly captures these features, and the agreement be-
 2881 tween data and simulation is good to within the available statistical limitations.

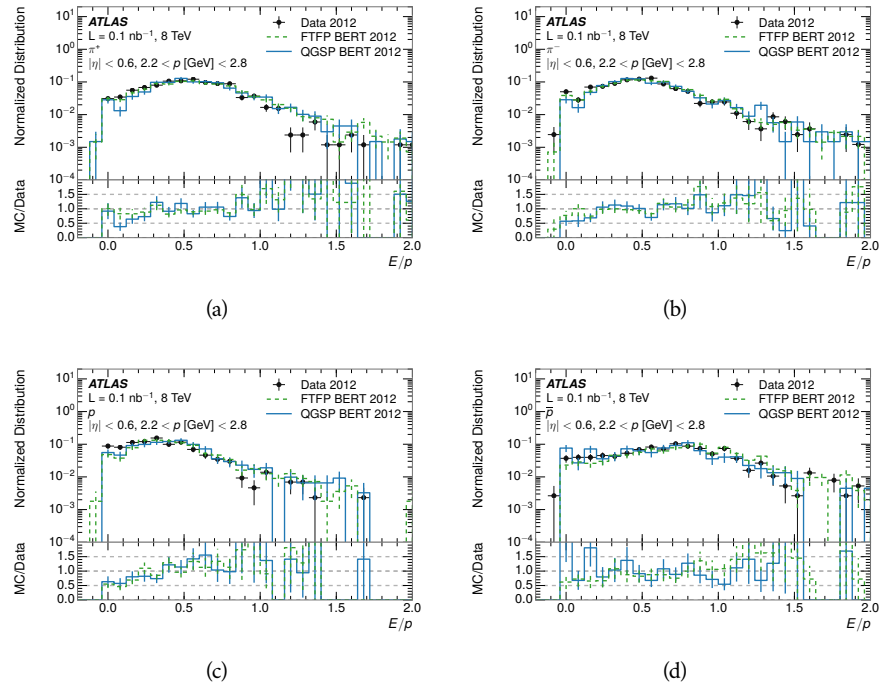


Figure 60: The E/p distribution for isolated (a) π^+ , (b) π^- , (c) proton, and (d) anti-proton tracks.

The zero fraction is further explored in Figure 61 for pions and protons in data and simulation. The simulation consistently underestimates the zero fraction independent of particle species, which implies that this discrepancy is not caused by the model of a particular species but rather a feature common to all. The zero fraction is larger for π^- than π^+ , which is evident in both data and simulation. However there is some suggestion that this increase in zero fraction leads to an even larger discrepancy in the modeling of π^- in simulation.

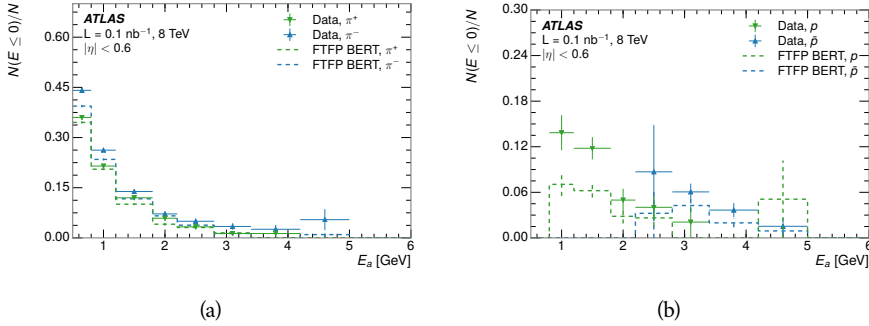


Figure 61: The fraction of tracks with $E \leq 0$ for identified (a) π^+ and π^- , and (b) proton and anti-proton tracks

It is also interesting to compare the response between the different particle species. One approach to do this is to measure the difference in $\langle E/p \rangle$ between two types, which has the advantage of removing the neutral background. These differences are shown in various combinations in Figure 62. The response for π^+ is greater on average than the response to π^- because of a charge-exchange effect which causes the production of additional neutral pions in the showers of π^+ [67]. This effect becomes less significant as the $\langle E/p \rangle$ increases, and the difference approaches zero. Both version of the simulation correctly model this trend. The response for π^+ is also greater on average than the response to p , because a large fraction of the energy of π^+ hadrons is converted to an electromagnetic shower [68, 69]. This effect is again reproduced by both simulations. The \bar{p} response, however, is significantly higher than the response to π^- because of the annihilation of the antiproton, but the difference decreases at higher energies where the additional energy has less relative importance. FTFP_BERT models this effect more accurately than QGSP_BERT because of their different descriptions of \bar{p} interactions with material.

It is also possible to remove the neutral background from these response distributions using the same technique as in Section 7.2.3. The technique is largely independent of the particle species and so can be directly applied to $\langle E/p \rangle$ for pions. The $\langle E/p \rangle_{\text{COR}}$ distributions for pions are shown in Figure 63, which are very similar to the inclusive results. The inclusive hadrons are comprised mostly of pions, so this similarity is not surprising. It is also possible to see the small differences between π^+ and π^- response here, where $\langle E/p \rangle_{\text{COR}}$ is higher on average for π^+ . The agreement between data and simulation is significantly worse for the π^- distributions than for the π^+ , with a discrepancy greater than 10% below 2-3 GeV.

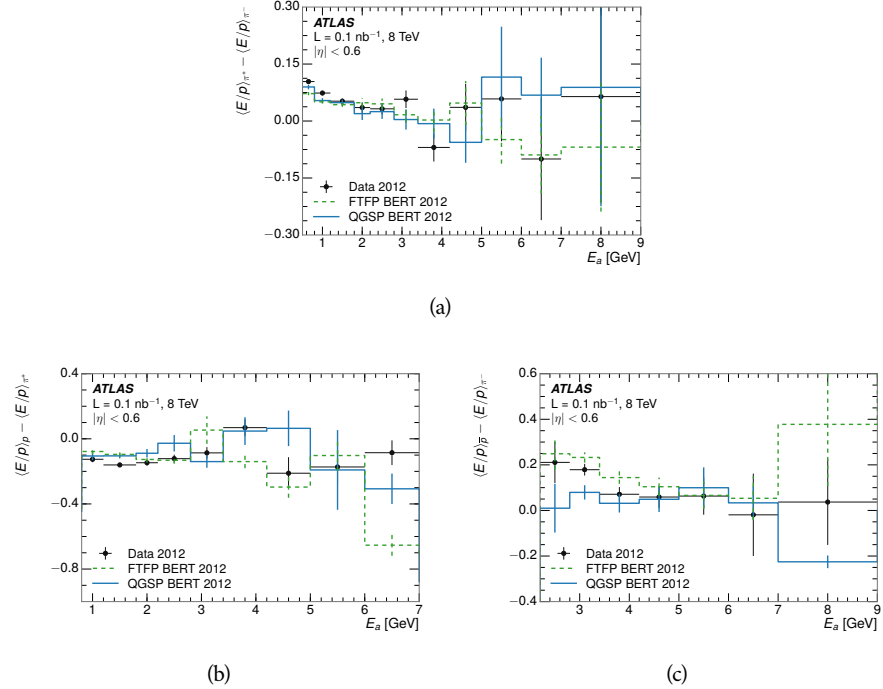


Figure 62: The difference in $\langle E/p \rangle$ between (a) π^+ and π^- (b) p and π^+ , and (c) \bar{p} and π^- .

2915 7.3.3 ADDITIONAL SPECIES IN SIMULATION

2916 The techniques above provide a method to measure the response separately for
 2917 only pions and protons. However the hadrons which forms jets include a number
 2918 of additional species such as kaons and neutrons. The charged kaons are an im-
 2919 portant component of the inclusive charged hadron distribution, which is com-
 2920 prised of roughly 60-70% pions, 15-20% kaons, and 5-15% protons [44]. These
 2921 fractions vary depending on the production mechanism, and the ranges are in-
 2922 dicative of the variations between different events. These are difficult to measure
 2923 in data at the ATLAS detector, as the particles which decay to kaons such as ϕ and
 2924 D mesons have shorter lifetimes and are comparatively rare. These properties
 2925 make it impractical to identify a sufficient number of decays to make statistically
 2926 meaningful measurements. The simulation of these particles includes noticeable
 2927 differences in response between species at low energies, which are shown in Fig-
 2928 ure 64 for FTFP_BERT. The significant differences in response between protons
 2929 and antiprotons below 1 GeV are accounted for above in the definitions of E_a .

2930 7.4 SUMMARY

2931 These various measurements of calorimeter response shown above for data and
 2932 simulation illuminate the accuracy of the simulation of hadronic interactions at
 2933 the ATLAS detector. The results were obtained using 2010 and 2012 data at 7
 2934 and 8 TeV, but reflect the most current understanding of the detector alignment

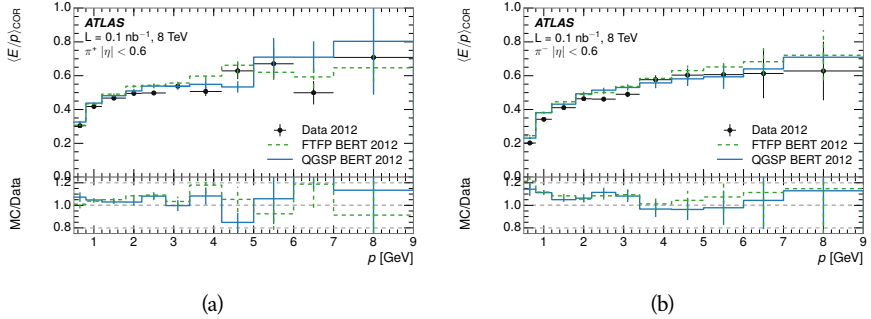


Figure 63: $\langle E/p \rangle_{\text{COR}}$ as a function of track momentum for (a) π^+ tracks and (b) π^- tracks.

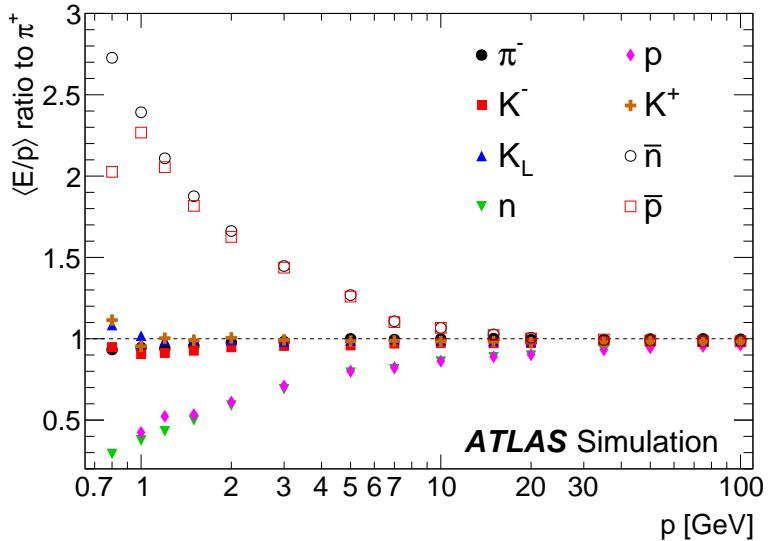


Figure 64: The ratio of the calorimeter response to single particles of various species to the calorimeter response to π^+ with the physics list FTFP_BERT.

and geometry. A number of measurements focusing on a comparison between protons and antiprotons suggest that FTFP_BERT models those interaction more accurately than QGSP_BERT. These measurements, among others, were the motivation to switch the default Geant4 simulation from QGSP_BERT to FTFP_BERT for all ATLAS samples.

Even with these updates, there are a number of approximately 5% discrepancies in response between the data and simulation. The differences result mostly from a difference in the modeling of the zero fraction, which is most significant at low energies. The difference in response without the zero fraction are primarily in the electromagnetic calorimeter, while the modeling of the hadronic calorimeter is accurate. At higher momenta the simulation of hadronic interactions is very consistent with data. Chapter 8 discusses how to use these observed differences to constrain the jet energy scale and its associated uncertainties.

2948

2949 JET ENERGY RESPONSE AND UNCERTAINTY

2950 8.1 MOTIVATION

2951 As jets form a major component of many physics analyses at ATLAS, it is crucial
 2952 to carefully calibrate the measurement of jet energies and to derive an uncer-
 2953 tainty on that measurement. These uncertainties are often the dominant sys-
 2954 tematic uncertainty in high-energy analyses at the LHC. Jet balance techniques,
 2955 as discussed in Section 6.4.3, provide a method to constrain the JES and its uncer-
 2956 tainty in data, and provide the default values used for ATLAS jet measurements at
 2957 most energies [70]. These techniques are limited by their reliance on measuring
 2958 jets in data, so they are statistically limited in estimating the jet energy scale at the
 2959 highest jet energies. This chapter presents another method for estimating the jet
 2960 energy scale and its uncertainty which builds up a jet from its constituents and
 2961 thus can be naturally extended to high jet momentum. Throughout this chapter
 2962 the jets studied are simulated using Pythia8 with the CT10 parton distribution
 2963 set [71] and the AU2 tune [48], and corrections are taken from the studies includ-
 2964 ing data and simulation in Chapter 7.

2965 As described in Section 6.4, jets are formed from topological clusters of energy
 2966 in the calorimeters using the anti- k_t algorithm. These clusters originate from a
 2967 diverse spectrum of particles, in terms of both species and momentum, leading to
 2968 significantly varied jet properties and response between jets of similar produced
 2969 momentum. Figure 65 shows the momentum and particle distributions of sim-
 2970 ultated particles within jets at a few examples energies. Each bin for each distri-
 2971 bution shows the fraction of jet constituents of that particle type and that truth
 2972 energy for a jet of the specified energy. These show that majority of particles in
 2973 jets are charged pions and photons, and the charged pions constituent carry the
 2974 highest energies on average. The figure also demonstrates that the majority of
 2975 the particles in a jet have much lower momentum than the jet itself; for example
 2976 in 90-100 GeV jets less than 1% of particles have energies above 20 GeV. The
 2977 E/p measurements provide a thorough understanding of the dominant particle
 2978 content of jets, the charged hadrons.

2979 8.2 UNCERTAINTY ESTIMATE

2980 A correct modeling of jets in the data by simulation requires that both the parti-
 2981 cle production inside jets as well as the response of the calorimeter to particles
 2982 are correctly modeled. Chapter 7 showed that the simulation does not perfectly
 2983 model the calorimeter response, and provided measurements that can be used
 2984 to correct for discrepancies. To determine the corrections appropriate for jets,
 2985 that is to evaluate a jet energy response, the simulated jet energies are compared

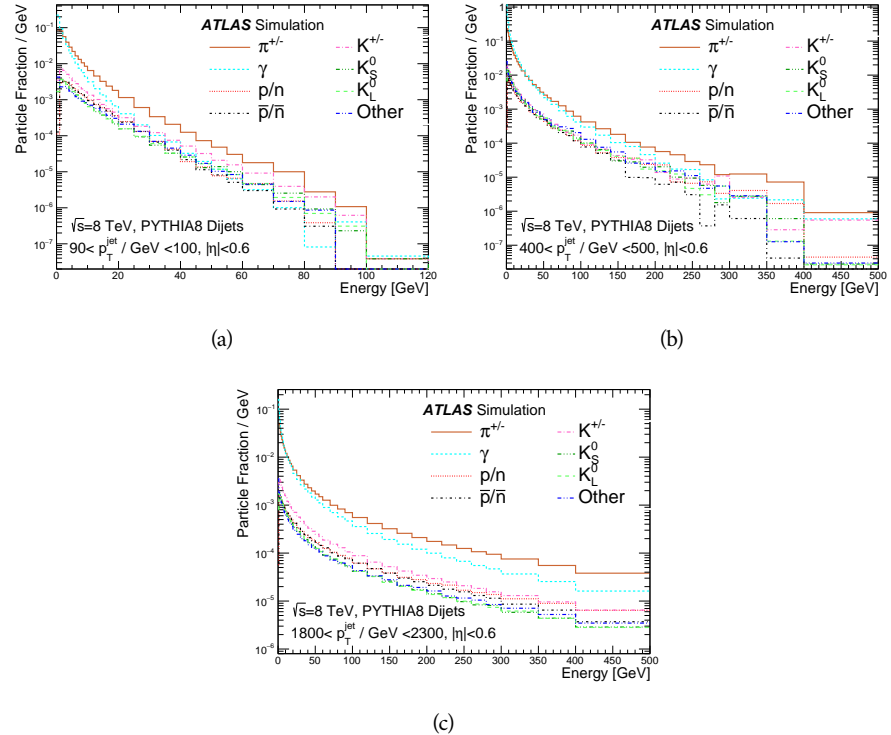


Figure 65: The spectra of true particles inside anti- k_t , $R = 0.4$ jets with (a) $90 < p_T/\text{GeV} < 100$, (b) $400 < p_T/\text{GeV} < 500$, and (c) $1800 < p_T/\text{GeV} < 2300$.

2986 to a corrected jet built up at the particle level. Each cluster in a jet is associated
 2987 to the truth particle which deposited it, and the energy in that cluster is then
 2988 corrected for a number of effects based on measurements in data. The primary
 2989 corrections come from the single hadron response measurements in addition to
 2990 response measured using the combined test beam which covers higher momen-
 2991 tum particles [72]. These corrections include both a shift (Δ), in order to make
 2992 the simulation match the average response in data, and an uncertainty (σ) asso-
 2993 ciated with the ability to constrain the difference between data and simulation.
 2994 Some of the dominant sources of uncertainty are itemized in Table 7 with typi-
 2995 cal values, and the full list considered is described in detail in the associated pa-
 2996 per [44]. These uncertainties cover differences between the data and simulation
 2997 in the modeling of calorimeter response to a given particle. The typical values
 2998 are listed as ranges to show the variation over momentum and pseudorapidity.
 2999 For the in situ E/p term, for example, Δ corresponds to the difference between
 3000 data and simulation for $\langle E/p \rangle_{\text{COR}}$ at the LCW scale (shown in Figure 53 (b)) and
 3001 σ is the uncertainty on that difference including the statistical uncertainties of
 3002 both the data and simulated events. No uncertainties are added for the differ-
 3003 ence between particle composition of jets in data and simulation, as this method
 3004 focuses on providing a response correction for discrepancies of particle interac-
 3005 tions rather than differences in particle composition.

3006 From these terms, the jet energy scale and uncertainty is built up from in-
 3007 dividual energy deposits in simulation. Each uncertainty term is treated inde-

Abbrev.	Description	Δ (%)	σ (%)
In situ E/p	The comparison of $\langle E/p \rangle_{\text{COR}}$, at the LCW scale, as described in Chapter 7 with statistical uncertainties from 500 MeV to 20 GeV.	0-3	1-5
CTB	The main $\langle E/p \rangle$ comparison uncertainties, binned in p and $ \eta $, as derived from the combined test beam results, from 20 to 350 GeV [72].	0-3	1-5
E/p Zero Fraction	The difference in the zero-fraction between data and MC simulation from 500 MeV to 20 GeV.	5-25	1-5
E/p Threshold	The uncertainty in the EM calorimeter response from the potential mismodeling of threshold effects in topological clustering.	0	0-10
Neutral	The uncertainty in the calorimeter response to neutral hadrons based on studies of physics model variations.	0	5-10
K_L	An additional uncertainty in the response to neutral K_L in the calorimeter based on studies of physics model variations.	0	20
E/p Misalignment	The uncertainty in the p measurement from misalignment of the ID.	0	1
Hadrons, $p > 350$ GeV	An energy independent uncertainty for all particles above the energy range or outside the longitudinal range probed with the combined test beam.	0	10

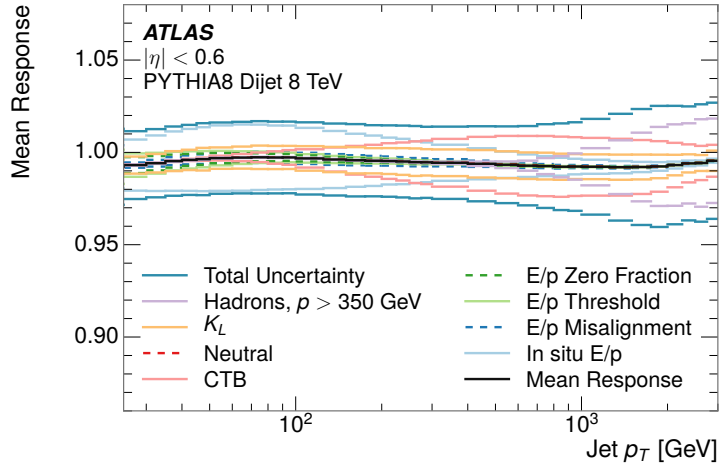
Table 7: The dominant sources of corrections and systematic uncertainties in the JES estimation technique, including typical values for the correcting shift (Δ) and the associated uncertainty (σ).

3008 pendently, and is taken to be gaussian distributed. The resulting scale and un-
 3009 certainty is shown in Figure 66, where the mean response is measured relative
 3010 to the calibrated energy reported by simulation. The mean response is slightly
 3011 below one, indicating that the simulation slightly overestimates the calorime-
 3012 ter response on average, and this response is relatively constant as a function
 3013 of the jet p_T . The dominant uncertainties come from the statistical uncertain-
 3014 ties on the E/p measurements at lower energies and the additional uncertainty
 3015 for out of range measurements at higher energies. Combined the resulting un-
 3016 certainty ranges from between 1.5% at low momentum and pseudorapidity to
 3017 as much as 4% at higher momentum and pseudorapidity. The total uncertainty
 3018 from this method at intermediate jet energies is comparable to other simulation-
 3019 based methods [73] and is about twice as large as in-situ methods using data [70].
 3020 This method is the only one which provides an estimation above 1.8 TeV, how-
 3021 ever, and so is still a crucial technique in analyses that search for very energetic
 3022 jets.

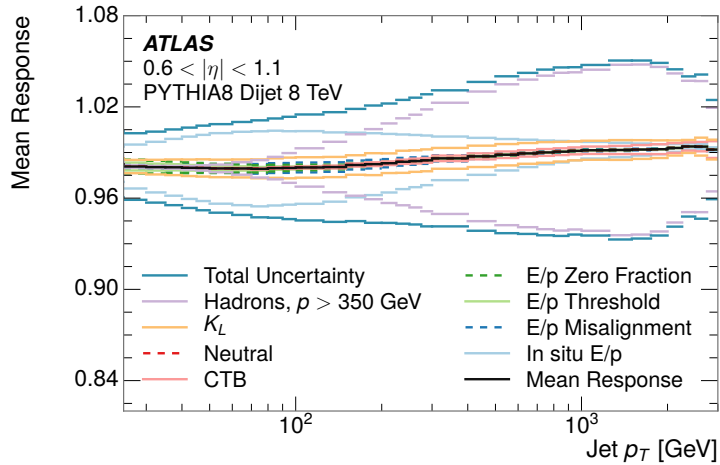
3023 These techniques can also be used to measure the correlation between bins of
 3024 average reconstructed jet momentum across a range of p_T and $|\eta|$, where cor-
 3025 relations are expected because of a similarity in particle composition at similar
 3026 energies. Figure 67 shows these correlations, where the uncertainties on jets in
 3027 neighboring bins are typically between 30% and 60% correlated. The uncertainty
 3028 on all jets becomes significantly correlated at high energies and larger pseudora-
 3029 pidities, when the uncertainty becomes dominated by the single term reflecting
 3030 out of range particles.

3031 8.3 SUMMARY

3032 The technique described above provides a jet energy scale and uncertainty by
 3033 building up jet corrections from the energy deposits of constituent particles. The
 3034 E/p measurements are crucial in providing corrections for the majority of parti-
 3035 cles in the jets. The uncertainty derived this way is between 2 and 5% and is about
 3036 twice as large at corresponding momentum than jet balance methods. However
 3037 this is the only uncertainty available for very energetic jets using 2012 data and
 3038 simulation, and repeating this method with Run 2 data and simulation will be
 3039 important in providing an uncertainty for the most energetic jets in 13 TeV col-
 3040 lisions.



(a)



(b)

Figure 66: The JES response uncertainty contributions, as well as the total JES uncertainty, as a function of jet p_T for (a) $|\eta| < 0.6$ and (b) $0.6 < |\eta| < 1.1$.

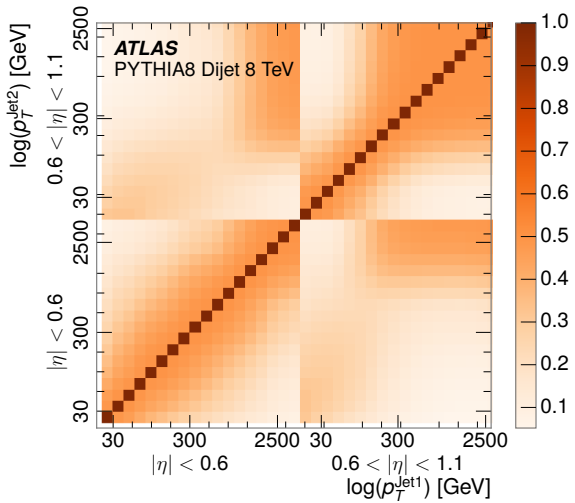


Figure 67: The correlations between bins of average reconstructed jet momentum as a function of jet p_T and $|\eta|$ for jets in the central region of the detector.

3041

PART IV

3042

SEARCH FOR LONG-LIVED PARTICLES

3043

3044

3045 LONG-LIVED PARTICLES IN ATLAS

3046 As discussed in Section 2.6, various limitations in the SM suggest a need for new
 3047 particles at the TeV scale. A wide range of extensions to the Standard Model
 3048 predict that these new particles can have lifetimes greater than approximately
 3049 one-hundredth of a nanosecond. These include theories with universal extra-
 3050 dimensions [74, 75], with new fermions [76], and with leptoquarks [77]. As dis-
 3051 cussed in Section 3.4, many SUSY theories also produce these LLPs, in both R-
 3052 Parity violating [78–80] and R-Parity conserving [81–84] formulations. Split
 3053 supersymmetry [12, 13], for example, predicts long-lived gluinos with O(TeV)
 3054 masses. This search focuses specifically on the SUSY case, but many of the results
 3055 are generic to any model with LLPs.

3056 Long-lived gluinos or squarks carry color-charge and will thus hadronize into
 3057 color neutral bound states called R-Hadrons. These are composit particles like
 3058 the known hadrons but with one supersymmetric constituent, for example $\tilde{g}q\bar{q}$
 3059 and $\tilde{q}\bar{q}$. In this hadronization process, the gluino can acquire an electric charge.
 3060 Gluino pair production, $pp \rightarrow \tilde{g}\tilde{g} + X$, where X denotes the proton remnants,
 3061 has the largest cross sectional increase with the increase in energy to 13 TeV,
 3062 and so this search uses gluino R-Hadrons as its benchmark model. The features,
 3063 techniques, and cross section limits discussed here are all largely independent
 3064 of the model. Planned future updates will extend the case to include additional
 3065 refinements for squark and chargino models, but the current method covers any
 3066 long-lived, charged, massive particle.

3067 9.1 EVENT TOPOLOGY

3068 R-parity conserving SUSY models predict that gluinos will be produced in pairs
 3069 at the LHC, through the processes shown in Figure 68, where the quarks and
 3070 gluons are proton constituents. The gluon-initiated mode dominates for the col-
 3071 lision energy and gluino masses considered for this search. During their produc-
 3072 tion, the long-lived gluinos hadronize into color singlet bound states including
 3073 $\tilde{g}q\bar{q}$ and even $\tilde{g}g$ [85]. The probability to form the gluon-only bound states is
 3074 a free parameter usually taken to be 0.1, and 90% of the remaining R-Hadrons
 3075 form meson states [86]. The charged and neutral states are approximately equally
 3076 likely for mesons, so the R-Hadrons will be charged roughly 50% of the time.

3077 These channels produce R-Hadrons with large p_T , but lower on average than
 3078 their mass, so that they typically propagate with $0.2 < \beta < 0.9$ [86]. Figure 69
 3079 shows the generated p_T and β distributions for a simulated example of R-Hadrons
 3080 with a mass of 1600 GeV. The mean p_T is roughly half of the mass at 800 GeV,
 3081 and so β peaks around 0.5. The fragmentation that produces that hadrons is
 3082 very hard, so the jet structure around the R-Hadron is minimal, with less than 5
 3083 GeV of summed particle momentum expected in a cone of $\Delta R < 0.25$ around

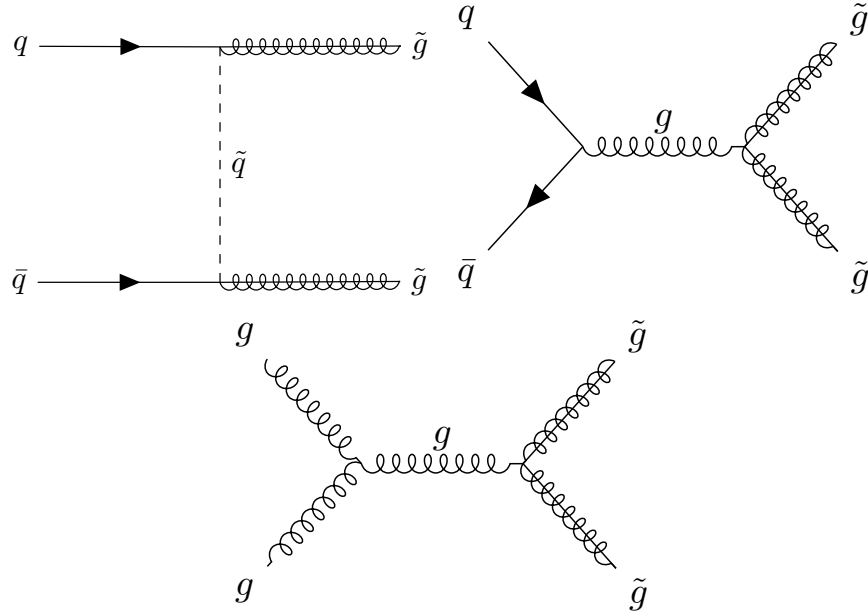


Figure 68: The processes which contribute to gluino pair production in the proton proton collisions, where the quarks and gluons are proton constituents.

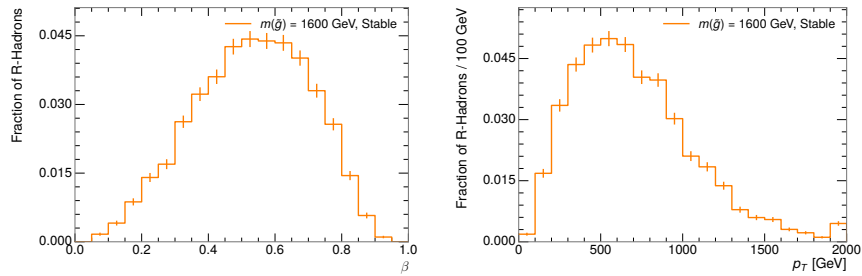


Figure 69: The generated p_T and β distributions for R-Hadrons with $M = 1600$ GeV.

3084 the R-Hadron [86]. After hadronization, depending on the gluino lifetime, the
 3085 R-Hadrons then decay into hadrons and a LSP [85].

3086 In summary, the expected event for pair-produced long-lived gluinos is very
 3087 simple: two isolated, high-momentum R-Hadrons that propagate through the
 3088 detector before decaying to jets. The observable features of such events depend
 3089 strongly on the interaction of the R-Hadron with the material of the detector
 3090 and also its lifetime. Section 9.1.1 describes the interactions of R-Hadrons which
 3091 reach the various detector elements in ATLAS and Section 9.1.2 provides a sum-
 3092 mary of the observable event descriptions for R-Hadrons of various lifetimes.

3093 9.1.1 DETECTOR INTERACTIONS

3094 Although the distribution of decay times can be parametrized with a single pa-
 3095 rameter, τ , the time before individual R-Hadrons decay follows an exponential
 3096 distribution, leading to a range of decay times for any individual lifetime. This is

further confounded by the distribution of β as well as η , so that each R-Hadron propagates at a different velocity and travels a different distance before reaching each detector element. Therefore, the lifetime-dependent event topologies must be discussed as an average, and all times referred to within this section will assume $\beta = 0.5$, an $\eta = 0$, and that the particle decays after a time equal to its lifetime. Table 8 lists the distances of various subdetectors and the time after which a LLP will arrive at that subdetector for a few values of β and with $\eta = 0$.

Subdetector	Distance	τ at $\beta = 0.3$	τ at $\beta = 0.5$	τ at $\beta = 0.7$
Pixel	3.1 cm	0.35 ns	0.20 ns	0.15 ns
Calorimeter	1.5 m	17 ns	10 ns	7.2 ns
Muon System	5 m	56 ns	33 ns	24 ns

Table 8: The radial distances of each of the subdetectors and example arrival times for an R-Hadron with $\eta = 0$ and the specified β .

After approximately 0.2 ns, the R-Hadron reaches the first layer of the pixel detector. If charged, it deposits energy into the material through repeated single collisions that result in ionization of the silicon substrate [3]. Because of its comparatively low β , the ionization energy can be significantly greater than expected for SM particles because the most-probable energy loss grows significantly as β decreases [3]. This large ionization can be measured through the ToT read out from the pixel detector as described in Section 6.1.2. Large ionization in the inner detector is one of the major characteristic features of LLPs. The particle propagates through all four layers of the pixel detector, where each provides a measurement of ionization, and then exits the pixel detector at 0.8 ns.

Throughout the next few nanoseconds, the R-Hadron propagates through the remainder of the inner detector. A charged R-Hadron will provide hits in each of these systems as would any other charged particle, and can be reconstructed as a track. The track reconstruction provides a measurement of its trajectory and thus its p as described in Section 6.1. The large p_T , shown in Figure 69, is another characteristic feature of massive particles produced at the LHC.

As of roughly 10 ns, the R-Hadron enters the calorimeter where it interacts hadronically with the material. Because of its large mass and p , the R-Hadron does not typically stop in the calorimeter, but rather deposits a small fraction of its energy through repeated interactions with nucleons. The probability of interaction between the gluino itself and a nucleon is low because the cross section drops off with the inverse square of its mass, so the interactions are primarily governed by the light constituents [87]. Each of these interactions can potentially change that quark content and thus change the sign of the R-Hadron, so that the charge at exit is typically uncorrelated with the charge at entry [86]. The total energy deposited in the calorimeters during the propagation is small compared to the kinetic energy of the R-Hadron, around 20-40 GeV, so that E/p is typically less than 0.1 [86].

Then, 30 ns after the collision, it reaches the muon system, where it again ionizes in the material if charged and can be reconstructed as a muon track. Because of the charge-flipping interactions in the calorimeter, this track may have

3135 the opposite sign of the track reconstructed in the inner detector, or there may
 3136 be a track present when there was none in the inner detector and vice-versa
 3137 for those which are detected. The propagation time at the typically lower β re-
 3138 sults in a significant delay compared to muons, and a delay over 25 ns causes
 3139 the muon signal to be lost outside the readout window. Between the probabili-
 3140 ty of charge-flip and late arrival, there is a significant chance that an R-Hadron
 3141 which was produced with a charge will not be identified as a muon. When it is
 3142 reconstructed as a muon, that delay can be assessed in terms of a time-of-flight
 3143 measurement, which is another characteristic feature of R-Hadrons.

3144 9.1.2 LIFETIME DEPENDENCE

3145 The above description assumed a lifetime long enough for the R-Hadron to exit
 3146 the detector, which through this search is referred to as [VLL](#), as the particle may
 3147 decay after exiting the detector. There are several unique signatures at shorter
 3148 lifetimes where the R-Hadron decays in various parts of the inner detector; these
 3149 lifetimes are referred to as [LL](#).

3150 The shortest case where the R-Hadron is considered [LL](#) is for lifetimes around
 3151 0.01 ns, where the particle decays before reaching any of the detector elements.
 3152 Although the R-Hadrons are produced opposite each other in the transverse
 3153 plane, each R-Hadron decays to a jet and an [LSP](#). The two decays are uncorrelated,
 3154 so the two [LSPs](#) carry different momenta and in different directions. And, since
 3155 the [LSPs](#) are not measured, the produced jets can be significantly imbalanced in
 3156 the transverse plane which results in large missing energy. That missing energy
 3157 can be used to trigger candidate events, and provides the most efficient trigger
 3158 option for shorter lifetimes. Additionally, the precision of the tracking system
 3159 allows the displaced vertex of the R-Hadron decay to be reconstructed from the
 3160 charged particles in the jet. The distance of that vertex from the interaction point
 3161 can be used to distinguish R-Hadron decays from other processes. Figure 70
 3162 shows a schematic diagram of an example R-Hadron event with such a lifetime.
 3163 The diagram is not to scale, but instead illustrates the detector interactions in the
 3164 pixel detector, calorimeters, and muon system. It includes a representation of a
 3165 charged R-Hadron and a neutral R-Hadron, as well as the [LSPs](#) and jets (shown as
 3166 charged hadrons) produced in the decay. Neutral hadrons may also be produced
 3167 in the decay but are not depicted. Previous searches on ATLAS have used the
 3168 displaced vertex to target [LLP](#) decays [88].

3169 The next distinguishable case occurs at lifetimes greater than 0.1 ns but less
 3170 than 10 ns, where the R-Hadron forms a partial track in the inner detector. This
 3171 forms a unique signature of a disappearing track. Two examples of such an event
 3172 are illustrated in Figure 71 and Figure 72, which show the short track in the inner
 3173 detector. The decay distance must be sufficiently long that it reaches the [SCT](#), or
 3174 else to track will not be reconstructed at all. Depending on the mass difference
 3175 between the R-Hadron and the [LSP](#), the decay products will either be a single, soft
 3176 charged hadron and a [LSP](#) (Figure 71), or a jet and a [LSP](#) (Figure 72). A dedicated
 3177 search on ATLAS used the disappearing track signature in the former case to
 3178 search for [LLP](#) in Run 1 [89].

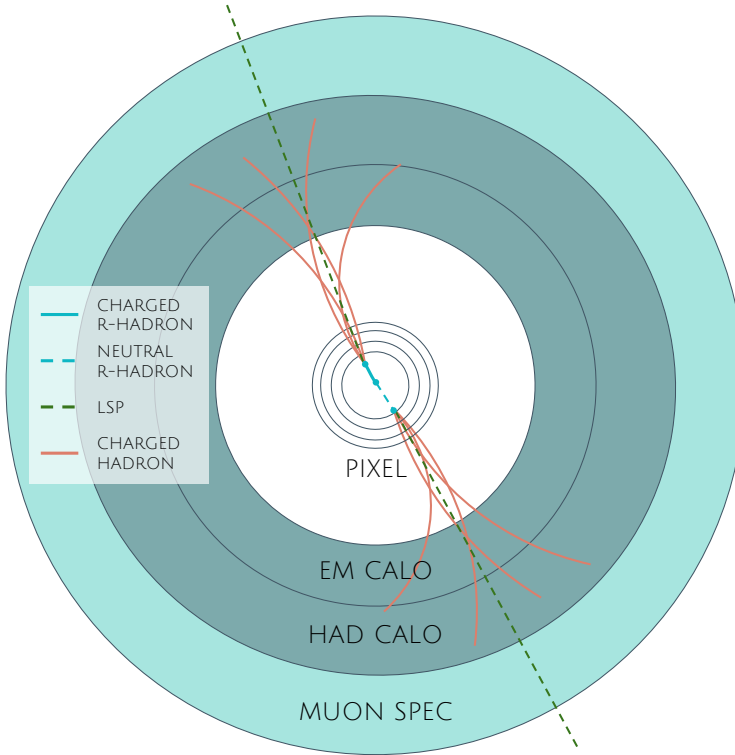


Figure 70: A schematic diagram of an R-Hadron event with a lifetime around 0.01 ns.

The diagram includes one charged R-Hadron (solid blue), one neutral R-Hadron (dashed blue), LSPs (dashed green) and charged hadrons (solid orange). The pixel detector, calorimeters, and muon system are illustrated but not to scale.

In the latter case, the decays result in an event-level signature of up to two high- p tracks, jets, and significant missing energy. The missing energy has the same origin as in the case of 0.01 ns lifetimes, from the decay to unmeasured particles, and again can be large. The high- p tracks will also have the characteristically high-ionization of massive, long-lived particles in the Pixel detector. Figure 72 shows how the jets from the decay can still be reconstructed in the calorimeter. Several previous searches on ATLAS from Run 1 have used this signature to search for R-Hadrons [90, 91], including a dedicated search for LL particles [92].

If the lifetime is longer than several nanoseconds, in the range of 10-30 ns, the R-Hadron decay can occur in or after the calorimeters, but prior to reaching the muon system. In the case that the decays occur early enough within the calorimeters that the decay can be measured, the event topology is very similar to the above with jets originating in the inner detector. If the decay occurs after the calorimeter, jets may not be reconstructed at all. The events still often have large missing energy, although it is generated through different mechanisms, and so the same search strategy can be used. The R-Hadrons do not deposit much energy in the calorimeters, so a neutral R-Hadron will not enter into the missing energy calculation. A charged R-Hadron opposite a neutral R-Hadron will thus generate significant missing energy, and close to 50% of pair-produced R-Hadron events fall into this category. If both R-Hadrons are neutral then the

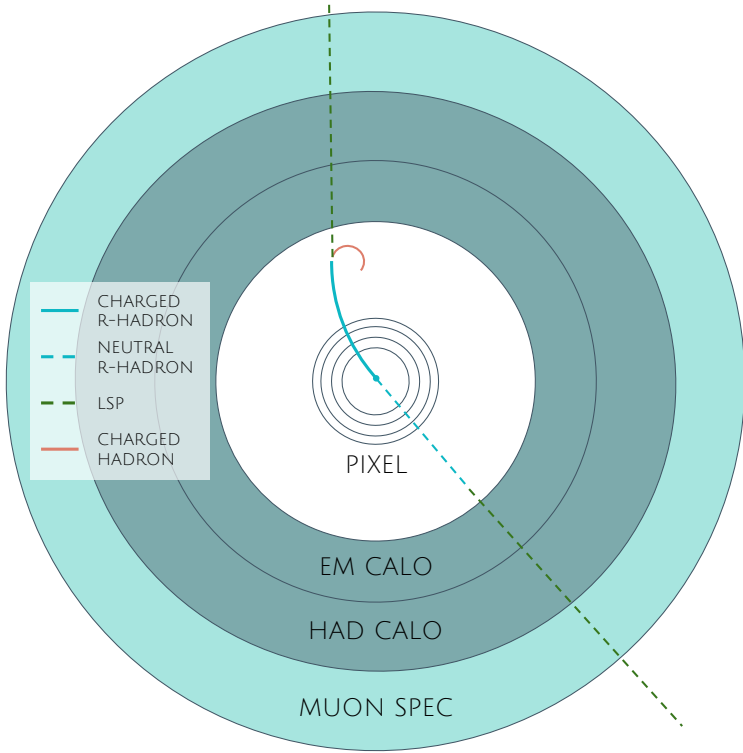


Figure 71: Schematic diagram of an R-Hadron event with a lifetime around 5 ns, where the masses of the R-Hadron and LSP are nearly degenerate. The diagram includes charged R-Hadrons (solid blue), neutral R-Hadrons (dashed blue), LSPs (dashed green) and charged hadrons (solid orange). The pixel detector, calorimeters, and muon system are illustrated but not to scale.

missing energy will be low because neither is detected. Two charged R-Hadrons will also result in low missing energy because both are reconstructed as tracks and will balance each other in the transverse plane. A small fraction of the time, one of the charged R-Hadron tracks may fail quality requirements and thus be excluded from the missing energy calculation and again result in significant missing energy. Figure 73 illustrates another example event with one charged R-Hadron which decays after approximately 20 ns, and shows how the jets from the decay might not be reconstructed.

The longest lifetimes, the VLL case, has all of the features of the 30-50 ns case but with the addition of muon tracks for any R-Hadrons that exit the calorimeter with a charge. That muon track can provide additional information from time-of-flight measurements to help identify LLPs. An example of the event topology for one charged and one neutral VLL R-Hadron is shown in Figure 74. Some searches on ATLAS have included this information to improve the search reach for VLL particles [91, 93].

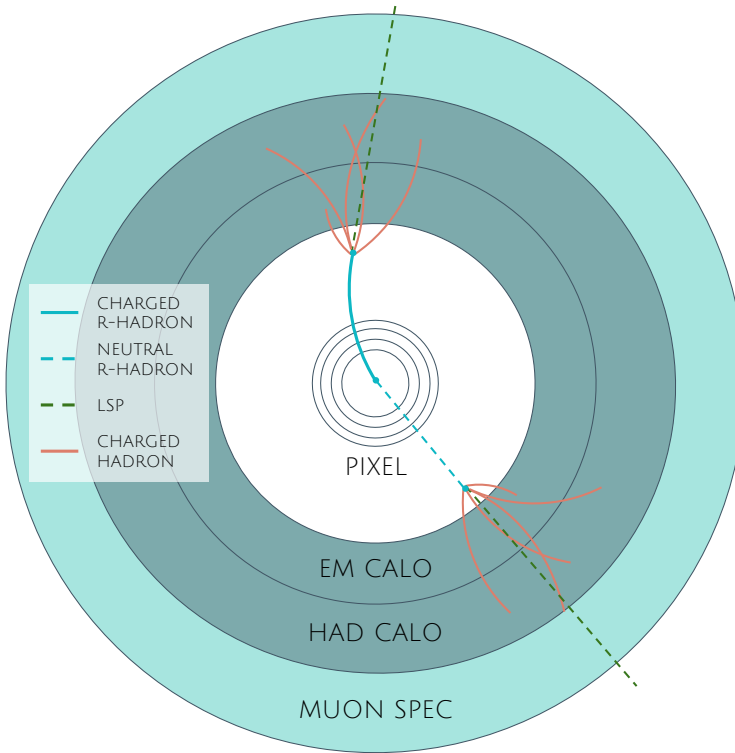


Figure 72: Schematic diagram of an R-Hadron event with a lifetime around 5 ns, where the masses of the R-Hadron and LSP are not degenerate. The diagram includes charged R-Hadrons (solid blue), neutral R-Hadrons (dashed blue), LSPs (dashed green) and charged hadrons (solid orange). The pixel detector, calorimeters, and muon system are illustrated but not to scale.

3214 9.2 SIMULATION

3215 All of the event topologies discussed above are modeled by simulations of R-
 3216 Hadron events in the ATLAS detector. A large number of such samples are
 3217 generated to determine efficiencies, to measure expected yields, and to estimate
 3218 uncertainties. The primary interaction, pair production of gluinos with masses
 3219 between 400 and 3000 GeV, is simulated using Pythia 6.4.27 [5] with the
 3220 AUET2B [94] set of tuned parameters for the underlying event and the CTEQ6L1 [71]
 3221 PDF set. The simulated interactions include a modeling of pileup by adding sec-
 3222 ondary, minimum bias interactions from both the same (in-time pileup) and
 3223 nearby (out-of-time pileup) bunch crossings. This event generation is then aug-
 3224 mented with a dedicated hadronization routine to hadronize the long-lived gluinos
 3225 into final states with R-Hadrons [95], with the probability to form a gluon-gluino
 3226 bound set at 10% [96].

3227 The cross sections used for these processes are calculated at NLO in the strong
 3228 coupling constant with a resummation of soft-gluon emmision at next-to-leading
 3229 logarithmic (NLL) [97–101]. The nominal predictions and the uncertainties for
 3230 each mass point are taken from an envelope of cross-section predictions using
 3231 different PDF sets and factorization and renormalization scales [102]. As dis-
 3232 cussed in Section 2.5.4, the PDFs and scales determine the cross section by pro-

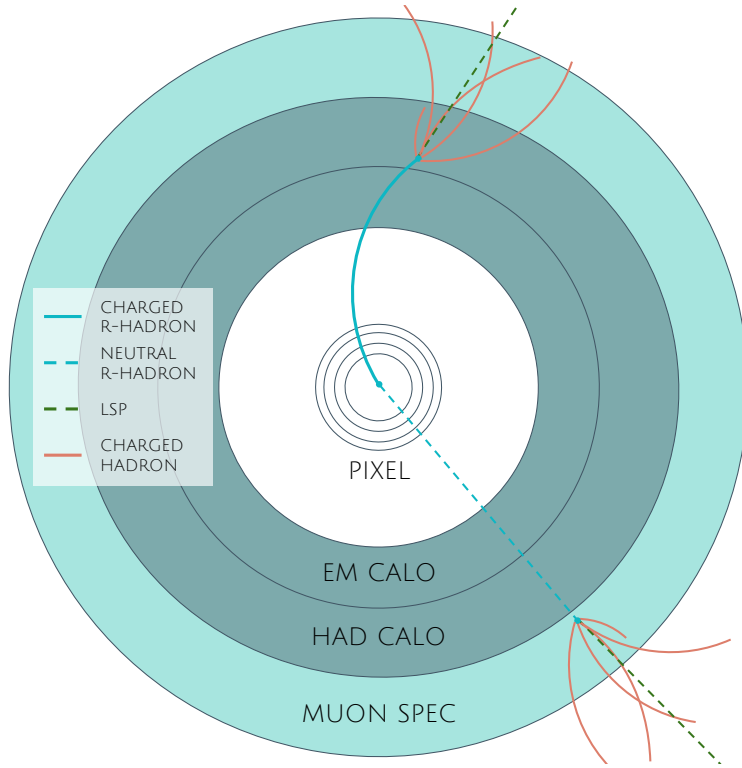


Figure 73: A schematic diagram of an R-Hadron event with a lifetime around 20 ns. The diagram includes one charged R-Hadron (solid blue), one neutral R-Hadron (dashed blue), LSPs (dashed green) and charged hadrons (solid orange). The pixel detector, calorimeters, and muon system are illustrated but not to scale.

3233 viding the probabilities of the proton constituents to interact. Multiple estimates
 3234 for the PDF and scales at 13 TeV can be used to provide an average cross section
 3235 calculation and its uncertainty.

3236 The R-Hadrons then undergo a full detector simulation [46], where the in-
 3237 teractions of the R-Hadrons with the material of the detector are described by
 3238 dedicated Geant4 [7] routines. These routines model the interactions described
 3239 in Section 9.1.1, including the ionizing interactions in the silicon modules of the
 3240 inner detector and the R-Hadron-nucleon interactions in the calorimeters [103,
 3241 104]. The specific routine chosen to describe the interactions of the R-Hadrons
 3242 with nucleons, the “generic model”, uses a pragmatic approach where the scatter-
 3243 ing cross section is taken to be a constant 12 mb per light quark. In this model
 3244 the gluino itself does not interact at all, although it carries most of the kinetic
 3245 energy of the bound state.

3246 The lifetimes of these R-Hadrons are then simulated at several working points,
 3247 $\tau = 0.1, 1.0, 3.0, 10, 30, 50$ and $> 50\text{ns}$. The actual decay times follow an expo-
 3248 nential distribution, where τ is the characteristic time. Only one decay mode is
 3249 simulated for these benchmark samples, $\tilde{g} \rightarrow q\bar{q}\tilde{\chi}_1^0$ with the neutralino mass set
 3250 to 100 GeV. The search discussed here is also efficient for heavier neutralinos,
 3251 which have very similar topologies but which generate less missing energy.

3252 All of the simulated events are then reconstructed using the same software
 3253 used for collision data. The fully reconstructed events are then reweighted to

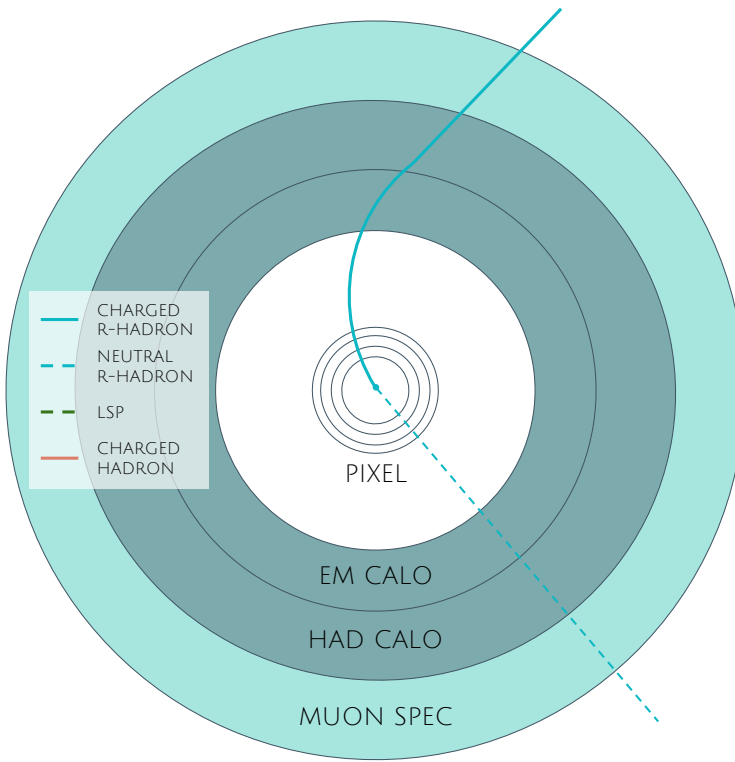


Figure 74: A schematic diagram of a [VLL](#) R-Hadron event. The diagram includes one charged R-Hadron (solid blue) and one neutral R-Hadron (dashed blue). The pixel detector, calorimeters, and muon system are illustrated but not to scale.

match the distribution of initial state radiation in an alternative sample of events,
 3254 generated with MG5_aMC@NLO [6], which has had a more accurate description of
 3255 radiate effects than Pythia6 in previous iterations [92]. MG5_aMC@NLO predicts
 3256 a harder distribution of initial state radiation, where 28% more simulated events
 3257 generate sufficient missing energy to trigger for [VLL](#) R-Hadrons. This reweighting
 3258 provides a more accurate description of the p of the gluino-gluino system
 3259 and is important in modeling the efficiency of triggering and offline event selec-
 3260 tion.
 3261

3262

3263 EVENT SELECTION

3264 The [LLPs](#) targeted by this search differ in their interactions with the detector from
 3265 [SM](#) particles primarily because of their large mass. When produced at the energies
 3266 available at the [LHC](#), that large mass results in a low β (typically $0.2 < \beta < 0.9$
 3267 as shown in Figure 69). Such slow-moving particles heavily ionize in detector
 3268 material. Each layer of the pixel detector provides a measurement of that ioniza-
 3269 tion, through [ToT](#), as discussed in Section 6.1.2. The ionization in the pixel
 3270 detector, quantified in terms of dE/dx , provides the major focus for this search
 3271 technique, along with the momentum measured in the entire inner detector. It is
 3272 effective both for its discriminating power and its use in reconstructing a parti-
 3273 cle's mass, and it can be used for a wide range of masses and lifetimes as discussed
 3274 in Section 9.1.2. However dE/dx needs to be augmented with a few additional
 3275 selection requirements to provide a mechanism for triggering and to further re-
 3276 duce backgrounds.

3277 Ionization itself is not currently accessible for triggering, so this search in-
 3278 stead relies on E_T^{miss} to trigger signal events. Although triggering on E_T^{miss} can
 3279 be inefficient, E_T^{miss} is often large for many production mechanisms of [LLPs](#), as
 3280 discussed in Section 9.1.

3281 The use of ionization to reject [SM](#) backgrounds relies on well-measured, high-
 3282 momentum tracks, so some basic requirements on quality and kinematics are
 3283 placed on the tracks considered in this search. A few additional requirements
 3284 are placed on the tracks considered for [LLP](#) candidates that increase background
 3285 rejection by targeting specific types of [SM](#) particles.

The ionization measurement with the Pixel detector can be calibrated to provide an estimator of $\beta\gamma$. That estimate, together with the momentum measurement provided by tracking, can be used to reconstruct a mass for each track which traverses the pixel detector,

$$m = \frac{p}{\beta\gamma} \quad (20)$$

3286 That mass variable will be peaked at the [LLP](#) mass for any signal, and provides an
 3287 additional tool to search for an excess. In addition to an explicit requirement on
 3288 ionization, this search constructs a mass-window for each targeted signal mass
 3289 in order to search for an excess of events.

3290 The strategy discussed here is optimized for lifetimes of $O(1) - O(10)$ ns.
 3291 The specific values for each requirement in signal region were optimized con-
 3292 sidering the increase in discovery reach for tightening the requirement on each
 3293 discriminating variable. Pixel ionization is especially useful in this regime as
 3294 particles only need to propagate through the first seven layers of the inner de-
 3295 tector, about 37 cm from the beam axis. The search is still competitive with
 3296 other searches for [LLPs](#) at longer lifetimes, because the primary discriminating

3297 variables are still applicable even for particles that do not decay within the de-
 3298 tector [93]. Although the majority of the requirements will be the same for all
 3299 lifetimes, two signal regions are defined to optimize separately for intermediate
 3300 and long lifetime particles.

3301 10.1 TRIGGER

3302 Triggering remains a significant difficulty in defining an event selection with
 3303 high signal efficiency in a search for **LLPs**. There are no triggers available in the
 3304 current ATLAS system that can fire directly from a high momentum track with
 3305 large ionization, as tracking is not available at L1 (Section 5.6). Although in some
 3306 configurations a charged **LLP** can fire muon triggers, this requirement introduces
 3307 significant model dependence on both the allowed lifetimes and the interactions
 3308 in the calorimeter [86], as discussed in Section 9.1.1.

3309 For a search targeting particles which may decay prior to reaching the muon
 3310 system, the most efficient available trigger is based on missing energy [86]. As
 3311 discussed in Section 9.1, signal events can produce significant E_T^{miss} by a few
 3312 mechanisms. At the trigger level however, the missing energy is only calculated
 3313 using the calorimeters (Section 5.6) where the R-Hadrons deposit little energy.
 3314 So, at short lifetimes, E_T^{miss} measured in the calorimeter is generated by an im-
 3315 balance between the jets and undetected **LSPs** produced in R-Hadron decays. At
 3316 longer lifetimes, without the decay products, missing energy is only produced in
 3317 the calorimeters when the R-Hadrons recoil against an **ISR** jet.

3318 These features are highlighted in Figure 75, which shows the E_T^{miss} distribu-
 3319 tions for simulated short lifetime (3 ns) and **VLL** R-Hadron events. The figure
 3320 includes both the offline E_T^{miss} , the missing energy calculated with all available
 3321 information, and Calorimeter E_T^{miss} , the missing energy calculated using only
 3322 information available at the calorimeter which approximates the missing energy
 3323 available at the trigger. The short lifetime sample has significantly greater E_T^{miss}
 3324 and Calorimeter E_T^{miss} than the **VLL** sample as expected. For the **VLL** sample,
 3325 a small fraction of events with very large E_T^{miss} (about 5%) migrate into the bin
 3326 with very small Calorimeter E_T^{miss} because the E_T^{miss} produced by a charged R-
 3327 Hadron track opposite a neutral R-Hadron track does not contribute any miss-
 3328 ing energy in the calorimeters.

3329 So, either case to some extent relies on kinematic degrees of freedom to pro-
 3330 duce missing energy, as the pair-produced **LLPs** tend to balance each other in
 3331 the transverse plain. For long lifetimes in particular, the presence of **ISR** is im-
 3332 portant in providing an imbalance in the transverse plane, and is an important
 3333 aspect of modeling the selection efficiency for R-Hadron events. The missing
 3334 energy trigger with the lowest threshold available is chosen for this selection in
 3335 order to maximize the trigger efficiency. The formation of the trigger decision
 3336 for missing energy was discussed in more detail in Section 5.6. During 2015
 3337 data collection this was the HLT_xe70 trigger, which used a 50 GeV threshold
 3338 on missing energy at L1 and a 70 GeV threshold on missing energy at the HLT
 3339 which is nearly 100% efficient after the L1 requirement. With these thresholds,
 3340 the incomplete balance of the **LSPs** results in a relatively low efficiency for long-

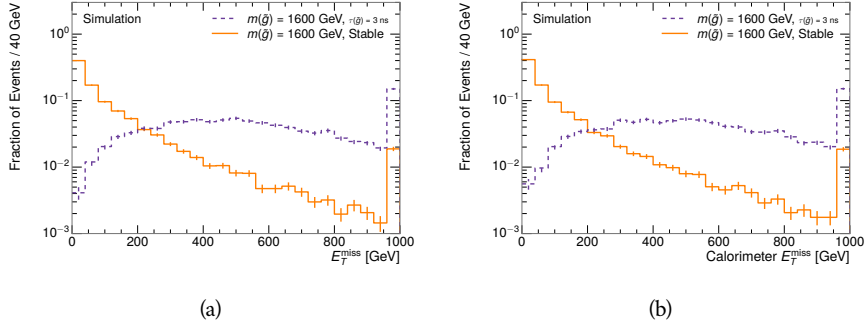


Figure 75: The distribution of (a) E_T^{miss} and (b) Calorimeter E_T^{miss} for simulated signal events before the trigger requirement. The final bin includes all events above the axis range.

3341 lifetime particles, roughly 40%, and efficiencies between 65% and 95% for shorter
 3342 lifetimes depending on both the mass and the lifetime.

3343 10.2 KINEMATICS AND ISOLATION

3344 After the trigger requirement, each event is required to have a primary vertex
 3345 reconstructed from at least two well-measured tracks in the inner detector, each
 3346 with $p_T > 400 \text{ MeV}$. If more than one such vertex exists, the primary vertex is
 3347 taken to be the one with the largest summed p_T^2 for all tracks associated to that
 3348 vertex. The offline reconstructed E_T^{miss} is required to be above 130 GeV to addi-
 3349 tionally reject **SM** backgrounds. The transverse missing energy is calculated us-
 3350 ing fully reconstructed and calibrated offline objects, as described in Section 6.5.
 3351 In particular the E_T^{miss} definition in this selection uses jets reconstructed with the
 3352 anti- k_t algorithm with radius $R = 0.4$ from clusters of energy in the calorimeter
 3353 (Section 6.4) and with $p_T > 20 \text{ GeV}$, as well as reconstructed muons, electrons,
 3354 and tracks not identified as another object type.

3355 The E_T^{miss} distributions are shown for data and a few simulated signals in Fig-
 3356 ure 76, after the trigger requirement. The data contains some events with E_T^{miss}
 3357 below the nominal trigger threshold of 70 GeV, which can occur because E_T^{miss}
 3358 at trigger level uses only calorimeter information while the full offline E_T^{miss}
 3359 additionally includes tracks and muons which can balance the event. The cut
 3360 placed at 130 GeV is 95% efficient for **LL** and 90% efficient for **VLL** particles, after
 3361 the trigger requirement, because of the missing energy generating mechanisms
 3362 discussed previously. The distribution of data in this figure and subsequent fig-
 3363 ures in this section can be interpreted as the distribution of backgrounds, as any
 3364 signal contamination would be negligible if present at these early stages of the
 3365 selection (prior to the final requirement on ionization). The background falls
 3366 rapidly with missing energy, motivating the direct requirement on E_T^{miss} for the
 3367 signal region.

3368 It is typically the practice for searches for new physics on ATLAS to place an
 3369 offline requirement on the triggering variable that is sufficiently tight to guar-

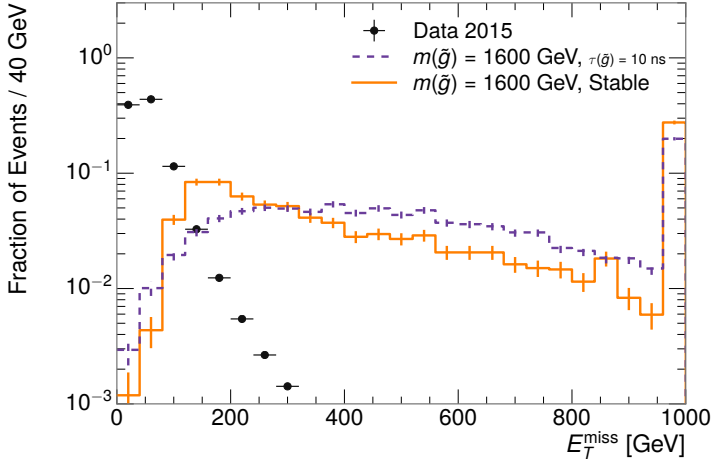


Figure 76: The distribution of E_T^{miss} for data and simulated signal events, after the trigger requirement. The final bin includes all events above the axis range.

3370 antee that the event would pass the trigger. Such a tight requirement makes the
 3371 uncertainty on the trigger efficiency of the simulation negligible, as modeling the
 3372 regime where the trigger is only partially efficient can be difficult. In this analy-
 3373 sis, however, because of the atypical interactions of R-Hadrons with the tracker
 3374 and the calorimeter, the offline requirement on E_T^{miss} is not sufficient to guar-
 3375 antee a 100% trigger efficiency even at large values, as can be seen in Figure 77.
 3376 This figure shows the efficiency for passing the HLT_xe70 trigger as a function
 3377 of the requirement on E_T^{miss} , which plateaus to roughly 85% even at large values.
 3378 This plateau does not reach 100% because events which have large offline miss-
 3379 ing energy from a neutral R-Hadron produced opposite of a charged R-Hadron
 3380 can have low missing energy in the calorimeters. The Calorimeter E_T^{miss} , on the
 3381 other hand, does not have this effect and reaches 100% efficiency at large values
 3382 because it is the quantity that directly corresponds to the trigger threshold. In
 3383 both cases the efficiency of triggering is greater for the short lifetime sample be-
 3384 cause the late decays to hadrons and LSPs produce an imbalance in the calorime-
 3385 ters even though they may not be reconstructed offline as tracks or jets. For this
 3386 reason, the requirement on E_T^{miss} is determined by optimizing the background
 3387 rejection even though it corresponds to a value of trigger efficiency significantly
 3388 below 1.0.

3389 The events are then required to have at least one candidate LLP track. Al-
 3390 though the LLPs are produced in pairs, many models do not consistently yield
 3391 two charged particles, as discussed in Chapter 9. For example, in the R-Hadron
 3392 model highlighted here, only 20% of events have two charged R-Hadrons while
 3393 47% of events have just one. A signal region requiring two charged particle can-
 3394 didates could be a powerful improvement in background rejection for a larger
 3395 dataset, but it is not considered in this version of the analysis as it was found to
 3396 be unnecessary to reject the majority of backgrounds.

3397 For a track to be selected as a candidate, it must have $p_T > 50 \text{ GeV}$ and pass
 3398 basic quality requirements. The track must be associated to the primary vertex.

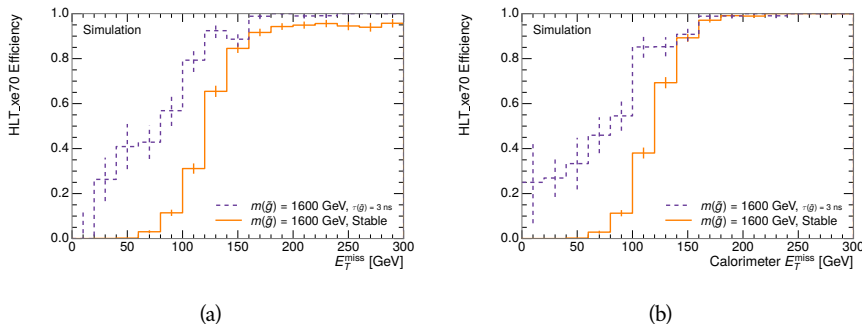


Figure 77: The trigger efficiency for the HLT_xe70 trigger requirement as a function of (a) E_T^{miss} and (b) Calorimeter E_T^{miss} for simulated signal events.

It must also have at least seven clusters in the silicon layers in the inner detector to ensure an accurate measurement of momentum. Those clusters must include one in the innermost layer if the extrapolated track is expected to pass through that layer. And to ensure a reliable measurement of ionization, the track is required to have at least two clusters in the pixel detector that provide a measurement of dE/dx .

At this point in the selection, there is a significant high-ionization background from multiple tracks that significantly overlap in the Pixel detector. Previous versions of this analysis have rejected these overlaps by an explicit overlap rejection between pairs of fully reconstructed tracks, typically by requiring no additional tracks within a cone around the candidate. This technique, however, fails to remove the background from tracks that overlap so precisely that the tracks cannot be separately resolved, which can be produced in very collimated photon conversions.

Another observable, which more directly targets track overlaps, identifies cluster shapes that are likely formed by multiple particles based on a neural network classification algorithm, as discussed in Section 6.1.1. The number of clusters on a given track that are estimated to have contributions from more than one particle is called N_{split} . As the shape of clusters requires significantly less spatial separation to identify overlaps than it does to reconstruct two fully resolved tracks, this variable is more effective at rejecting backgrounds from overlaps. Figure 78 shows the dependence of ionization on N_{split} ; as N_{split} increases the most probable value of dE/dx grows significantly up to twice the expected value when $N_{\text{split}} = 4$.

A requirement of $N_{\text{split}} = 0$ is very successful in reducing the long positive tail of the dE/dx distributions, as can be seen in Figure 79. Comparing the distribution for “baseline tracks”, tracks with only the above requirements on clusters applied and before the requirement on N_{split} , to the distribution with $N_{\text{split}} = 0$, it is clear that the fraction of tracks with large dE/dx is reduced by several orders of magnitude. The tracks without split hits are very close to the dE/dx distribution of identified muons, which are usually well isolated. Figure 79 also includes the distribution of dE/dx in an example signal simulation to demonstrate how effective dE/dx is as a discriminating variable with this isolation applied. The

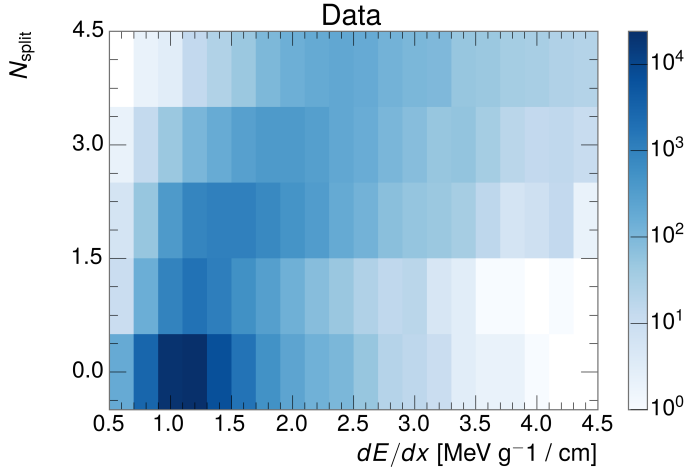


Figure 78: The dependence of dE/dx on N_{split} in data after basic track hit requirements have been applied.

background falls rapidly for $dE/dx > 1.8 \text{ MeV g}^{-1} \text{ cm}^2$ while the majority of the signal, approximately 90% depending on the mass, falls above that threshold. Over 90% of LLP tracks in simulated signal events pass the N_{split} -based isolation requirement.

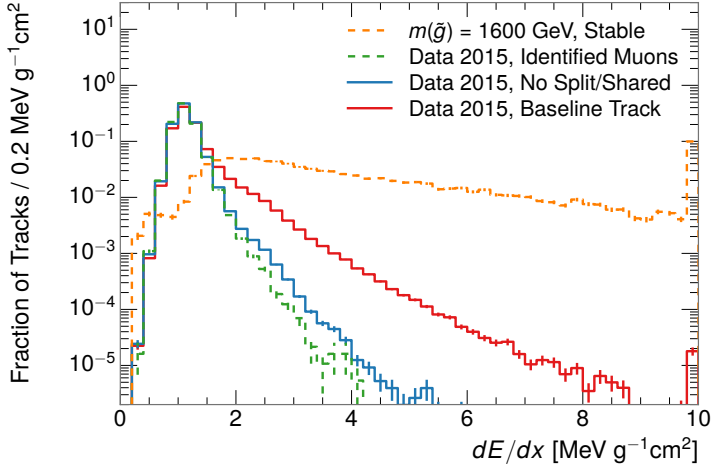


Figure 79: The distribution of dE/dx with various selections applied in data and simulated signal events. The final bin includes all tracks above the axis range.

A few additional kinematic requirements are imposed to help reduce SM backgrounds. The momentum of the candidate track must be at least 150 GeV, and the uncertainty on that measurement must be less than 50%. The distribution of momentum is shown in Figure 80 for tracks in data and simulated signal events after the previously discussed requirements on clusters, transverse momentum, and isolation have been imposed. The signal particles are much harder on av-

verage than their backgrounds as shown in Figure 69. The transverse mass, M_T , defined as

$$M_T = \sqrt{2p_T E_T^{\text{miss}} (1 - \cos(\Delta\phi(E_T^{\text{miss}}, \text{track})))} \quad (21)$$

estimates the mass of a decay of to a single charged particle and an undetected particle and is required to be greater than 130 GeV to reject contributions from the decay of W bosons. Figure 81 shows the distribution of M_T for data and simulated signal events. The signal is distributed over a wide range of M_T , with about 90% above the threshold value of 130 GeV. The data has a large number of contributions below 100 GeV from W boson decays and an additional peak from a kinematic shaping imposed by the requirements on E_T^{miss} and the track p_T in dijet events.

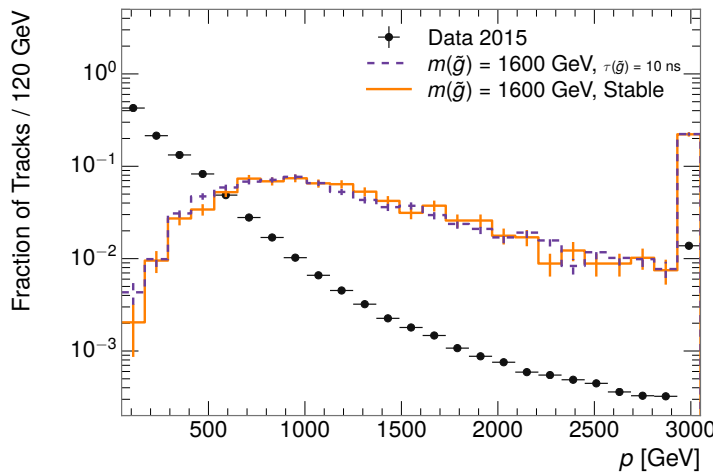


Figure 80: The distribution of track momentum for data and simulated signal events, after previous selection requirements have been applied. The final bin includes all tracks above the axis range.

10.3 PARTICLE SPECIES REJECTION

The amount of ionization deposited by particles with low mass and high momentum has a large positive tail [3], so backgrounds can be formed by a wide variety of SM processes when various charged particles have a few randomly large deposits of energy in the pixel detector. Those backgrounds can be additionally reduced by targeting other interactions with the detector where they are expected to have different behavior than R-Hadrons. The interactions with the detector depend on the types of particles produced rather than the processes which produce them, so this search forms a series of rejections to remove backgrounds from individual particle species. These rejections focus on using additional features of the event, other than the kinematics of the candidate track, as they can provide a powerful source of background rejection with very high signal efficiency. However, the lifetime of an R-Hadron can significantly change

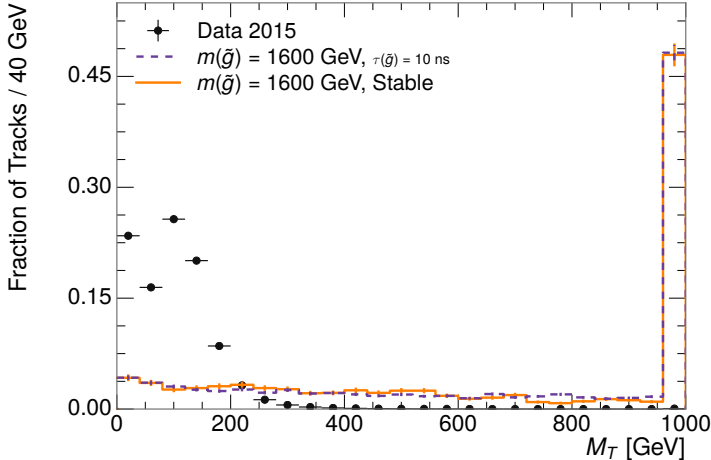


Figure 81: The distribution of M_T for data and simulated signal events, after previous selection requirements have been applied. The final bin includes all tracks above the axis range.

its detector characteristics, as discussed in Section 9.1.2. To accommodate these differences, the **SM** rejections defined in this section are split to form two signal regions, one for long-lifetimes particles, the **VLL** region ($\tau[\text{ns}] \geq 50 \text{ ns}$), and one for intermediate lifetime particles, the **LL** region ($0.4 < \tau[\text{ns}] < 50$).

Jets can contribute high momentum track backgrounds when an individual jet constituent carries large p_T . These tracks can be sufficiently well isolated from the other constituents that they are separately reconstructed and pass the N_{split} requirement. However, jets can be very effectively rejected by considering the larger-scale isolation of the candidate track. In this case the isolation focuses on the production of nearby particles as a jet-veto, rather than the isolation from overlapping tracks based on N_{split} that was used to reduce high-ionization backgrounds. As explained in Section 9.1, the fragmentation process which produces an R-Hadron is very hard and thus is not expected to produce additional particles with a summed momentum of more than 5 GeV. Nearby particles may be produced in the decay of the R-Hadron, but they will be significantly displaced, so the jet-veto only considers tracks associated to the primary vertex. The jet-veto uses the summed momentum of tracks with a cone of $\Delta R < 0.25$, referred to as p_T^{Cone} , which is shown in Figure 82 for data and simulated signal events. In the data this value has a peak at zero from isolated tracks such as leptons, and a long tail from jets which contains as much as 80% of the background above 20 GeV at this stage of the selection. In signal events p_T^{Cone} is strongly peaked at zero and significantly less than 1% of signal events have p_T^{Cone} above 20 GeV. This makes a requirement of $p_T^{\text{Cone}} < 20 \text{ GeV}$ a very effective method to reject background without losing signal efficiency. For the **VLL** signal region, this cut is further tightened to $p_T^{\text{Cone}} < 5 \text{ GeV}$ as it is the most effective variable remaining to extend the search reach for long lifetimes.

Even for fully isolated particles, there are additional methods to reject each type of particle using information in the muon system and calorimeters. Muons

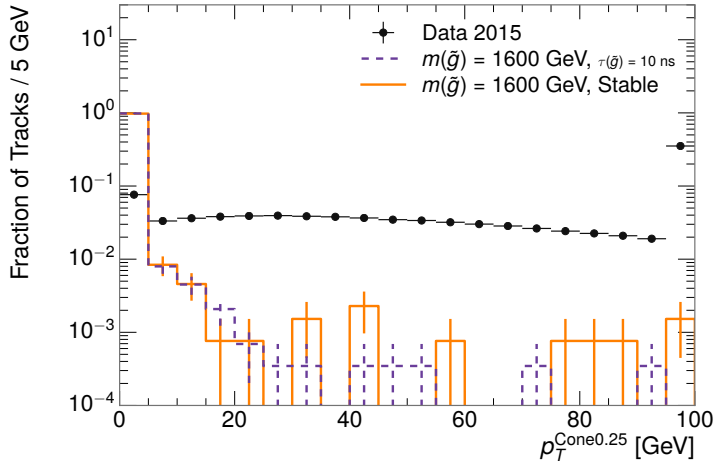


Figure 82: The distribution of summed tracked momentum within a cone of $\Delta R < 0.25$ around the candidate track for data and simulated signal events, after previous selection requirements have been applied. The final bin includes all tracks above the axis range.

3493 can be identified very reliably using the tracks in the muon system, as described
 3494 in Section 6.3. For intermediate lifetimes ($0.4 < \tau[\text{ns}] < 30$), the LLPs do not sur-
 3495 vive long enough to reach the muon system, and so muons are vetoed by rejecting
 3496 tracks that associate to a muon with medium muon identification requirements
 3497 (Section 6.3). For longer lifetimes ($\tau > 30$ ns), this rejection is not applied be-
 3498 cause LLPs which reach the muon system can be identified as muons as often as
 3499 30% of the time in simulated samples.

3500 Calorimeter-based particle rejection relies on the expected small deposits of
 3501 energy from LLPs. When the lifetime is long enough to reach the calorimeter, a
 3502 LLP deposits little of its energy as it traverses the material, as discussed in Sec-
 3503 tion 9.1. Even when the particle does decay before the calorimeter, the majority
 3504 of its energy is carried away by the LSP and not deposited in the calorimeter.
 3505 In both cases the energy is expected to be distributed across the layers of the
 3506 calorimeters and not peaked in just one layer. This can be quantified in terms of
 3507 E/p , the ratio of calorimeter energy of a nearby jet to the track momentum, and
 3508 f_{EM} , the fraction of energy in that jet within the electromagnetic calorimeter.
 3509 When no jets fall within a cone of 0.05 of the particle, E/p and f_{EM} are both de-
 3510 fined as zero. E/p is expected to be above 1.0 for electrons and hadrons because
 3511 of the contributions from other nearby particles. At these momenta there is no
 3512 significant fraction of tracks with no associated clusters due to interactions with
 3513 the detector or insufficient energy deposits (see Section 7.2.2). f_{EM} is peaked
 3514 close to 1.0 for electrons, and distributed between 10% and 90% for hadrons.

3515 These trends can be seen in the two dimensional distribution for signal in
 3516 Figure 83 for VLL and LL (10 ns) signal events. The majority of R-Hadrons in
 3517 both samples fall into the bin for $E/p = 0$ and $f_{\text{EM}} = 0$ because the majority of
 3518 the time there is no associated jet. In the VLL sample, when there is an associated
 3519 jet, E/p is typically still below 0.1, and the f_{EM} is predominantly less than 0.8.

3520 In the LL sample, on the other hand, E/p is larger on average because of the jets
 3521 produced in the R-Hadron decay. It is still typically below 0.1, however, because
 3522 most of the energy of the R-Hadron is carried by the LSP and not the jet. The
 3523 f_{EM} is much lower on average in this case, below 0.1, because the 10 ns lifetime
 3524 particles rarely decay before passing through the electromagnetic calorimeter.
 3525 Figure 83 also includes simulated Z decays to electrons or tau leptons. From the
 3526 decays to electrons it is clear that the majority of electrons have f_{EM} above 0.9.
 3527 The τ decays include a variety of products. Muons can be seen in the bin where
 3528 $E/p = 0$ and $f_{EM} = 0$ because they do not have an associated jet. Electrons fall
 3529 into the range where $E/p > 1$ and $f_{EM} > 0.9$. Hadronic tau decays are the most
 3530 common, and fall in the range of $0.1 < f_{EM} < 0.9$ and $E/p > 1.0$.

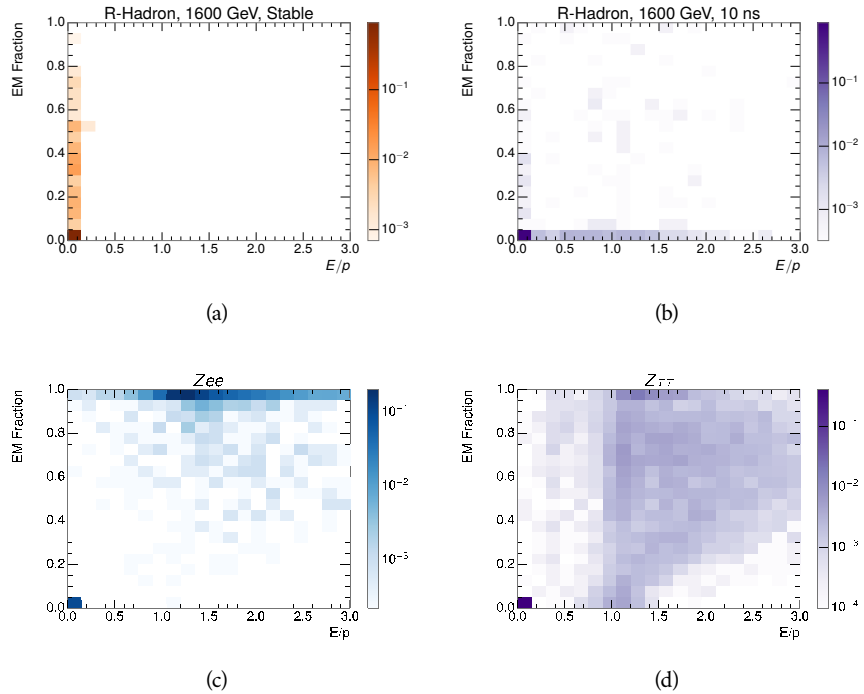


Figure 83: The normalized, two-dimensional distribution of E/p and f_{EM} for simulated
 (a) 1200 GeV VLL R-Hadron, and (b) 1200 GeV, 10 ns R-Hadron, (c) $Z \rightarrow ee$,
 and (d) $Z \rightarrow \tau\tau$ events.

3531 The differences motivate an electron rejection by requiring $f_{EM} < 0.9$. Simi-
 3532 larly, isolated hadrons are rejected by requiring $E/p < 1.0$. These requirements
 3533 combine to remove the majority of isolated electrons and hadrons but retain over
 3534 95% of the simulated signal across a range of masses and lifetimes. The suite of
 3535 particle species rejection techniques provide a significant analysis improvement
 3536 over previous iterations of ionization-based searches on ATLAS by providing
 3537 additional background rejection with minimal loss in signal efficiency.

3538 10.4 IONIZATION

3539 The final requirement on the candidate track is the primary discriminating vari-
 3540 able, the ionization in the pixel detector. That ionization is measured in terms
 3541 of dE/dx , which was shown for data and simulated signal events in Figure 79.
 3542 dE/dx is dramatically greater for the high mass signal particles than the back-
 3543 grounds, which start to fall immediately after the minimally ionizing peak at 1.1
 3544 MeV g $^{-1}$ cm 2 . The dE/dx for candidate tracks must be greater than a pseudorapidity-
 3545 dependent threshold, specifically $1.80 - 0.11|\eta| + 0.17\eta^2 - 0.05|\eta|^3$ MeV g $^{-1}$ cm $^{-2}$,
 3546 in order to correct for an approximately 5% dependence of the MIP peak position
 3547 on η . The requirement was chosen as part of the signal region optimization, and
 3548 reduces the backgrounds by a factor of 100 while remaining 70-90% efficient for
 3549 simulated signal events depending on the mass.

3550 10.4.1 MASS ESTIMATION

3551 The mean value of ionization in silicon is governed by the Bethe equation and
 3552 the most probable value follows a Landau-Vavilov distribution [3]. Those forms
 3553 inspire a parametric description of dE/dx in terms of $\beta\gamma$,

$$(dE/dx)_{\text{MPV}}(\beta\gamma) = \frac{p_1}{\beta^{p_3}} \ln(1 + [p_2\beta\gamma]^{p_5}) - p_4 \quad (22)$$

3554 which performs well in the range $0.3 < \beta\gamma < 1.5$. This range includes the
 3555 expected range of $\beta\gamma$ for the particles targeted for this search, with $\beta\gamma \approx 2.0$
 3556 for lower mass particles (O(100 GeV)) and $\beta\gamma \approx 0.5$ for higher mass parti-
 3557 cles (O(1000 GeV)). The parameters, p_i , are fit using a 2015 data sample of
 3558 low-momentum pions, kaons, and protons as described in Ref. [105]. Figure 84
 3559 shows the two-dimensional distribution of dE/dx and momentum along with
 3560 the above fitted values for $(dE/dx)_{\text{MPV}}$.

3561 The above equation (22) is then numerically inverted to estimate $\beta\gamma$ and the
 3562 mass for each candidate track. In simulated signal events, the mean of this mass
 3563 value reproduces the generated mass up to around 1800 GeV to within 3%. The
 3564 mass distributions are shown for a few VLL mass points in Figure 85. The large
 3565 widths of these distributions come from the high variability in energy deposits
 3566 in the pixel detector as well as the uncertainty on momentum measurements at
 3567 high momentum, but the means converge to the expected values. A constant
 3568 shift of 3% is observed between the mean of the reconstructed mass distribution
 3569 and the generated mass, which is then corrected by applying a 3% shift in the
 3570 opposite direction.

3571 This analysis evaluates expected yields and the resulting cross sectional limits
 3572 using windows in this mass variable. The windows are formed by fitting mass
 3573 distributions in simulated signal events like those in Figure 85 to Gaussian distri-
 3574 butions and taking all events that fall within $\pm 1.4\sigma$ of the mean. As can be seen
 3575 in Figure 85, typical values for this width are $\sigma \approx 300 - 500$ GeV depending on
 3576 the generated mass.

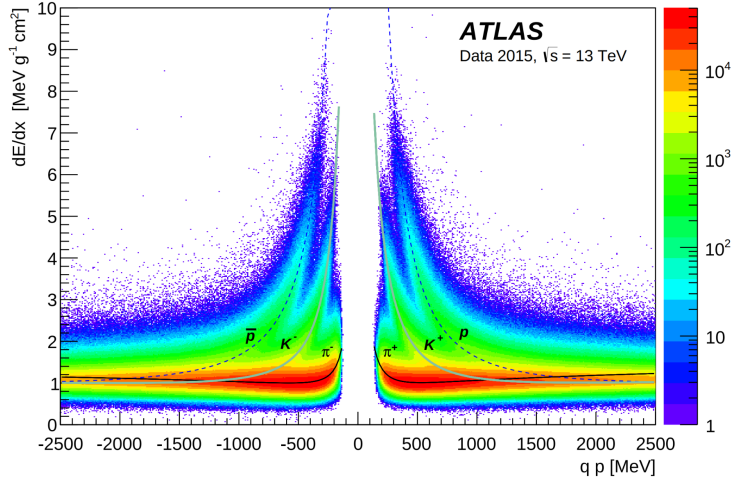


Figure 84: Two-dimensional distribution of dE/dx versus charge signed momentum (q_p) for minimum-bias tracks. The fitted distributions of the most probable values for pions, kaons and protons are superimposed.

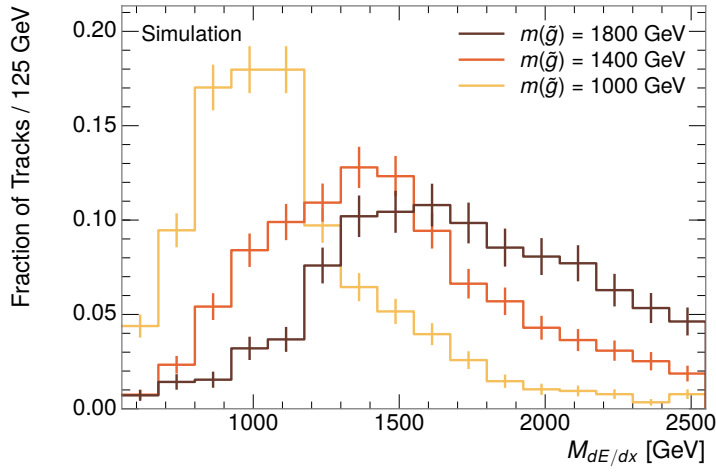


Figure 85: The distribution of mass estimated using dE/dx for simulated [VLL](#) R-Hadrons with masses between 1000 and 1600 GeV.

3577 10.5 EVENT SELECTION

3578 The numbers of events passing each requirement are shown in Table 9 for the full
 3579 2015 dataset and a simulated 1600 GeV, 10 ns lifetime R-Hadron sample. The
 3580 table highlights the overall acceptance \times efficiency for signal events, which for
 3581 this example is 19%. Between SM rejection and ionization, the selection require-
 3582 ments reduce the background of tracks which pass the kinematic requirements
 3583 down by an additional factor of almost 2000.

Selection	Signal Events (%)	Data Events	Rejection
Generated	26.0 ± 0.3		
E_T^{miss} Trigger	24.8 ± 0.3 (95%)		
$E_T^{\text{miss}} > 130$ GeV	23.9 ± 0.3 (92%)		
Track Quality and p_T	10.7 ± 0.2 (41%)	368324	1.0
Isolation Requirement	9.0 ± 0.2 (35%)	108079	3.4
Track $p > 150$ GeV	6.6 ± 0.2 (25%)	47463	7.8
$M_T > 130$ GeV	5.8 ± 0.2 (22%)	18746	20
Electron/Hadron Veto	5.5 ± 0.2 (21%)	3612	100
Muon Veto	5.5 ± 0.2 (21%)	1668	220
Ionization Requirement	5.0 ± 0.1 (19%)	11	33000

Table 9: The expected number of events at each level of the selection for LL 1600 GeV, 10 ns R-Hadrons, along with the number of events observed in data, for 3.2 fb^{-1} . The simulated yields are shown with statistical uncertainties only. The total efficiency \times acceptance is also shown for the signal and the rejection factor relative to initial track requirement is shown for data.

3584 There is a strong dependence of this efficiency on lifetime and mass, with effi-
 3585 ciencies dropping to under 1% at low lifetimes. Figure 86 shows the dependence
 3586 on both mass and lifetime for all signal samples considered in this search. The
 3587 dependence on mass is relatively slight and comes predominantly from the in-
 3588 creasing fraction of R-Hadrons which pass the ionization cut with increasing
 3589 mass. The trigger and E_T^{miss} requirements are most efficient for particles that
 3590 decay before reaching the calorimeters. However, the chance of a particle to be
 3591 reconstructed as a high-quality track decreases significantly at low lifetimes as
 3592 the particle does not propagate sufficiently through the inner detector. These
 3593 effects lead to a maximum in the selection efficiency for lifetimes around 10-30
 3594 ns. The lifetimes up to and including 30 ns are shown with the LL selection and
 3595 the 50 ns and stable points are shown with the VLL selection.

3596 The inefficiency of this signal region at short lifetimes comes almost exclu-
 3597 sively from an acceptance effect, in that the particles do not reach the necessary
 3598 layers of the SCT. This can be seen more clearly by defining a fiducial region
 3599 which includes events with at least one R-Hadron that is produced with non-
 3600 zero charge, $p_T > 50$ GeV, $p > 150$ GeV, $|\eta| < 2.5$, and a decay distance greater
 3601 than 30 cm in the transverse plane. At short (1 ns) lifetimes, the acceptance into

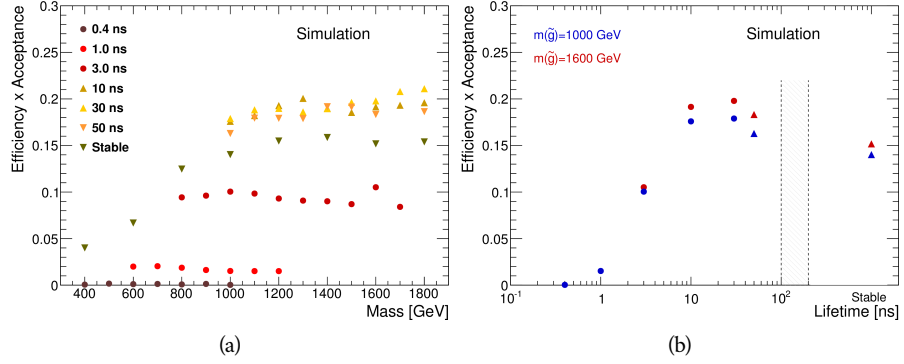


Figure 86: The acceptance \times efficiency as a function of R-Hadron (a) mass and (b) lifetime. (a) shows all of the combinations of mass and lifetime considered in this search, and (b) highlights the lifetime dependence for 1000 GeV and 1600 GeV R-Hadrons.

3602 this region is as low as 4%. Once this acceptance is accounted for, the selection
 3603 efficiency ranges from 25% at lifetimes of 1 ns up to 45% at lifetimes of 10 ns.

3604

3605 BACKGROUND ESTIMATION

3606 The event selection discussed in the previous section focuses on detector signa-
 3607 tures, emphasizing a single high-momentum, highly-ionizing track. That track
 3608 is then required to be inconsistent with the expected properties of SM particles,
 3609 with various requirements designed to reject jets, hadrons, electrons, and muons
 3610 (Section 10.3). Therefore the background for this search comes entirely from
 3611 backgrounds that are outliers of various distributions including dE/dx , f_{EM} ,
 3612 and p_T^{Cone} . The simulation can be tuned in various ways to do an excellent job of
 3613 modeling the average properties of each particle type [106], but it is not necessarily
 3614 expected to accurately reproduce outliers. For this reasons, the background
 3615 estimation used for this search is estimated entirely using data.

3616 11.1 BACKGROUND SOURCES

3617 SM charged particles with lifetimes long enough to form tracks in the inner de-
 3618 tector can be grouped into three major categories based on their detector in-
 3619 teractions: hadrons, electrons, and muons. Every particle that contributes to the
 3620 background for this search belongs to one of these types. Relatively pure samples
 3621 of tracks from each of these types can be formed in data by inverting the various
 3622 rejection techniques in Section 10.3. Specifically, muons are selected requiring
 3623 medium muon identification, electrons requiring $E/p > 1.0$ and $f_{EM} > 0.95$,
 3624 and hadrons requiring $E/p > 1.0$ and $f_{EM} < 0.95$.

3625 Figure 87 shows the distributions of momentum and dE/dx for these cate-
 3626 gories in data, after requiring the event level selection as well as the track re-
 3627 quirements on p_T , hits, and N_{split} , as discussed in Section 10.2. Simulated signal
 3628 events are included for reference. These distribution are only illustrative of the
 3629 differences between types, as the rejection requirements could alter their shape.
 3630 This is especially significant for momentum which enters directly into E/p and
 3631 can indirectly affect muon identification. However it is clear that there are some
 3632 differences between types in both distributions, even though the trends are sim-
 3633 ilar. The distributions of momentum are not necessarily expected to match be-
 3634 tween the various types because the production mechanisms for each type result
 3635 in different kinematic distributions. dE/dx is also different between types be-
 3636 cause of incomplete isolation; although the requirement on N_{split} helps to reduce
 3637 the contribution of nearby particles it does not completely remove the effect
 3638 of overlaps. Muons are better isolated because they do not have the additional
 3639 particle from hadronization present for hadrons and they are significantly less
 3640 likely do interact with the detector and produce secondary particles compared to
 3641 hadrons and electrons. Thus muons have the smallest fraction of dE/dx above
 3642 the threshold of $1.8 \text{ MeVg}^{-1}\text{cm}^2$; hadrons and electrons have a larger fraction
 3643 above this threshold.

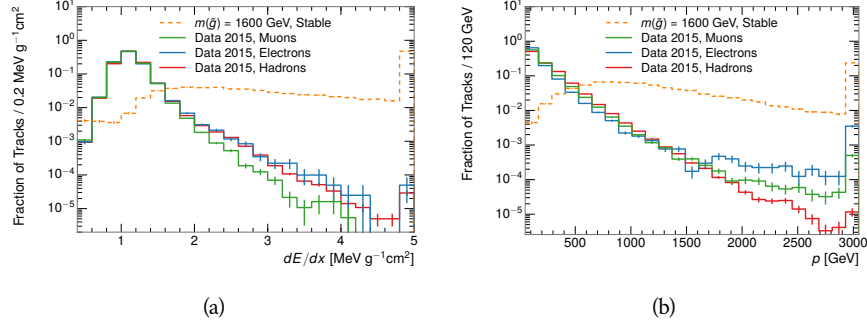


Figure 87: The distribution of (a) dE/dx and (b) momentum for tracks in data and simulated signal after requiring the event level selection and the track selection on p_T , hits, and N_{split} . Each sub-figure shows the normalized distributions for tracks classified as hadrons, electrons, and muons in data and R-Hadrons in the simulated signal.

3644 It is difficult to determine what fraction of each particle type enters into the fi-
3645 nal signal region. The background method will not have significant dependence
3646 on the relative contributions of each species, but it is useful to understand the
3647 differences between each when considering the various tests of the method.

3648 11.2 PREDICTION METHOD

The data-driven background estimation relies on the independence between the ionization measurement and other kinematic variables in the event. For standard model particles with momenta above 50 GeV, dE/dx is not correlated with momentum; though there is a slight relativistic rise as momentum increases, the effect is small compared to the width of the distribution of ionization energy deposits.. So, the proposed method to estimate the mass distribution of the signal region is to use the momentum from a track with low dE/dx (below the threshold value) and to combine it with a random dE/dx value from a dE/dx template. The resulting track is just as likely as the original, so a large set of random generations provide the expected distributions of momentum and ionization. These are then combined using the parametrization described in Section 10.4.1 to estimate $\beta\gamma$ and then form a distribution of mass for the signal region using Equation 20.

Algorithmically this method is implemented by forming two distinct Control Regions ([CRs](#)). The first [CR](#), CR1, is formed by applying the entire event selection from Chapter [10](#) apart from the dE/dx and mass requirements. The dE/dx requirement is instead inverted for this region. Because of the independence of dE/dx and p , the tracks in this control region have the same kinematic distribution as the tracks in the signal region, and are used to measure a two-dimensional template of p and η . The second [CR](#), CR2, is formed from the event selection through the dE/dx requirement, but with an inverted E_T^{miss} requirement. The tracks in this control region are expected to have similar dE/dx distributions as the signal region before the ionization requirement, and so this region is used to measure a two-dimensional template of dE/dx and η .

3672 The contribution of any signal to the control regions is minimized by the in-
 3673 verted selection requirements. Only less than 10% of simulated signal events
 3674 have either dE/dx or E_T^{miss} below the threshold values in the original signal re-
 3675 gion, while the backgrounds are significantly enhanced by inverting those re-
 3676 quirements. The signal contamination is less than 1% in both control regions
 3677 for all of the simulated masses and lifetimes considered in this analysis.

3678 With those measured templates, the shape of the mass estimation is generated
 3679 by first selecting a random (p, η) combination from CR1. This momentum
 3680 value is combined with a dE/dx value taken from the appropriate distribution
 3681 of dE/dx for the selected η from CR2. The use of η in both random samplings
 3682 controls for any correlation between p , dE/dx , and η . Those values are then
 3683 used to calculate a mass in the same way that is done for regular tracks in data,
 3684 see Section 10.4.1. As this procedure includes all dE/dx values, the cut at 1.8
 3685 MeVg $^{-1}$ cm 2 is then enforced to fully model the signal region. The generated
 3686 mass distribution is then normalized by scaling the background estimate to the
 3687 data in the region $M < 160$ GeV, where signals of this type have already been
 3688 excluded [92]. This normalization uses the distributions of mass generated with-
 3689 out the ionization requirement.

3690 The statistical uncertainties on these background distributions are calculated
 3691 by independently fluctuating each bin of the input templates according to their
 3692 Poisson uncertainties. These fluctuations are repeated a large number of times,
 3693 and the uncertainty on the resulting distribution is taken as the root mean square
 3694 (RMS) deviation of the fluctuations from the average. As the procedure uses one
 3695 million random combinations to generate the distributions, The statistical un-
 3696 certainty from the actual random generations is negligible compared to the un-
 3697 certainty from measuring the templates.

3698 11.3 VALIDATION

3699 The validity of the background estimation technique can be evaluated in both
 3700 data and simulation. The underlying assumption that random combinations of
 3701 dE/dx and momentum can predict a mass distribution in an orthogonal region
 3702 can be tested using simulated samples where concerns like multiple particle types
 3703 can be controlled. Using the same technique in another set of signal-depleted
 3704 regions in data then extends this confidence to the more complicated case where
 3705 several particle species are inherently included.

3706 11.3.1 CLOSURE IN SIMULATION

3707 The first test of the procedure is done using a simulated sample of $W \rightarrow \mu\nu$
 3708 decays. These types of events provide the ingredients required to test the back-
 3709 ground estimate, E_T^{miss} and isolated tracks, with high statistics. In this example
 3710 there is no signal, so simulated events in the orthogonal CRs are used to estimate
 3711 the shape of the mass distribution of the simulated events in the signal region. To
 3712 reflect the different topology for W boson decays, the CRs use slightly modified
 3713 definitions. In all CRs, the requirement of $p > 150$ GeV and the SM rejection

3714 requirements are removed. Additionally, for the signal region the requirement
 3715 on E_T^{miss} is relaxed to 30 GeV and the corresponding inverted requirement on
 3716 CR2 is also set at 30 GeV.

3717 With these modified selections, the simulated and randomly generated distri-
 3718 butions of $M_{dE/dx}$ are shown in Figure 88. This figure includes the mass distri-
 3719 butions before and after the requirement on dE/dx , which significantly shapes
 3720 the distributions. In both cases the background estimation technique repro-
 3721 duces the shape of $M_{dE/dx}$ in the signal region. There is a small difference in the pos-
 3722 itive tail of the mass distribution prior to the ionization cut, where the random
 3723 events underestimate the fraction of tracks with mass above 150 GeV by about
 3724 20%. After the ionization requirement, however, this discrepancy is not present
 3725 and the two distributions agree to within statistical uncertainties in the positive
 3726 tail.

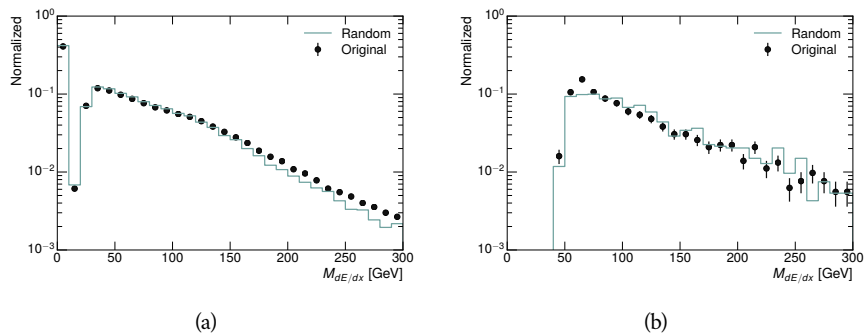


Figure 88: The distribution of $M_{dE/dx}$ (a) before and (b) after the ionization requirement for tracks in simulated W boson decays and for the randomly generated back-
 ground estimate.

3727 This ability to reproduce the shape of the mass distribution in simulated events
 3728 shows that the technique works as expected. No significant biases are acquired
 3729 in using low dE/dx events to select kinematic templates or in using low E_T^{miss}
 3730 events to select ionization templates, as either would result in a mismodeling of
 3731 the shape of the mass distribution. The simulated events contain only one par-
 3732 ticle type, however, so this test only establishes that the technique works well
 3733 when the the CRs are populated by exactly the same species.

3734 11.3.2 VALIDATION REGION IN DATA

3735 The second test of the background estimate is performed using data in an or-
 3736 thogonal validation region. The validation region, and the corresponding CRs,
 3737 are formed using the same selection requirements as in the nominal method but
 3738 with a modified requirement on momentum, $50 < p[\text{GeV}] < 150$. This allows
 3739 the technique to be checked in a region with very similar properties but where
 3740 the signal is depleted, as the majority of the signal has momentum above 150
 3741 GeV while the backgrounds are enhanced below that threshold. Any biases on
 3742 the particle composition of the CRs for the signal region will be reflected in the
 3743 CRs used to estimate the mass distribution in the validation region.

3744 Figure 89 shows the measured and randomly generated mass distributions for
 3745 data before and after the ionization requirement. The background estimate mod-
 3746 els the actual background before the ionization requirement very well, with good
 3747 agreement to within the statistical uncertainties out to the limit of the mass dis-
 3748 tribution. There are very few events in the validation region after the ionization
 3749 requirement, but the few observed events are consistent with the background
 3750 prediction. The good agreement in this validation region provides a confirma-
 3751 tion that the technique works even in the full-complexity case with multiple par-
 3752 ticle types entering the distributions. Any bias from changes in particle compo-
 3753 sition between regions is small compared to statistical uncertainties.

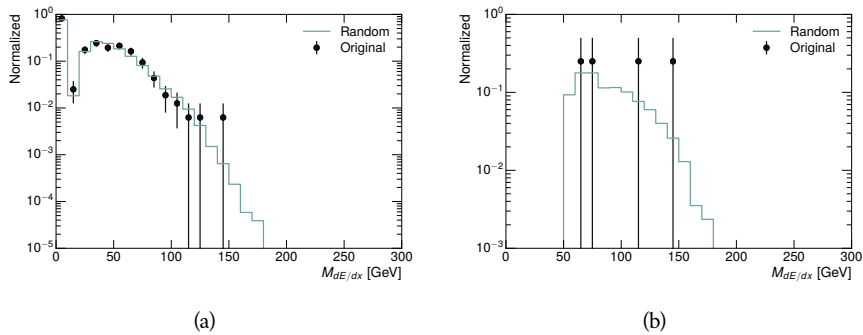


Figure 89: The distribution of $M_{dE/dx}$ (a) before and (b) after the ionization require-
 ment for tracks in the validation region and for the randomly generated back-
 ground estimate.

3754 11.4 EXPECTED BACKGROUND

3755 Using the full technique in the primary regions described in Section 11.2 pro-
 3756 vides a final background estimate for the signal region of this search. It predicts
 3757 a total background of 11.1 ± 1.7 events in the LL region and 17.2 ± 2.6 events in
 3758 the VLL region. Table 10 shows the number of events predicted in mass windows
 3759 for the grid of mass points, for each of the LL and VLL signal regions. Only one
 3760 to two events are expected in each mass window, as the background distribution
 3761 falls with increasing mass.

Mass	Expected Background, LL	Expected Background, VLL
1000	1.328 ± 0.063	1.803 ± 0.081
1100	1.255 ± 0.060	1.409 ± 0.069
1200	1.193 ± 0.058	1.310 ± 0.066
1300	0.997 ± 0.051	1.431 ± 0.069
1400	1.131 ± 0.056	1.273 ± 0.065
1500	1.111 ± 0.055	1.115 ± 0.059
1600	1.193 ± 0.058	1.041 ± 0.057
1800	1.138 ± 0.056	0.918 ± 0.053

Table 10: The expected number of background events within each of the mass windows for the stable and metastable signal regions.

3762

3763 SYSTEMATIC UNCERTAINTIES

3764 A number of systematic uncertainties affect the interpretation of the results of
 3765 the search. These uncertainties can be broken down into two major categories,
 3766 those which affect the estimate of the background using data and those which
 3767 affect the measurement of the signal yield estimated with simulated events. The
 3768 total measured systematic uncertainties range between 6-7% for the background
 3769 estimation and 29-33% for the signal yield depending on lifetime. These system-
 3770 atic uncertainties are expected to be small compared to the statistical fluctuations
 3771 of the measured yields so that measured cross-sectional limits will be dominated
 3772 by statistical uncertainties. Only the systematic uncertainties on the background
 3773 estimation are relevant for the search for LLPs, as the systematics on the signal
 3774 yield enter only into the calculation of limits in the absence of a signal. The fol-
 3775 lowing sections describe each source of systematic uncertainty for each of the
 3776 two types.

3777 12.1 BACKGROUND ESTIMATE

3778 The systematic uncertainties on the background estimate come primarily from
 3779 considering alternative methods for generating the background distributions.
 3780 These uncertainties are small compared to the statistical uncertainties on the
 3781 background estimate which come from the limited statistics in measuring the
 3782 template distributions, as described in Section 11.2. They are summarized in
 3783 Table 11.

Source of Uncertainty:	Value [%]
Analytic Description of dE/dx	4.0
Muon Fraction (VLL Region only)	3.0
IBL Ionization Correction	3.8
Normalization	3.0
Total (LL Region):	6.3
Total (VLL Region):	7.0

Table 11: A summary of the sources of systematic uncertainty for the data-driven back-
 ground in the signal region. If the uncertainty depends on the mass, the maxi-
 mum values are reported.

3784 12.1.1 ANALYTIC DESCRIPTION OF dE/dx

3785 The background estimate uses a binned template distribution to estimate the
 3786 dE/dx of tracks in the signal region, as described in Section 11.2. It is also possi-
 3787 ble to fit that measured distribution to a functional form to help smooth the dis-
 3788 tribution in the tails of dE/dx where the template is driven by a small number
 3789 of tracks. Both Landau convolved with a Gaussian and Crystal Ball functions
 3790 are considered as the functional form and used to re-estimate the background
 3791 distribution. The deviations compared to the nominal method are found to be
 3792 4%, and this is taken as a systematic uncertainty to cover the inability to care-
 3793 fully predict the contribution from the long tail of dE/dx where there are few
 3794 measurements available in data.

3795 12.1.2 MUON FRACTION

3796 The signal region for **VLL** R-Hadrons explicitly includes tracks identified as muons,
 3797 which have a known difference in their dE/dx distributions compared to non-
 3798 muon tracks (Section 11.1). To account for a difference in muon fraction be-
 3799 tween the background region and the signal region for this selection, the dE/dx
 3800 templates for muons and non-muons are measured separately and then the rel-
 3801 ative fraction of each is varied in the random generation. The muon fraction
 3802 is varied by its statistical uncertainty and the resulting difference of 3% in back-
 3803 ground yield is taken as the systematic uncertainty.

3804 12.1.3 **IBL** CORRECTIONS

3805 The **IBL**, described in Section 5.3.1, received a significant dose of radiation during
 3806 the data collection in 2015. The irradiation can cause a drift in the **ToT** calibra-
 3807 tion of the frontend electronics and thus alter the dE/dx measurement which
 3808 includes the **ToT** output by the **IBL**. These effects are corrected for in the nomi-
 3809 nal analysis by scaling the dE/dx measurements by a constant factor derived for
 3810 each run to match the average dE/dx value to a reference run. However, this
 3811 corrective factor does not account for inter-run variations. To account for the
 3812 potential drift of dE/dx within a single run, the correction procedure is repeated
 3813 by varying the corrections up and down by the maximal run-to-run variation
 3814 from the full data-taking period, which results in an uncertainty of 3.8%.

3815 12.1.4 NORMALIZATION

3816 As described in Section 11.2, the generated distribution of masses is normalized
 3817 in a shoulder region ($M < 160$ GeV) where signals have been excluded by pre-
 3818 vious analyses. That normalization factor is varied by its statistical uncertainty
 3819 and the resulting fluctuation in the mass distribution of 3% is taken as a system-
 3820 atic uncertainty on the background estimate.

3821 12.2 SIGNAL YIELD

3822 The systematic uncertainties on the signal yield can be divided into three categories; those on the simulation process, those on the modeling of the detector
 3823 efficiency or calibration, and those affecting the overall signal yield. They are
 3824 summarized in Table 11. The largest uncertainty comes from the uncertainty on
 3825 the production cross section for gluinos.

Source of Uncertainty	-[%]	+[%]
ISR Modeling (<code>LL</code> Region)	1.5	1.5
ISR Modeling (<code>VLL</code> Region)	14	14
Pile-up Reweighting	1.1	1.1
Trigger Efficiency Reweighting	0.9	0.9
E_T^{miss} Scale	1.1	2.2
Ionization Parametrization	7.1	0
μ Identification	4.3	4.3
Luminosity	5	5
Signal size uncertainty	28	28
Total (<code>LL</code> Region)	30	29
Total (<code>VLL</code> Region)	33	32

Table 12: A summary of the sources of systematic uncertainty for the simulated signal yield. The uncertainty depends on the mass and lifetime, and the maximum negative and positive values are reported in the table.

3827 12.2.1 ISR MODELING

3828 As discussed in Section 9.2, `MadGraph` is expected to reproduce the distribution
 3829 of `ISR` in signal events more accurately than the nominal `Pythia` samples [92].
 3830 The analysis reweights the distribution of `ISR` in the simulated signal events to
 3831 match the distribution found in generated `MadGraph` samples. This has an effect
 3832 on the selection efficiency in the signal samples, where `ISR` contributes to the
 3833 generation of E_T^{miss} . To account for the potential inaccuracy on the simulation
 3834 of `ISR` at high energies, half of the difference between the signal efficiency with
 3835 the reweighted distribution and the original distribution is taken as a systematic
 3836 uncertainty.

3837 12.2.2 PILEUP REWEIGHTING

3838 The simulated events were generated prior to data collection with an estimate of
 3839 the average number of interactions per bunch crossing. This estimate does not
 3840 match the value of pileup during actual data collection, but a large fraction of the

3841 simulated events would be discarded in order to match the distribution in data.
 3842 Therefore the simulated signal events are not reweighted for pileup by default
 3843 in the analysis. The effect of the pileup on signal efficiency is not expected to
 3844 depend on the mass or lifetime of the generated signal events, which allows all
 3845 of the generated signal events to be used together to assess the pileup dependence.
 3846 To account for the potential effect of the difference in the number of interactions
 3847 per bunch crossing between data and simulation, the difference in yield between
 3848 the nominal signal events and the reweighted events averaged over all masses
 3849 and lifetimes is taken as a systematic uncertainty on the yield for each mass and
 3850 lifetime (1.1%).

3851 12.2.3 TRIGGER EFFICIENCY REWEIGHTING

3852 As described in Section 10.2, the selection for this analysis does not require a suf-
 3853 ficiently large value of E_T^{miss} to be above the plateau of trigger efficiency. There-
 3854 fore, some signal events which would otherwise pass the event selection can be
 3855 excluded because of the trigger requirement. These effects can be difficult to es-
 3856 timate in simulation, and thus are constrained by comparing data and simulated
 3857 events in an alternative W boson region which uses decays to muons to find a rel-
 3858 atively pure sample of events with missing energy. The trigger efficiencies for
 3859 data and simulated W events are shown in Figure 90. The comparison between
 3860 data and MC in this region constrains the simulation of the trigger efficiency.
 3861 The simulated signal events are reweighted by the ratio of data to simulation in
 3862 the W boson decays, while the difference between the data and simulation in
 3863 those decays is taken as a systematic uncertainty. This results in an uncertainty
 3864 of only 0.9% as the majority of events are well above the plateau and the disagree-
 3865 ment between data and simulation is small even below that plateau.

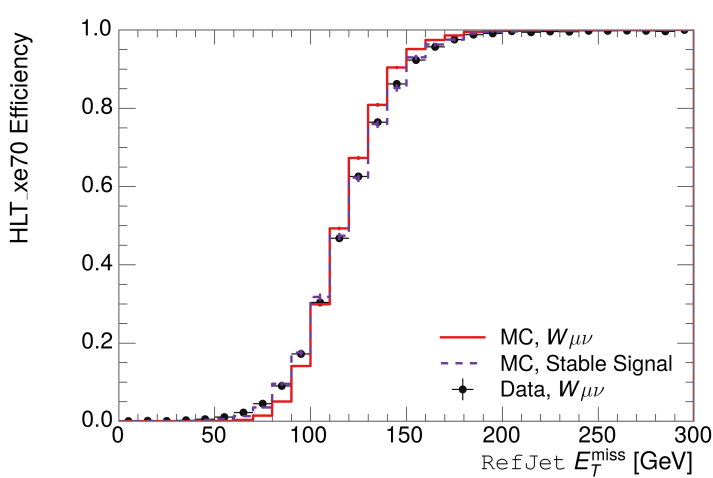


Figure 90: The trigger efficiency for the HLT_xe70 trigger requirement as a function of Calorimeter E_T^{miss} for simulated data events with a W boson selection. Simulated signal events and simulated W boson events are also included.

Systematic Variation	-[%]	+[%]
JET_GroupedNP_1	-0.7	1.3
JET_GroupedNP_2	-0.7	1.2
JET_GroupedNP_3	-0.5	1.3

Table 13: Example of the contributing systematic variations to the total systematic for the E_T^{miss} Scale, as measured in a 1200 GeV, [VLL](#) R-Hadron signal sample.

3866 12.2.4 MISSING TRANSVERSE MOMENTUM SCALE

3867 Variations on the [JES](#) enter into this analysis only in the requirement on E_T^{miss} ,
 3868 as variations on individual jets can alter the reconstructed E_T^{miss} in signal events.
 3869 The effect of the measured E_T^{miss} is evaluated by varying the E_T^{miss} scale accord-
 3870 ing to the one sigma variations on objects affecting event kinematics in simu-
 3871 lated signal events. Missing energy is reconstructed from fully reconstructed
 3872 objects so any systematic uncertainties affecting jets, muons, electrons, or the
 3873 E_T^{miss} soft terms are included. The variations on these objects are taken from
 3874 measurements in data using balance techniques as discussed in Section 6.4.3.
 3875 The resulting difference in selection efficiency is expected to be small, because
 3876 the jet variations only alter energies by a few percent. The only non-negligible
 3877 contributions found using this method are itemized in Table 13 for an example
 3878 signal sample (1200 GeV, [VLL](#) R-Hadron), where the systematic is measured as
 3879 the relative difference in the final signal efficiency after applying the associated
 3880 variation through the CP tools. The only variations that are significant are the
 3881 grouped jet systematic variations, which combine recommended jet systematic
 3882 uncertainties into linearly independent variations.

3883 As the peak of the reconstructed E_T^{miss} distribution in the signal is significantly
 3884 above the current threshold for events which pass the trigger requirement, the
 3885 effect of scale variation is expected to be small, which is consistent with the mea-
 3886 sured systematic error of approximately 2%. Events which do not pass the trigger
 3887 requirement usually fail because there are no ISR jets in the event to balance the
 3888 R -hadrons' transverse momentum, so the reconstructed E_T^{miss} is low and there-
 3889 fore also expected to be not very sensitive to scale changes.

3890 12.2.5 MOMENTUM PARAMETRIZATION

3891 The uncertainty on the signal efficiency from track momentum is calculated us-
 3892 ing the sagitta bias for q/P_{γ} , the only systematic variation of tracking that effects
 3893 track momentum. The systematic is only important for tracks that are near the
 3894 150 GeV momentum threshold, as the variation may push these tracks above
 3895 or below the selection requirement. Because the majority of R-Hadron tracks
 3896 are well above this value (Figure 80), the resulting uncertainty is expected to be
 3897 small. This uncertainty is propagated to the final selection efficiency by varying

3898 the track momentum by the measured one sigma variations from tracking mea-
 3899 surements [30], and the associated uncertainty is found to be negligible (0.3%).

3900 12.2.6 IONIZATION REQUIREMENT

3901 The dE/dx distributions in data and simulated events have different most prob-
 3902 able values, which is due in part to radiation effects in the detector that are not
 3903 fully accounted for in the simulation. The difference does not affect the mass
 3904 measurement used in this analysis, as independent calibrations are done in sim-
 3905 ulation and in data. However, it does affect the efficiency of the high dE/dx
 3906 selection requirement. To calculate the size of the effect on the signal efficiency,
 3907 the dE/dx distribution in signal simulation is scaled by a factor obtained from
 3908 comparing the dE/dx distribution of inclusive tracks in data and in simulation.
 3909 The difference in efficiency for this sample with a scaled dE/dx distribution, rel-
 3910 ative to the nominal case, is taken as a systematic uncertainty on signal efficiency.
 3911 The uncertainty is as large as 7% for low masses and falls to a negligible effect for
 3912 large masses.

3913 12.2.7 ELECTRON AND JET REJECTION

3914 The systematic uncertainty on the electron rejection is measured by varying the
 3915 EM fraction requirement significantly, from 0.95 to 0.9. This is found to have
 3916 a less than 0.04% effect on signal acceptance, on average, and so is completely
 3917 negligible. Similarly, the uncertainty on jet rejection is measured by tightening
 3918 the E/p requirement from 0.5 to 0.4. This is found to have no effect on signal
 3919 acceptance, so again the systematic is again negligible.

3920 12.2.8 MUON VETO

3921 The signal region for [LL](#) particles has a requirement that the candidate tracks are
 3922 not identified as medium muons because the majority of R-Hadrons in the life-
 3923 time range included in that region do not reach the muon spectrometers before
 3924 they decay. However, the exponential tail of the R-Hadron lifetime distribution
 3925 results in some R-Hadrons traversing the muon spectrometer. Even these R-
 3926 Hadrons can still fail the muon medium identification some of the time, because
 3927 they may arrive late to the muon spectrometer as discussed in Section 9.1.1. The
 3928 hits generated by a R-Hadron will not be readout if it arrives 25 ns after the
 3929 bunch crossing, causing it to fail the loose muon selection (Section 6.3.1). This
 3930 can be seen in Figure 91, which shows the efficiency of the muon veto as a func-
 3931 tion of $1/\beta$, for two simulated [VLL](#) R-Hadron samples.

3932 Thus, the efficiency of the muon veto depends on the timing resolution of
 3933 the spectrometer, so an uncertainty is applied to the signal efficiency to cover
 3934 differences in timing resolution between data and simulation. First, a sample of
 3935 $Z \rightarrow \mu\mu$ events is selected in data in which one of the muons has a late arrival
 3936 time measured in the [MDT](#). Then the reconstructed β distribution is compared
 3937 to the distribution in simulated $Z \rightarrow \mu\mu$ events; the difference between these

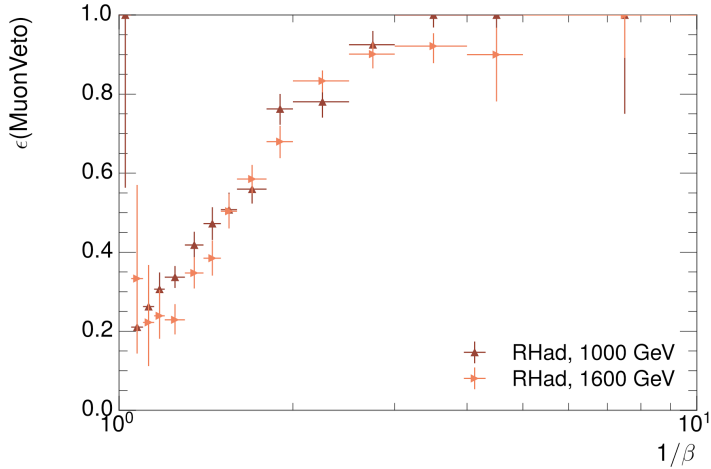


Figure 91: The efficiency of the muon veto for R -hadrons of two different masses, as a function of $\frac{1}{\beta}$ for simulated R-Hadron tracks.

3938 two distributions reflects the difference in timing resolution between data and
 3939 simulation. To emulate this difference in simulated signal events, the magnitude
 3940 of the difference is used to scale and shift the true β distribution of R -Hadrons in
 3941 simulation. Signal events are then reweighted based on this varied β distribution,
 3942 and the difference in the efficiency of the muon veto selection is compared with
 3943 the nominal and reweighted true β distributions. The difference in muon veto
 3944 efficiency is taken as a systematic uncertainty of the muon veto.

3945 The comparison of reconstructed β between data and simulation is performed
 3946 separately in the barrel, transition, and endcap regions of the spectrometer, and
 3947 the reweighting of the true β distribution in signal is done per region. The com-
 3948 parison of average reconstructed MDT β between data and simulation for the
 3949 barrel region is shown in Figure 92 for $Z \rightarrow \mu\mu$ events. As expected, The uncer-
 3950 tainty is found to be negligible for R -hadrons with short lifetimes, and is only
 3951 significant for lifetimes above 30 ns.

3952 12.2.9 LUMINOSITY

3953 The luminosity uncertainty is provided by a luminosity measurement on ATLAS
 3954 and was measured to be 5% at the time of the publication of this analysis. The
 3955 uncertainty is estimated by comparing luminosity measurements using several
 3956 independent luminometers [107].

3957 12.2.10 SIGNAL CROSS SECTION

3958 As discussed in Section 9.2, the signal cross sections are calculated at NLO in the
 3959 strong coupling constant with a resummation of soft-gluon emission at NLL. The
 3960 nominal predictions and the uncertainties for each mass point are taken from an
 3961 envelope of cross-section predictions using different PDF sets and factorization

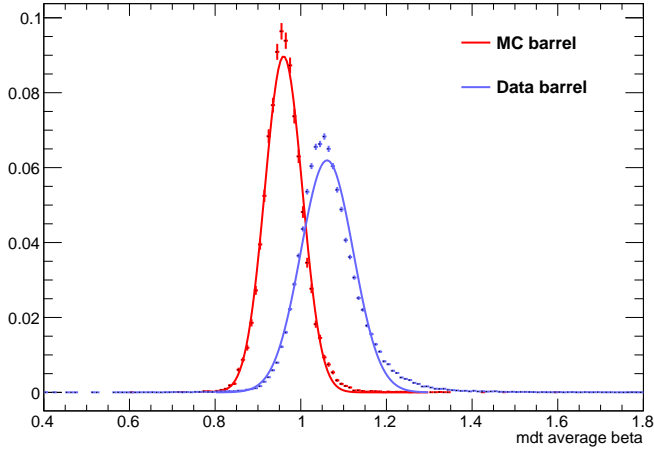


Figure 92: The average reconstructed MDT β distribution for $Z \rightarrow \mu\mu$ events in which one of the muons has a late arrival time in the MDT, for both data and simulation. A gaussian fit is superimposed.

3962 and renormalization scales [102], as discussed in Section 9.2. The uncertainties
3963 on those cross sections range between 14% and 28% for R-Hadrons in the range
3964 of 400 to 1800 GeV [103, 104]. The uncertainty increases with the mass.

3965

3966 RESULTS

3967 Sixteen events were observed in the **VLL** signal region and eleven events were
 3968 observed in the **LL** signal region, prior to requirements on the candidate track
 3969 mass. The background estimate predicts $17 \pm 2.6(\text{stat}) \pm 1.2(\text{syst})$ events for
 3970 the **VLL** region and $11.1 \pm 1.7(\text{stat}) \pm 0.7(\text{syst})$ events for the **LL** region. These
 3971 counts are summarized in Table 14.

3972 The mass estimated using dE/dx (Section 10.4.1) provides the final discriminating
 3973 variable, where the signal would be expected as an excess in the falling exponential tail of the expected background. The observed distribution of masses
 3974 is shown in Figure 93, along with the predicted distribution from the background
 3975 estimate for each signal region. Both include a few example simulated signal dis-
 3976 tributions, which show the scale of an excess were the R-Hadron signals present.
 3977 Their is no statistically significant evidence of an excess in the data over the back-
 3978 ground estimation. From this distribution it is clearly possible to rule out signals
 3979 with lower masses, around 1200 GeV, which have larger cross sections.
 3980

3981 13.1 CROSS SECTION LIMITS

3982 Because there is no significant excess of events observed in the signal region, this
 3983 analysis sets upper limits on the allowed cross section for R-Hadron production.
 3984 These limits are set for each mass point by counting the observed events in data,
 3985 along with the expected background and simulated signal events, in windows of
 3986 mass. The mass windows are formed by fitting the distribution of signal events to
 3987 a Gaussian distribution, and the window is then $\pm 1.4\sigma$ around the center of that
 3988 Gaussian. Two examples of the windows formed by this procedure are shown in
 3989 Tables 15–16, for the **VLL** and 10 ns working points. The corresponding counts of
 3990 observed data, expected background, and simulated signal for those same work-
 3991 ing points are shown in Tables 17–18. Appendix A includes the mass windows
 3992 and counts for all of the considered signal points.

3993 The 95% confidence level upper limits on the cross sections for a large grid
 3994 of masses (between 800 and 1800 GeV) and lifetimes (between 0.4 and **VLL**) are

Selection Region	Expected Background	Data
VLL	$17.2 \pm 2.6 \pm 1.2$	16
LL	$11.1 \pm 1.7 \pm 0.7$	11

Table 14: The estimated number of background events and the number of observed events in data for the specified selection regions prior to the requirement on mass. The background estimates show statistical and systematic uncertainties.

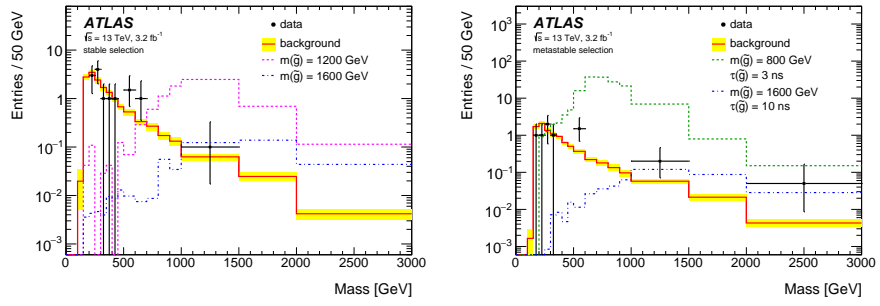


Figure 93: The observed mass distribution of events in data and the generated background distribution in (a) the **VLL** and (b) the **LL** signal region. A few example simulated signal distributions are superimposed.

$m(\tilde{g})$ [GeV]	Left Extremum [GeV]	Right Extremum [GeV]
1000	655	1349
1100	734	1455
1200	712	1631
1300	792	1737
1400	717	1926
1500	815	2117
1600	824	2122
1700	900	2274
1800	919	2344

Table 15: The left and right extremum of the mass window for each generated mass point with a 10 ns lifetime.

$m(\tilde{g})$ [GeV]	Left Extremum [GeV]	Right Extremum [GeV]
800	627	1053
1000	726	1277
1200	857	1584
1400	924	1937
1600	993	2308
1800	1004	2554

Table 16: The left and right extremum of the mass window used for each generated **VLL** mass point.

$m(\tilde{g})$ [GeV]	Expected Signal	Expected Background	Observed Data
800	462.83 ± 14.86	1.764 ± 0.080	2
1000	108.73 ± 3.38	1.458 ± 0.070	1
1200	31.74 ± 0.95	1.137 ± 0.060	1
1400	10.22 ± 0.29	1.058 ± 0.058	1
1600	3.07 ± 0.09	0.947 ± 0.054	1
1800	1.08 ± 0.05	0.940 ± 0.054	1

Table 17: The expected number of signal events, the expected number of background events, and the observed number of events in data with their respective statistical errors within the respective mass window for each generated **VLL** mass point

$m(\tilde{g})$ [GeV]	Expected Signal	Expected Background	Observed Data
1000	144.48 ± 5.14	1.499 ± 0.069	2
1100	73.19 ± 2.61	1.260 ± 0.060	2
1200	41.54 ± 1.41	1.456 ± 0.067	2
1300	22.58 ± 0.77	1.201 ± 0.058	2
1400	12.70 ± 0.42	1.558 ± 0.071	2
1500	6.73 ± 0.24	1.237 ± 0.060	2
1600	3.90 ± 0.13	1.201 ± 0.058	2
1700	2.27 ± 0.07	1.027 ± 0.052	2
1800	1.34 ± 0.04	1.019 ± 0.052	2

Table 18: The expected number of signal events, the expected number of background events, and the observed number of events in data with their respective statistical errors within the respective mass window for each generated mass point with a lifetime of 10 ns.

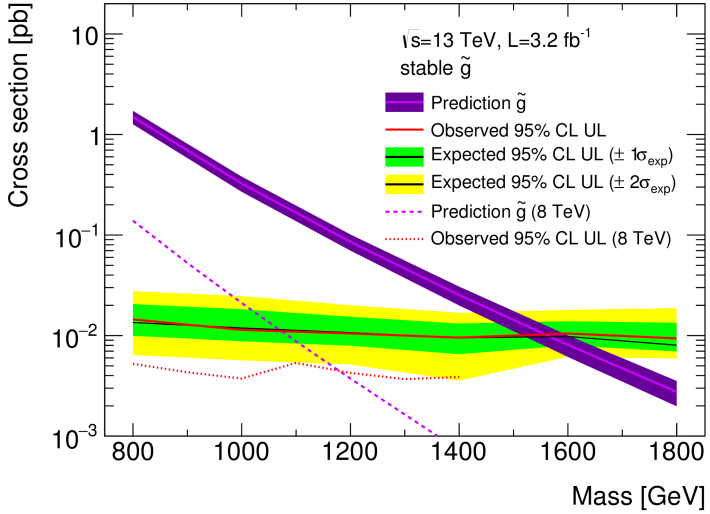


Figure 94: The observed and expected cross section limits as a function of mass for the `VLL` simulated signal. The predicted cross section values for the corresponding signals are also shown.

3995 extracted from these counts with the CL_S method using the profile likelihood
 3996 ratio as a test statistic [108]. For this procedure, the systematic uncertainties esti-
 3997 mated for the signal and background yields are treated as Gaussian-distributed
 3998 nuisance parameters. The uncertainty on the normalization of the expected
 3999 background distribution is included in the expected background events. At this
 4000 point the expected cross section limit is calculated for both the `LL` and `VLL` signal
 4001 region for each lifetime point, and the region with the best expected limit is se-
 4002 lected for each lifetime. Using that procedure, the `LL` region is used for lifetimes
 4003 up to and including 30 ns, and the `VLL` region for lifetimes above it.

4004 The resulting upper limits on the cross sections are shown as a function of
 4005 mass in Figure 94 and Figure 95 for each lifetime considered. The limits are
 4006 interpolated linearly between each mass point, and the dependence of the limit
 4007 on the mass is small as the efficiency is relatively constant for large R-Hadron
 4008 masses. There is however a strong dependence on lifetime, as discussed in Sec-
 4009 tion 10.5, where the probability to form a fully reconstructed track and the kine-
 4010 matic freedom to produce E_T^{miss} result in a local maximum in the limit at 10-30
 4011 ns. The figures also include the expected cross section for pair-produced gluino
 4012 R-Hadrons for reference. For the 10 ns and `VLL` cross section limits, both the
 4013 observed limit and expected cross section for the Run 1, 8 TeV version of this
 4014 analysis are also shown. There the cross section limits are lower because of the
 4015 larger available luminosity. The signal cross sections are also much lower be-
 4016 cause of the lower collision energy.

4017 13.2 MASS LIMITS

4018 The cross section limits can then be used to derive a lower mass limit for gluino
 4019 R-Hadrons by comparing them to the theoretically predicted production cross

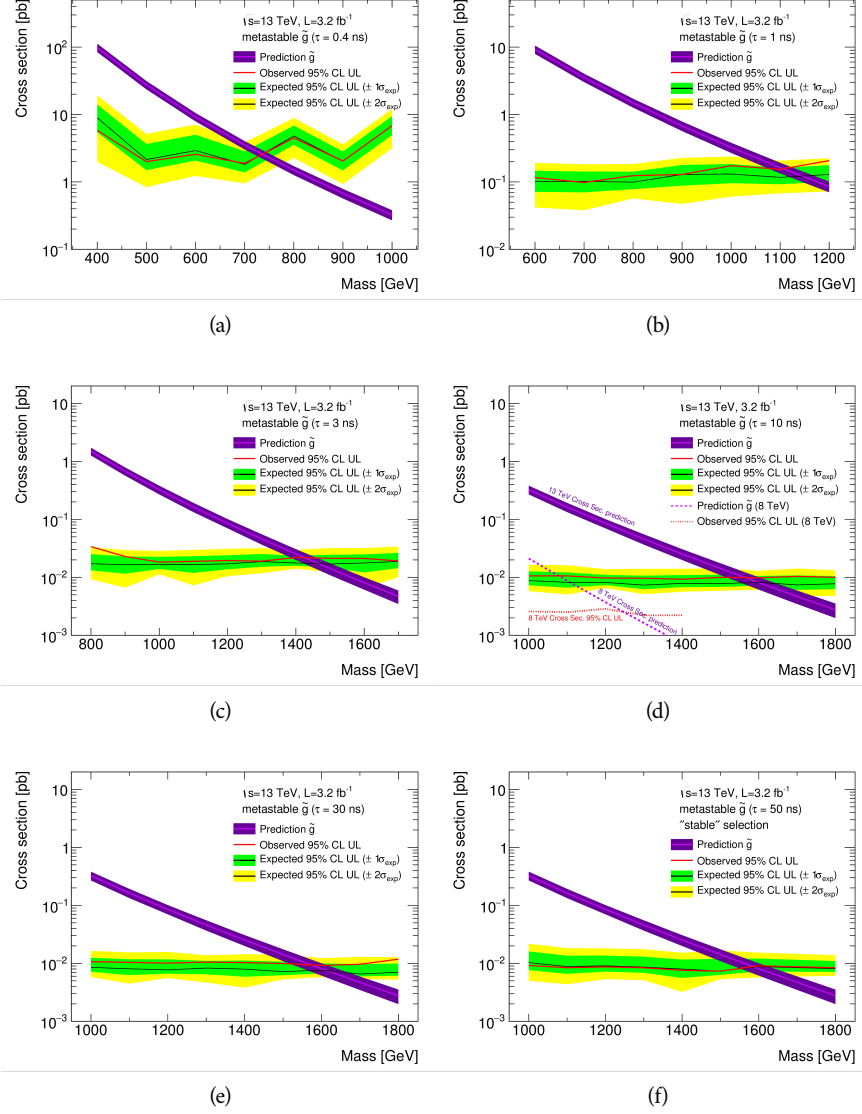


Figure 95: The observed and expected cross section limits as a function of mass for each generated lifetime. The predicted cross section values for the corresponding signals are also shown. An example of Run 1 cross section limits and predicted cross sections are shown in (d) for comparison.

4020 sections. These mass limits range from only 740 GeV at the lowest lifetimes con-
 4021 sidered, where the selection efficiency is very low, to up to 1580 GeV at 30 ns
 4022 where the selection efficiency is maximized. The observed and expected mass
 4023 limits for each lifetime point are detailed in Table 19, which also lists which se-
 4024 lection region was used for each lifetime. These excluded range of masses as a
 4025 function of lifetime is also shown in Figure 96. The Run 1 limits are included for
 4026 comparison; the limits have increased by about 200 GeV on average. The search
 4027 has also improved since the previous incarnation from Run 1 in optimizing the
 4028 region between 30 GeV and detector-stable lifetimes by introducing the second
 4029 signal region. The definition of the **VLL** region prevents the significant drop in
 4030 mass limit that occurred above 30 GeV in the Run 1 analysis.

Selection	τ [ns]	$M_{\text{obs}} > [\text{GeV}]$	$M_{\text{exp}} > [\text{GeV}]$
LL	0.4	740	730
"	1.0	1110	1150
"	3.0	1430	1470
"	10	1570	1600
"	30	1580	1620
VLL	50	1590	1590
"	VLL	1570	1580

Table 19: The observed and expected 95% CL lower limit on mass for gluino R-Hadrons for each considered lifetime.

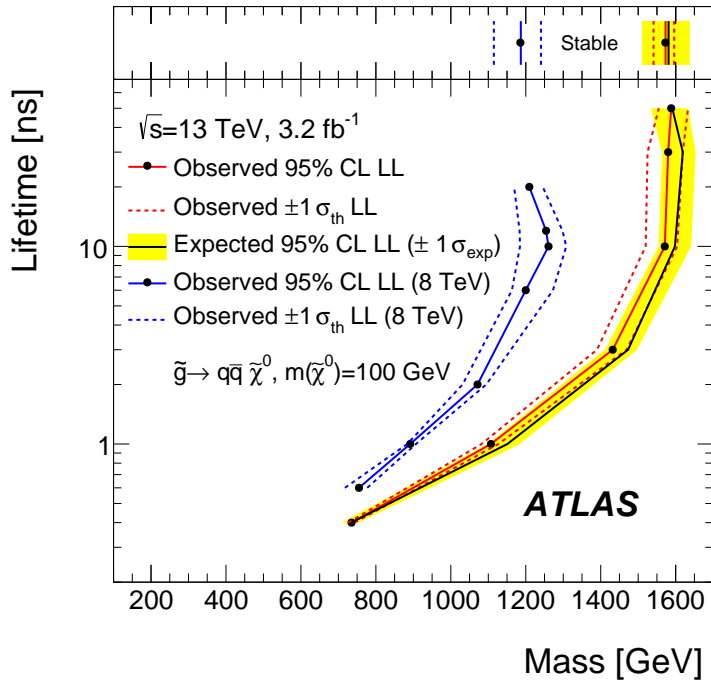


Figure 96: The excluded range of masses as a function of gluino lifetime. The expected lower limit (LL), with its experimental $\pm 1\sigma$ band, is given with respect to the nominal theoretical cross section. The observed 95% LL obtained at $\sqrt{s} = 8 \text{ TeV}$ [92] is also shown for comparison.

4031

4032 SUMMARY AND OUTLOOK

4033 The search described herein targetted the unique signature of TeV-scale, charged
 4034 **LLPs**, which are predicted in a variety of extensions to the **SM** including some
 4035 versions of **SUSY**. The dataset of 13 TeV proton-proton collisions was collected
 4036 during 2015 by the ATLAS detector at the **LHC**, with an integrated luminosity
 4037 of 3.2 fb^{-1} . The specific search strategy focused on identifying massive, charged
 4038 particles which propagate through the Pixel detector in ATLAS by their characteris-
 4039 tically large ionization. Recent updates to the strategy also include a num-
 4040 ber of rejection techniques that significantly reduce **SM** backgrounds compared
 4041 to previous iterations. The analysis also provided a data-driven background es-
 4042 timation method that was shown to be effective with validation tests in both
 4043 simulation and actual data.

4044 No significant excesses above the background prediction were found in the
 4045 data, and so limits were placed on the production of massive, charged, **LLPs**. Us-
 4046 ing a benchmark model of simulated R-Hadrons, cross sections above 10-100
 4047 fb were excluded at 95% confidence level, depending on the lifetime of the R-
 4048 Hadron. Together with the predicted gluino pair-production cross sections, these
 4049 lead to mass limits on R-Hadrons up to 1600 GeV where the search is most sen-
 4050 sitive. Though these specific values assume an R-Hadron **LLP**, the search strat-
 4051 egy accomodates a number of other species and the limits can be interpreted for
 4052 other models.

4053 This search plays an important role in the current, combined ATLAS search
 4054 for long lived particles. The mass limits provided by various ATLAS searches for
 4055 long-lived gluino R-Hadrons can be seen in Figure 97. This search provides the
 4056 most competitive limit for lifetimes between 3 ns up through very long lifetimes,
 4057 where it is still competitive with dedicated searches for **VLL** particles. The limits
 4058 placed on gluino production are very similar to the limits on promptly decaying
 4059 models.

4060 These results are expected to be significantly improved in the following years,
 4061 primarily because of continuing data collection at 13 TeV at the **LHC**. During
 4062 2016, but after the release of this analysis, ATLAS recorded an additional 35.5
 4063 fb^{-1} of collisions, and analysis of this data would significantly extend the limits
 4064 presented here. The next iteration of the analysis can also provide additional
 4065 interpretations of the search, by explicitly including other models like stop R-
 4066 Hadrons and charginos in the limit calculations, as has been done in previous
 4067 searches [92]. This strategy will continue to provide a competitive approach to
 4068 discovering new **LLPs** throughout the lifetime of the **LHC**.

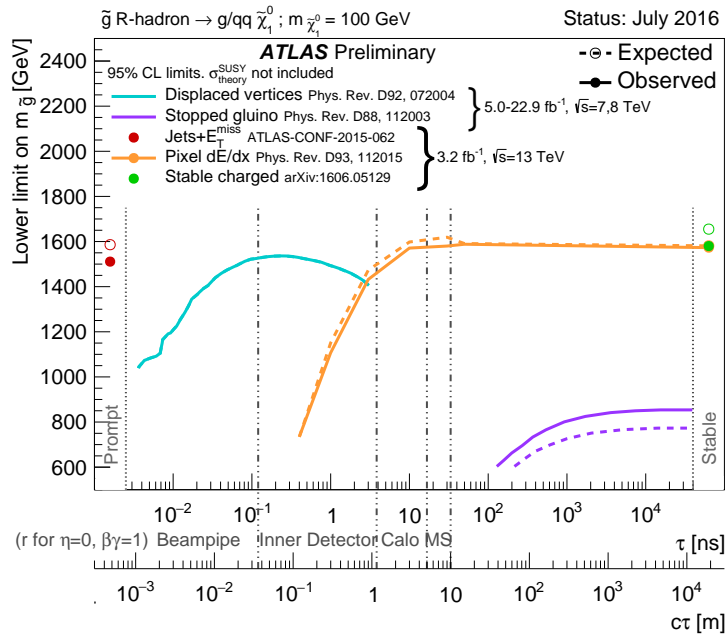


Figure 97: The constraints on the gluino mass as a function of lifetime for a split-supersymmetry model with the gluino R-Hadrons decaying into a gluon or light quarks and a neutralino with mass of 100 GeV. The solid lines indicate the observed limits, while the dashed lines indicate the expected limits. The area below the curves is excluded. The dots represent results for which the particle is assumed to be prompt or VLL. This curve representing this analysis is shown in orange.

4069

PART V

4070

APPENDIX

4071

$m(\tilde{g})$ [GeV]	Left Extremum [GeV]	Right Extremum [GeV]
1000	682	1387
1100	763	1478
1200	801	1606
1300	809	1841
1400	861	2011
1500	920	2032
1600	952	2173
1800	1017	2422

Table 20: The left and right extremum of the mass window for each generated mass point with a 50 ns lifetime.

$m(\tilde{g})$ [GeV]	Left Extremum [GeV]	Right Extremum [GeV]
1000	689	1321
1100	746	1513
1200	788	1670
1300	860	1734
1400	833	1925
1500	852	2048
1600	833	2283
1700	946	2379
1800	869	2505

Table 21: The left and right extremum of the mass window for each generated mass point with a 30 ns lifetime.

$m(\tilde{g})$ [GeV]	Left Extremum [GeV]	Right Extremum [GeV]
1000	655	1349
1100	734	1455
1200	712	1631
1300	792	1737
1400	717	1926
1500	815	2117
1600	824	2122
1700	900	2274
1800	919	2344

Table 22: The left and right extremum of the mass window for each generated mass point with a 10 ns lifetime.

$m(\tilde{g})$ [GeV]	Left Extremum [GeV]	Right Extremum [GeV]
800	531	1065
900	576	1165
1000	610	1345
1100	635	1432
1200	663	1563
1300	620	1667
1400	742	1727
1500	761	1937
1600	573	2000
1700	621	2182

Table 23: The left and right extremum of the mass window used for each generated mass point with a lifetime of 3 ns.

$m(\tilde{g})$ [GeV]	Left Extremum [GeV]	Right Extremum [GeV]
600	411	758
700	385	876
800	486	970
900	406	987
1000	408	1136
1100	555	1196
1200	516	1378

Table 24: The left and right extremum of the mass window used for each mass point with a lifetime of 1 ns.

$m(\tilde{g})$ [GeV]	Left Extremum [GeV]	Right Extremum [GeV]
400	204	510
500	295	639
600	288	702
700	323	701
800	190	771
900	277	677
1000	249	688

Table 25: The left and right extremum of the mass window for each generated mass point with a lifetime of 0.4 ns.

$m(\tilde{g})$ [GeV]	Left Extremum [GeV]	Right Extremum [GeV]
800	627	1053
1000	726	1277
1200	857	1584
1400	924	1937
1600	993	2308
1800	1004	2554

Table 26: The left and right extremum of the mass window used for each generated stable mass point.

$m(\tilde{g})$ [GeV]	Expected Signal	Expected Background	Observed Data
1000	131.18 ± 6.35	1.803 ± 0.081	1
1100	71.11 ± 3.35	1.409 ± 0.069	1
1200	37.18 ± 1.75	1.310 ± 0.066	1
1300	20.76 ± 0.95	1.431 ± 0.069	1
1400	12.63 ± 0.57	1.273 ± 0.065	1
1500	6.57 ± 0.29	1.115 ± 0.059	1
1600	3.56 ± 0.16	1.041 ± 0.057	1
1800	1.27 ± 0.05	0.918 ± 0.053	1

Table 27: The expected number of signal events, the expected number of background events, and the observed number of events in data with their respective statistical errors within the respective mass window for each generated mass point with a lifetime of 50 ns.

$m(\tilde{g})$ [GeV]	Expected Signal	Expected Background	Observed Data
1000	144.65 ± 6.34	1.328 ± 0.063	2
1100	75.28 ± 3.27	1.255 ± 0.060	2
1200	40.51 ± 1.75	1.193 ± 0.058	2
1300	20.91 ± 0.93	0.997 ± 0.051	2
1400	11.97 ± 0.51	1.131 ± 0.056	2
1500	6.81 ± 0.28	1.111 ± 0.055	2
1600	4.19 ± 0.16	1.193 ± 0.058	2
1700	2.42 ± 0.09	0.963 ± 0.050	2
1800	1.46 ± 0.05	1.138 ± 0.056	3

Table 28: The expected number of signal events, the expected number of background events, and the observed number of events in data with their respective statistical errors within the respective mass window for each generated mass point with a lifetime of 30 ns.

$m(\tilde{g})$ [GeV]	Expected Signal	Expected Background	Observed Data
1000	144.48 ± 5.14	1.499 ± 0.069	2
1100	73.19 ± 2.61	1.260 ± 0.060	2
1200	41.54 ± 1.41	1.456 ± 0.067	2
1300	22.58 ± 0.77	1.201 ± 0.058	2
1400	12.70 ± 0.42	1.558 ± 0.071	2
1500	6.73 ± 0.24	1.237 ± 0.060	2
1600	3.90 ± 0.13	1.201 ± 0.058	2
1700	2.27 ± 0.07	1.027 ± 0.052	2
1800	1.34 ± 0.04	1.019 ± 0.052	2

Table 29: The expected number of signal events, the expected number of background events, and the observed number of events in data with their respective statistical errors within the respective mass window for each generated mass point with a lifetime of 10 ns.

$m(\tilde{g})$ [GeV]	Expected Signal	Expected Background	Observed Data
800	362.97 ± 14.68	1.841 ± 0.080	5
900	169.20 ± 6.69	1.710 ± 0.076	3
1000	84.78 ± 3.23	1.727 ± 0.076	2
1100	40.06 ± 1.60	1.679 ± 0.075	2
1200	20.06 ± 0.81	1.598 ± 0.072	2
1300	10.76 ± 0.43	1.851 ± 0.080	2
1400	5.52 ± 0.22	1.374 ± 0.064	2
1500	3.16 ± 0.13	1.355 ± 0.064	2
1600	2.13 ± 0.11	2.235 ± 0.093	3
1700	1.10 ± 0.06	1.995 ± 0.085	2

Table 30: The expected number of signal events, the expected number of background events, and the observed number of events in data with their respective statistical errors within the respective mass window for each generated mass point with a lifetime of 3 ns.

$m(\tilde{g})$ [GeV]	Expected Signal	Expected Background	Observed Data
600	431.80 ± 36.60	2.418 ± 0.099	3
700	192.77 ± 15.28	3.267 ± 0.126	3
800	69.63 ± 5.90	2.125 ± 0.089	3
900	28.91 ± 2.59	3.114 ± 0.121	3
1000	13.64 ± 1.22	3.359 ± 0.129	5
1100	6.13 ± 0.57	1.879 ± 0.081	3
1200	3.24 ± 0.30	2.387 ± 0.098	5

Table 31: The expected number of signal events, the expected number of background events, and the observed number of events in data with their respective statistical errors within the respective mass window for each generated mass point with a lifetime of 1 ns.

$m(\tilde{g})$ [GeV]	Expected Signal	Expected Background	Observed Data
400	181.71 ± 75.59	6.780 ± 0.238	4
500	103.88 ± 30.05	4.310 ± 0.160	4
600	28.34 ± 9.34	4.868 ± 0.177	4
700	13.62 ± 4.00	3.908 ± 0.147	4
800	2.75 ± 1.15	9.001 ± 0.308	8
900	2.25 ± 0.71	5.045 ± 0.183	5
1000	0.34 ± 0.19	6.026 ± 0.214	6

Table 32: The expected number of signal events, the expected number of background events, and the observed number of events in data with their respective statistical errors within the respective mass window for each generated mass point with a lifetime of p4 ns.

$m(\tilde{g})$ [GeV]	Expected Signal	Expected Background	Observed Data
800	462.83 ± 14.86	1.764 ± 0.080	2
1000	108.73 ± 3.38	1.458 ± 0.070	1
1200	31.74 ± 0.95	1.137 ± 0.060	1
1400	10.22 ± 0.29	1.058 ± 0.058	1
1600	3.07 ± 0.09	0.947 ± 0.054	1
1800	1.08 ± 0.05	0.940 ± 0.054	1

Table 33: The expected number of signal events, the expected number of background events, and the observed number of events in data with their respective statistical errors within the respective mass window for each generated stable mass point

- 4075 [1] Michael E Peskin and Daniel V Schroeder. *An Introduction to Quantum*
4076 *Field Theory; 1995 ed.* Boulder, CO: Westview, 1995. URL: <https://cds.cern.ch/record/257493>.
- 4078 [2] Nobelprize.org. “The 2004 Nobel Prize in Physics - Popular Information”. 2014. URL: <https://cds.cern.ch/record/1165534>.
- 4080 [3] K. A. Olive et al. “Review of Particle Physics”. In: *Chin. Phys. C* 38 (2014),
4081 p. 090001. doi: [10.1088/1674-1137/38/9/090001](https://doi.org/10.1088/1674-1137/38/9/090001).
- 4082 [4] A. D. Martin, W. J. Stirling, R. S. Thorne, and G. Watt. “Parton distributions
4083 for the LHC”. In: *Eur. Phys. J. C* 63 (2009), pp. 189–285. doi: [10.1140/epjc/s10052-009-1072-5](https://doi.org/10.1140/epjc/s10052-009-1072-5). arXiv: [0901.0002 \[hep-ph\]](https://arxiv.org/abs/0901.0002).
- 4085 [5] Torbjorn Sjöstrand, Stephen Mrenna, and Peter Skands. “PYTHIA 6.4
4086 Physics and Manual”. In: *JHEP* 0605 (2006), p. 026. doi: [10.1088/1126-6708/2006/05/026](https://doi.org/10.1088/1126-6708/2006/05/026). arXiv: [hep-ph/0603175](https://arxiv.org/abs/hep-ph/0603175).
- 4088 [6] J. Alwall, R. Frederix, S. Frixione, V. Hirschi, F. Maltoni, O. Mattelaer, H.
4089 S. Shao, T. Stelzer, P. Torrielli, and M. Zaro. “The automated computation
4090 of tree-level and next-to-leading order differential cross sections, and
4091 their matching to parton shower simulations”. In: *JHEP* 07 (2014), p. 079.
4092 doi: [10.1007/JHEP07\(2014\)079](https://doi.org/10.1007/JHEP07(2014)079). arXiv: [1405.0301 \[hep-ph\]](https://arxiv.org/abs/1405.0301).
- 4093 [7] S. Agostinelli et al. “GEANT4: A simulation toolkit”. In: *Nucl. Instrum.*
4094 *Meth. A* 506 (2003), pp. 250–303. doi: [10.1016/S0168-9002\(03\)01368-8](https://doi.org/10.1016/S0168-9002(03)01368-8).
- 4096 [8] Prajwal Raj Kafle, Sanjib Sharma, Geraint F. Lewis, and Joss Bland-Hawthorn.
4097 “On the Shoulders of Giants: Properties of the Stellar Halo and the Milky
4098 Way Mass Distribution”. In: *Astrophys. J.* 794.1 (2014), p. 59. doi: [10.1088/0004-637X/794/1/59](https://doi.org/10.1088/0004-637X/794/1/59). arXiv: [1408.1787 \[astro-ph.GA\]](https://arxiv.org/abs/1408.1787).
- 4100 [9] Savas Dimopoulos and Howard Georgi. “Softly broken supersymmetry
4101 and SU(5)”. In: *Nuclear Physics B* 193.1 (1981), pp. 150 – 162. ISSN: 0550-
4102 3213. doi: [http://dx.doi.org/10.1016/0550-3213\(81\)90522-8](http://dx.doi.org/10.1016/0550-3213(81)90522-8).
- 4104 [10] A. Djouadi et al. “The Minimal supersymmetric standard model: Group
4105 summary report”. In: *GDR (Groupement De Recherche) - Supersymetrie Mont-*
4106 *pellier, France, April 15-17, 1998*. 1998. arXiv: [hep-ph/9901246 \[hep-ph\]](https://arxiv.org/abs/hep-ph/9901246).
4107 URL: https://inspirehep.net/record/481987/files/arXiv-hep-ph_9901246.pdf.
- 4109 [11] Lawrence J. Hall, Yasunori Nomura, and Satoshi Shirai. “Spread Super-
4110 *symmetry with Wino LSP: Gluino and Dark Matter Signals*. In: *JHEP* 01
4111 (2013), p. 036. doi: [10.1007/JHEP01\(2013\)036](https://doi.org/10.1007/JHEP01(2013)036). arXiv: [1210.2395 \[hep-ph\]](https://arxiv.org/abs/1210.2395).

- 4113 [12] G. F. Giudice and A. Romanino. "Split supersymmetry". In: *Nucl. Phys. B*
 4114 699 (2004), p. 65. doi: [10.1016/j.nuclphysb.2004.11.048](https://doi.org/10.1016/j.nuclphysb.2004.11.048). arXiv:
 4115 [hep-ph/0406088](https://arxiv.org/abs/hep-ph/0406088).
- 4116 [13] N. Arkani-Hamed, S. Dimopoulos, G. F. Giudice, and A. Romanino. "As-
 4117 pects of split supersymmetry". In: *Nucl. Phys. B* 709 (2005), p. 3. doi: [10.1016/j.nuclphysb.2004.12.026](https://doi.org/10.1016/j.nuclphysb.2004.12.026). arXiv: [hep-ph/0409232](https://arxiv.org/abs/hep-ph/0409232).
- 4119 [14] Lyndon Evans and Philip Bryant. "LHC Machine". In: *JINST* 3 (2008),
 4120 S08001. doi: [10.1088/1748-0221/3/08/S08001](https://doi.org/10.1088/1748-0221/3/08/S08001).
- 4121 [15] C Lefevre. "LHC: the guide (English version). Guide du LHC (version
 4122 anglaise)". 2009. URL: <https://cds.cern.ch/record/1165534>.
- 4123 [16] "LEP Design Report Vol.1". In: (1983).
- 4124 [17] ATLAS Collaboration. "The ATLAS Experiment at the CERN Large Hadron
 4125 Collider". In: *JINST* 3 (2008), S08003. doi: [10.1088/1748-0221/3/08/S08003](https://doi.org/10.1088/1748-0221/3/08/S08003).
- 4127 [18] S. Chatrchyan et al. "The CMS experiment at the CERN LHC". In: *JINST*
 4128 3 (2008), S08004. doi: [10.1088/1748-0221/3/08/S08004](https://doi.org/10.1088/1748-0221/3/08/S08004).
- 4129 [19] A. Augusto Alves Jr. et al. "The LHCb Detector at the LHC". In: *JINST* 3
 4130 (2008), S08005. doi: [10.1088/1748-0221/3/08/S08005](https://doi.org/10.1088/1748-0221/3/08/S08005).
- 4131 [20] K. Aamodt et al. "The ALICE experiment at the CERN LHC". In: *JINST*
 4132 3 (2008), S08002. doi: [10.1088/1748-0221/3/08/S08002](https://doi.org/10.1088/1748-0221/3/08/S08002).
- 4133 [21] Collaboration LHCb. "For LHCb Talks". 2012. URL: <http://cds.cern.ch/record/1463546>.
- 4135 [22] ATLAS Collaboration. "Luminosity Public Results". 2016. URL: <https://twiki.cern.ch/twiki/bin/view/AtlasPublic/LuminosityPublicResultsRun2>
- 4136 [23] Ars Technica. "Following protons on a trip to (and through) the LHC".
 4137 2010. URL: [http://arstechnica.com/science/2010/08/following-
 4138 protons-on-a-trip-to-and-through-the-lhc/](http://arstechnica.com/science/2010/08/following-protons-on-a-trip-to-and-through-the-lhc/).
- 4139 [24] M Capeans, G Darbo, K Einsweiller, M Elsing, T Flick, M Garcia-Sciveres,
 4140 C Gemme, H Pernegger, O Rohne, and R Vuillermet. *ATLAS Insertable B-*
 4141 *Layer Technical Design Report*. Tech. rep. CERN-LHCC-2010-013. ATLAS-
 4142 TDR-19. 2010. URL: <https://cds.cern.ch/record/1291633>.
- 4144 [25] ATLAS Collaboration. "A New Sub Detector for ATLAS". 2014. URL: <http://atlasexperiment.org/news/2014/a-new-sub-detector-for-ATLAS.html>.
- 4147 [26] ATLAS Collaboration. *2015 start-up trigger menu and initial performance*
 4148 *assessment of the ATLAS trigger using Run-2 data*. ATL-DAQ-PUB-2016-
 4149 001. 2016. URL: <https://cds.cern.ch/record/2136007>.
- 4150 [27] T. Cornelissen, M. Elsing, S. Fleischmann, W. Liebig, and E. Moyse. "Con-
 4151 cepts, Design and Implementation of the ATLAS New Tracking (NEWT)".
 4152 In: (2007). Ed. by A. Salzburger.
- 4153 [28] "Performance of the ATLAS Inner Detector Track and Vertex Recon-
 4154 struction in the High Pile-Up LHC Environment". In: (2012).

- 4155 [29] A. Salzburger. "The ATLAS Track Extrapolation Package". In: (2007).
- 4156 [30] ATLAS Collaboration. *Early Inner Detector Tracking Performance in the*
4157 *2015 Data at $\sqrt{s} = 13 \text{ TeV}$* . ATL-PHYS-PUB-2015-051. 2015. URL: <https://cds.cern.ch/record/2110140>.
- 4158
- 4159 [31] ATLAS Collaboration. "A neural network clustering algorithm for the
4160 ATLAS silicon pixel detector". In: *JINST* 9 (2014), P09009. doi: [10.1088/1748-0221/9/09/P09009](https://doi.org/10.1088/1748-0221/9/09/P09009). arXiv: [1406.7690 \[hep-ex\]](https://arxiv.org/abs/1406.7690).
- 4161
- 4162 [32] ATLAS Collaboration. *Performance of primary vertex reconstruction in proton-*
4163 *proton collisions at $\sqrt{s} = 7 \text{ TeV}$ in the ATLAS experiment*. ATLAS-CONF-
4164 2010-069. 2010. URL: <https://cds.cern.ch/record/1281344>.
- 4165 [33] ATLAS Collaboration. *Vertex Reconstruction Performance of the ATLAS De-*
4166 *tector at $\sqrt{s} = 13 \text{ TeV}$* . ATL-PHYS-PUB-2015-026. 2015. URL: <https://cds.cern.ch/record/2037717>.
- 4167
- 4168 [34] ATLAS Collaboration. "Electron reconstruction and identification effi-
4169 ciency measurements with the ATLAS detector using the 2011 LHC proton-
4170 proton collision data". In: *Eur. Phys. J. C* 74 (2014), p. 2941. doi: [10.1140/epjc/s10052-014-2941-0](https://doi.org/10.1140/epjc/s10052-014-2941-0). arXiv: [1404.2240 \[hep-ex\]](https://arxiv.org/abs/1404.2240).
- 4171
- 4172 PERF-2013-03.
- 4173 [35] ATLAS Collaboration. *Electron efficiency measurements with the ATLAS*
4174 *detector using the 2012 LHC proton–proton collision data*. ATLAS-CONF-
4175 2014-032. 2014. URL: <https://cds.cern.ch/record/1706245>.
- 4176 [36] ATLAS Collaboration. *Measurements of the photon identification efficiency*
4177 *with the ATLAS detector using 4.9 fb^{-1} of pp collision data collected in 2011*.
4178 ATLAS-CONF-2012-123. 2012. URL: <https://cds.cern.ch/record/1473426>.
- 4179
- 4180 [37] ATLAS Collaboration. "Muon reconstruction performance of the AT-
4181 LAS detector in proton–proton collision data at $\sqrt{s} = 13 \text{ TeV}$ ". In: (2016).
4182 arXiv: [1603.05598 \[hep-ex\]](https://arxiv.org/abs/1603.05598). PERF-2015-10.
- 4183
- 4184 [38] ATLAS Collaboration. "Topological cell clustering in the ATLAS calorime-
4185 ters and its performance in LHC Run 1". In: (2016). arXiv: [1603.02934](https://arxiv.org/abs/1603.02934)
[hep-ex]. PERF-2014-07.
- 4186
- 4187 [39] ATLAS Collaboration. *Properties of jets and inputs to jet reconstruction and*
4188 *calibration with the ATLAS detector using proton–proton collisions at $\sqrt{s} =$*
4189 *13 TeV* . ATL-PHYS-PUB-2015-036. 2015. URL: <https://cds.cern.ch/record/2044564>.
- 4190 [40] Matteo Cacciari, Gavin P. Salam, and Gregory Soyez. "The anti- k_t jet
4191 clustering algorithm". In: *JHEP* 04 (2008), p. 063. doi: [10.1088/1126-6708/2008/04/063](https://doi.org/10.1088/1126-6708/2008/04/063). arXiv: [0802.1189 \[hep-ph\]](https://arxiv.org/abs/0802.1189).
- 4192
- 4193 [41] ATLAS Collaboration. *Jet global sequential corrections with the ATLAS de-*
4194 *tector in proton–proton collisions at $\sqrt{s} = 8 \text{ TeV}$* . ATLAS-CONF-2015-002.
4195 2015. URL: <https://cds.cern.ch/record/2001682>.

- 4196 [42] ATLAS Collaboration. “A study of the material in the ATLAS inner detector
 4197 using secondary hadronic interactions”. In: *JINST* 7 (2012), P01013.
 4198 doi: [10.1088/1748-0221/7/01/P01013](https://doi.org/10.1088/1748-0221/7/01/P01013). arXiv: [1110.6191](https://arxiv.org/abs/1110.6191)
 4199 [[hep-ex](#)]. PERF-2011-08.
- 4200 [43] ATLAS Collaboration. “Electron and photon energy calibration with the
 4201 ATLAS detector using LHC Run 1 data”. In: *Eur. Phys. J. C* 74 (2014),
 4202 p. 3071. doi: [10.1140/epjc/s10052-014-3071-4](https://doi.org/10.1140/epjc/s10052-014-3071-4). arXiv: [1407.5063](https://arxiv.org/abs/1407.5063)
 4203 [[hep-ex](#)]. PERF-2013-05.
- 4204 [44] ATLAS Collaboration. “A measurement of the calorimeter response to
 4205 single hadrons and determination of the jet energy scale uncertainty us-
 4206 ing LHC Run-1 pp -collision data with the ATLAS detector”. In: (2016).
 4207 arXiv: [1607.08842](https://arxiv.org/abs/1607.08842) [[hep-ex](#)]. PERF-2015-05.
- 4208 [45] ATLAS Collaboration. “Single hadron response measurement and calorime-
 4209 ter jet energy scale uncertainty with the ATLAS detector at the LHC”. In:
 4210 *Eur. Phys. J. C* 73 (2013), p. 2305. doi: [10.1140/epjc/s10052-013-2305-1](https://doi.org/10.1140/epjc/s10052-013-2305-1). arXiv: [1203.1302](https://arxiv.org/abs/1203.1302) [[hep-ex](#)]. PERF-2011-05.
- 4212 [46] ATLAS Collaboration. “The ATLAS Simulation Infrastructure”. In: *Eur.*
 4213 *Phys. J. C* 70 (2010), p. 823. doi: [10.1140/epjc/s10052-010-1429-9](https://doi.org/10.1140/epjc/s10052-010-1429-9). arXiv: [1005.4568](https://arxiv.org/abs/1005.4568) [[hep-ex](#)]. SOFT-2010-01.
- 4215 [47] T. Sjöstrand, S. Mrenna, and P. Skands. “A Brief Introduction to PYTHIA
 4216 8.1”. In: *Comput. Phys. Commun.* 178 (2008), pp. 852–867. doi: [10.1016/j.cpc.2008.01.036](https://doi.org/10.1016/j.cpc.2008.01.036). arXiv: [0710.3820](https://arxiv.org/abs/0710.3820).
- 4218 [48] ATLAS Collaboration. *Summary of ATLAS Pythia 8 tunes*. ATL-PHYS-PUB-
 4219 2012-003. 2012. url: <http://cds.cern.ch/record/1474107>.
- 4220 [49] A.D. Martin, W.J. Stirling, R.S. Thorne, and G. Watt. “Parton distribu-
 4221 tions for the LHC”. In: *Eur. Phys. J. C* 63 (2009). Figures from the [MSTW Website](#),
 4222 pp. 189–285. doi: [10.1140/epjc/s10052-009-1072-5](https://doi.org/10.1140/epjc/s10052-009-1072-5).
 4223 arXiv: [0901.0002](https://arxiv.org/abs/0901.0002).
- 4224 [50] A. Sherstnev and R.S. Thorne. “Parton Distributions for LO Generators”.
 4225 In: *Eur. Phys. J. C* 55 (2008), pp. 553–575. doi: [10.1140/epjc/s10052-008-0610-x](https://doi.org/10.1140/epjc/s10052-008-0610-x). arXiv: [0711.2473](https://arxiv.org/abs/0711.2473).
- 4227 [51] A. Ribon et al. *Status of Geant4 hadronic physics for the simulation of LHC*
 4228 *experiments at the start of LHC physics program*. CERN-LCGAPP-2010-02.
 4229 2010. url: <http://lcgapp.cern.ch/project/docs/noteStatusHadronic2010.pdf>.
- 4231 [52] M. P. Guthrie, R. G. Alsmiller, and H. W. Bertini. “Calculation of the
 4232 capture of negative pions in light elements and comparison with experi-
 4233 ments pertaining to cancer radiotherapy”. In: *Nucl. Instrum. Meth.* 66
 4234 (1968), pp. 29–36. doi: [10.1016/0029-554X\(68\)90054-2](https://doi.org/10.1016/0029-554X(68)90054-2).
- 4235 [53] H. W. Bertini and P. Guthrie. “News item results from medium-energy
 4236 intranuclear-cascade calculation”. In: *Nucl. Instr. and Meth. A* 169 (1971),
 4237 p. 670. doi: [10.1016/0375-9474\(71\)90710-X](https://doi.org/10.1016/0375-9474(71)90710-X).

- [54] V.A. Karmanov. "Light Front Wave Function of Relativistic Composite System in Explicitly Solvable Model". In: *Nucl. Phys. B* 166 (1980), p. 378. doi: [10.1016/0550-3213\(80\)90204-7](https://doi.org/10.1016/0550-3213(80)90204-7).
- [55] H. S. Fesefeldt. *GHEISHA program*. Pitha-85-02, Aachen. 1985.
- [56] G. Folger and J.P. Wellisch. "String parton models in Geant4". In: (2003). arXiv: [nucl-th/0306007](https://arxiv.org/abs/nucl-th/0306007).
- [57] N. S. Amelin et al. "Transverse flow and collectivity in ultrarelativistic heavy-ion collisions". In: *Phys. Rev. Lett.* 67 (1991), p. 1523. doi: [10.1103/PhysRevLett.67.1523](https://doi.org/10.1103/PhysRevLett.67.1523).
- [58] N. S. Amelin et al. "Collectivity in ultrarelativistic heavy ion collisions". In: *Nucl. Phys. A* 544 (1992), p. 463. doi: [10.1016/0375-9474\(92\)90598-E](https://doi.org/10.1016/0375-9474(92)90598-E).
- [59] L. V. Bravina et al. "Fluid dynamics and Quark Gluon string model - What we can expect for Au+Au collisions at 11.6 AGeV/c". In: *Nucl. Phys. A* 566 (1994), p. 461. doi: [10.1016/0375-9474\(94\)90669-6](https://doi.org/10.1016/0375-9474(94)90669-6).
- [60] L. V. Bravin et al. "Scaling violation of transverse flow in heavy ion collisions at AGS energies". In: *Phys. Lett. B* 344 (1995), p. 49. doi: [10.1016/0370-2693\(94\)01560-Y](https://doi.org/10.1016/0370-2693(94)01560-Y).
- [61] B. Andersson et al. "A model for low-pT hadronic reactions with generalizations to hadron-nucleus and nucleus-nucleus collisions". In: *Nucl. Phys. B* 281 (1987), p. 289. doi: [10.1016/0550-3213\(87\)90257-4](https://doi.org/10.1016/0550-3213(87)90257-4).
- [62] B. Andersson, A. Tai, and B.-H. Sa. "Final state interactions in the (nuclear) FRITIOF string interaction scenario". In: *Z. Phys. C* 70 (1996), pp. 499–506. doi: [10.1007/s002880050127](https://doi.org/10.1007/s002880050127).
- [63] B. Nilsson-Almqvist and E. Stenlund. "Interactions Between Hadrons and Nuclei: The Lund Monte Carlo, Fritiof Version 1.6". In: *Comput. Phys. Commun.* 43 (1987), p. 387. doi: [10.1016/0010-4655\(87\)90056-7](https://doi.org/10.1016/0010-4655(87)90056-7).
- [64] B. Ganhuyag and V. Uzhinsky. "Modified FRITIOF code: Negative charged particle production in high energy nucleus nucleus interactions". In: *Czech. J. Phys.* 47 (1997), pp. 913–918. doi: [10.1023/A:1021296114786](https://doi.org/10.1023/A:1021296114786).
- [65] ATLAS Collaboration. "Topological cell clustering in the ATLAS calorimeters and its performance in LHC Run 1". In: (2016). arXiv: [1603.02934 \[hep-ex\]](https://arxiv.org/abs/1603.02934).
- [66] Peter Speckmayer. "Energy Measurement of Hadrons with the CERN ATLAS Calorimeter". Presented on 18 Jun 2008. PhD thesis. Vienna: Vienna, Tech. U., 2008. URL: <http://cds.cern.ch/record/1112036>.
- [67] CMS Collaboration. "The CMS barrel calorimeter response to particle beams from 2 to 350 GeV/c". In: *Eur. Phys. J. C* 60.3 (2009). doi: [10.1140/epjc/s10052-009-0959-5](https://doi.org/10.1140/epjc/s10052-009-0959-5).
- [68] J. Beringer et al. (Particle Data Group). "Review of Particle Physics". In: *Chin. Phys. C* 38 (2014), p. 090001. URL: <http://pdg.lbl.gov>.

- [69] P. Adragna et al. "Measurement of Pion and Proton Response and Longitudinal Shower Profiles up to 20 Nuclear Interaction Lengths with the ATLAS Tile Calorimeter". In: *Nucl. Instrum. Meth. A* 615 (2010), pp. 158–181. doi: [10.1016/j.nima.2010.01.037](https://doi.org/10.1016/j.nima.2010.01.037).
- [70] ATLAS Collaboration. "Jet energy measurement and its systematic uncertainty in proton–proton collisions at $\sqrt{s} = 7$ TeV with the ATLAS detector". In: *Eur. Phys. J. C* 75 (2015), p. 17. doi: [10.1140/epjc/s10052-014-3190-y](https://doi.org/10.1140/epjc/s10052-014-3190-y). arXiv: [1406.0076 \[hep-ex\]](https://arxiv.org/abs/1406.0076). PERF-2012-01.
- [71] Hung-Liang Lai, Marco Guzzi, Joey Huston, Zhao Li, Pavel M. Nadolsky, et al. "New parton distributions for collider physics". In: *Phys. Rev. D* 82 (2010), p. 074024. doi: [10.1103/PhysRevD.82.074024](https://doi.org/10.1103/PhysRevD.82.074024). arXiv: [1007.2241 \[hep-ph\]](https://arxiv.org/abs/1007.2241).
- [72] E. Abat et al. "Study of energy response and resolution of the ATLAS barrel calorimeter to hadrons of energies from 20 to 350 GeV". In: *Nucl. Instrum. Meth. A* 621.1-3 (2010), pp. 134 –150. doi: <http://dx.doi.org/10.1016/j.nima.2010.04.054>.
- [73] ATLAS Collaboration. "Jet energy measurement with the ATLAS detector in proton–proton collisions at $\sqrt{s} = 7$ TeV". In: *Eur. Phys. J. C* 73 (2013), p. 2304. doi: [10.1140/epjc/s10052-013-2304-2](https://doi.org/10.1140/epjc/s10052-013-2304-2). arXiv: [1112.6426 \[hep-ex\]](https://arxiv.org/abs/1112.6426). PERF-2011-03.
- [74] Nausheen R. Shah and Carlos E. M. Wagner. "Gravitons and dark matter in universal extra dimensions". In: *Phys. Rev. D* 74 (2006), p. 104008. doi: [10.1103/PhysRevD.74.104008](https://doi.org/10.1103/PhysRevD.74.104008). arXiv: [hep-ph/0608140 \[hep-ph\]](https://arxiv.org/abs/hep-ph/0608140).
- [75] Jonathan L. Feng, Arvind Rajaraman, and Fumihiro Takayama. "Graviton cosmology in universal extra dimensions". In: *Phys. Rev. D* 68 (2003), p. 085018. doi: [10.1103/PhysRevD.68.085018](https://doi.org/10.1103/PhysRevD.68.085018). arXiv: [hep-ph/0307375 \[hep-ph\]](https://arxiv.org/abs/hep-ph/0307375).
- [76] Paul H. Frampton and Pham Quang Hung. "Long-lived quarks?" In: *Phys. Rev. D* 58 (5 1998), p. 057704. doi: [10.1103/PhysRevD.58.057704](https://doi.org/10.1103/PhysRevD.58.057704). URL: <http://link.aps.org/doi/10.1103/PhysRevD.58.057704>.
- [77] C. Friberg, E. Norrbin, and T. Sjostrand. "QCD aspects of leptoquark production at HERA". In: *Phys. Lett. B* 403 (1997), pp. 329–334. doi: [10.1016/S0370-2693\(97\)00543-1](https://doi.org/10.1016/S0370-2693(97)00543-1). arXiv: [hep-ph/9704214 \[hep-ph\]](https://arxiv.org/abs/hep-ph/9704214).
- [78] Herbert K. Dreiner. "An introduction to explicit R-parity violation". In: (1997). arXiv: [hep-ph/9707435](https://arxiv.org/abs/hep-ph/9707435).
- [79] Edmond L. Berger and Zack Sullivan. "Lower limits on R-parity-violating couplings in supersymmetry". In: *Phys. Rev. Lett.* 92 (2004), p. 201801. doi: [10.1103/PhysRevLett.92.201801](https://doi.org/10.1103/PhysRevLett.92.201801). arXiv: [hep-ph/0310001](https://arxiv.org/abs/hep-ph/0310001).
- [80] R. Barbieri, C. Berat, M. Besancon, M. Chemtob, A. Deandrea, et al. "R-parity violating supersymmetry". In: *Phys. Rept.* 420 (2005), p. 1. doi: [10.1016/j.physrep.2005.08.006](https://doi.org/10.1016/j.physrep.2005.08.006). arXiv: [hep-ph/0406039](https://arxiv.org/abs/hep-ph/0406039).

- [81] M. Fairbairn et al. “Stable massive particles at colliders”. In: *Phys. Rept.* 438 (2007), p. 1. doi: [10.1016/j.physrep.2006.10.002](https://doi.org/10.1016/j.physrep.2006.10.002). arXiv: [hep-ph/0611040](https://arxiv.org/abs/hep-ph/0611040).
- [82] Christopher F. Kolda. “Gauge-mediated supersymmetry breaking: Introduction, review and update”. In: *Nucl. Phys. Proc. Suppl.* 62 (1998), p. 266. doi: [10.1016/S0920-5632\(97\)00667-1](https://doi.org/10.1016/S0920-5632(97)00667-1). arXiv: [hep-ph/9707450](https://arxiv.org/abs/hep-ph/9707450).
- [83] Howard Baer, Kingman Cheung, and John F. Gunion. “A Heavy gluino as the lightest supersymmetric particle”. In: *Phys. Rev. D* 59 (1999), p. 075002. doi: [10.1103/PhysRevD.59.075002](https://doi.org/10.1103/PhysRevD.59.075002). arXiv: [hep-ph/9806361](https://arxiv.org/abs/hep-ph/9806361).
- [84] S. James Gates Jr. and Oleg Lebedev. “Searching for supersymmetry in hadrons”. In: *Phys. Lett. B* 477 (2000), p. 216. doi: [10.1016/S0370-2693\(00\)00172-6](https://doi.org/10.1016/S0370-2693(00)00172-6). arXiv: [hep-ph/9912362](https://arxiv.org/abs/hep-ph/9912362).
- [85] Glennys R. Farrar and Pierre Fayet. “Phenomenology of the Production, Decay, and Detection of New Hadronic States Associated with Supersymmetry”. In: *Phys. Lett. B* 76 (1978), pp. 575–579. doi: [10.1016/0370-2693\(78\)90858-4](https://doi.org/10.1016/0370-2693(78)90858-4).
- [86] A. C. Kraan, J. B. Hansen, and P. Nevski. “Discovery potential of R-hadrons with the ATLAS detector”. In: *Eur. Phys. J. C* 49 (2007), pp. 623–640. doi: [10.1140/epjc/s10052-006-0162-x](https://doi.org/10.1140/epjc/s10052-006-0162-x). arXiv: [hep-ex/0511014](https://arxiv.org/abs/hep-ex/0511014) [hep-ex].
- [87] Rasmus Mackeprang and David Milstead. “An Updated Description of Heavy-Hadron Interactions in GEANT-4”. In: *Eur. Phys. J. C* 66 (2010), pp. 493–501. doi: [10.1140/epjc/s10052-010-1262-1](https://doi.org/10.1140/epjc/s10052-010-1262-1). arXiv: [0908.1868](https://arxiv.org/abs/0908.1868) [hep-ph].
- [88] ATLAS Collaboration. “Search for massive, long-lived particles using multitrack displaced vertices or displaced lepton pairs in pp collisions at $\sqrt{s} = 8$ TeV with the ATLAS detector”. In: *Phys. Rev. D* 92 (2015), p. 072004. doi: [10.1103/PhysRevD.92.072004](https://doi.org/10.1103/PhysRevD.92.072004). arXiv: [1504.05162](https://arxiv.org/abs/1504.05162) [hep-ex]. SUSY-2014-02.
- [89] ATLAS Collaboration. “Search for charginos nearly mass degenerate with the lightest neutralino based on a disappearing-track signature in pp collisions at $\sqrt{s} = 8$ TeV with the ATLAS detector”. In: *Phys. Rev. D* 88 (2013), p. 112006. doi: [10.1103/PhysRevD.88.112006](https://doi.org/10.1103/PhysRevD.88.112006). arXiv: [1310.3675](https://arxiv.org/abs/1310.3675) [hep-ex]. SUSY-2013-01.
- [90] ATLAS Collaboration. “Searches for heavy long-lived sleptons and R-Hadrons with the ATLAS detector in pp collisions at $\sqrt{s} = 7$ TeV”. In: *Phys. Lett. B* 720 (2013), p. 277. doi: [10.1016/j.physletb.2013.02.015](https://doi.org/10.1016/j.physletb.2013.02.015). arXiv: [1211.1597](https://arxiv.org/abs/1211.1597) [hep-ex]. SUSY-2012-01.
- [91] ATLAS Collaboration. “Searches for heavy long-lived charged particles with the ATLAS detector in proton–proton collisions at $\sqrt{s} = 8$ TeV”. In: *JHEP* 01 (2015), p. 068. doi: [10.1007/JHEP01\(2015\)068](https://doi.org/10.1007/JHEP01(2015)068). arXiv: [1411.6795](https://arxiv.org/abs/1411.6795) [hep-ex]. SUSY-2013-22.

- 4364 [92] ATLAS Collaboration. “Search for metastable heavy charged particles
 4365 with large ionisation energy loss in pp collisions at $\sqrt{s} = 8$ TeV using the
 4366 ATLAS experiment”. In: *Eur. Phys. J. C* 75 (2015), p. 407. doi: [10.1140/epjc/s10052-015-3609-0](https://doi.org/10.1140/epjc/s10052-015-3609-0). arXiv: [1506.05332 \[hep-ex\]](https://arxiv.org/abs/1506.05332). SUSY-
 4367 2014-09.
- 4369 [93] ATLAS Collaboration. “Search for heavy long-lived charged R -hadrons
 4370 with the ATLAS detector in 3.2 fb^{-1} of proton–proton collision data at
 4371 $\sqrt{s} = 13$ TeV”. In: *Phys. Lett. B* 760 (2016), pp. 647–665. doi: [10.1016/j.physletb.2016.07.042](https://doi.org/10.1016/j.physletb.2016.07.042). arXiv: [1606.05129 \[hep-ex\]](https://arxiv.org/abs/1606.05129).
- 4373 [94] ATLAS Collaboration. *Further ATLAS tunes of Pythia 6 and Pythia 8*. ATL-
 4374 PHYS-PUB-2011-014. 2011. URL: <https://cds.cern.ch/record/1400677>.
- 4376 [95] Aafke Christine Kraan. “Interactions of heavy stable hadronizing parti-
 4377 cles”. In: *Eur. Phys. J. C* 37 (2004), pp. 91–104. doi: [10.1140/epjc/s2004-01946-6](https://doi.org/10.1140/epjc/s2004-01946-6). arXiv: [hep-ex/0404001 \[hep-ex\]](https://arxiv.org/abs/hep-ex/0404001).
- 4379 [96] M. Fairbairn et al. “Stable massive particles at colliders”. In: *Phys. Rept.*
 4380 438 (2007), p. 1. doi: [10.1016/j.physrep.2006.10.002](https://doi.org/10.1016/j.physrep.2006.10.002). arXiv:
 4381 [hep-ph/0611040](https://arxiv.org/abs/hep-ph/0611040).
- 4382 [97] W. Beenakker, R. Hopker, M. Spira, and P. M. Zerwas. “Squark and gluino
 4383 production at hadron colliders”. In: *Nucl. Phys. B* 492 (1997), p. 51. doi:
 4384 [10.1016/S0550-3213\(97\)00084-9](https://doi.org/10.1016/S0550-3213(97)00084-9). arXiv: [hep-ph/9610490](https://arxiv.org/abs/hep-ph/9610490).
- 4385 [98] A. Kulesza and L. Motyka. “Threshold resummation for squark-antisquark
 4386 and gluino-pair production at the LHC”. In: *Phys. Rev. Lett.* 102 (2009),
 4387 p. 111802. doi: [10.1103/PhysRevLett.102.111802](https://doi.org/10.1103/PhysRevLett.102.111802). arXiv: [0807.2405 \[hep-ph\]](https://arxiv.org/abs/0807.2405).
- 4389 [99] A. Kulesza and L. Motyka. “Soft gluon resummation for the production
 4390 of gluino-gluino and squark-antisquark pairs at the LHC”. In: *Phys. Rev.*
 4391 D 80 (2009), p. 095004. doi: [10.1103/PhysRevD.80.095004](https://doi.org/10.1103/PhysRevD.80.095004). arXiv:
 4392 [0905.4749 \[hep-ph\]](https://arxiv.org/abs/0905.4749).
- 4393 [100] Wim Beenakker, Silja Brening, Michael Kramer, Anna Kulesza, Eric Lae-
 4394 nen, et al. “Soft-gluon resummation for squark and gluino hadroprodu-
 4395 tion”. In: *JHEP* 0912 (2009), p. 041. doi: [10.1088/1126-6708/2009/12/041](https://doi.org/10.1088/1126-6708/2009/12/041). arXiv: [0909.4418 \[hep-ph\]](https://arxiv.org/abs/0909.4418).
- 4397 [101] W. Beenakker, S. Brening, M.n Kramer, A. Kulesza, E. Laenen, et al. “Squark
 4398 and Gluino Hadroproduction”. In: *Int. J. Mod. Phys. A* 26 (2011), p. 2637.
 4399 doi: [10.1142/S0217751X11053560](https://doi.org/10.1142/S0217751X11053560). arXiv: [1105.1110 \[hep-ph\]](https://arxiv.org/abs/1105.1110).
- 4400 [102] Michael Krämer et al. *Supersymmetry production cross sections in pp colli-*
 4401 *sions at $\sqrt{s} = 7$ TeV*. 2012. arXiv: [1206.2892 \[hep-ph\]](https://arxiv.org/abs/1206.2892).
- 4402 [103] Rasmus Mackeprang and Andrea Rizzi. “Interactions of Coloured Heavy
 4403 Stable Particles in Matter”. In: *Eur. Phys. J. C* 50 (2007), pp. 353–362. doi:
 4404 [10.1140/epjc/s10052-007-0252-4](https://doi.org/10.1140/epjc/s10052-007-0252-4). arXiv: [hep-ph/0612161](https://arxiv.org/abs/hep-ph/0612161)
 4405 [hep-ph].

- 4406 [104] Rasmus Mackeprang and David Milstead. “An Updated Description of
4407 Heavy-Hadron Interactions in GEANT-4”. In: *Eur. Phys. J.* C66 (2010),
4408 pp. 493–501. doi: [10.1140/epjc/s10052-010-1262-1](https://doi.org/10.1140/epjc/s10052-010-1262-1). arXiv:
4409 [0908.1868 \[hep-ph\]](https://arxiv.org/abs/0908.1868).
- 4410 [105] “dE/dx measurement in the ATLAS Pixel Detector and its use for particle
4411 identification”. In: (2011).
- 4412 [106] ATLAS Collaboration. “The ATLAS Simulation Infrastructure”. In: *Eur.*
4413 *Phys. J.* C70 (2010), pp. 823–874. doi: [10.1140/epjc/s10052-010-1429-9](https://doi.org/10.1140/epjc/s10052-010-1429-9). arXiv: [1005.4568 \[physics.ins-det\]](https://arxiv.org/abs/1005.4568).
- 4415 [107] ATLAS Collaboration. “Luminosity determination in pp collisions at \sqrt{s}
4416 = 8 TeV using the ATLAS detector at the LHC”. In: (2016). arXiv: [1608.03953 \[hep-ex\]](https://arxiv.org/abs/1608.03953).
- 4418 [108] Alexander L. Read. “Presentation of search results: The CL(s) technique”.
4419 In: *J. Phys.* G28 (2002). [,11(2002)], pp. 2693–2704. doi: [10.1088/0954-3899/28/10/313](https://doi.org/10.1088/0954-3899/28/10/313).
- 4420